Guided Waves Systems with Embedded Two-Dimensional Materials

von Gia Quyet Ngo, Master of Science

geboren am 25.08.1987 in Hung Yen, Vietnam

Contents

1. Introduction

Stemming from the discovery of graphene in 2004 using mechanical exfoliation via Scotch tape [1], two-dimensional (2D) materials received great attention from the scientific community [2-11], opening a new era of atomically thin semiconducting materials. The atomically thin thickness of 2D materials provides excellent access to the bound electron-hole pairs, such as excitons [8, 12-14] or new degrees of freedom of the electronic valley [13-15]. Figure 1.1 presents the atomic structures of some outstanding 2D materials, such as graphene, molybdenum disulfide MoS_2, black phosphorus, and hexagonal boron nitride (hBN). Each material has different bandgap energies corresponding to different spectral ranges and may find interest in many applications.
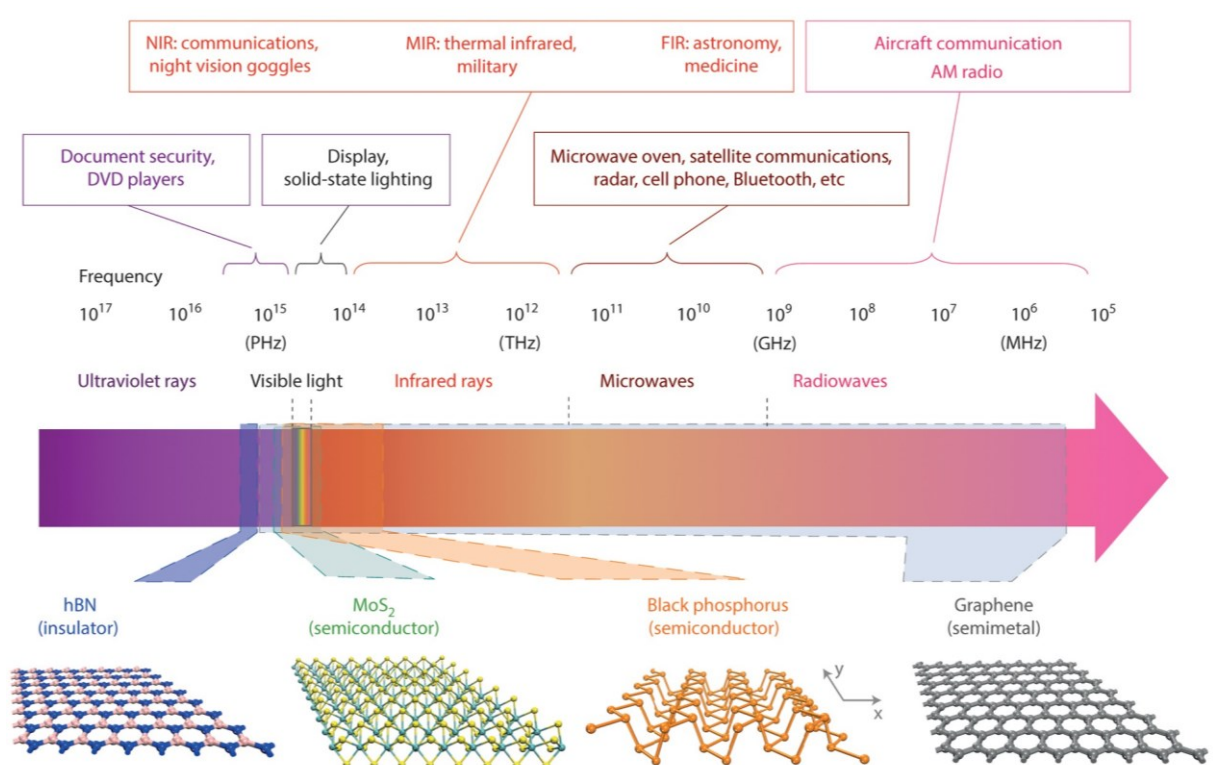
Figure 1.1: The atomic structures of hBN, MoS_2, black phosphorus, and graphene. The electromagnetic spectrum is divided into different spectral ranges covered by various 2D materials according to their bandgap. Some typical applications for each spectral range are presented accordingly. Figure is adapted from [15].

Pristine graphene is a monocrystalline form of graphite with one atom thickness, and thus it is classified in the group of 2D materials. With only one carbon atom layer, graphene is the thinnest material that has been discovered so far with a thickness of about 0.4 nm [16, 17]. This material has a hexagonal honeycomb lattice comprised of strongly bound carbon atoms. Graphene possesses many outstanding properties compared to bulk graphite [1, 4], for instance, an ultrahigh charge carrier mobility up to 200,000 cm^2/Vs at 5 K [3] or more than 100,000 cm^2/Vs at room temperature [18-20] and a long mean free pathway of electrons in the order of one micrometer [1, 3]. Due to the massless Dirac fermions in graphene, electrons at low-energy states near the Dirac point exhibit an unprecedented high Fermi velocity of approximately 10^6 m/s [17, 21]. Therefore, the resistivity

of graphene is very low (~1.0 μΩ/cm) and less than silver (~1.5 μΩ/cm) [17, 21]. Together with the highest in-plane strength amongst known materials with a tensile strength of 130 GPa and Young's modulus of 1 TPa [2, 20, 22], graphene is in a unique position in the 2D materials family.

Remarkably, the zero bandgap of the graphene at the Dirac points, the intersection between the valance band and the conduction band, results in the absorption of a broad spectrum of light from UV to THz frequencies [23]. Despite the ultrathin thickness, graphene has a significant light-matter interaction with a flat absorption rate of 2.3 % in the visible spectral range [20, 24]. All the above appealing physical properties make graphene a strong contender for ultrafast and broadband photodetectors. The supreme properties of graphene are highly attractive to multiple functional devices such as broadband optical modulators [25, 26], photodetectors [23, 27, 28], sensors [29], mode-locked lasers [30, 31], substantial nonlinear optical response [32-34] and many more [20, 35, 36]. Additionally, the strong adhesion of graphene on SiO_2/Si substrates can lead to pressure sensors [37] and support a scalable integration of graphene in data and telecommunication [38], high-speed computer chips [39], flexible electronics [20], and energy storage [40], to name a few.

Although graphene is an intriguing semimetal with extraordinary mechanical strength [2, 20], ultrahigh charge mobility [3, 18], and a prime example in the 2D materials family, the lack of a bandgap [1, 13, 15, 41] limits its applicability in many practical applications which require a finite bandgap such as transistors [9, 42, 43]. A bright perspective of ultrathin, ultrafast, and flexible electronic devices in the future triggered the emergence of other 2D materials besides graphene to realize a new generation of extremely thin transistors and integrated photonics [13, 43-45]. In general, 2D materials are not restricted to only single-layer materials but also refer to few-layers, multilayers, and heterostructures whose total thickness can be up to tens of nanometers [14, 15, 23, 43]. Similar to graphite, each layer of 2D materials is stacked on top of each other by a weak van der Waals force. Recently, van der Waals heterostructures drew lots of attention because of exciting physics, including but not limited to polariton, electroluminescence, photovoltaic effect, band-to-band tunnel transistors, and long-lived interlayer excitons [46-50].

To date, there are about 1800 different materials that can be exfoliated or are predicted to have a stable monolayer form [46, 51]. The simplicity of mechanical exfoliation to prepare high-quality semiconducting samples with extraordinary physical properties is the main reason for the popularity of 2D materials [52, 53]. Besides graphene, many 2D-semiconductor materials have been studied intensively, including hBN [54-56], black phosphorus [57-60], and transition metal dichalcogenides [13, 15, 43, 45]. Hexagonal BN is a direct bandgap semiconductor with a wide bandgap and hence is often utilized as a substrate or encapsulator for other 2D materials [52, 54, 56, 61]. Furthermore, hBN can be used as a gate dielectric for field-effect transistors [62, 63].

1. Introduction

Recently, hBN has shown the potential for quantum technology as it can host deep defects within its wide bandgap, and those deep states can emit single photons at room temperature [64, 65]. Black phosphorus is quite young amongst other 2D materials; the earliest works with this atomically thin material were reported in 2014 [57, 58]. The charge carrier mobility of black phosphorus is in the range from 100 to 1000 $cm^2V^{-1}s^{-1}$ [52, 57, 58], and it has a direct bandgap of 1.0 eV in the monolayer limit [58]. The fascinating electronic properties of black phosphorus make them attractive for CMOS applications [57, 58]. Although black phosphorus has significant potential in optoelectronics, it behaves hydrophilic and unstable under long-term exposure to ambient air [59, 60].

In the 2D-materials family, transition metal dichalcogenides (TMDs) recently received the most attention besides graphene [7, 10, 13-15, 31, 43, 45]. 2D TMDs are highly appealing for photonics [13, 15] and optoelectronics [14, 43, 45] due to their unique physical properties and substantial interaction with light. The semiconductors constructed from transition metal atoms (e.g., Mo, W) and chalcogen atoms (e.g., S, Se, Te) have attracted the most interest from research groups in the last few years [7-11, 13-15, 43-45, 66].

There is a massive change in the optical and electronic properties of TMDs when their thickness decreases from bulk down to the monolayer [7, 8, 43, 66]. As a result of the reduced dielectric screen effect [67-69], these monolayer TMDs possess a direct bandgap with energies ranging from 1.5 - 2 eV (visible to near-infrared frequencies) with high photoluminescence (PL) quantum yield compared to the bulk crystal [7, 8, 44]. Their exceptional light absorption per unit thickness [11, 70] makes them appealing for numerous applications. For instance, the large surface-to-volume ratio of monolayer TMDs offers a gateway to highly sensitive and rapid-response sensors for gas sensing and bioanalytics [10, 45, 71-73]. Likewise, other excellent properties of 2D TMDs, such as sensitive photodetection [74, 75], low threshold lasing [76, 77], and valley Hall effect [78, 79], are fascinating for valley-based information storage and processing [80-82]. Additionally, the excitons in monolayer TMDs are particularly interesting for spin valley coupling [78, 83-85] and single-photon emission [86-90].

The high surface-to-volume ratio is an advantage of 2D materials in general or monolayer TMDs in particular. This feature makes 2D TMDs a potential candidate for remote sensing [91-96]. The adsorption of the gas molecules on the surface of TMD crystals can alter the charge distribution via the charge transfer process. Many research groups used the semiconductor TMDs as a channel in a field effect transistor to detect the sensing target by monitoring the resistivity. The charge transfer process between the gas molecules and semiconductors leads to a certain doping level of semiconductors. As a result, the resistance of the transistor channel or the current running through

it will vary, and this variation is measurable. In another approach, some groups have used the high PL quantum yield of monolayer TMDs and monitored the modulation of PL signal during contact with gas species. This method does not require the fabrication of any transistor, and an optical light source will be employed to stimulate PL emission from TMD crystals. In this thesis, we will discuss optical gas sensing via the monitor of PL from monolayer MoS_2 as one proof of concept.

The impact of nonlinear optics in our daily life can be easily recognized with Q-switching, mode-locking, and second harmonic in the applications of lasers. In terms of nonlinear optics, monolayer TMDs are well-known for their substantial nonlinear susceptibility per unit thickness. Some typical nonlinear optical phenomena, such as second-harmonic generation (SHG) and third-harmonic generation (THG) of 2D materials, have been studied intensively in the last few years [97-105]. SHG is the lowest-order nonlinear process and was first observed in 1961 [106], right after the demonstration of the first working laser in 1960 [107]. This nonlinear process is also responsible for the tunable optical parametric oscillators (OPO) [108] and optical parametric amplifiers [109], which are used in many applications. Analogous to SHG, spontaneous parametric down-conversion (SPDC) is another second-order nonlinear process that is highly attractive for quantum information, quantum imaging, and several others [110]. Up to now, nonlinear optical devices are working upon bulk nonlinear crystals produced via a complex manufacturing process. Through progress like nanostructuring, defect engineering, and heterostructure fabricating, nanomaterials are desired to open a novel pathway toward nano-optoelectronic devices [15, 111-113].

TMDs possess a remarkable second-order nonlinearity compared to traditional bulk crystals, although they have a sub-nanometer thickness [98, 114]. For example, the reported nonlinear susceptibilities $\chi^{(2)}$ are 2.2 pm/V for beta barium borate at 1064 nm [115], 0.4 pm/V with quartz at 1052.8 nm [115], 0.43 pm/V for potassium dihydrogen phosphate at 1064 nm [116], and 27.2 pm/V for lithium niobate $LiNbO_3$ at 1064 nm [117]. Meanwhile, the reported nonlinear susceptibilities of monolayer MoS_2 vary from a few pm/V to 10^5 pm/V. Specifically, Säynätjoki *et al*. [99] reported an effective $\chi^{(2)}$ value of 2.2 pm/V at 1560 nm for an exfoliated monolayer of MoS_2 on SiO_2/Si substrate. Woodward *et al*. reported an effective $\chi^{(2)}$ value of 29 pm/V at 1560 nm for a CVD-grown monolayer MoS_2 [100]. Both of these works confirmed that monolayer MoS_2 offers a higher nonlinear response than graphene in the same condition. Malard *et al*. characterized an exfoliated monolayer MoS_2 on SiO_2/Si substrate and reported a $\chi^{(2)}$ value of 123 pm/V at 800 nm, which is near the C-exciton band [97]; meanwhile, Li *et al*. reported a $\chi^{(2)}$ value of 160 pm/V at 810 nm for a monolayer MoS_2 [105]. The highest reported $\chi^{(2)}$ value so far is 10^5 pm/V by Kumar *et al*., measured from a mechanically exfoliated monolayer MoS_2 at 810 nm [101]. The

discrepancy in the reported $\chi^{(2)}$ values here is likely due to the differences in estimation method, substrate, excitonic effects, and sample preparation. All the highest reported second-order susceptibility are in resonance with the C-exciton of the monolayer MoS_2. The results from different research groups show a significant potential of this 2D materials family in nonlinear optics. The large and ultrafast nonlinear optical processes in 2D TMDs are highly sought-after in applications like all-optical modulators, saturable absorbers, and frequency converters [97, 118-120].

In contrast to bulk nonlinear crystals where the phase-matching condition cannot be ignored in a nonlinear process, monolayer thickness is nevertheless far shorter than the coherence length; therefore, the phase mismatch is negligible. The nonlinear efficiency is now solely dependent on the conservation of the transverse momentum [121]. Besides, many studies on THG and high harmonic generation responses of monolayer TMDs suggest their promising applications in nonlinear optics and photonics. Hence, the integration of highly nonlinear monolayer TMDs on photonic devices may pave the way for future nanophotonic chips.

There are many ways to obtain monolayer TMDs, and they can be classified into two categories: top-down and bottom-up approaches. Some examples of top-down methods are mechanical exfoliation with adhesive tapes and solution processing, whereas some typical bottom-up techniques are chemical vapor deposition (CVD) [44, 122], molecular beam epitaxy [44, 123], physical vapor deposition [124], atomic layer deposition [125, 126], or metal-organic chemical vapor deposition (MOCVD) [44, 127]. The choice of the growth method depends on many factors, including crystal size, quality, and price. For example, the molecular beam epitaxy provides a high-quality standard in growing pristine graphene [128]; nevertheless, the cost is much higher than in CVD techniques [20]. Although the mechanical exfoliation technique has shown its advantage of producing high crystal quality, the low yield and time consumption are the drawbacks hindering them from a scalable integration with 2D materials. On the other hand, the CVD method can produce high-quality TMD crystals in a scalable way. In the scope of this thesis, TMD crystals were grown from a modified CVD process by the group of Prof. Dr. Andrey Turchanin at the Institute of Physical Chemistry at Friedrich Schiller University Jena.

The common approach of experiments with monolayer TMDs in the research community is to mechanically exfoliate and transfer them onto a substrate for characterization, as mentioned in many research works [97, 99, 101, 105, 118]. However, for monolayer TMDs, the light-matter interaction length is limited to sub-nanometers due to their infinitesimal thickness. There are two crucial things one should consider here. First, the minuscule thickness will reduce the total optical response from the monolayers significantly. Second, the mechanical transferring may not be

scalable and applicable to promising and complex integrated structures. To solve the first issue, the light-matter interaction has to be enhanced before it can be used for any application. Therefore, any approach to boost the light-matter interaction is highly sought-after. One strategy is to couple TMDs with optical resonators. This method was demonstrated in planar open [129, 130] and monolithic resonators [131, 132], as well as with photonic crystal resonators [76, 133], microdisk cavities [134], and nanoresonators [135]. These resonators, nevertheless, are limited to narrowband resonances, whereas broadband and ultrafast operations are not supported with this approach.

Alternatively, the integration of 2D materials with waveguides or optical fibers can increase the interaction length tremendously and thus maybe suitable for non-resonant, ultrafast, and broadband operation. The validity of the 2D material-coated waveguides approach has already been proven by some works. For example, graphene with significant optical nonlinearity has been integrated as a saturable absorber onto photonic crystal fibers to demonstrate pulsed fiber lasers [17, 32]. Similarly, few-layer MoS_2 has been deposited on microfibers as a saturable absorber to establish a passively harmonic mode-locked fiber laser [136]. Another investigation into 2D material-coated waveguides has also been undertaken, where side-polished telecom fibers with multilayer MoS_2-coating [137] displayed enhanced self-phase modulation (SPM). Additionally, silicon waveguides with $MoSe_2$ [138] or MoS_2 [139, 140] coatings have shown the enhancement of SHG and SPM [141]. Recently, silica fibers have been functionalized with MoS_2 to enhance the SHG and THG processes [142, 143].
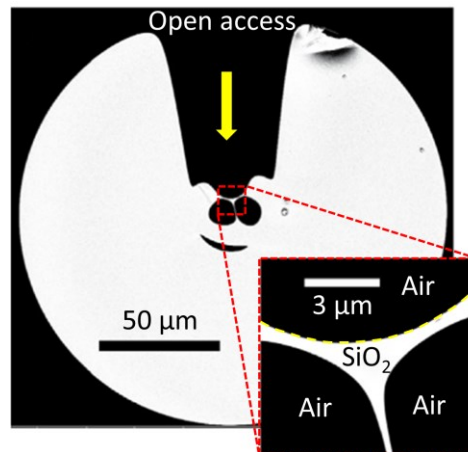
Figure 1.2: Scanning electron microscope image of an exposed-core fiber and the core area (inset). The open access is highlighted by a yellow arrow, and the exposed surface is highlighted by a yellow dashed curve. Figure is adapted from [144].

Most of the above-mentioned works relied on the mechanical transfer of 2D materials onto waveguides or optical fibers. This manual transfer is likely to bring unexpected stress fields, and its results are difficult to reproduce. It is also not scalable and thus hardly suitable for many types of future integration technologies. Furthermore, the mechanical transfer of 2D materials is only

applicable to a flat surface. Therefore, a process that can grow high-quality monolayer TMDs directly on optical fibers or waveguides is extremely desired to bring 2D material-coated waveguides to the next level.

This work has overcome this obstacle by directly growing monolayer TMDs on the core of exposed-core optical fibers (ECFs) [144, 145], turning them into TMD-coated ECFs, in a scalable and non-transfer process [146]. These TMD-coated ECFs operate via the interaction of monolayer TMDs with the evanescent fields of the guided light because the monolayers are in direct physical contact with the fiber core. TMD-coated ECFs can perform outstandingly due to their functional design to exploit the nonlinear and excitonic properties of monolayer TMDs, for instance, by changing geometry or constituent components. More precisely, the aim of this work is to show the ability to grow monolayer TMDs directly on the guiding core of all-silica ECFs, which exhibit strong field confinement. In contrast to suspended core fibers, where the core is covered by the outer solid part of the fiber, ECFs support partial access to the fiber core, as displayed in Figure 1.2. The precursors of MoS_2, for instance, sulfur and MoO_3, can interact and grow crystals on the entire surface of ECFs, including the upper part of the core. The design of ECFs makes them more suitable for applications like real-time gas sensing than suspended core fibers because it provides instant contact between 2D materials and gas molecules. The open access to the fiber core also makes any modification on the fiber core easier. Based on their versatility and flexibility, ECFs have been chosen in this research work. In this thesis, ECFs were fabricated by the collaboration between the research group of Prof. Dr. Heike Ebendorff-Heidepriem at the University of Adelaide and the group of Prof. Dr. Markus Schmidt at the Leibniz Institute of Photonic Technology.

To wrap up this introduction part, both linear and nonlinear properties of 2D TMDs have been investigated in this thesis. The entire aims of this thesis are as follows:

1. Construct a numerical model to quantify the linear and nonlinear properties of TMD-coated ECFs and use this model to optimize the structure of ECFs for high nonlinear conversion efficiency.

2. Demonstrate a proof-of-concept by directly growing monolayer TMDs on the ECFs to functionalize the fiber core and showing the distinct possibilities: in-fiber excitonic excitation, PL collection, and enhanced THG.

3. Demonstrate that ECF functionalized with the monolayer TMDs can be used for remote sensing of gases.

4. Demonstrate that the SHG can be generated from the ECFs functionalized by monolayer TMDs. Calculate quantitatively the nonlinear parameters of this hybrid system.

The thesis is organized as follows. The introduction chapter provides all important information about semiconducting 2D materials, including graphene, hexagonal boron nitride, black phosphorous, and TMDs; their interesting physical phenomena; and updates on the research activities from the scientific community related to these materials. An overview of ECFs is also given in Chapter 1 to highlight their excellent properties as a platform to integrate with 2D materials. Chapter 2 describes the fundamental theoretical overview of 2D TMDs, such as exciton, band structure, types, and nonlinearities. It explains shortly the change of band structure in terms of the number of atomic layers and the spin-orbit coupling happening in monolayer TMDs. The general nonlinear optical process and especially the nonlinearities of monolayer TMDs are discussed here with the perspective of using them for photonics and nonlinear optics. This chapter will provide more information about ECFs and how to integrate monolayer TMDs on this waveguide. Chapter 3 covers all the characterization methods used in this thesis to examine the optical properties and crystallographic structure of as-grown monolayer TMDs. Chapter 4 will discuss the exciton excitation of monolayer TMDs, and photoluminescence-related experimental results. Coming up with the idea to realize gas sensing based on PL, Chapter 5 contains a theoretical discussion about the fluorescence capture fraction, gas sensing mechanisms, refractive index sensing, and gas sensing experimental results. Here, the realization of gas sensing using optical fibers and monolayer MoS_2 is discussed in detail. Chapter 6 presents the numerical modeling of guided modes in the fiber core, the numerical calculation of the nonlinear coefficient, and experimental results of the THG generated from ECFs and TMD-coated ECF. Evaluating the second-order nonlinear susceptibility of the TMD-coated ECF is a challenge because the monolayers have different orientations, random locations and sizes. In Chapter 7, we will demonstrate a new approach to create a single crystal on the ECF and present the benchmarked susceptibility from the hybrid system. This chapter also includes the numerical modeling of the SHG process in TMD-coated ECF and the experimental results of the SHG enhancement by TMD-coated ECF in resonance with excitons. Finally, Chapter 8 gives a summary of the work and discusses future perspectives and outlooks.

2. Sample properties and fabrication

2.1 Types of TMD and their symmetries

TMDs are structured as MX_2, comprising a transition metal atom (M) and two chalcogen atoms (X), and have hexagonal or rhombohedral symmetry [43]. Figure 2.1a shows a three-dimensional view of TMDs. A monolayer TMD is constructed with three atomic planes, where the top and bottom planes are chalcogen atoms (S, Se, Te), while the middle plane contains transition metal atoms (Mo, W). The variation in the arrangement of six X atoms around the central M atom results in two symmetries, as illustrated in Figure 2.1b where trigonal prismatic is on the left side, and octahedral phase is on the right side. In the former case, the X atoms will define the vertices of a triangular prism, whereas in the latter case, the X atoms will define the vertices of an octahedron. The difference in the atom arrangement between these two phases is clear from the basal plane view.

Figure 2.1c displays the covalent bonds between M atoms and X atoms within the monolayer and the weak bond between adjacent layers. Noticeably, different layers of TMDs are bound together by a weak van der Waals force and stackable either vertically or horizontally to form vertical or lateral van der Waals heterostructures, respectively [147]. The van der Waals force of the interlayer is significantly weaker than the covalent bond of the intralayer [15, 43, 46], and hence, we can easily exfoliate the monolayer TMD analogous to graphene. Moreover, this unique structure enables them for ease of integration and miniaturization for future nanophotonic devices. Additionally, the monolayer TMDs can grow conformally on numerous substrates via van der Waals forces, also called van der Waals epitaxy, with a large relaxation in the lattice mismatch of up to 50 % [148, 149]. This van der Waals epitaxy is different from the conventional heteroepitaxy for three-dimensional materials, which requires a proper lattice matching between the epitaxial layer and substrate to achieve heterostructures [149, 150]. The lack of dangling bonds at the surface of monolayer TMDs leads to a chemically inert surface and supports the van der Waals epitaxy [149]. This terminated surface provides the stability against the reaction with surrounding chemical species [151, 152] and the ability to form heterostructures by vertical stacking of different TMDs [153, 154].

One of the most striking features of TMDs is that not all of them are semiconductors. Depending on the pairing of the M atom and X atoms, different phases such as semiconductor, metal, or superconductor can be formed [43]. For instance, some intriguing semiconductors are MoS_2, WS_2, $MoSe_2$, and WSe_2. $NbTe_2$ and $TaTe_2$ are metallic, while NbS_2 and $NbSe_2$ are super-conducting
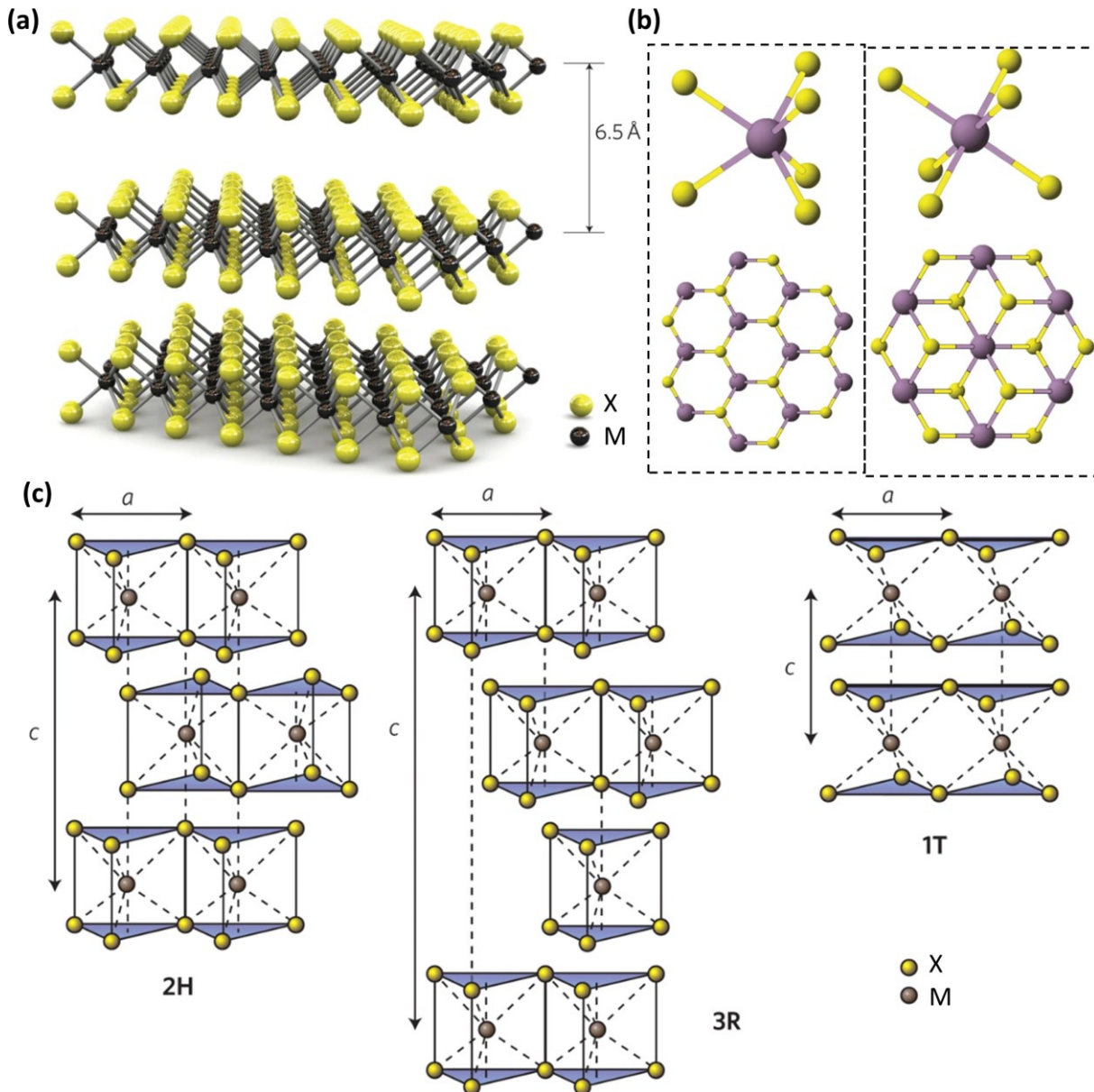
Figure 2.1: (a) The TMD structure of MX_2 in a three-dimensional representation with chalcogen atoms (X) in yellow and the transition metal atoms (M) in black. The subfigure is adapted from [9]. **(b)** The left panel shows the crystal structure and the top view of monolayer TMD with trigonal prismatic coordination (2H phase). The right panel shows the crystal structure and the top view of monolayer TMD with octahedral coordination (1T phase). The subfigure is adapted from [155]. **(c)** Schematic of 2H, 3R, and 1T phases with six covalent bonds between a transition metal atom with upper and lower chalcogen atoms creating a trigonal prismatic geometry for 2H and 3R. An octahedral geometry is found in the 1T phase. A monolayer of MX_2 lacks inversion symmetry, while a bilayer MX_2 is centrosymmetric in the 2H form. The broken symmetry happens for each layer in the 3R phase. c index indicates the number of layers in each stacking order. The subfigure is adapted from [43].

materials [156]. Both monolayer and a few layers of the group-VI TMDs are stable in the air at room temperature [157] and are well-suitable for daily-life electronic applications.

Furthermore, there are multiple crystal structures of TMDs, including hexagonal (2H), rhombohedral (3R), and tetragonal (1T) forms depending on the arrangement of chalcogen atoms around the central transition metal atoms and the stacking of layers. Figure 2.1c displays the arrangement of X atoms around the central M atom in the 2H, 3R, and 1T phases. In the 2H phase,

the unit cell consists of two layers joined together by weak van der Waals forces. In the 3R phase, the unit cell consists of three layers, and there is only one layer in the unit cell for the 1T phase. So the 2H phase TMD has two layers in the unit cell and has a hexagonal crystal structure. The monolayer TMD in the 2H phase belongs to the D_{3h} point group [14, 103, 158, 159]. In general, 2H TMDs have the D_{3h} point group for odd-numbered layers and the D_{3d} point group for even-numbered layers [99, 159, 160]. The 1T phase has a tetragonal symmetry and belongs to the D_{3d} point group [161, 162]. The electronic and phase properties of 2D TMDs are strongly dependent on the filling status of the d orbitals of transition metal atoms. The complete filling of d orbitals leads to semiconducting character, whereas the partial filling of d orbitals favors metallic behavior [161]. For example, 2H and 3R phases are semiconductors, whereas 1T phase TMDs are metals [163]. Within the 2H phase, monolayer TMDs can be intrinsic n-type semiconductors (MoS_2, WS_2, $MoSe_2$) or p-type semiconductors (WSe_2) [45, 164-166]. Normally, the 1T phase is less stable than the semiconducting phases due to the high reactivity of metals [157]. On the other hand, both hexagonal 2H and rhombohedral 3R phases are semiconductors and stable, nevertheless, the lack of scalable growth of the 3R phase is a challenge for future photonics applications. In this work, only semiconducting layers in the 2H phase are investigated for optical properties considering the simplicity, scalability, and stability of this form.
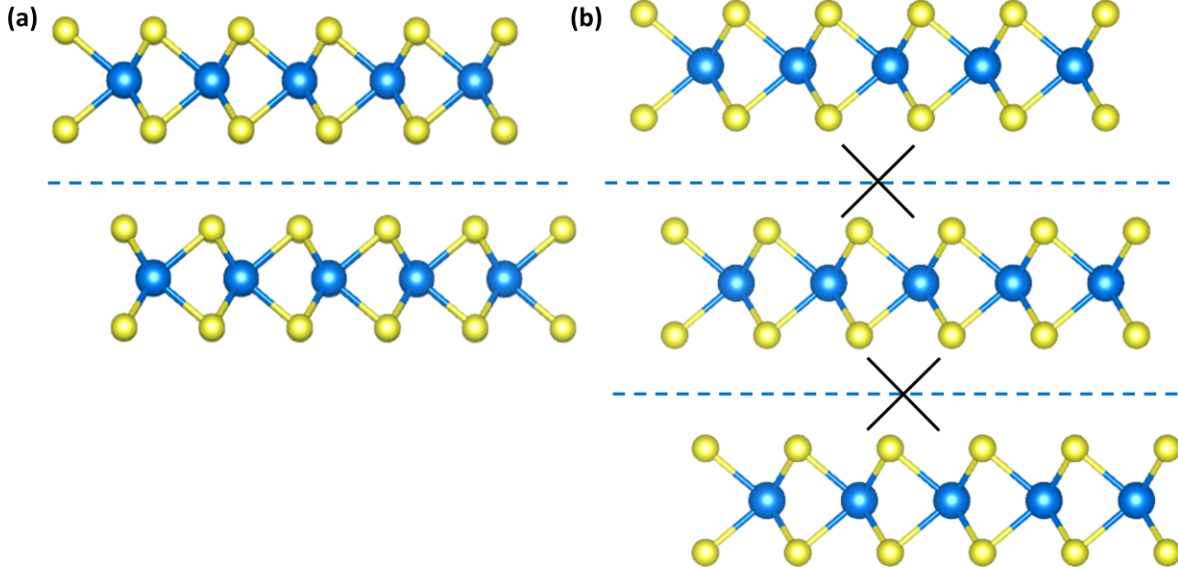
Figure 2.2: (a) Side view of symmetric 2H phase bilayer TMD. **(b)** Side view of asymmetric 3R phase TMD. Dashed line indicates the mirror symmetry of in-plane dipoles. Black cross indicates the mirror symmetry does not exist.

Because the 2H and 3R phase TMD are fascinating semiconductors, it would be necessary to discuss their behavior concerning the number of layers. Figure 2.2a illustrates the side view of the symmetric 2H phase for two layers in the unit cell. There is a mirror symmetry for bilayer or even-numbered layers, as shown by a dashed line in Figure 2.2a. The odd-numbered layers are noncentrosymmetric. The stacking of an adjacent layer to 2H TMD restores the inversion symmetry

of in-plane dipoles because they mirror the orientation compared to the previous layer. Figure 2.2b exhibits the crystal arrangement in the 3R phase TMD. The adjacent layers in the 3R TMD are shifted along the in-plane direction without changing the orientation. Thus, the 3R TMD does not possess an inversion symmetry in even-numbered layers. The inversion symmetry will strongly affect the SHG process and will be discussed in detail in Chapter 7.

2.2 Band structure of TMDs

The band structure of TMD crystals changes drastically with the decreasing number of layers. For instance, TMDs such as MoS_2, WS_2, $MoSe_2$, and WSe_2 possess an indirect bandgap in the form of a bilayer to bulk crystal and a direct bandgap in the form of a monolayer [7, 8, 167]. Figure 2.3 displays the calculated electronic band structure of the MoS_2 crystal. There is an abrupt change from an indirect bandgap at the Γ point to a direct bandgap at the K point in the first Brillouin zone because of the perpendicular quantum confinement in the monolayer [7]. In the bulk form, MoS_2 has an indirect bandgap of 1.2 eV, whereas, in the monolayer limit, it has a direct bandgap of 1.9 eV [7, 167, 168].
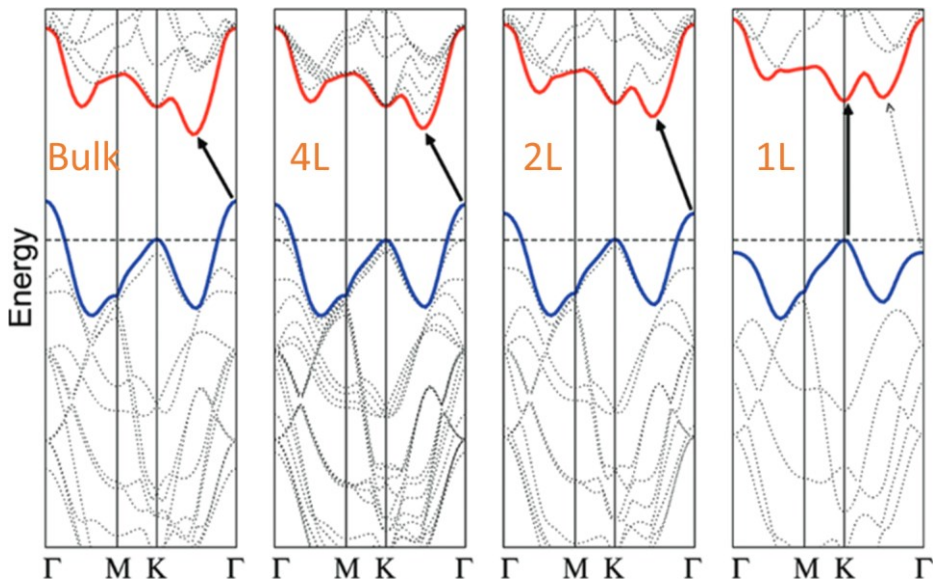
Figure 2.3: Calculated electronic band structure of MoS_2 crystal. From left to right: bulk, four layers, bilayer, and monolayer. The black solid arrow indicates the bandgap that is the lowest energy transition between the valence band maximum and the conduction band minimum. Figure is adapted from [8].

From Figure 2.3, one may notice that the direct excitonic transition at the K point in the first Brillouin zone is mostly unchanged for different thicknesses of MoS_2. The major change comes from the indirect bandgap transition at the Γ point in the first Brillouin zone due to the interlayer interactions [169]. When the thickness decreases, the indirect bandgap transition increases gradually. In other words, the relative change of the indirect bandgap transition to the direct

bandgap transition determines the electronic band structure of MoS$_2$ according to the number of layers.

In the monolayer limit, the indirect bandgap at the Γ point becomes significantly larger than the direct bandgap at the K point, and MoS$_2$ changes from an indirect-bandgap semiconductor to a direct-bandgap semiconductor. The unique transition in the band structure originates from the d orbitals of Mo atoms [8, 170]. The advantage of a direct bandgap is the high quantum efficiency because only two species (an electron and a hole) are involved in the absorption and luminescence processes. In contrast, an indirect bandgap requires a further involvement of a phonon to compensate for the mismatch of momentum.
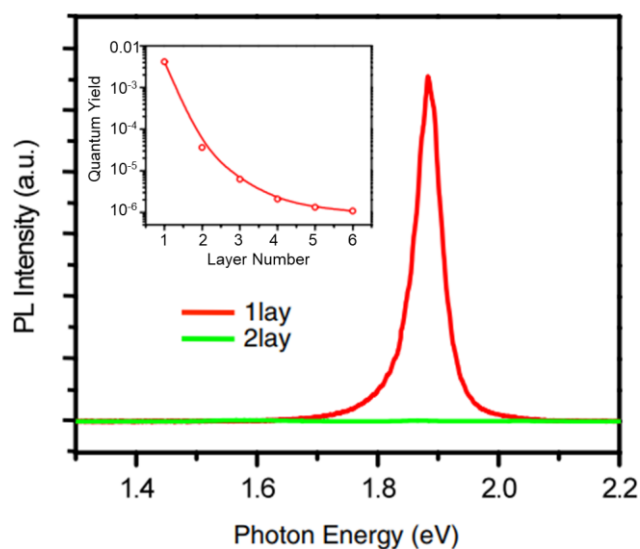
Figure 2.4: PL spectra of monolayer and bilayer MoS$_2$ samples. Inset: PL quantum yield of thin layers versus the layer numbers from 1–6. Figure is adapted from [7].

Figure 2.4 compares the PL quantum yield depending on the layer numbers and exhibits the PL spectra of monolayers and bi-layers. As a result of quantum confinement and direct bandgap, the PL of monolayer MoS$_2$ has an increase of quantum efficiency up to 10^4 times higher than that of the bilayer MoS$_2$. The impressive surge of quantum efficiency in the monolayer limit is attributed to an extremely slow electronic relaxation process in contrast to an ultrahigh rate in indirect bandgap semiconductors [8]. On the other hand, the optical absorption of the monolayer TMD is also electrically tunable by modifying the electron density or applying a voltage to change the resonance frequency [171]. Horng *et al*. have demonstrated that the absorption of monolayer MoSe$_2$ placed in front of a flat mirror could reach nearly 100 % [172] under the critical coupling condition where the radiative decay rate balances the scattering rate enabling low-power photonic applications. The strong light absorption of monolayer TMDs and the ability to bear high strain without degradation [112, 173] are advantages of these materials for electronics and optoelectronics.

2.3 Excitons in monolayer TMDs

An exciton is a quasiparticle created by the Coulomb force between an electron and a hole and hence is neutral in charge. In the thermal equilibrium condition, the electrons are mostly located at the valence band of a semiconductor. Under excitation, for instance, by an electromagnetic field with suitable energy, an electron can jump to the conduction band and leaves behind a hole in the valence band. The electron-hole pair obeys the conservation of charge, momentum, and energy. After the excitation, the electron and hole still attract each other by the electrostatic Coulomb force quantifying a binding energy. Their motion is correlated by that force. There are three types of exciton such as the Frenkel exciton, the Wannier-Mott exciton, and the charge-transfer exciton, as illustrated in Figure 2.5. Understanding the formation of these excitons and the energy transfer mechanism may help explain the optical properties of semiconductors.

A Frenkel exciton is formed by a tightly binding Coulomb force between an electron and a hole in organic or ionic crystals. As a result, the exciton has the size in the order of the unit cell and can be localized to one molecule, as displayed in Figure 2.5a. Frenkel excitons have a large effective mass in the momentum space with the binding energy ranging from 0.1-1 eV [174]; therefore, they are characterized by low mobility. In contrast to Frenkel excitons, Wannier-Mott excitons can be found in inorganic semiconductors with a high dielectric constant leading to a weak bond due to the screening by nearby electrons, as illustrated in Figure 2.5b. Consequently, electron-hole pairs have a large distance and small binding energies [175]. In Figure 2.5c, an electron and a hole are located on adjacent molecules, for example, in molecular crystals, and the pair is called charge-transfer exciton. In the monolayer limit of 2D TMDs, the wave function of electron-hole relative motion spreads over many unit cells similar to Wannier-Mott excitons (large size), while the strong exciton binding energy is analogous to Frenkel excitons [14, 67, 168, 174, 176].
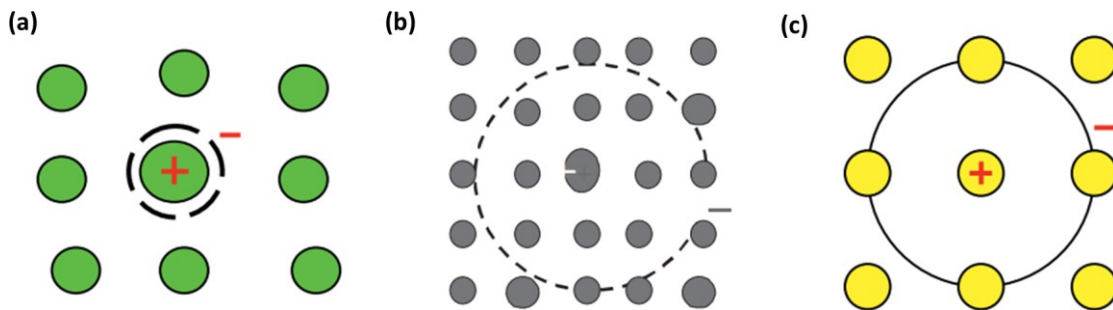

Figure 2.5: Illustration of a Frenkel exciton (a), a Wannier-Mott exciton (b), and a charge-transfer exciton (c). Figure is adapted from [177].

The binding energy of excitons in semiconductors is an important topic because it provides information about the characteristics of excitons in different semiconductor types. In general, the

exciton binding energy depends on the dielectric constant of the material and the dimensionality. Exciton binding energy E_b in an α dimensional system reads as [178, 179]

$$E_{b,n} = -\frac{E_0}{\left(n + \frac{\alpha - 3}{2}\right)^2} \, , \tag{2.1}$$

where n is the principal quantum number, and E_0 is the effective Rydberg constant.
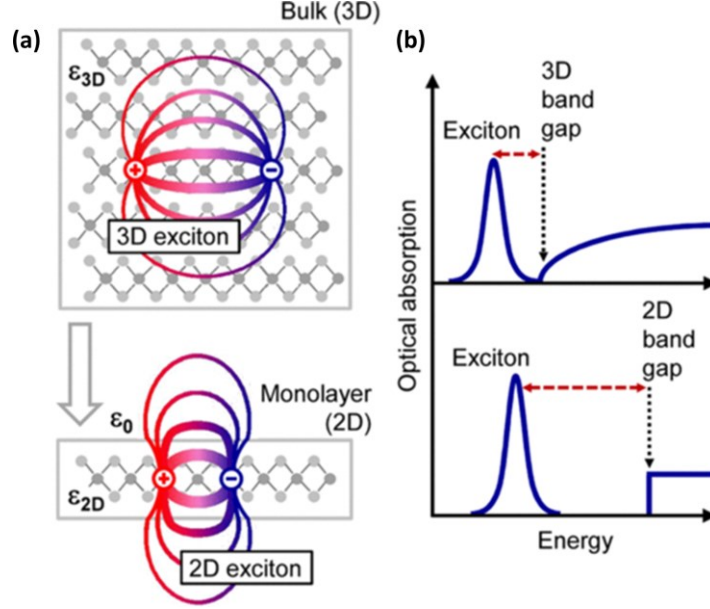
Figure 2.6: (a) A representation of an electron-hole pair in a bulk (3D) versus in a monolayer (2D) scheme with the corresponding change in the dielectric environment. **(b)** The increase of bandgap and exciton binding energy with the transition from 3D to 2D caused by the dimensionality. Figure is adapted from [68].

Without considering the effect of the dielectric constant, the transition of space from 3D to 2D increases the exciton binding energy four times with $n = 1$. In the monolayer limit, electrons and holes strongly interact via the Coulomb potential with the reduced dielectric screening. To calculate the binding energy of Wannier-Mott excitons in monolayer TMDs, one can think about a simple 2D hydrogenic Rydberg model, where the energy spectrum is also the Rydberg series [168, 174, 178, 179]. The binding energy of the nth excitonic state is expressed by [168, 178]

$$E_{b,n} = \frac{\mu_{ex}^* e^4}{2\hbar^2 \varepsilon^2 \left(n - \frac{1}{2}\right)^2} \tag{2.2}$$

Here, e is the elementary charge, $\hbar$ is the reduced Planck constant, ε is the dielectric constant, and μ_{ex}^* is the reduced effective mass of the electron-hole system defined by

$$\frac{1}{\mu_{ex}^*} = \frac{1}{m_e^*} + \frac{1}{m_h^*} \, , \tag{2.3}$$

where m_e^* and m_h^* are the effective masses of the electron and the hole, respectively. From Equation 2.2, the bonding strength is inversely proportional to the dielectric constant of the material, whereas

proportional to the reduced effective mass of the electron-hole pair. The excitonic transition energy is the result of $E_G - E_{b,n}$ with E_G is the quasiparticle bandgap.

Figure 2.6a shows the excitons in a bulk and in a monolayer. Due to the screening by the surrounding electrons, the electron-hole pair in three-dimensional space is less confined. In contrast, the reduced screening of the environment leads to the stronger confinement of exciton in the monolayer, and as a result, the bright excitons are driven solely by the in-plane dipole moment [180]. Consequently, in the monolayer form, excitons have higher binding energy and exhibit an increase in the bandgap compared to bulk. The binding energy of neutral excitons in monolayer TMDs can be up to several hundreds of meV as a character of the Wannier-Mott type [14, 176]. These are the reasons why the observation of excitons in these materials is possible at room temperature. The extraordinarily large binding energy of excitons in monolayer TMDs originates from the large effective masses of electron-hole pairs, the reduced dielectric screening by the surrounding free charges, and the spatial confinement of the charge carriers. The influence of dimensionality on the binding energy and the bandgap is depicted in Figure 2.6b.
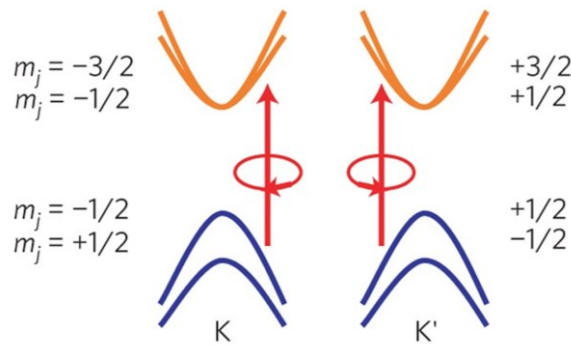
Figure 2.7: Excitonic selection rule of monolayer MoS_2. The band structure of monolayer MoS_2 showing the conduction and valence bands labeled by the z-component of the total angular momentum near the K and K' point of the first Brillouin zone. The d-orbitals cause spin-orbit interactions, which leads to spin polarization and splitting of the valence bands. To preserve time-reversal symmetry, the spin polarization of the K valley at the valence band must be the opposite of the K' valley. The valley and spin degrees of freedom are coupled. Under the left-circularly polarized excitation, only the K valley is populated, whereas, under the right-circularly polarized excitation, only the K' valley is populated. Figure is adapted from [181].

Another striking feature of excitons in the monolayer TMD is the spin-orbit splitting, which defines the excitonic species and spin polarization. Figure 2.7 illustrates the effect of spin-orbit splitting with the split of the valence band and spin selection rule. As discussed before, the monolayer MoS_2 possesses a direct gap with energy gaps located at the K and K' points of the first Brillouin zone. Due to the spin-orbit splitting, the valence band is split into two sub-bands with a gap of 200 meV for Mo-based TMDs and 400 meV for W-based TMDs. The spin-orbit coupling originates from the d orbitals of transition metal atoms such as W and Mo, and the heavier atoms (W) have larger splitting [179]. The splitting also occurs in the conduction band but only a few meV [182].

Consequently, two separate interbands create two direct optical transitions in the band structure, causing A and B excitons [183, 184]. Remarkably, two corresponding excitonic transitions can be observed at room temperature in absorption and PL spectra.

In monolayer TMDs, we can observe three charged particles which are called trions or four charged particles, known as bi-excitons. A trion is formed when an exciton combines with an extra electron or hole to create a negatively or positively charged exciton, respectively. Furthermore, if two electrons and two holes combine, a bi-exciton can be formed. The binding energy of trions is much smaller than that of excitons and determined by the difference between the fluorescence energy of the neutral exciton and the trion [181]. For instance, the monolayer MoS_2 has a trion binding energy of about 20 meV, and the monolayer $MoSe_2$ has a trion binding energy of approximately 30 meV, which makes trions from monolayer TMDs observable at room temperature [181, 185]. Additionally, trions are widely found due to the material fabrication process and the doping by surface defects and the substrate [186].

2.4 Nonlinearities in monolayer TMDs

2.4.1 Nonlinear optical processes

When an electromagnetic field **E** applies to a dielectric medium, a dielectric polarization is induced and can be seen as the oscillation of charges in the medium. Under a low field intensity, the induced polarization behaves linearly to the applied field **E** via the well-known expression

$$\mathbf{P}^{(1)}(\omega) = \varepsilon_0 \chi^{(1)}(\omega) \mathbf{E}(\omega),$$

where ε_0 is the vacuum permittivity, $\chi^{(1)}(\omega)$ is the first-order susceptibility tensor at the angular frequency ω.

In the case of an intense electromagnetic field, the response of the medium is composed of not only a linear but also a nonlinear manner. The induced polarization **P** can generate a new electromagnetic field because of the accelerated movement of charges in the medium. The dielectric polarization **P** in a general case is simplified and expressed by a power series of different orders [116, 187]

$$\begin{aligned} \mathbf{P} &= \mathbf{P}^{(1)} + \mathbf{P}^{(2)} + \mathbf{P}^{(3)} + \cdots \\ &\equiv \mathbf{P}^{(1)} + \mathbf{P}^{\mathrm{NL}}. \end{aligned} \tag{2.4}$$

Here the nonlinear polarization $\mathbf{P}^{\mathrm{NL}} = \mathbf{P}^{(2)} + \mathbf{P}^{(3)} + \cdots$.

The first-order susceptibility $\chi^{(1)}$ describes the linear response and the conventional effects, such as refraction and absorption, whereas the higher-order terms describe the nonlinear effects. When

the **E** field is in the order of magnitude of the interatomic electric field (10^5-10^8 V/m), the optical nonlinear response is observable [188]. The nonlinear susceptibility $\chi^{(2)}$ is responsible for second-order nonlinear optical effects, including SHG, sum-frequency generation, and difference frequency generation. $\chi^{(3)}$ is responsible for third-order nonlinear optical effects, including THG, four-wave mixing, SPM, and saturable absorption, to name a few. In general, the interaction strength of the nonlinear processes decreases for the higher n[th]-order susceptibility [116, 187].
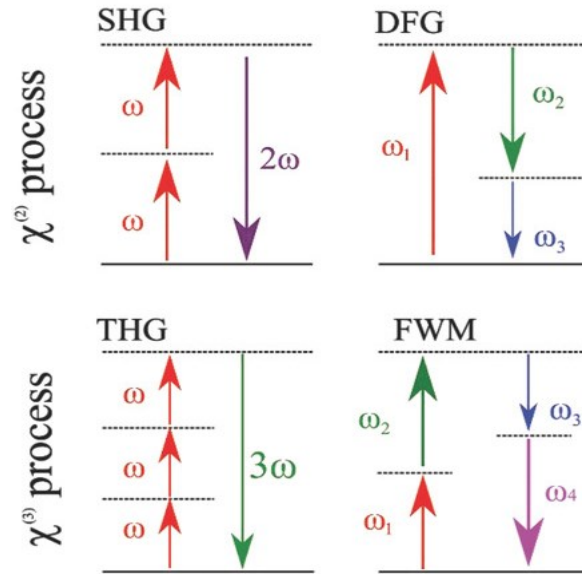
Figure 2.8: Schematic diagrams of SHG and THG processes. DFG: difference frequency generation. FWM: four-wave mixing. Figure is adapted from [98].

Figure 2.8 shows the schematic diagrams of the $\chi^{(2)}$ and $\chi^{(3)}$ processes. In a $\chi^{(2)}$ process like SHG, two incident photons of the same frequency ω interact with the nonlinear medium and generate another photon at frequency 2ω. Contrarily, when one incident photon at frequency ω_1 is divided into two photons with frequencies ω_2 and ω_3, the process is called difference frequency generation. In a $\chi^{(3)}$ process like THG, three incident photons with the same frequency ω will interact with a nonlinear medium to generate another photon at frequency 3ω. If two photons with different frequencies ω_1 and ω_2 come and interact with the nonlinear medium, two other photons with frequencies ω_3 and ω_4 can be generated. In this case, the interaction of two different frequencies in a nonlinear medium to produce two new frequencies is called non-degenerate four-wave mixing. It is important to note that many factors can influence the nonlinear optical process, including phase matching, mode matching, and nonlinear strength of materials, for instance, the $\chi^{(3)}$ value. Hence, these parameters must be carefully considered when using nonlinear materials in any application process.

The high-order nonlinear effects become significant only under an intense electromagnetic field, and hence, it requires a pulsed laser. Here, the peak power of the pulse is responsible for SHG and

inversely proportional to the pulse width expressed by Peak power (W) = Pulse energy (J) / Pulse width (s), where Pulse energy (J) = Average power (W) / Repetition rate (Hz). Thus, an ultrashort pulsed laser can generate an enormous peak power even with moderate pulse energy. Therefore, in the work with THG and SHG, ultra-short pulsed lasers are always used to excite the nonlinear medium. Furthermore, these nonlinear processes are sensitive to the crystal orientation and layer numbers and thus are a versatile tool to probe the material structure.

There are many applications of nonlinear optics in our daily life, for instance, ultrafast laser, optical modulators, ultraviolet sources, THz generation, OPO, optical parametric amplifiers, and quantum optics [98]. As discussed before, the nonlinear optical effects of materials are significantly weaker compared to the linear optical effect. Most photonic devices are using some common bulk materials, such as potassium dihydrogen phosphate, potassium titanyl phosphate, beta barium borate, and $LiNbO_3$. However, the technology nowadays is driven to miniaturize optoelectronic and photonic devices, for example, on-chip nanophotonics and quantum nanophotonics. Processing the above-mentioned nonlinear bulk materials to the nanoscale is a challenge. Hence, any material which can scale down in size while maintaining high nonlinearity is greatly desired. For that reason, 2D materials, by having a large nonlinear optical response and compatibility for on-chip integration, change the game in the next generation of integrated photonics. In this thesis, THG and SHG processes of monolayer MoS_2 grown on optical fiber will be discussed.

2.4.2 Phase matching condition

The phase-matching condition is required for SHG and THG processes, and the momentum mismatch in the SHG process is given as

$$\Delta k^{\text{SHG}} = 2k_1 - k_2, \tag{2.5}$$

where k_1 is the wavenumber of the incident fundamental waves, and k_2 is the wavenumber of the generated second harmonic wave.

The wavenumber is related to the refractive index by $k_i = \frac{n_i \omega_i}{c}$, where i is an integer.

In the case of the THG process, the momentum mismatch is written as follows

$$\Delta k^{\text{THG}} = 3k_1 - k_3, \tag{2.6}$$

where k_3 is the wavenumber of the generated third harmonic wave.

We can express the SHG intensity at the output of a nonlinear medium with a length L depending on momentum mismatch as [116]

$$I_2 = \frac{8d_{\text{eff}}^2 \omega_2^2 I_1^2}{n_1^2 n_2 \varepsilon_0 c^2} L^2 \text{sinc}^2\left(\frac{\Delta k^{\text{SHG}} L}{2}\right) = \frac{2\left(\chi^{(2)}\right)^2 \omega_2^2 I_1^2}{n_1^2 n_2 \varepsilon_0 c^2} L^2 \text{sinc}^2\left(\frac{\Delta k^{\text{SHG}} L}{2}\right), \qquad (2.7)$$

where ε_0 is the vacuum permittivity; c is the light speed in vacuum; d_{eff} is the effective nonlinear susceptibility; n_1 and n_2 are the refractive indices of the medium at frequencies ω_1 and ω_2, respectively; $\chi^{(2)}$ is the second-order susceptibility of the medium; Δk^{SHG} is the phase mismatch between the fundamental waves and the second harmonic wave; I_1 is the incident power of the fundamental wave.

Similarly, the THG intensity is given as [189]

$$I_3 = \left(\frac{2\pi}{n_1 c}\right)^4 \left(\chi^{(3)}\right)^2 (3\omega_1)^2 I_1^3 L^2 \text{sinc}^2\left(\frac{\Delta k^{\text{THG}} L}{2}\right) \gamma^{(\text{THG})}, \qquad (2.8)$$

where $\chi^{(3)}$ is the third-order susceptibility of the nonlinear medium, Δk^{THG} is the phase mismatch between the fundamental wave and the third harmonic wave, $\gamma^{(\text{THG})}$ is the spatial overlap between two modes.
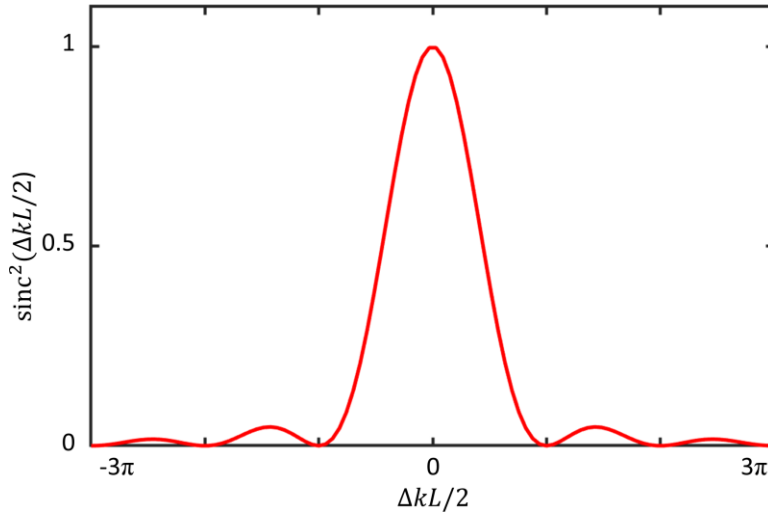
Figure 2.9: Phase matching influence on the modulation of SHG and THG wave amplitude.

From Eqs 2.7 and 2.8, the intensity of both SHG and THG waves are modulated by the $\text{sinc}^2(\Delta k L/2)$ function, which is called the phase mismatch factor. Figure 2.9 shows the plot of this function as a function of $\Delta k L$. Ideally, the phase mismatch factor becomes maximum if $\Delta k L = 0$, and then $\text{sinc}^2(\Delta k L/2) = 1$. In the case of $\Delta k = 0$, then $\Delta k L = 0$, so the amplitude of generated SH and TH waves increases quadratically with the length L, and it is also said that the phase is matched. Due to the one-atom thin thickness of monolayer TMD, and $L \ll \lambda$, the momentum conservation requirement is free [190].

2.5 Exposed-core fiber

Figure 2.10 displays the fiber facet of a typical ECF used in this work, which is imaged by a scanning electron microscope (SEM). Here, the ECFs have an outer cladding diameter of 175 µm, and the effective core diameter is around 2µm which can be seen in Figure 2.10b. The core is supported by three thin struts and surrounded by two air holes at the bottom and one open space on top. The struts are long enough to define the guiding core. All parts of the ECF are made of fused silica at the temperature range of 1900 °C to 2000 °C by a thermal fiber drawing process. Details of the fabrication technique can be found in Appendix D.
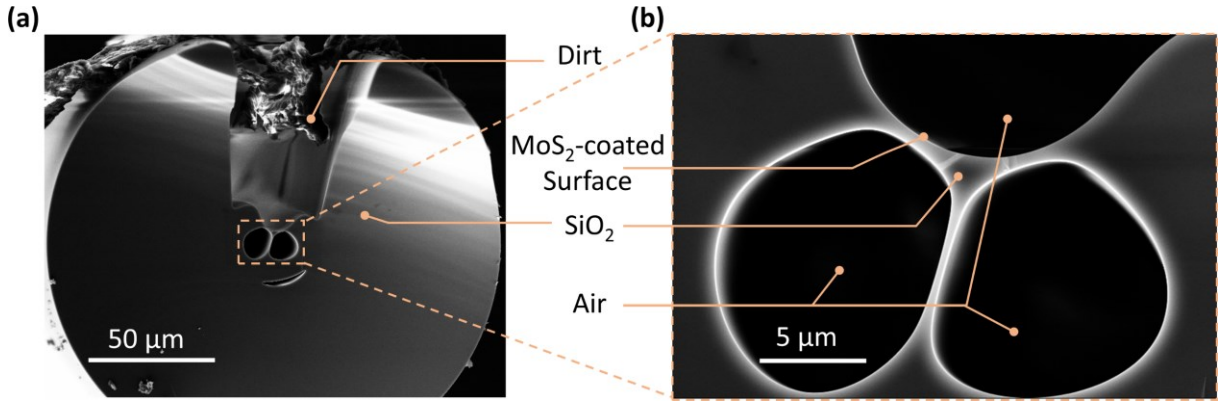
Figure 2.10: Scanning electron microscope image of an ECF. **(a)** SEM image of the entire facet of an ECF. **(b)** The core area of the ECF is marked by the orange box in **(a)**. Figure is adapted from [146].

Table 1.1: Calculated V parameter and numerical aperture NA at some typical wavelengths for silica ECF

Wavelength (nm)	Core radius (µm)	n_{co} (silica)	n_{cl} (air)	V parameter	NA
532	1.0	1.461	1.0	12.5	1.06
800	1.0	1.453	1.0	8.3	1.05
1360	1.0	1.446	1.0	4.82	1.04

One important parameter to characterize a step-index optical fiber is the V parameter [191], which approximately quantifies the number of guided modes within the fiber core. The V parameter is given by

$$V = k_0 a \sqrt{\left(n_{\mathrm{co}}^2 - n_{\mathrm{cl}}^2\right)} = k_0 a NA, \tag{2.9}$$

where $k_0 = 2\pi/\lambda_0$ is the vacuum wavenumber; a is the core radius; λ_0 is the vacuum wavelength; n_{co} and n_{cl} are the refractive indices of the core and cladding, respectively; and NA is the numerical aperture.

Here, we have calculated the NA value and the V parameter of our ECFs at different excitation wavelengths used in this thesis. The cladding is the air with a refractive index of 1.0. The refractive

index of the silica core slightly decreases when the spectral wavelength increases, leading to a decrease in the NA value. Using Equation 2.9, we calculated the value of the V parameter. Table 1.1 shows the calculated values of the V parameter and the NA for three different wavelengths. The V parameter declines from the value of 12.5 at 532 nm to the value of 4.82 at 1360 nm. We can say that at shorter excitation wavelengths, there are more guided modes inside the fiber core than at longer excitation wavelengths. Because the calculated V parameters in Table 1.1 are higher than the value of a single-mode fiber ($V < 2.405$), our ECF supports multiple modes for all working excitation wavelengths.

2.6 TMDs growth on ECFs

The growth of TMDs involves a modified CVD process [192]. This process produces high-quality monolayer TMDs with a typical length ranging from 7 - 20 µm on few-centimeter-long microstructured silica ECFs. The ECFs are suitable for the high-temperature conditions of the CVD reactor (~ 800 $^{\circ}$C). Moreover, ECFs provide free access from the outside to the core, enabling the growth of various 2D materials directly on the fiber core. Different precursors are employed based on the type of TMDs being grown. For instance, sulfur or selenium is used in the first zone of the CVD chamber and heated to around 200 $^{\circ}$C or 400 $^{\circ}$C. In the second zone of the reactor, a metal oxide, such as MoO_3 or WO_3, is employed and heated up to 800 $^{\circ}$C to provide the transition metal source.
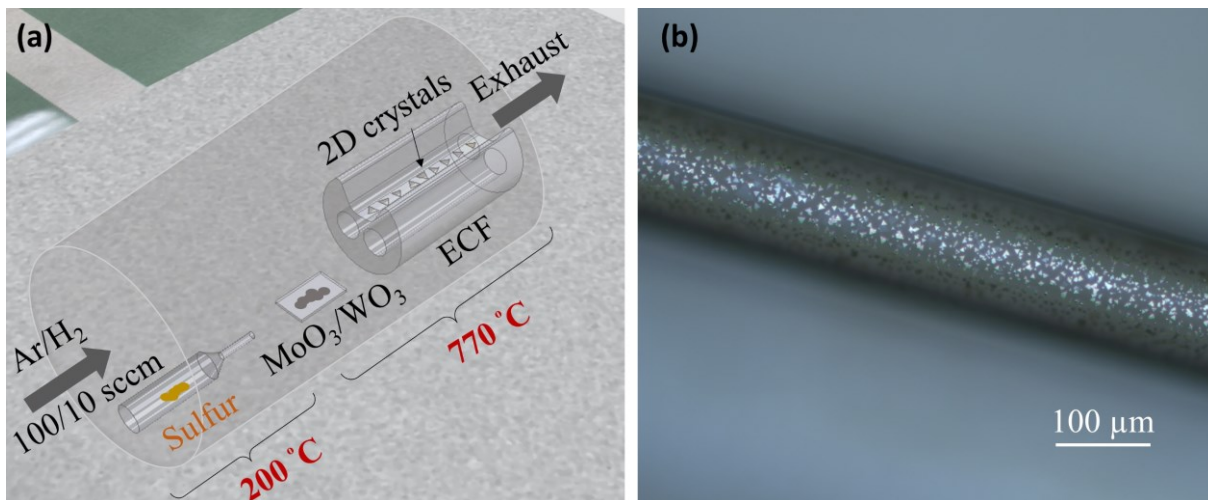
Figure 2.11: (a) Illustration of a modified CVD process. **(b)** Microscopic image of an ECF with distinguishable as-grown monolayer and few-layer MoS_2.

Figure 2.11a shows the schematic of the modified CVD process. The fiber was fixed on a silica substrate so that the exposed side is upward oriented, while the gas flow was controlled via a mass flow controller, and the position of ECF was carefully adjusted to optimize the effective coating region. Argon gas is used to carry the sulfur precursor from the first zone to the second zone, where

MoO$_3$ or WO$_3$ is located. Hydrogen is introduced as an element of the reaction process when the temperature of the second zone reaches 750 $^\circ$C. The formation of MoS$_2$ and WS$_2$ happens at the downstream side of the second zone. Figure 2.11b demonstrates the conformal growth of MoS$_2$ crystals on an ECF. The bright triangles are multilayer MoS$_2$, whereas the grey triangles are monolayers. Due to the difference in the refractive index and thickness between a multilayer and a monolayer, the monolayer can be distinguishable under a normal optical microscope by observing the color [8]. In this case, the fiber was high-density coated with MoS$_2$ crystals. By adjusting the position of the optical fiber in the reaction zone and the flow rate of the precursor, the density coating could be partially controlled. Different kinds of monolayer TMDs such as MoS$_2$, WS$_2$, WSe$_2$, and MoSe$_2$ have been grown successfully on ECFs, and details can be found in Appendix E of this thesis. In this research work, it was impossible to grow monolayer TMDs only on the core region from the powder precursor. However, this difficulty may be solved by controlling the location of the liquid precursor only on the core region using micro-molding in capillaries [193].

3. Sample characterizations

3.1 Atomic force microscopy

Atomic force microscopy (AFM) is one of the most powerful tools to examine the morphological structure of as-grown MoS_2 on the fiber because of its high vertical resolution, albeit the curved surface of the fiber induces some difficulties. Hence, AFM measurements were carried out over a mapping area of roughly 10 μm x 10 μm to perform the characterization. These AFM measurements were conducted with the Ntegra system (NT-MDT) at ambient conditions using n-doped silicon cantilever tips (NSG01 from NT-MDT with a tip radius smaller than 6 nm). The tapping mode was used for AFM imaging.
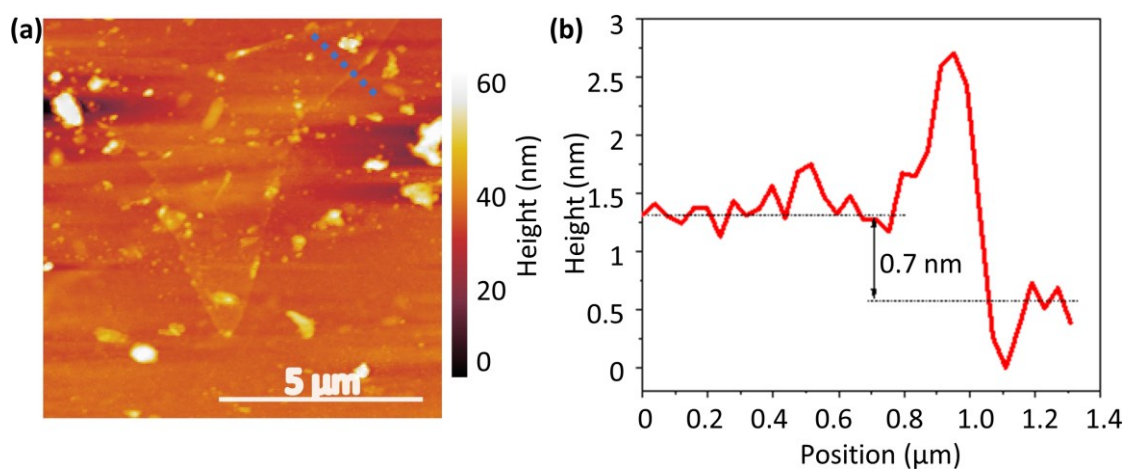
Figure 3.1: (a) Atomic force microscopy image of a typical monolayer MoS_2 on the fiber core. **(b)** The height of the monolayer is measured along the blue line in **(a)**. Figure is adapted from [146].

A typical MoS_2-coated ECF has been selected to measure the thickness of as-grown flakes on the core region. Figure 3.1a displays the topological map, where a triangular flake can be seen in the center of the image. The size of a triangular TMD flake is around 7 μm. There are some contaminations near the flake because the ECF has been used in a normal lab environment for a long time before this AFM measurement. The height of the crystal was determined by measuring the profile along the blue dashed line, as marked in Figure 3.1a. Figure 3.1b reveals that the height of the flake is 0.7 nm crossing the boundary, which is the thickness of a monolayer TMD [9]. This evidence has confirmed the successful growth of monolayer MoS_2 in the core region.

3.2 Raman spectroscopy

Raman spectroscopy is a versatile technique to obtain valuable chemical information regarding the crystal structures based on the vibrational and rotational modes in materials [194-196]. This technique is quick, convenient, and non-destructive and has been widely used for characterizing 2D materials [160, 194-198]. Raman spectrometer can operate at room temperature and ambient

conditions. This device can measure not only Raman signals but also PL spectra, making it more convenient for users [199]. There is no special requirement in the sample preparation with Raman spectroscopy. Molecules in the sample will be excited by the chosen laser light source, and Raman scattered light will be filtered out by optics in the spectrometer to show a Raman spectrum.

Figure 3.2 shows that different types of scattering processes can happen when a photon interacts with a molecule. When photons interact with molecules, the energy of photons is transferred to electrons in molecules and promotes them to a short-lived higher energy state, often called a virtual energy state. Because this state is unstable, the excited electron will quickly return to the initial ground state. The radiative relaxation of the excited electron to the ground state will emit a photon. In most cases, the incident photons interact with electrons in the molecule without any energy change, and hence, the scattered photon has the same energy as the incident photon. This elastic process is called Rayleigh scattering. The only change in the Rayleigh scattering is the propagation direction of photons. In a much lower probability, the scattered photon has different energy from the incident photon, and this inelastic process is called Raman scattering [194, 200]. The Raman scattering is divided into Stokes and anti-Stokes processes. The Stoke process happens when an incident photon transfers its energy $\hbar\omega_i$ to the molecule and creates another electron-hole pair. The recombination process of this electron-hole pair creates a phonon and an emitted photon with a slightly lower energy $\hbar\omega_s$. Here, the total energy is conserved ($\hbar\omega_i = \hbar\Omega + \hbar\omega_s$, where $\hbar\Omega$ is the phonon energy). On the other hand, if a phonon couples to an incident photon during the light-matter interaction process, the emitted photon after the recombination process has an increased energy because $\hbar\omega_{as} = \hbar\Omega + \hbar\omega_i$. This is the anti-Stokes process. In the Raman spectrum, the energy difference between the incident and the scattered photons is called the Raman shift, and the unit is often displayed in cm^{-1}.
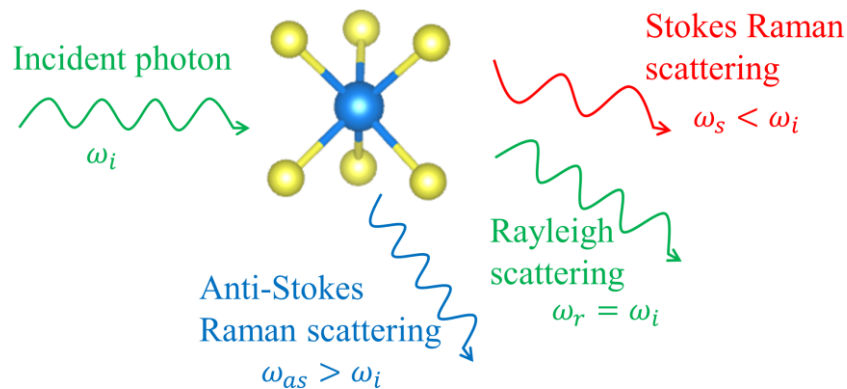

Figure 3.2: Illustration of Raman and Rayleigh scattering processes when light interacts with a molecule.

Raman spectroscopy is a reliable method to characterize 2D TMDs as well as to identify unknown substances and monitor the change in molecular structures and crystallinity such as strain, charge

doping, and defect types. The number of Raman modes is different for odd- and even-numbered layers of 2D TMDs, and the shift of Raman modes is expected when there is a transition from bulk to monolayer limit [160, 194-198]. Two dominant peaks, the E_{2g} mode and the A_{1g} mode, in the Raman spectrum of MoS_2 crystals originate from the in-plane vibration of Mo-S bonds and the out-of-plane vibration of S atoms, respectively [197, 198]. The separation in Raman shift between the two modes is often used to identify the layer number of MoS_2. The E_{2g} and A_{1g} modes experience red and blue shifts in the Raman spectrum, respectively, when the thickness decreases from bulk to monolayer. As a result, the separation between the two modes increases from around 20 cm^{-1} for monolayer MoS_2 to 25 cm^{-1} for bulk MoS_2 [160, 167, 192, 197]. The evolution of these modes also takes place in WS_2, $MoSe_2$, and WSe_2 crystals [160, 196].
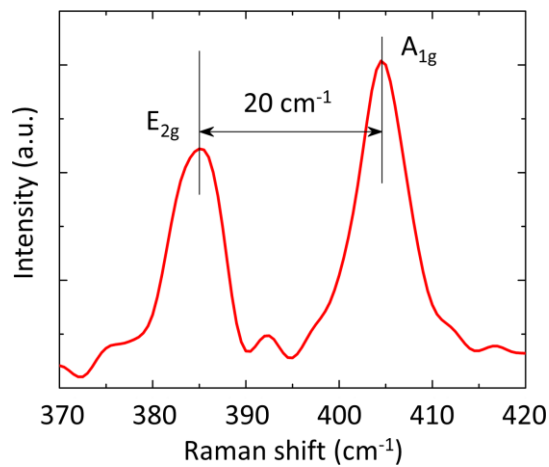
Figure 3.3: Raman spectrum of an as-grown monolayer MoS_2 on the fiber core.

Here, the crystal was characterized by a Senterra Raman spectroscopy by Bruker operated in backscattering mode with a 532 nm excitation, obtained from a frequency-doubled Nd:YAG laser, a 100x objective, and a thermoelectrically cooled CCD detector. The system has a spectral resolution of 2 cm^{-1}. Figure 3.3 shows a typical Raman spectrum of the MoS_2 crystals on the fiber core. There are two dominant peaks in the Raman spectrum at the E_{2g} mode at 385 cm^{-1} and the A_{1g} mode at 405 cm^{-1} for the as-grown MoS_2. This mode separation of 20 cm^{-1} is expected for monolayers [167, 192, 197]. Together with AFM measurement, Raman spectroscopy measurements further confirm the successful growth of MoS_2 monolayers in the core region of ECFs.

3.3 PL spectroscopy

Photoluminescence is a phenomenon that happens when an electromagnetic radiation (photon) is absorbed by a medium and emitted again after some time at slightly lower energy (luminescence). Figure 3.4 illustrates that photons with enough energy are absorbed by electrons in the medium,

and these electrons are excited to higher energy and vibration states (S_1 and S_2). S_1 and S_2 are the singlet excited states where the excited electron has the spin in pair with the electron in the ground state. Conversely, T_1 and T_2 are the triplet excited states, where excited electrons have the same spin as the electrons in the ground state. According to the Pauli exclusion principle, the transition of electrons from a singlet state to a triplet state is forbidden since a pair of electrons in the same energy level cannot have the same spin. The duration for the absorption process is typically on a femtosecond.
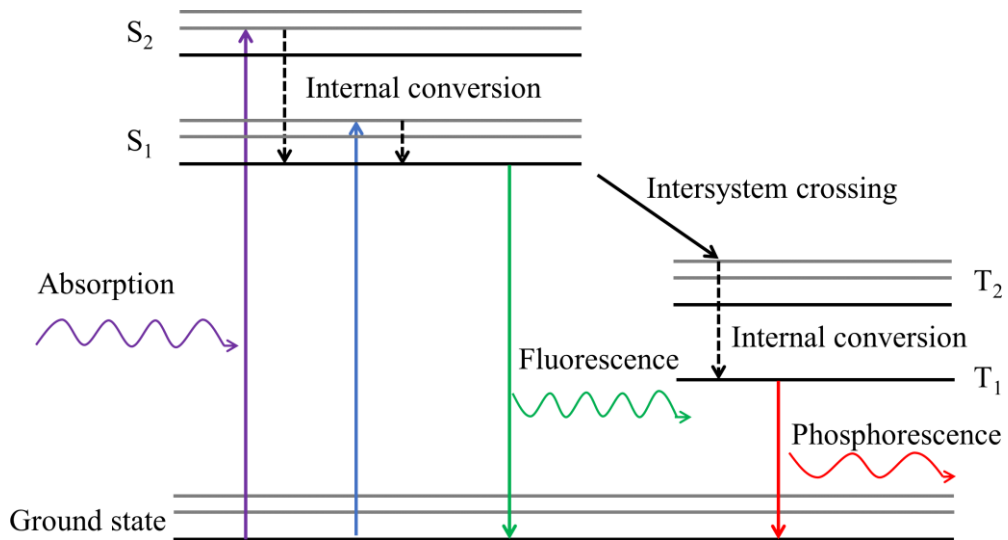
Figure 3.4: Jablonski diagram. Figure is adapted from [201].

There are two main ways for electrons to relax from a high-energy level to the ground level, such as non-radiative and radiative processes. In the case of a non-radiative process, an electron in the S_1 and S_2 states relaxes to a lower excited state either by internal conversion or by intersystem crossing to triplet states. In this process, the energy of electrons is partly transferred to the vibration of the lattice (phonon), and heat is generated in the system. In the case of a radiative process, electrons return from the excited state to the ground state to recombine with holes, and then photons are emitted by this relaxation process in a picosecond or nanosecond timescale [201, 202].

PL emission can be further divided into two major groups: fluorescence and phosphorescence. The main difference between the two groups is the duration between the absorption and emission of photons. The time range for a fluorescence process is from femtoseconds (fs) to microseconds (µs), whereas the phosphorescence process occurs in a time window of milliseconds (ms) to hours [201, 202]. From the diagram, fluorescence emission takes place with singlet excited states, and this process is not forbidden and hence can happen in a short time. Because the excited electron experiences a non-radiative relaxation (internal conversion) before recombination with the hole, the emitted photon from fluorescence has lower energy than the incident photon. The transition

from a triplet state to a singlet state requires a change of spin, leading to a longer time scale for phosphorescence. In the case of 2D TMDs, fluorescence emission is the main process.

PL spectroscopy is a very useful technique to characterize the optical and electronic properties of materials. This technique is also quick, convenient, and non-destructive and thus has been used widely to examine 2D materials [7, 8, 14, 15, 125, 131, 135, 161, 166, 192]. Based on the characteristics of PL spectra, one can obtain information about the band structure (direct versus indirect), crystallographic structure (crystal size, orientation, phases, thickness), and optoelectronic phenomena such as the exciton of 2D TMDs. PL measurement can be conducted at ambient conditions without any special requirements from sample preparation. A laser source is commonly used in PL spectroscopy. As discussed in Chapter 2, the monolayer TMD has a bandgap; therefore, the incident photons need higher energy than the bandgap to interact with crystals.
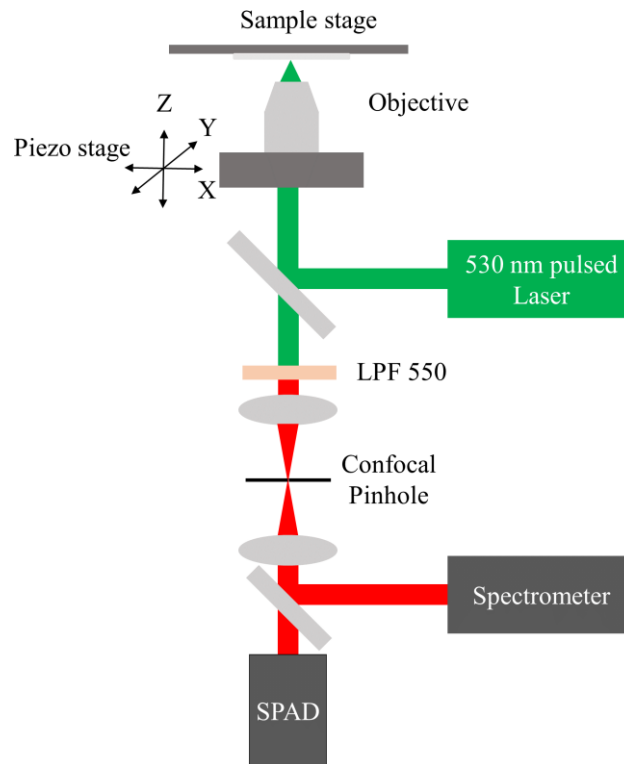
Figure 3.5: Confocal fluorescence imaging microscopy from Picoquant Microtime 200 to characterize monolayer TMDs grown on planar substrates and ECFs. LPF: long-pass filter. SPAD: single-photon avalanche diode.

To characterize as-grown monolayer TMDs on the planar substrates and carry out the PL mapping on the fiber core, we have used a grating spectrometer (Horiba Jobin Yvon Triax). Figure 3.5 illustrates the fluorescence imaging microscopy that has been used. This device can scan the sample in XY, YZ, and XZ planes which can help us to confirm the direct deposition of monolayers on the exposed core. By using a high magnification objective from 60x to 100x, we can observe the orientation and size of as-grown monolayers on the core region. In this fluorescence imaging microscopy setup, a pulsed laser at 530 nm has been used to stimulate the PL emission of monolayer

TMDs, and an Andor spectrometer with a Si-cooled CCD camera was used to record the spectra from the measured samples.
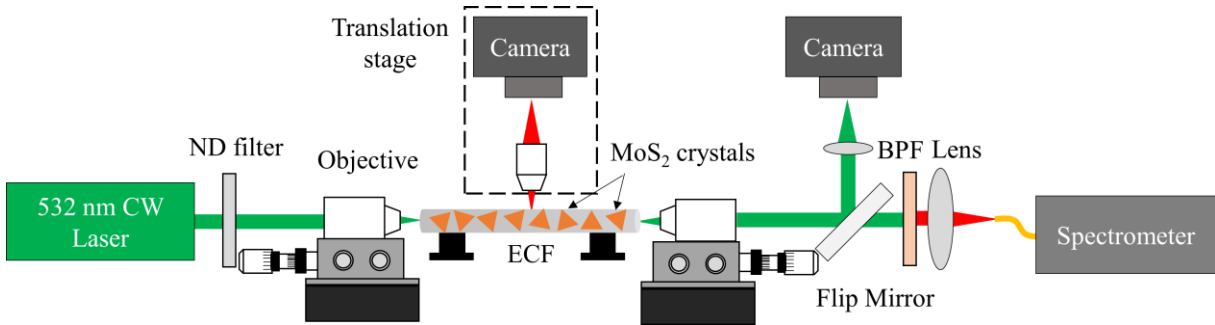
Figure 3.6: The through-fiber PL spectroscopy setup to investigate the interaction between monolayer TMDs and guided modes. ND: neutral density. BPF: band-pass filter.

Although the fluorescence imaging microscopy setup is very useful to examine the properties of monolayer TMDs on planar substrates or as-grown monolayers on ECFs, it does not support an investigation of light-matter interaction via guided modes. To demonstrate the exciton excitation and PL collection through the fiber, a self-built PL spectroscopy setup has been utilized, as displayed in Figure 3.6. Here, a continuous wave (CW) laser (Lighthouse Photonics Sprout) at 532 nm was coupled to the fiber core with the support of a visible camera. The coupling of the excitation light source into the fiber was manually handled by a three-axis Nanomax flexure stage. The signal was recorded by a Horiba grating spectrometer. To measure the filling factor of as-grown monolayers on ECFs, a Zyla plus 4.2 camera was mounted on a translation stage to collect the PL emission from the core region. This stage can travel along the fiber length.

3.4 Transmission spectroscopy

UV-VIS spectroscopy is a technique to measure the absorption or transmission of matter in the ultraviolet-visible region. Although transmission and absorption spectra provide the equivalent information, the interpretation is different. The transmission spectra will have the maximum intensity at the spectral range where the absorption is the lowest. Meanwhile, the absorption spectra will have the maximum intensity at the spectral range, where the absorption is the highest. Some other factors, such as reflection and scattering, may involve in the transmission process. If such factors are constant during the measurement, the transmission or absorption spectrum still gives meaningful information about the absorption of matter. In the technique with transmission spectroscopy, a broadband light source is usually used to get the absorption of a sample as a function of wavelength. As we know from the band structure of monolayer TMDs, only the incident photon with enough energy can excite the electrons to create electron-hole pairs. In other words, only high-energy photons will be absorbed by the monolayers. Using that fact, the transmission of

the 2D-coated fibers can be characterized and compared to the bare fibers with identical lengths to extract information about the absorption of as-grown monolayers on the fiber core. This measurement reveals the excitonic absorption peaks of monolayer TMDs when a part of the excitation light source is absorbed to excite electrons from the ground state to the excited state. The transmission spectroscopy was performed using the setup in Figure 3.6, but the light source is a fiber-coupled LED white light (MWWHF2 from Thorlabs).

To calculate the transmission spectra of 2D TMD-coated ECF at an arbitrary wavelength, the following formula was used

$$T_\lambda(\%) = 100\left(\frac{I_{s,\lambda}}{I_{0,\lambda}}\right), \tag{3.1}$$

where $I_{s,\lambda}$ is the transmitted light intensity at the output of a 2D TMD-coated fiber, $I_{0,\lambda}$ is the transmitted light intensity at the output of an identical bare fiber. Both $I_{s,\lambda}$ and $I_{0,\lambda}$ are the net contribution from the fiber after correcting the background.

4. In-fiber exciton excitation and PL collection

4.1 Experimental results

Before characterizing the excitonic properties of monolayer TMDs grown on ECF, we examined the PL emission from the monolayer MoS_2 grown on a planar SiO_2 substrate. This sample was grown together with ECFs by the CVD process to give us an insight into the influence of the substrate on the excitonic properties of as-grown monolayers. Using the fluorescence imaging microscopy setup in Figure 3.5, Figure 4.1a displays the PL mapping from MoS_2 monolayers grown on a SiO_2/Si substrate. The monolayers have a crystal size of around 10 μm, and the PL emission is fairly homogeneous within the crystal boundary. Figure 4.1b shows the PL spectrum from a monolayer with pronounced A and B excitons at 678 nm and 625 nm, respectively. These values are consistent with reported work using the same CVD process [192] and agree with reported values from the exfoliated monolayer MoS_2 [8]. This agreement confirms the high quality of monolayer MoS_2 from the CVD method. This PL spectrum will be used as a reference to compare with the exciton characteristics of monolayer MoS_2 on ECFs to give us a thoughtful evaluation of the quality of as-grown monolayers on ECFs.
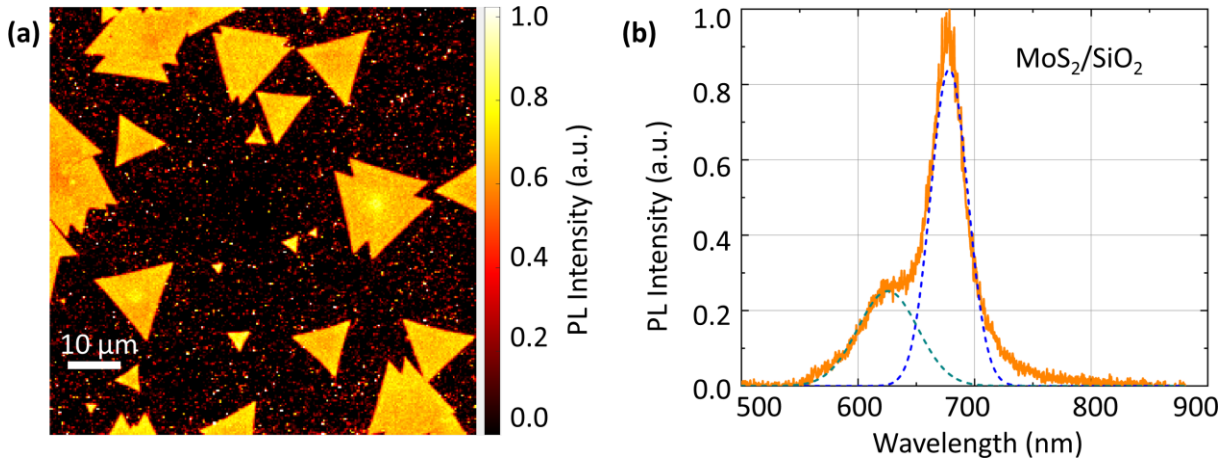
Figure 4.1: **(a)** PL mapping from an area of MoS_2 grown on SiO_2/Si substrate. **(b)** PL spectrum from a typical monolayer MoS_2 in **(a)** under the excitation of 530 nm pulsed laser.

Figure 4.2a illustrates the fundamental concepts of our waveguide system with embedded 2D materials. Here we want to establish a new integrated photonic platform through the scalable integration of high-quality TMD crystals on the ECFs [203]. In this demonstration, monolayer TMDs such as MoS_2 and WS_2 have been coated on the upper surface of the fiber core by a modified CVD process. The excitation light source was coupled to the fundamental modes (FMs) of the fiber. The evanescent field from the guided modes interacts with the TMDs and excites charge carriers to emit PL. Each monolayer TMDs may act as a distinct photon emitter and emits PL light both in the free space and coupled back into the fiber modes. As a result, the PL emission through

the hybrid system is the incoherent sum of all photon emissions from active monolayers and the fiber itself. There are two ways to collect the PL emission, either from a single crystal in free space or from the sum emission through the guided modes. To stimulate the PL emission, the incident photons should have higher energy than the band energies of the exciting materials, which are around 1.9 eV for the monolayer MoS_2 and 2.0 eV for the monolayer WS_2.
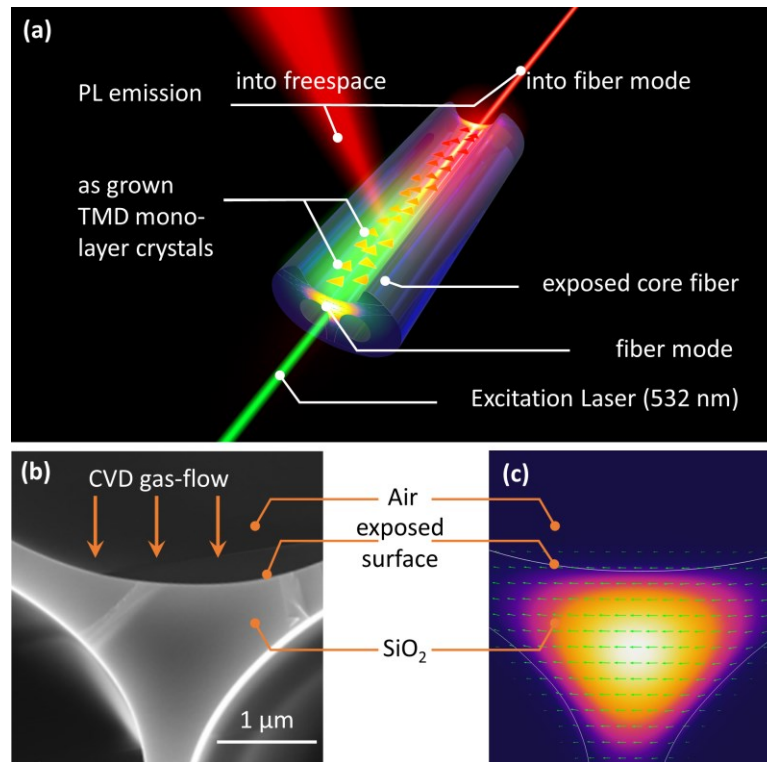
Figure 4.2: The illustration for the concept and fiber characterization. **(a)** The schematic diagram of the work concept for in-fiber PL. **(b)** Scanning electron microscopy of the fiber core region to show the exposed surface. **(c)** Electric field distribution of the fundamental mode inside the fiber core to show the evanescent field. Figure is adapted from [146].

Figure 4.2b displays the cross-section of the fiber's core area. The image was taken by an SEM to obtain precisely the geometry of the fiber core. This geometry was employed for simulation in Comsol Multiphysics for mode analysis, mode overlap, phase matching, and other numerical calculations. The fiber has a core diameter of around 2 μm surrounded by two air holes at the bottom and one open access on the top surface. The entire fiber is made of fused silica. The monolayer TMDs will be deposited on the exposed surface with a random distribution and orientation. From the cross-section of the fiber, the silica core with a refractive index of 1.46 at 532 nm [204] is well isolated by three air regions with a refractive index of 1.0. Therefore, the electromagnetic field will be tightly confined inside the silica core by the total internal reflection, except for a small amount of evanescent field localized near the interface. This evanescent wave is located outside the core and decays exponentially with the distance from the air-silica interface. However, monolayer TMDs are so thin that they can interact efficiently with this field if they are

deposited directly on the exposed surface. Figure 4.2c shows the electric field distribution within the fiber core region. The main flux of energy is located at the core center, while a small amount of energy leaks out of the core and is guided as the evanescent field. The portion of the evanescent field is larger for longer excitation wavelengths. By depositing monolayer TMDs directly on top of the fiber core, the evanescent field can interact efficiently and excite the PL emission from the monolayers.
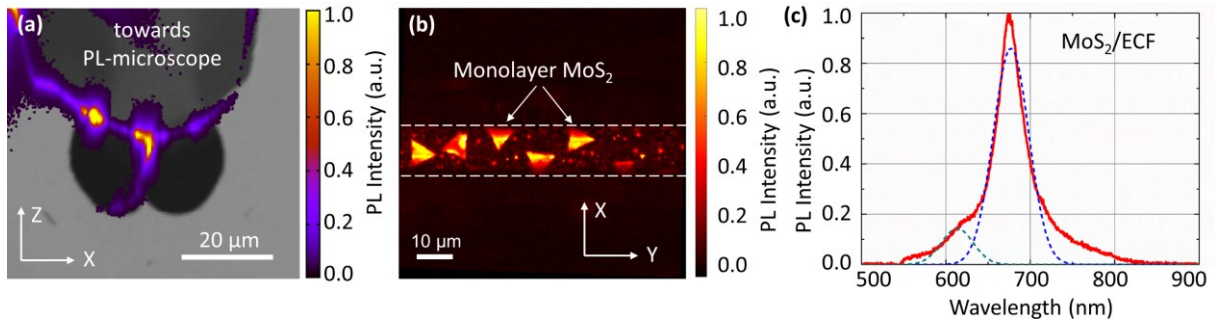
Figure 4.3: (a) XZ scanning of an MoS$_2$-coated ECF. **(b)** Top view PL mapping from the coated ECF. Dashed lines indicate the core region. **(c)** PL spectrum from a typical monolayer MoS$_2$ in the subfigure **(b)**. Subfigure (a) is adapted from [146]. Subfigures (b-c) are adapted from [205].

First of all, we used the fluorescence imaging microscopy setup in Figure 3.5 to demonstrate the direct contact between the monolayer MoS$_2$ and the fiber core. Because only the monolayers on the fiber core can interact with the guided modes, this demonstration is greatly important for the success of the concept. The fiber was fixed on the specimen table, and the laser beam was focused by a 100x objective on the bottom of the trench. The spatial resolution is expected to be around 400 nm. The map was obtained by moving the objective in the XZ plane perpendicular to the fiber groove. For ease of presentation, the fiber cross-section from PL mapping was superimposed with an SEM image of the identical fiber (Figure 4.3a). The bright emission from the core region is reliable evidence for the successful deposition of high-quality MoS$_2$ monolayers and proved the direct physical contact between the atomic monolayer and the boundary of the core. The emission from the fiber was negligible compared to the monolayer MoS$_2$ and the PL emission peak from monolayers was distinct. The unphysical extension of PL light downwards at the core is due to the diffraction of the light when it was collected by a confocal pinhole aperture.

To observe the morphology of monolayers, we switched to performing the PL mapping along the fiber length in the XY plane (Figure 4.3b). By moving the objective along the fiber, the crystal size and orientation of monolayer MoS$_2$ were clearly seen with a typical triangular shape. The PL signal was detected by a single-photon avalanche diode after passing through a set of long-pass filters. Figure 4.3c reveals the PL spectrum from a monolayer MoS$_2$ exhibiting A and B excitons fitted by the dashed blue and cyan lines. The excitons have the typical peaks at 677 nm and 613 nm with the full width at half maximum of around 45 nm for A and B excitons, respectively. These

characteristics are almost similar to the monolayers grown on the SiO_2 substrate in Figure 4.1b. It has proved that growing monolayer TMDs on ECF can maintain the high quality of these materials without bringing extra strain compared to growing on the planar substrate.

In the next step, we want to conduct the optical measurement through the fiber modes using a self-built PL spectroscopy setup (Figure 3.6). For the experiment with PL, an uncontrolled polarization 532 nm CW laser has been used, whereas a fiber-coupled LED white light was employed for transmission measurement. There are two ways to examine the PL emission in this work: in the free space and via the guided modes. In the former case, a camera will be mounted on a translation stage that can move along the fiber length and collect the PL emission via a 10x objective imaging system from every single monolayer on the fiber core. In the latter case, the fiber core will be imaged onto a Horiba spectrometer to collect the PL emission through the fiber modes.
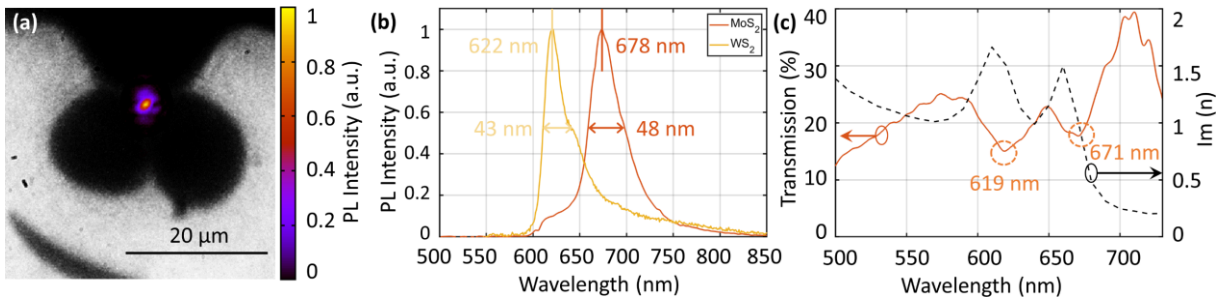
Figure 4.4: The through-fiber characterization. **(a)** False color image of PL emission from an MoS_2-coated ECF after excitation of a 532 nm CW laser. The cross-sectional image is the fiber facet recorded by the same camera. **(b)** Normalized PL spectra of MoS_2 and WS_2-coated ECFs excited by a 532 nm CW laser. **(c)** Transmission spectrum through an MoS_2-coated ECF excited by a fiber-coupled LED white light source. The inaccuracy for $\lambda > 700$ nm is affected by the relative low power of the light source in this spectral range. Figure is adapted from [146].

Figure 4.4a displays the PL light leaving the fiber core after passing through a set of long-pass filters to remove the signal from the laser excitation. This PL emission from the core is superimposed with a cross-section image of ECF. The tight confinement of emitted PL in the core region demonstrates that there is no collected emission from the cladding or other parts of ECF. Figure 4.4b exhibits the PL spectra of an MoS_2 and a WS_2-coated ECF with the PL emission peaks at 622 nm and 678 nm, respectively. The full width at half-maximum is about 43 nm for MoS_2 and 48 nm for WS_2. These values are analogous to the spectrum collected from a monolayer MoS_2 emitted in free space in Figure 4.3c. It has proved that the ECF is a versatile platform to excite and collect PL via fiber modes, hence paving a novel way to in-fiber PL and fiber-based sensing.

Figure 4.4c shows the transmission spectrum of MoS_2-coated fiber in comparison with an identical bare fiber with the same length. The formula calculation of the transmission spectrum is from Equation 3.1. There are two absorption peaks (transmission troughs) at 671 nm and 619 nm which are ascribed to the resonance of A and B excitons from the monolayer MoS_2, respectively. The experimental data is put together with the extinction coefficient of the monolayer MoS_2 from the
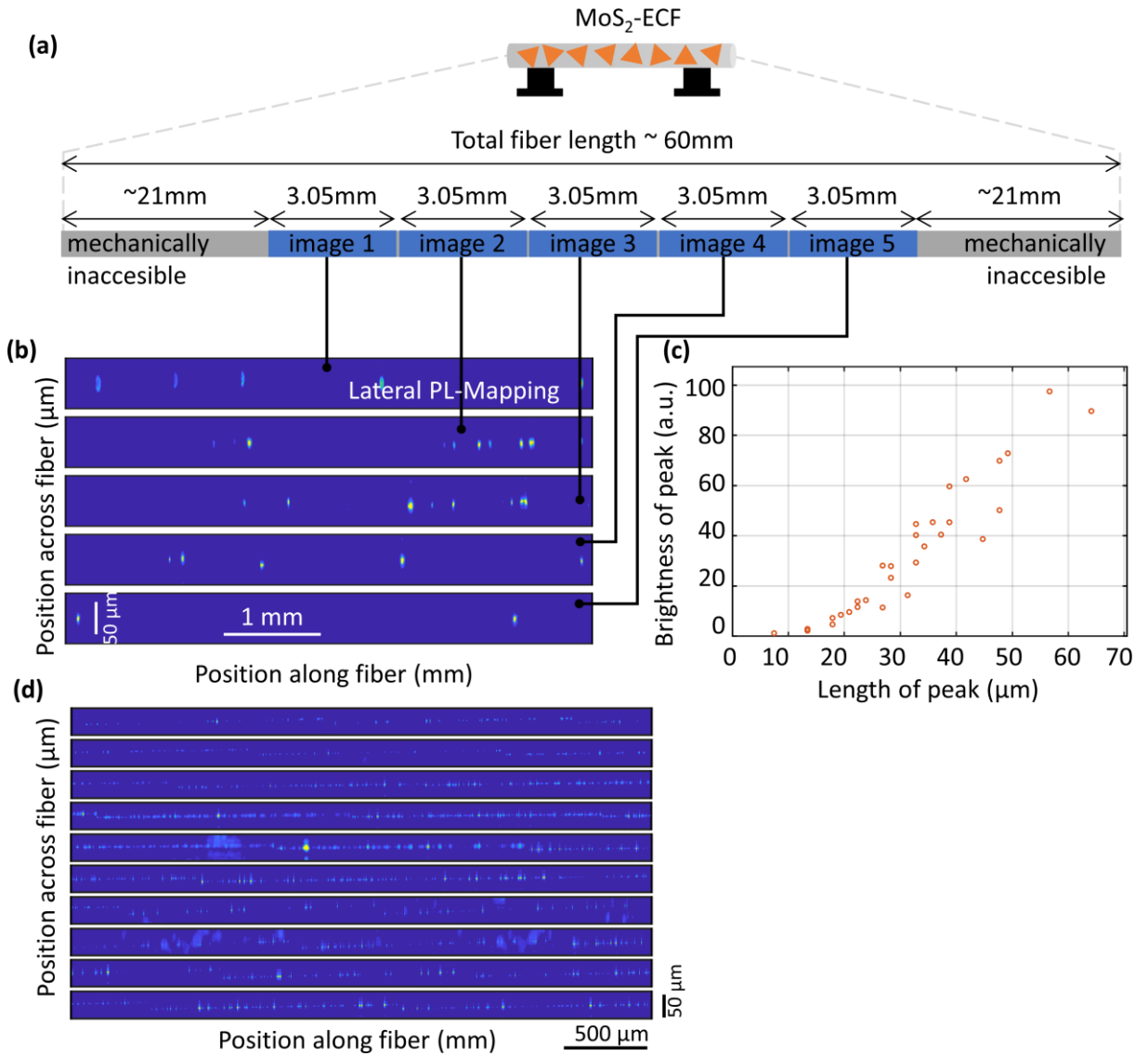
Figure 4.5: Characterization of TMD-monolayer distribution and crystal size. **(a)** Schematic setup to illustrate the sideways PL-characterization along the fiber. The gray areas on the fiber are inaccessible due to the fixing of the fiber holder. The scanned region is marked in blue. **(b)** The compound image from the accessible 18.3 mm-long section of an MoS_2-coated ECF. The bright spots are the collected PL emission from active monolayers on the fiber core with an excitation of a 532 nm CW laser. There are 39 distinct peaks with a total length of 0.99 mm, corresponding to a coverage of 5.4 %. **(c)** The length of measured PL peaks versus the brightness. The average peak has the length of 29.5 µm. Subfigures **(b-c)** adapted from [146]. **(d)** The compound image from the accessible 35 mm-long section of an MoS_2-coated ECF. The bright spots are the collected PL emission from active monolayers on the fiber core excited by the identical laser. The total length of accumulated bright spots is 15.1 mm, corresponding to a coverage of 43.4 %. Subfigure **(d)** adapted from [205].

literature [206] for comparison. The discrepancy in the excitonic resonances between the monolayer MoS_2 on a planar substrate [206] and our monolayer MoS_2 on ECF is likely due to the difference in substrates, measurement, and the growth method. The monolayer MoS_2 in the literature [206] was transferred on a SiO_2/Si substrate, and a deterministic measurement of the permittivity in a scheme of ellipsometry was carried out. In the case of monolayer MoS_2 on silica ECF, the monolayers were grown directly, and the excitonic resonances were observed by the stronger absorption of the transmitted light compared to off-resonant wavelengths. The observation of the exciton species in the transmission is empirical evidence for the strong light-matter

interaction of MoS_2 monolayers. This technique can be used to monitor the dynamic change of exciton characteristics in contact with an opening environment, for example, in gas sensing.

For further understanding of the statistics of active monolayers on the fiber core, a lateral PL mapping was performed, as shown in Figure 4.5a, using the PL spectroscopy setup. The TMD-coated ECF was fixed on a fiber holder and coupled with a 532 nm laser beam. A translation stage, including a camera, a set of long-pass filters, and a 10x objective, moved longitudinally throughout the fiber and focused on the bottom of the fiber groove. We have to emphasize that there are two "levels" in the growing process on ECFs. In the first phase, we could grow only a low-density coating of the monolayer MoS_2 on the fibers. After some improvement, we were able to functionalize ECFs with high-density coated monolayers. In Figure 4.5b, a low-density coated ECF was investigated first. Scanning results are a compound image of PL emission from an 18.3 mm-long section and are presented in five subsections. We found 39 distinct MoS_2-monolayers with a cumulative length of 0.99 mm observed from this specific fiber. The average length of each crystal is 29.5 μm with a filling factor of 5.4 %. A threshold of brightness was set to exclude the noise level and count only the spots with values over this threshold as PL-active monolayers. Figure 4.5c reveals the connection between the accumulated brightness and the length of the active crystals. The linear behavior means that the material quality is independent of the crystal size. In other words, the PL quantum yield of grown monolayer MoS_2 is homogeneous.

In the latter batch of fibers, the growth process has been improved to obtain a higher density of monolayer TMDs on the fiber core. Using the identical setting an MoS_2-coated fiber with a length of 40 mm has been investigated. A total length of approximately 35 mm has been measured by collecting the PL emission from as-grown monolayer MoS_2 on the core region. The PL mapping along the fiber is displayed in Figure 4.5d as a compound from 10 distinct stacked images. The analysis of collected PL as bright spots from the camera after filtering out the laser excitation reveals a total length of 15.1 mm of monolayers. This emission length corresponds to a coverage of 43.4 %, which is almost eight times higher than previously coated fibers in Figure 4.5b. This optimization enables us to obtain a higher filling factor and extend the interaction length of the functionalized ECFs.

4.2 Summary of the results

In this chapter, we have shown that monocrystalline TMD, such as MoS_2 and WS_2, can be grown directly on the ECF core without any manual transfer. The optical properties of monolayer TMDs on ECF are virtually unchanged in comparison with those grown on the planar substrate. Hence, the modified CVD is a versatile method to functionalize the exposed core of the optical fibers with

2D materials. The combination of CVD with ECF creates a new platform to investigate the excitonic nature and exploit the optoelectronic properties of 2D materials in a scalable manner. Here, the coated ECF has demonstrated its function with the excitation of excitons and the collection of PL via the interaction between monolayer TMDs and the evanescent field of guided modes. This approach may be suitable for remote sensing schemes based on photoluminescence and transmission spectroscopy. Additionally, the higher density coating of TMDs on the ECF might increase the sensitivity and selectivity of the fiber-based sensors. Our effort to increase the filling factor of TMD-coated ECF is a stepping stone to bringing this approach closer to a fully controllable and scalable process.

Because the dynamics of excitons, for instance, a transition from bright excitons to trions and vice versa, will be varied by the charge transfer process of active monolayers and the surrounding environment. This mechanism can be employed to detect the target gases. The sensitivity is supposed to be proportional to the interaction strength of gas molecules and TMDs, hence longer interaction length or higher mode overlap is highly sought-after. The former case can be done by different growth techniques to achieve a higher filling factor, for instance, by predetermining the location of grown monolayer TMDs [193]. The latter case requires some modification of the fiber geometry or structure, for instance, by a dielectric thin film coating or with a smaller fiber core. Experimental and theoretical data for the charge transfer process will be discussed in Chapter 5.

Remarkably, monolayer TMDs have been demonstrated to support long-lived dark exciton, which is spin forbidden, such as triplet state [207-210]. These excitonic species might find potential applications in information processing and communication [211]. Wang *et al.* have used a high NA objective to collect the intrinsic PL from this out-of-plane dipole [212]. As a new approach, the dark exciton excitation can be investigated by TMD grown on ECF because our fiber supports the out-of-plane polarized wave propagation to the crystallographic plane. The successful demonstration of in-fiber exciton excitation and PL collection opens a new door to single-quantum emission sources [87, 90] embedded in ECFs. The function of these single photon emitters (SPE) is based on the defect states in monolayer TMDs grown on SiO_2/Si substrate. So far, there is no investigation of such SPEs on ECF, hence we can expand this field of research.

5. Remote sensing with exposed-core fibers

5.1 Fundamentals of gas sensing

In previous chapters, microstructured optical fibers [213], particularly ECFs, have shown their ability as a promising photonics platform to grow 2D materials for exciton investigation and photoluminescence collection. In terms of optical sensing, microstructured optical fibers are highly attractive because of their low loss, long interaction length, scalability, and small volumes together with freedom in architecture design [214-219]. For microstructured optical fibers that are working based on the evanescent field, the sensitivity is resolved by the field overlap between the guided modes and the sensing medium and thus is strongly affected by the structure of the optical fiber. For example, the mode overlap is reported as high as 0.1-0.2 % for D-shaped fibers [214], 5.2 % for photonic crystal fibers [215], 6.5 % in multi-core optical fibers [216], and up to 95 % in hollow-core photonic fibers [220]. The low overlap value in a D-shaped fiber is ascribed to the large distance from the fiber core to the air-silica interface where the sensing material is deposited on. The light-matter interaction in the cases of photonic crystal fiber, multi-core fiber, and hollow-core fiber has been increased due to the high number of cores, hence, boosting the interaction area between the sensing target inside the air holes and the guided modes. Another approach to increase the power fraction is using the microstructured optical fiber with an embedded nanowire core [221], which can reach up to 70 %. This strategy can apply to different geometries in the family of microstructured optical fibers. Although the aforementioned fibers have a substantial field overlap, nevertheless, they are still limited to practical applications. These suspended-core fibers need a long time to fill the core and have a slow response time. For instance, the filling time can take about 7 hours for gas diffusion [222], around 100 minutes for water filling along a 1 m-long fiber [223], and more than 4 hours to fill a 0.5 m-long fiber with isopropanol [217]. This disadvantage makes suspended-core fibers inappropriate for real-time sensing in practice.

A fast-response sensing fiber is, therefore, highly desired. Here, ECFs with high transmission from UV to NIR enable fast response and hence open up a versatile platform for biochemical and gas sensing applications [144]. Remarkably, an ECF needs about one second to reach the maximum fluorescence, while a suspended core fiber requires 70 minutes in the same condition [224]. Thus, ECF is more appropriate for real-time sensing. In most cases, ECF plays a role as a substrate, while the sensing is performed by fluorophores. The viability of the ECF platform for sensing has already been demonstrated for nitric oxide [225] and salinity [226]. Also, theoretical models of ECFs for fluorescence and absorption-based sensing with liquid have been studied, leveraging the applicability of ECFs [227]. Furthermore, the evanescent field of ECFs can be enhanced by the

incorporation of a polymeric analyte layer [228]. Most previous works used organic dye or quantum dots as fluorophores, which exhibit phototoxicity and photo-bleaching. Moreover, the short lifetime of such organic fluorophores in the non-aqueous environment is another disadvantage for practical applications. The photo-bleaching of the fluorophores will reduce the stability and precision of sensors.

Recently, Motala *et al.* have demonstrated selective chemical sensing using thin-film MoS_2-coated optical fibers employing transmission and excitons [229]. In their approach, a 10 nm-thin film was coated over the top surface of glass fibers by a magnetron sputtering. By monitoring the loss in transmission spectra in the visible range of the MoS_2-coated fibers, they can detect different aliphatic and aromatic compounds, for example, the detection of aniline down to 6 ppm. The mechanism is attributed to the absorption or scattering of the excitons leading to the change of transmission spectrum.

The emergence of 2D materials-based sensors [230] arises from the conformal growth of such high-quality crystals on various substrates by the weak van der Waals force [146, 205, 231]. There is a great demand from public health and industry in monitoring toxic gases and aqueous solutions without direct contact. The value of adsorption energy is an important parameter to quantify the interaction strength between gas molecules and monolayer TMDs. This interaction can be in the form of adsorption or desorption of gas molecules on the monolayer's surface [232, 233]. Some gases can donate electrons to TMDs' electronic bands, whereas other gases can receive electrons from TMDs [91-94, 230]. The acceptance or depletion of electrons in monolayer TMDs leads to the change of major charge carriers in TMDs. For example, the monolayer MoS_2, an n-type semiconductor, will gain more electrons if it receives charges from gas molecules. In contrast, the monolayer MoS_2 will lose electrons and have more holes if it donates charge carriers to gas molecules. Because an exciton is the bound state of an electron-hole pair, and a trion is the bound state of three charges (two electrons and one hole or two holes and one electron). Any charge transfer process can result in the variation of charge carriers in the monolayer TMDs. Consequently, the PL or absorption spectra of monolayer TMDs will vary, and it is the main way to detect gases.

The binding energy between gas molecules and the monolayer MoS_2's surface can be calculated using the density functional theory [95]. The adsorption of gas molecules such as O_2, NO_2, and NO molecules can vary the dielectric constant of monolayer MoS_2 [96]. Tongay *et al.* have demonstrated that the PL signal of exfoliated monolayer MoS_2 increases 10x, 35x, and 100x when exposed to O_2, H_2O, and a combination of O_2 and H_2O in a vacuum chamber, respectively [233].

Hence, one may detect the presence of these gases by analyzing the PL signal. However, the PL of monolayer TMDs is also found to be highly susceptible to the substrate [234].
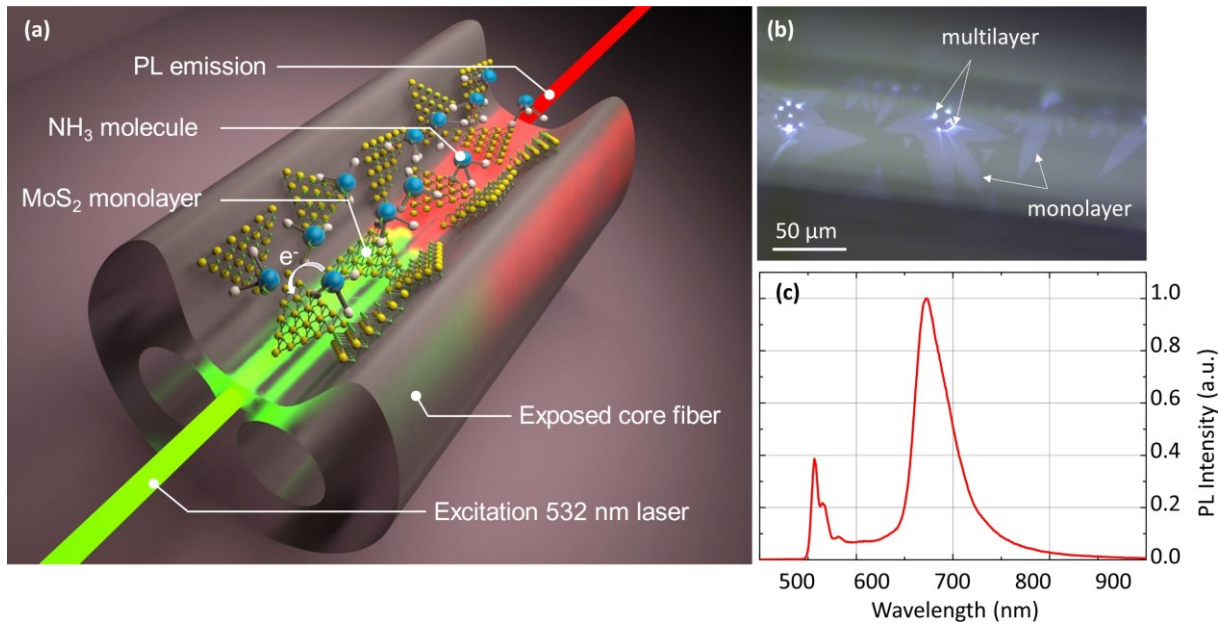
Figure 5.1: (a) Illustration of the sensing based on monolayer MoS_2 deposited on exposed-core fibers. **(b)** Microscopic image of a typical MoS_2-coated ECF used for sensing. **(c)** PL from an MoS_2-functionalized ECF under the excitation of 532 nm CW laser coupled into the fiber core.

In this work, we show that TMD-coated ECFs maybe suitable for highly sensitive optical remote sensing with fast response times. More specifically, monolayer TMDs on the guiding core of ECF were used as active sensing elements. The high surface-to-volume ratio of 2D materials is a plus to increase the sensitivity. Additionally, monolayer TMDs have better PL stability and biocompatibility than organic fluorophores [235, 236]. The functionalized ECFs employ the charge transfer mechanism between monolayers and gas molecules for the detection, and the moderate adsorption energy keeps the gas molecules adsorbing on the surface of TMDs but does not require heating for gas removal. The deposition of high-quality monolayer TMDs on the fiber's guiding core yields a highly dense coating of single crystals TMDs over lengths of a few centimeters. Thus, a long light-matter interaction length can improve the sensitivity and selectivity of this hybrid system. TMD-coated ECFs have proved that they can maintain the high PL quantum yield of as-grown monolayer TMDs, therefore, it can be assumed that the massive interaction length of TMD-coated ECF is a substantial advantage for future large-scale integration of micro-biosensors.

Figure 5.1a exhibits the fundamental concept of fiber-based sensing. The excitation coming from a visible CW laser is coupled into ECFs functionalized with monolayer MoS_2 by CVD. The high-quality monolayers grew directly on the waveguide to provide a high-quantum yield of PL from optical fibers. The charge transfer process between analyte molecules and MoS_2 monolayers will vary the concentration of charge carriers in the monolayers due to the doping process. It will lead

to the variation of the PL intensity of the hybrid waveguides. Figure 5.1b displays the MoS_2 monolayers with a size of roughly 50 μm grown on the ECF for gas sensing measurement. Some bright spots in the center of MoS_2 flakes are bulk or multilayers. The change in optical contrast between different crystal thicknesses can help to recognize monolayers under an optical microscope. To demonstrate efficient PL emission of an ECF functionalized by high-quality MoS_2 monolayers through the fiber mode, we first coupled a green laser with a wavelength of 532 nm into the fiber core. The fundamental wave interacts with MoS_2 coating via the evanescent field to excite excitons. PL emission originating from the monolayer TMDs is either emitted into free space modes or coupled back into fibers modes. Since the sum of incoherent PL emission through the fiber mode is much greater than PL emitted from a single monolayer, we monitored only the PL via the fiber mode. Figure 5.1c displays the recorded spectrum from a typical MoS_2-coated ECF. They exhibit characteristic exciton peaks at 678 nm, as expected for the monolayer MoS_2.

5.2 Charge transfer process

There are two key factors in the sensing mechanism: the adsorption energy and charge transfer process between monolayer TMD and gases. Furthermore, the band structure of monolayer TMDs in contact with the gases has been theoretically investigated to have more insights into the influence of the gas-based dopants. Yue *et al.* have calculated the band structure of pristine monolayer MoS_2, and from the theoretical calculations presented in [237], the authors derive that MoS_2 has a direct bandgap of 1.86 eV at the K point in the first Brillouin zone displayed in Figure 5.2a. The band structure, including the conduction and valence bands, is virtually unaffected by the adsorption of numerous gases such as NH_3, CO, NO, and NO_2, except for additional energy levels introduced by the gas molecules. While NO introduces three impurity states (two occupied states from the up-spin band and one occupied state from the down-spin band) into the bandgap, as in Figure 5.2b, NO_2 introduces only one occupied state from the down-spin band, as shown in Figure 5.2c.

An important parameter to quantify the sensing performance between a gas and monolayer TMD is the adsorption energy and given as

$$E_{\mathrm{ad}} = E_{\mathrm{MoS_2+gas}} - (E_{\mathrm{MoS_2}} + E_{\mathrm{gas}}), \qquad (5.1)$$

where $E_{\mathrm{MoS_2+gas}}$ is the total energy of monolayer MoS_2 and adsorbed gas molecules in the optimized configuration, $E_{\mathrm{MoS_2}}$ is the total energy of the pristine MoS_2, and E_{gas} is the total energy of the isolated gas. If $E_{\mathrm{ad}} < 0$, the total energy of the gas and MoS_2 after the adsorption process is less than the sum of energy of each isolated component, then the process is exothermic. The negative value of adsorption energy shows the energetically favorable status, and the adsorption process is likely to take place. The van der Waals force is the dominant contributor to the adsorption

energy, and hence, the magnitude of the adsorption energy will increase if the van der Waals force is included in the calculation [95]. Note that the adsorption energy here is calculated at 0 K without any external thermal energy.
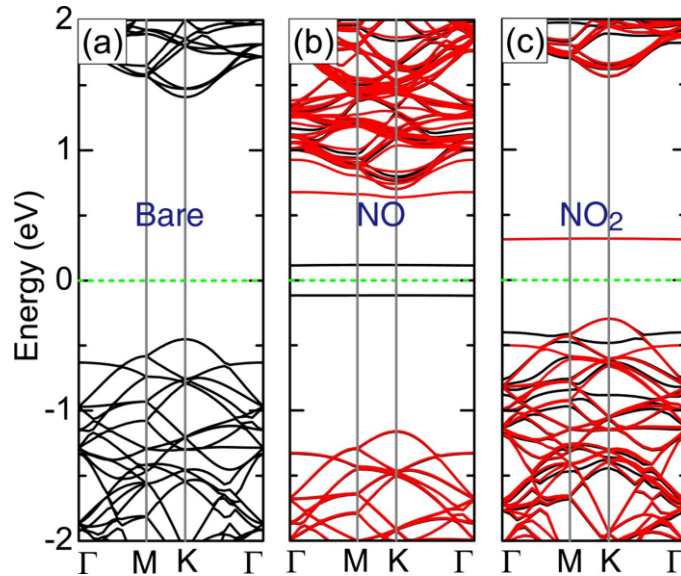
Figure 5.2: Band structures of different systems. **(a)** pristine MoS$_2$, **(b)** NO-adsorbed monolayer MoS$_2$, and **(c)** NO$_2$-adsorbed monolayer MoS$_2$. The black (red) line corresponds to the up-spin (down-spin) bands, whereas the dashed green line indicates the Fermi level. Figure is adapted from [237].

The mechanism of gas sensing with 2D materials is comprehensively based on the doping properties of the gas. To enable the charge transfer, the gas molecules should be bound to monolayers indicated by the sign and magnitude of adsorption energy. Zhao *et al.* have shown that many gases such as CO, NH$_3$, NO, NO$_2$, H$_2$O, N$_2$, and SO$_2$ tend to adsorb on the monolayer MoS$_2$ surface, which is necessary for gas sensing with TMDs [95]. Figure 5.3 displays the adsorption energies between the monolayer MoS$_2$ and various gases. All gases show negative adsorption energy to the monolayer surface. Amongst them, NO and NO$_2$ have greater adsorption energies in absolute value than others, suggesting that these gases can bind strongly to the monolayer surface and can lead to an effective interaction. The first principle calculations in Figure 5.3 have been performed using Density Functional Theory (DFT) employing the Vienna ab initio simulation package. All calculations, for instance, band structure, adsorption energy, and charge transfer, are simulated based on Perdew, Burke, and Ernzerhof (PBE) functionals.

Another key parameter of the sensing process is the quantitative charge transferring between the absorbates and the host material. If a gas molecule can donate or accept more electrons from monolayer TMDs, it can be possible to detect the gas at a low concentration because the modulation of PL intensity is still significant. Yue *et al.* have calculated the charge density difference for various gases-MoS$_2$ systems using the formula

$$\Delta\rho = \rho_{MoS_2+gas} - (\rho_{MoS_2} + \rho_{gas}), \tag{5.2}$$

where ρ_{MoS_2+gas} is the charge density of the gas-MoS_2 system, ρ_{MoS_2} and ρ_{gas} are the charge density of the pristine monolayer MoS_2 and the isolated gas molecule, respectively.
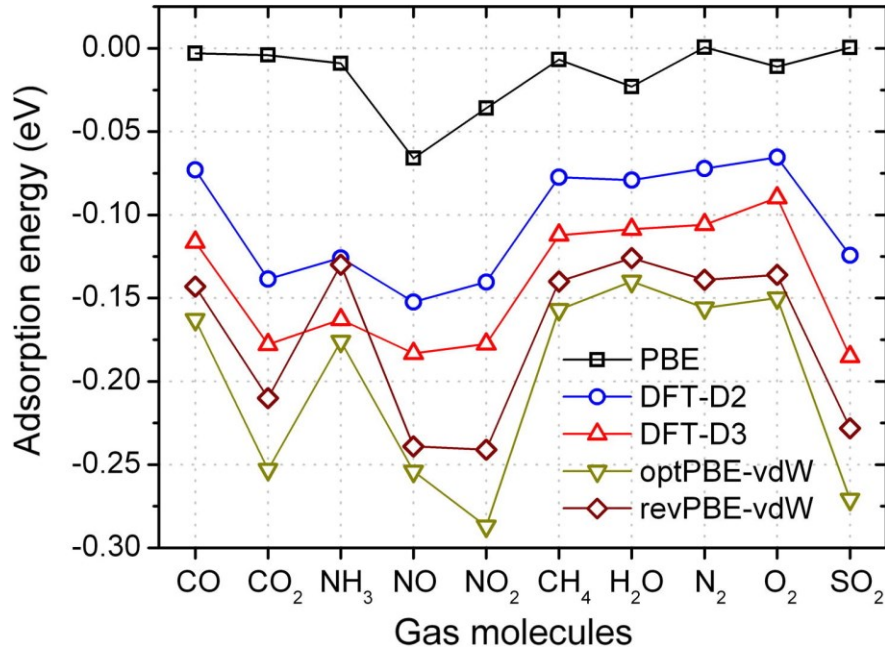
Figure 5.3: Adsorption energies of several gas molecules on the surface of the monolayer MoS_2 determined by different methods: PBE, DFT-D2, DFT-D3, optPBE and revPBE. Figure is adapted from [95].
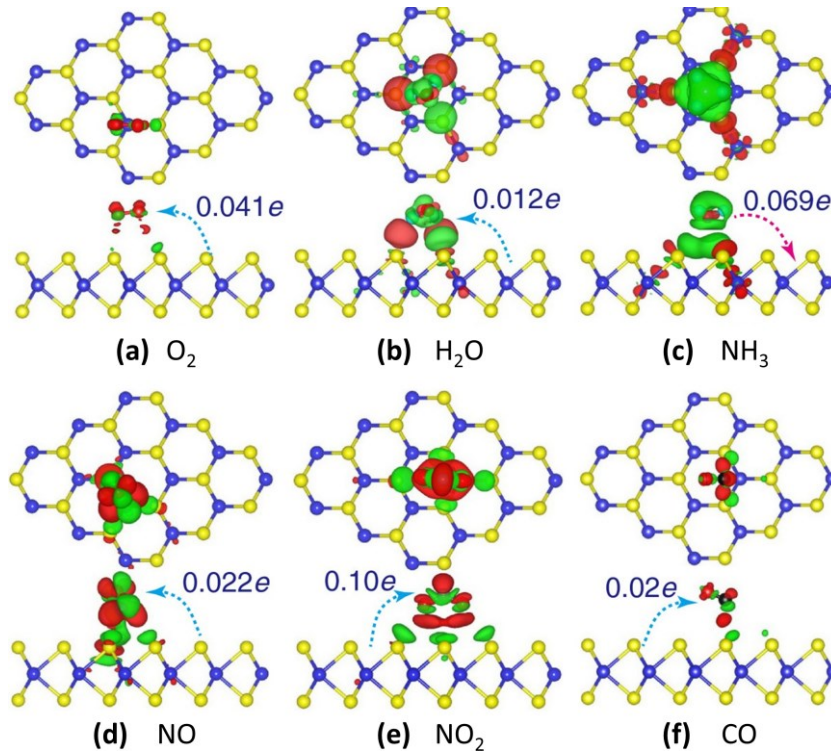
Figure 5.4: Charge transfer process and density difference plots for various gases from **(a-f)**: O_2, H_2O, NH_3, NO, NO_2, and CO interacting with monolayer MoS_2, respectively. The red (green) distribution corresponds to charge accumulation (depletion). Figure is adapted from [237].

Figure 5.4 reveals the calculated charge density difference for numerous gases. While almost all gases play the role of an acceptor to receive the transferred charge from MoS_2, NH_3 exhibits the opposite behavior as a donor. Amongst the acceptors, NO_2 shows the strongest interaction when it

can accept 0.1 e$^-$ from MoS_2. In the case in which the gas is an acceptor, the depletion of charge carriers in the monolayer MoS_2 leads to a dynamic change from trion to neutral exciton and vice versa in the case of a donor such as NH_3. We can expect to see the reverse characteristics of PL for donor and acceptor gases. For optical-based sensing, the charge transfer between gas molecules and the monolayer TMD is the most crucial parameter to obtain the PL modulation, which is a benchmark for gas sensors [233].

5.3 Sensing experiment with TMD-coated ECFs

To perform the remote sensing schemes, we fabricated a vacuum chamber from aluminum with an inner dimension of 460 mm x 420 mm x 300 mm. The net volume is 40 dm^3 after subtracting the occupied volume of optical elements. The chamber is sealed by O-rings and has two optical windows to conduct the light. The purpose of a large size volume is to build an optical setup inside the chamber that can be accessed by hand. The components inside the chamber include the translational stages, aspheric lenses, and samples. In this section, only NH_3 and N_2 were used for the testing due to the restriction of using toxic gases in the lab. The chamber allows us to reach a slightly negative pressure of - 900 mbar and inject the N_2 or other gases from the connecting pipes.
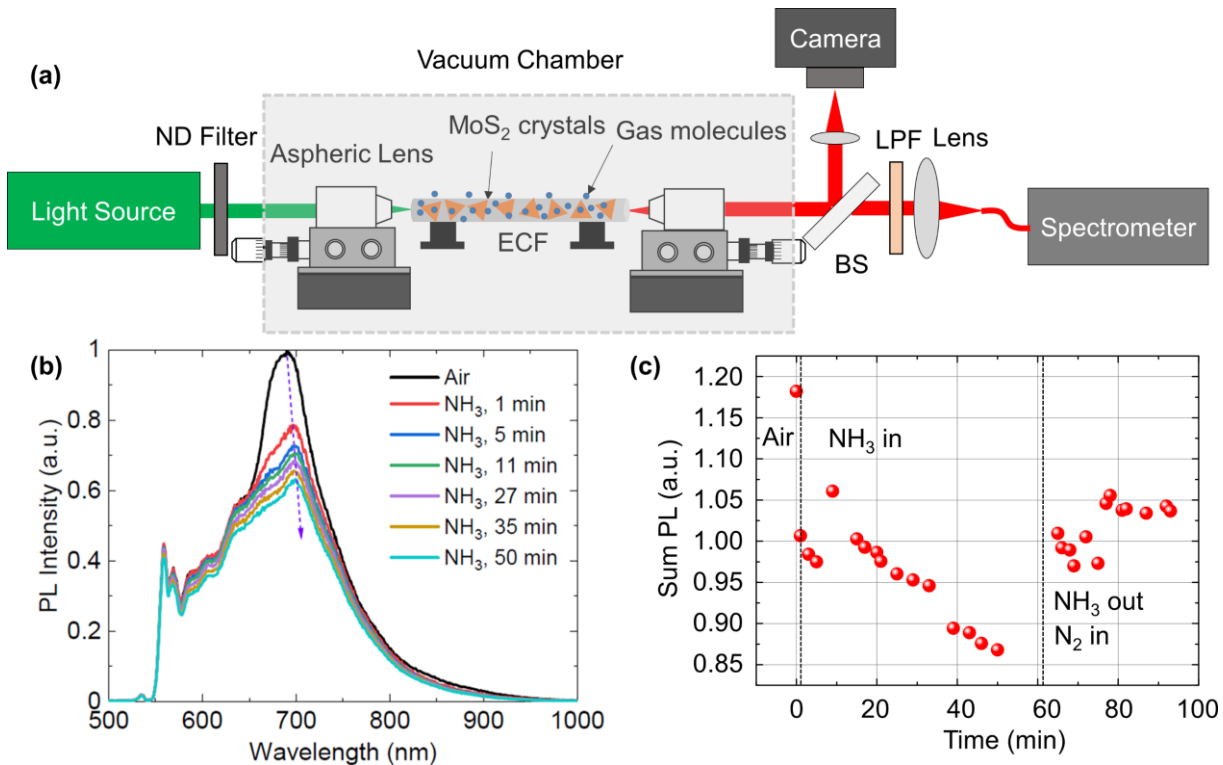
Figure 5.5: Schematic diagram of the experimental setup for MoS_2-coated fibers. **(a)** PL-based sensing configuration. The orange triangles present the MoS_2 monolayers, whereas the blue dots indicate the gas molecules. The dashed box shows the scope of the vacuum chamber for sensing measurement. The excitation is a 532nm continuous wave laser. **(b)** PL spectra of an MoS_2-coated ECF in air and in contact with NH_3 gas. **(c)** Analysis of sum PL in air, with NH_3, and without NH_3. ND: neutral density, ECF: exposed-core fiber, BS: beam splitter, LPF: long-pass filter 550 nm.

Figure 5.5a displays the experimental setup for NH_3 sensing. Here, we used an aspheric lens with a focal length of 4.03 mm to couple the light from the 532 nm CW laser into the fiber core. The outcoming light was collected by another aspheric lens. To monitor the guided modes and to collect the output signal simultaneously, we used a beam splitter. A major part of the outcoming light was imaged on a grating spectrometer (Horiba Jobin Yvon Triax), while a smaller part was focused on a camera.

In this measurement, 20ml of NH_4OH (25 % NH_3 in H_2O, density: 0.91 g/cm^3, bought from Carl Roth GmbH) in a beaker has been put inside the vacuum chamber. NH_3 was evaporated due to the transferred heat from a hot aluminum cube inside the chamber. We have to clarify here that there is no control over the concentration of the target NH_3 gas. Because there is no precise control of the NH_3 flow rate, in this case, we determined the lowest detection level by assuming all the NH_3 in the solution evaporated at the same time. Then 5 ml of NH_3 (25 % of 20 ml solution) is assumed to be present inside the 40 dm^3 net volume of the gas chamber, which leads to a concentration of 125 ppm. Hence, this work only shows a lower boundary in NH_3 detection but is not limited to any higher sensitivity using the above assumption.

Figure 5.5b reveals the PL spectra of an MoS_2-coated ECF excited by a CW 532 nm laser. The setting was identical for the whole set of measurements, and the N_2 gas was injected inside the chamber to set the background condition. A vacuum pump was used to exhaust the target gas. The normalized PL peak intensity was maximum in air conditions and showed a peak at 689 nm, which is related to the A-exciton of the monolayer MoS_2. After the injection of NH_3 gas from a solution of NH_4OH by thermal heating, the normalized PL dropped to 0.8 after 1 min and gradually decreased to 0.6 after 50 mins. We also observed the redshift of the PL peak from 689 nm to 700 nm, which is proportional to the concentration of NH_3 in the chamber. This may be explained by the charge transfer process between the MoS_2 and NH_3 [238, 239]. In this case, NH_3 plays a role as a donor, and it donates the electron to the monolayer MoS_2. Since MoS_2 is an n-type TMDs [233, 240], the acceptance of free charge to MoS_2 leads to the transition from an exciton to a negative trion [238, 239]. Because the trion has lower energy than the bright exciton, the red shift of the PL peak is expected. This behavior has been reported by Mouri *et al.* with the tunability of PL from monolayer MoS_2 by chemical dopants [241]. The enhancement of PL was observed with the exposure to the p-type dopants, while the quenching occurred by the n-type dopants.

The change in PL spectra happened not only with the peak but also with the sum of emissions. By analyzing the PL signal in the region of interest from 600 nm to 800 nm, as plotted in Figure 5.5c, we observed the drop of the PL signal in the presence of NH_3 in the chamber. This process can be recovered by purging out NH_3 by the injection of N_2 in the chamber until the whole chamber is

fully occupied by N$_2$. If we consider the large volume of the chamber and the small flow rate of N$_2$, the recovery occurs only by the exchange of the gas molecules, not by air pressure. The purge of N$_2$ inside the chamber has reversed the charge transfer process due to the removal of NH$_3$ from the monolayer MoS$_2$. In contact with N$_2$, MoS$_2$ tends to donate electrons to this gas with the opposite effect compared to NH$_3$ and therefore recovered the PL feature [242]. However, the adsorption energy and the charge transfer between N$_2$ and monolayer MoS$_2$ are small, and hence it is not suitable to detect N$_2$ directly, but likely efficient to recover the original state of TMDs.

5.4 Refractive index sensing

As demonstrated in the previous section, the exposure of the core is not only beneficial for the TMD coating but also for real-time sensing with the gas species. When the gas is adsorbed onto the fiber core or the surface of TMD in the exposed region, the propagating light will be absorbed by the gas species expressed by the Beer-Lambert law [243]

$$I = I_0 \exp[-r\alpha(\lambda)lC], \tag{5.3}$$

where I and I_0 are the output light intensities with and without the presence of gas, respectively. $\alpha(\lambda)$ is the absorption coefficient of the measured gas and as a function of wavelength, l is the interaction length of the ECFs for gas detection, C is the gas concentration, and r is the relative sensitivity coefficient.

The relative sensitivity coefficient r is defined as [243]

$$r = \left(\frac{n_\mathrm{r}}{n_\mathrm{eff}}\right) \frac{\int_{A_s} \Re\mathrm{e}\big(E_x H_y^* - E_y H_x^*\big)dxdy}{\int_{A\infty} \Re\mathrm{e}\big(E_x H_y^* - E_y H_x^*\big) dxdy}, \tag{5.4}$$

where n_r is the refractive index of the gas, which is approximately equal to 1.0, n_eff is the effective refractive index of the guided mode, E_x, E_y and H_x, H_y are the transverse electric and magnetic field components of the propagating mode. * denotes the conjugate variables, A_s indicates the integration over the exposed region, $A\infty$ refers to the transverse cross section.

We present here the simulation results on the relative sensitivity of ECFs. Our optical fiber has a core diameter of 2 μm, and there are two near-degenerate fundamental modes with almost horizontal and vertical polarization, leading to different modal overlaps with TMDs. Due to the stronger influence of the *x*-polarized FM, the numerical data in Figure 5.6a-b are only calculated for this specific polarization. Figure 5.6a shows the effect of varying the core diameter and the incident wavelength. Please note that the fiber geometries to produce the data in Figure 5.6a are depicted in Appendix C (Figure C1), and this fiber geometry is different from the actual fiber geometry. However, this simple model is helpful to investigate the relative sensitivity as a function

of the core diameter. When the core diameter is smaller, the guided modes are less confined within the core boundary resulting in a larger fraction of the evanescent field. This behavior is similar to the longer excitation wavelength.

From Equation 5.4, the relative sensitivity r is proportional to the fraction of power flow into the exposed core region where monolayers are deposited. Hence, the relative sensitivity increases for smaller core diameters and longer excitation wavelengths. This parameter is not only valuable for photoluminescence but also valid for transmission-based performance. Although Figure 5.6a only reveals the calculation for gases with a constant refractive index, from Equation 5.4, we also can notice that the relative sensitivity is also proportional to the refractive index of the sensing target, and Equation 5.4 is also applicable to aqueous media.
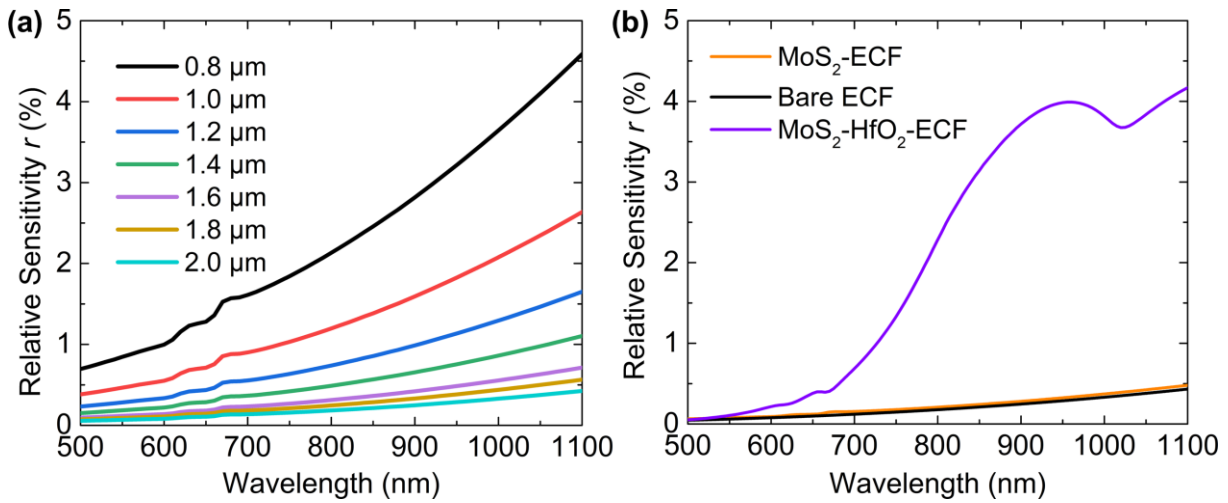
Figure 5.6: Calculated relative sensitivity of ECFs. **(a)** Swept sensitivity as a function of core diameter and wavelength for MoS$_2$-coated ECFs. The geometry of ECF is made simple to scale the core diameter. **(b)** Relative sensitivity as function of wavelength in comparison between MoS$_2$-coated ECF and bare ECF with two orthogonal fundamental modes.

The deposition of TMD has a slight impact on the relative sensitivity, as exhibited in Figure 5.6b. The increase in relative sensitivity r is due to the shift of the guided mode towards the exposed side because of the higher refractive index of monolayer TMD. Nevertheless, TMD in our model has a sub-nanometer thickness, therefore, the shift of the guided mode is less pronounced. Additionally, another way to enhance the sensitivity coefficient is using smaller core fibers, which are less confined to the guided mode than the larger ones. Despite this advantage, the small-core fibers also have some difficulties in handling due to their fragility and a higher loss. We also can increase the sensitivity by coating a high dielectric constant thin film between monolayer TMD and silica core to drag the guided mode upwards. The calculated relative sensitivity of MoS$_2$-ECF with another coating of HfO$_2$ as a buffer has shown an increase of up to 220 %, compared to without HfO$_2$ at $\lambda_0 = 680$ nm. The enhancement increases proportionally to the growth of wavelengths and can reach 700 % at $\lambda_0 = 1100$ nm. The reason to select HfO$_2$ thin film to modify the guided modes

stems from its large bandgap (5.3 - 5.8 eV) [244]. This material has negligible absorption in the visible spectral range and hence no PL quenching from monolayer TMDs. By coating a high dielectric constant thin film such as HfO_2, the guided modes are relocated towards the monolayer TMDs.

As mentioned hereinbefore, the fraction of optical power that propagates through the exposed region and interacts with monolayer TMDs and sensing medium is the key parameter for fiber sensing. While Equations 5.3 and 5.4 are appropriate to quantify the transmitted light intensity change because of the absorption and scattering processes, they are inappropriate for fluorescence-based sensing. Moreover, semiconducting monolayers superimposed on the fiber core can work as a fluorophore source. The efficiency of coupling back the fluorescence by the guided modes of the fiber has been introduced by Afshar *et al.* for the FMs [217] and by Warren-Smith *et al.* for HOMs [245]. This theoretical model has been experimentally validated for Rhodamine B dissolved in water [245]. The fraction of fluorescence (FCF) that is excited by mode j^{th}, captured into all guided modes v of the fiber at the fluorescence wavelength λ, and propagates to the output end of the fiber is expressed as [245]

$$FCF_j = \frac{\xi\lambda^2}{16\pi n_F^{A_s\,2}} \sum_v \frac{NOI_{jv}}{A_{\text{eff},v}} \frac{\gamma_j^{A_s} e^{-\gamma_v L}}{\gamma_v - \gamma_j} \left[e^{(\gamma_v - \gamma_j)L} - 1\right], \qquad (5.5)$$

$$NOI_{jv} = n_F^{A_s} \left(\frac{\varepsilon_0}{\mu_0}\right)^{\frac{1}{2}} \left[\frac{\int_{A\infty} |S_v(\vec{r})| dA}{\int_{A_s} S_j(\vec{r})\, dA}\right] \left[\frac{\int_{A_s} |\vec{e}_v|^2 S_j(\vec{r}) dA}{\int_{A\infty} |S_v(\vec{r})|^2\, dA}\right], \qquad (5.6)$$

$$A_{\text{eff},v} = \frac{\left|\int_{A\infty} S_v(\vec{r}) dA\right|^2}{\int_{A\infty} |S_v(\vec{r})|^2\, dA} = \frac{\left|\int_{A\infty} Re[(\boldsymbol{E}_v \times \boldsymbol{H}_v^*).\hat{z} dA]\right|^2}{\int_{A\infty} |Re[(\boldsymbol{E}_v \times \boldsymbol{H}_v^*).\hat{z}]|^2\, dA}, \qquad (5.7)$$

where $A\infty$ defines the transverse cross section of the boundary, A_s refers to the exposed region, L is the fiber length, $S_j(\vec{r})$ is the z-component of the Poynting vector of the jth mode, $\boldsymbol{E}_j(\vec{r}), \boldsymbol{H}_j(\vec{r})$ are the electric and magnetic fields of the jth mode, ξ is the fluorophore efficiency, λ is the fluorescence wavelength, $n_F^{A_s}$ is the refractive index in the exposed region at the fluorescence wavelength, NOI is a normalized field-matter overlap integral, A_{eff} is the modal effective area, $\hat{z}$ is the unit vector along the propagation direction, and γ is the attenuation coefficient [246]. We assume that the fluorescent sources are contained within the exposed region, and they have random phase and orientation.

The ability of ECF for refractive index sensing has been demonstrated by Ding *et al.* employing CdTe/CdS quantum dots as photon emitters to detect NO [225]. The change in the environment, for instance, the refractive index surrounding the photo emitters and fiber core, will have a

significant impact on the guided modes. The PL efficiency of monolayer TMDs grown on ECFs is strongly affected by the field overlap between fiber modes and the monolayer. As a result, the change of refractive index from the environment will vary the PL emission of the hybrid waveguides and can be exploited for refractive index sensing. Figure 5.7a-c display the FMs with x-polarization at $\lambda_0 = 532$ nm for three different sensing media in the exposed region including air, ethanol, and water. The evanescent field in the exposed side area is increasingly proportional to the increase of refractive indices, hence raising the mode overlap to monolayers. The complex refractive indices of water and ethanol were taken from the literature [247, 248] for the simulation.
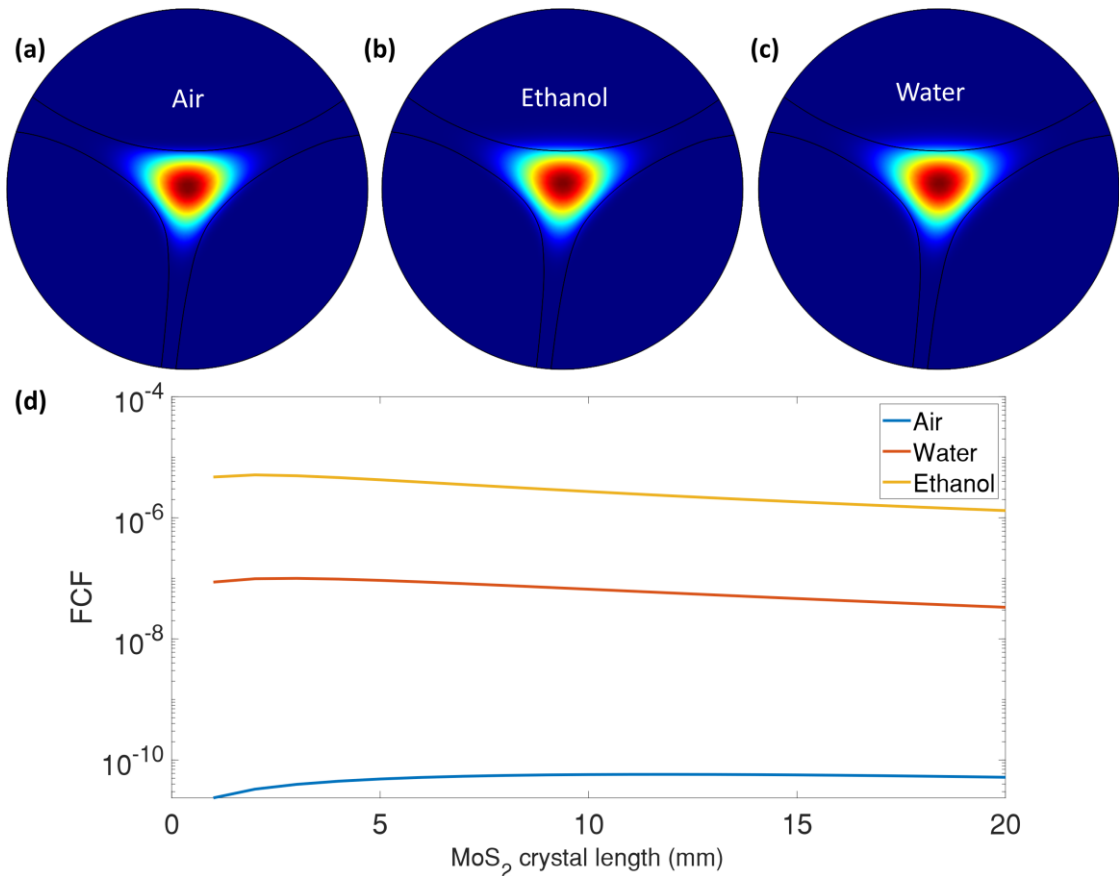
Figure 5.7: Electric field distribution for three different sensing media. **(a)** Air. **(b)** Ethanol. **(c)** Water. **(d)** FCF was calculated for different analyte media as a function of the total accumulative crystal length. Propagation loss was included.

Figure 5.7d displays the fluorescence fraction which can be coupled into multiple guided modes of the fiber and calculated for three different media: air, water, and ethanol using Equations 5.5-5.7. FCF values are plotted as a function of the monolayer MoS_2 length, with the contribution of 50 HOMs. The FCF first steadily goes up to the maximum with the increase of the crystal length, and until the loss becomes dominant, then FCF decreases gradually. The calculated FCF value at $\lambda_0 = 532$ nm and fluorescence wavelength of 678 nm is given in Table 5.1 for three media. The localized field inside the sensing region is strongly influenced by its refractive index and will vary the FCF. This mechanism might be interesting to monitor the leakage of aqueous or vapor solvents using

TMD-coated ECFs. Because our ECF can support multiple modes, and many HOMs can involve in the fluorescence capture process, thus, in our calculation, the FCF value increase with the included number of HOMs. In Table 5.1, FCF was calculated with the contribution of only x-polarized FM and 20 HOMs but with the assumption of no loss in the system. That explains the substantial FCF captured by 20 HOMs without loss here in comparison to 50 HOMs with loss in Figure 5.7d.

Table 5.1: Calculated FCF for different sensing media with the excitation wavelength at $\lambda_0 = 532$ nm and the fluorescence wavelength at 678 nm, with assumed fluorescence efficiency of 1 % and there is no loss included for the calculation. Crystal length is assumed to be 100 mm with a filling factor of 100 %.

Sensing medium	Refractive index, n	FCF captured by FM only	FCF captured by 20 HOMs
Air	1.000	$6.3 \cdot 10^{-7}$	$1.5 \cdot 10^{-5}$
Water	1.331	$1.5 \cdot 10^{-6}$	$2.8 \cdot 10^{-5}$
Ethanol	1.358	$1.8.10^{-6}$	$3.4 \cdot 10^{-5}$

5.5 Summary of the results

In summary, we have for the first time demonstrated remote sensing from exposed-core optical fibers functionalized with the monolayer MoS_2. This demonstration is also applicable to other fiber architectures and 2D materials. Our measurements show the capability of the system to detect NH_3 with a response time of 1 min and with the detectable level of less than 125 ppm. The real response time may be decreased by reducing chamber volume to decrease the traveling duration of the gas, thus further reducing the time required for an accurate measurement. The response of TMD-coated ECF is reversible by replacing the target gas with an N_2 injection. The sensitivity level is not limited to 125 ppm of NH_3 for our fiber, and it may detect lower gas concentrations by an improved gas experimental setup. The work that has been performed here is a solid foundation for further future studies of gas sensing with 2D materials on ECF.

Furthermore, our simulations reveal the potential application of optical fiber sensors for the detection of the surrounding environment based on the refractive index, which is suitable to monitor aqueous solutions. While the demonstration was carried out in a non-optimized fiber geometry, there is still room for further improvement by more sophisticated designs. We believe that a further improvement of response time and sensitivity may open fresh perspectives for enhanced optical gas sensing and surface-sensitive bio-analytics. All of these open new possibilities for a scalable, modest, and compact lab-on-a-chip technology.

6. Third-harmonic generation in hybrid waveguides

6.1 Fundamentals of THG in 2D materials

2D TMDs are well-known for their substantial nonlinear optical response per unit thickness, quantified by the third-order susceptibility [98]. The efficiency of nonlinear light generation at the TH frequency is characterized by the nonlinear refractive index [139, 249]: $n_2 = \frac{3}{4cn^2\varepsilon_0}\Re e(\chi^{(3)})$, where $\Re e$ indicates the real part of $\chi^{(3)}$, n is the refractive index of the nonlinear medium, ε_0 is vacuum permittivity, and c is the speed of light. As emerging semiconductors, THG in TMDs has been studied by many groups [99, 100, 250-252] on a planar substrate.
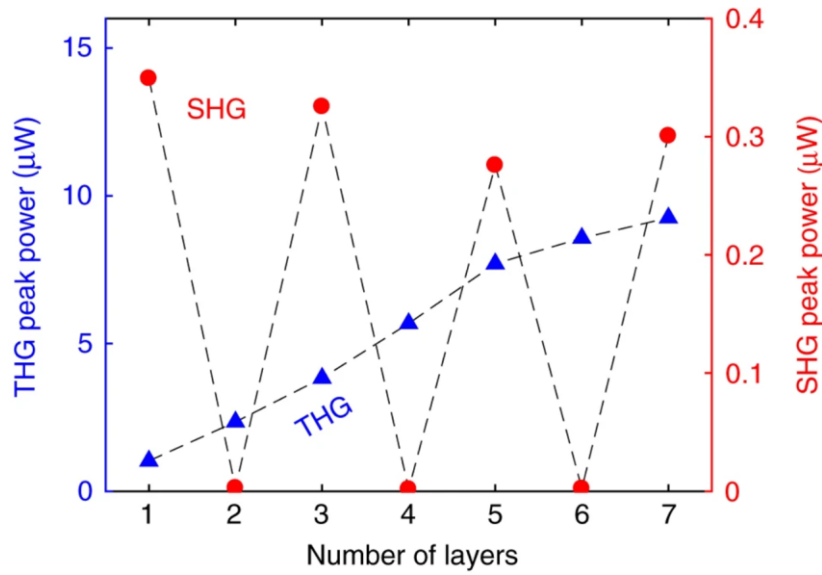
Figure 6.1: Layer-dependent SHG and THG emission from 2H-phase MoS$_2$. Figure is adapted from [99].

Figure 6.1 exhibits the dependence of THG and SHG peak power on the thickness of 2H-phase MoS$_2$. While SHG shows the maximum peak intensity in the monolayer and negligible intensity for even-number layers, THG reveals a stable increase with the number of layers in MoS$_2$. That is due to the independence of THG on the crystal symmetry, which leads to a monotonic modulation by the interaction thickness. Noticeably, the nonlinearity is not equal for different 2D materials. For example, under similar experimental conditions, monolayer MoS$_2$ exhibits a larger THG response than graphene with a factor of three to four [99, 100]. Furthermore, 2D TMDs also have much larger optical nonlinearity than that of SiO$_2$ substrate, enabling a high contrast nonlinear microscopy [97, 100]. A high value of n_2 of 2.7×10^{-16} m^2/W has been reported from monolayer MoS$_2$ transferred on waveguides [141], which is four orders of magnitude greater than the value from SiO$_2$ ($n_2 \sim 2.2 \times 10^{-20}$ m^2/W) [253]. There is a proportional relation between n_2 and $\chi^{(3)}$, therefore, THG efficiency shows a monotonic increase with the quantitative value of n_2. Remarkably, THG in 2D materials is sensitive to the change of many parameters, for instance,

defects [254], doping [255], strain [256], and chemical treatment [257]. Additionally, THG from 2D materials can be tuned broadly by an electric field [258]. The above characteristics bring both advantages and challenges to the $\chi^{(3)}$-based promising applications.

The generation of an electromagnetic field at the frequency 3ω from an incident field at the frequency ω via interacting with a nonlinear medium can be expressed by a nonlinear polarization

$$\boldsymbol{P}_i^{(3)}(3\omega) = \varepsilon_0 \sum_{jkl} \chi_{ijkl}^{(3)}(\omega + \omega + \omega)\,\boldsymbol{E}_j(\omega)\boldsymbol{E}_k(\omega)\boldsymbol{E}_l(\omega), \tag{6.1}$$

here i, j, k, l are the Cartesian components of the incident fields.

Monolayer TMDs belong to the symmetry group D_{3h}, therefore the third-order nonlinear tensor is written as [36, 99, 256]

$$\chi_{1L}^{(3)} = \chi_{1L,xxxx}^{(3)} = \chi_{1L,yyyy}^{(3)} = \chi_{1L,xxyy}^{(3)} + \chi_{1L,xyyx}^{(3)} + \chi_{1L,xyxy}^{(3)}, \tag{6.2}$$

where x is the armchair direction of the monolayer, and y is the orthogonal zigzag direction.

Also, due to the symmetry, the following tensors are equal

$$\chi_{1L,xxyy}^{(3)} = \chi_{1L,yyxx}^{(3)},$$
$$\chi_{1L,xyyx}^{(3)} = \chi_{1L,yxxy}^{(3)},$$
$$\chi_{1L,xyxy}^{(3)} = \chi_{1L,yxyx}^{(3)}. \tag{6.3}$$

From Equation 6.1, a cubic dependence of THG intensity on the excitation power is a fingerprint of a THG process. Hence, a THG process can be confirmed by the cubic dependence of THG intensity ($I_{3\omega}$) on the pump intensity (I_ω), expressed by $I_{3\omega} = A \times I_\omega^3$, with A is a coefficient or prefactor.

6.2 Nonlinear simulation and analysis

The nonlinear and linear properties of the MoS$_2$-coated ECF are calculated using finite element simulations (Comsol Multiphysics v5.4). The geometry of the ECF was taken from the SEM image displayed in Figure 2.10 with a boundary of 9 µm in diameter, which is sufficient to analyze the guided modes inside the core region (core diameter: 2 µm). In this simulation model, a high-refractive index layer with a thickness of 0.65 nm is put on top of the exposed surface to present a monolayer MoS$_2$. The refractive index n of silica fiber is calculated using the Sellmeier equation, and the complex refractive index of MoS$_2$ is taken from Jung *et al.* [206]. The Sellmeier equation for silica is expressed by [191]

$$n^2(\omega) = 1 + \sum_{i=1}^{3} \frac{B_i \omega_i^2}{\omega_i^2 - \omega^2}, \tag{6.4}$$

where ω_i is the resonance frequency, and B_i is the strength of ith resonance. For fused silica optical fiber, the coefficients are found to be $B_1 = 0.6961663$, $B_2 = 0.4079426$, $B_3 = 0.8974794$, $\lambda_1 = 0.0684043$ μm, $\lambda_2 = 0.1162414$ μm, $\lambda_3 = 9.896161$ μm. Resonance frequency and wavelength are related by $\lambda_i = 2\pi c/\omega_i$, where c is the speed of light in vacuum.

A scattering boundary condition was applied for the numerical simulation. There are two non-degenerate FMs with almost orthogonal polarization. A typical FM for different wavelengths is displayed in Figure 6.2a-c. In this thesis, we called the part where the energy flows outside of the core region the evanescent field. When the excitation wavelength increases from 400 nm to 2000 nm, the evanescent field in all three air holes increases significantly because of the reduced confinement of the guided wave. As a result, the mode overlap with the monolayer TMD goes up for longer wavelengths. In this simulation, silica is considered a lossless medium; therefore, the attenuation of the traveling light is solely caused by the high-loss MoS₂, as shown in Figure 6.2d (orange line). There are two sharp peaks in the visible range of the attenuation spectrum due to the stronger absorption of the monolayer MoS₂ near the A and B exciton bands. For longer spectral wavelengths ($\lambda > 700$ nm), the attenuation is much less pronounced because the photon energies are lower than the bandgap of the monolayer. Besides, the modal dispersion can provide insights about the spectral broadening of the fundamental wave due to soliton in optical fibers. Here, the group velocity dispersion calculated by Equation 6.7 is virtually unchanged for both models, with and without the monolayer MoS₂. It indicates that the infinitesimal coating of a high-index semiconductor has an insignificant effect on the modal dispersion. This finding is in good agreement with the report by Feng *et al.* [259] about graphene/silicon hybrid waveguides when they reported that graphene has a negligible influence on the group velocity dispersion of their waveguide. It can be explained by the minuscule thickness of the monolayer and the minor fraction of the evanescent field in the waveguide system.

The mode propagation β of a central pulse at a frequency ω_0 can be expressed in a Taylor expansion in the frequency domain, containing the higher-order constants

$$\beta(\omega) = n(\omega)\frac{\omega}{c} = \beta_0 + \beta_1(\omega - \omega_0) + \frac{1}{2}\beta_2(\omega - \omega_0)^2 + \cdots \tag{6.5}$$

$$\beta_k = \left[\frac{\partial^k \beta}{\partial \omega^k}\right]_{\omega=\omega_0} \quad (k = 0, 1, 2 \dots) \tag{6.6}$$

From the above definition, the group velocity dispersion of fiber is calculated as follows

$$\beta_2 = \left[\frac{\partial^2 \beta}{\partial \omega^2}\right]_{\omega = \omega_0} = \frac{1}{c}\left(2\frac{\partial n_{\text{eff}}}{\partial \omega} + \omega \frac{\partial^2 n_{\text{eff}}}{\partial \omega^2}\right), \tag{6.7}$$

here n_{eff} is the effective mode index of the fundamental mode. The pulse broadening is determined by group velocity dispersion as a consequence of the frequency dependence of the refractive mode index. When $\beta_2(\omega) = 0$, we have zero dispersion at the frequency ω. Using Equation 6.7, the group velocity dispersion of our ECFs is plotted in Figure 6.2d (blue line). Our ECFs have zero-dispersion wavelengths at around 800 nm. This zero-dispersion wavelength in microstructured optical fibers is an active field of research with soliton-based supercontinuum generation (SCG) [260, 261]. Besides, the nonlinear processes in optical fibers or waveguides are heavily dependent on phase-matching, which is governed by chromatic dispersion. For example, the four-wave mixing process in the optical fiber is optimum at zero-dispersion wavelength [262]. Although SCG is not investigated in this thesis, it might be a fascinating topic in the future for TMD-coated ECFs.

To extract the fraction of power flowing through the MoS$_2$, a time-averaged Poynting vector has been calculated and integrated for the area of the monolayer and compared to the total energy flux within the boundary. The power fraction flowing in different domains of the model, including the monolayer TMD, has been calculated using finite element simulations, and the time-averaged Poynting vector is determined as

$$\langle \mathbf{S}(\mathbf{r}) \rangle = \frac{1}{2}\Re e[\mathbf{E}(\mathbf{r}) \times \mathbf{H}(\mathbf{r})^*]$$
$$= \frac{1}{2}\Re e \begin{bmatrix} E_y H_z^* - E_z H_y^* \\ E_z H_x^* - E_x H_z^* \\ E_x H_y^* - E_y H_x^* \end{bmatrix} \tag{6.8}$$

Here we consider the time-averaged Poynting vector with the z-component, which is along the propagation direction, then read as

$$\langle \mathbf{S}_z(\mathbf{r}) \rangle = \frac{1}{2}\Re e\left[E_x H_y^* - E_y H_x^*\right], \tag{6.9}$$

where $\Re e$ denotes the real part of the complex, $\mathbf{E}_{x,y}$ is the x and y components of the electric field, $\mathbf{H}_{x,y}^*$ is the complex conjugate of the x and y components of the magnetic field.

Table 6.1: Calculated Poynting vector z-component for two nondegenerate FMs of the ECFs at $\lambda_0 = 1570$ nm.

Cross-sectional part of the ECF	Bare ECF x-pol. FM	Bare ECF y-pol. FM	MoS$_2$ coated ECF x-pol. FM	MoS$_2$ coated ECF y-pol. FM
Three air regions	3.5 %	3.3 %	3.5 %	3.3 %
Air region above exposed surface only	1.6 %	0.9 %	1.7 %	0.9 %
Monolayer	n/a	n/a	0.008 %	0.007 %
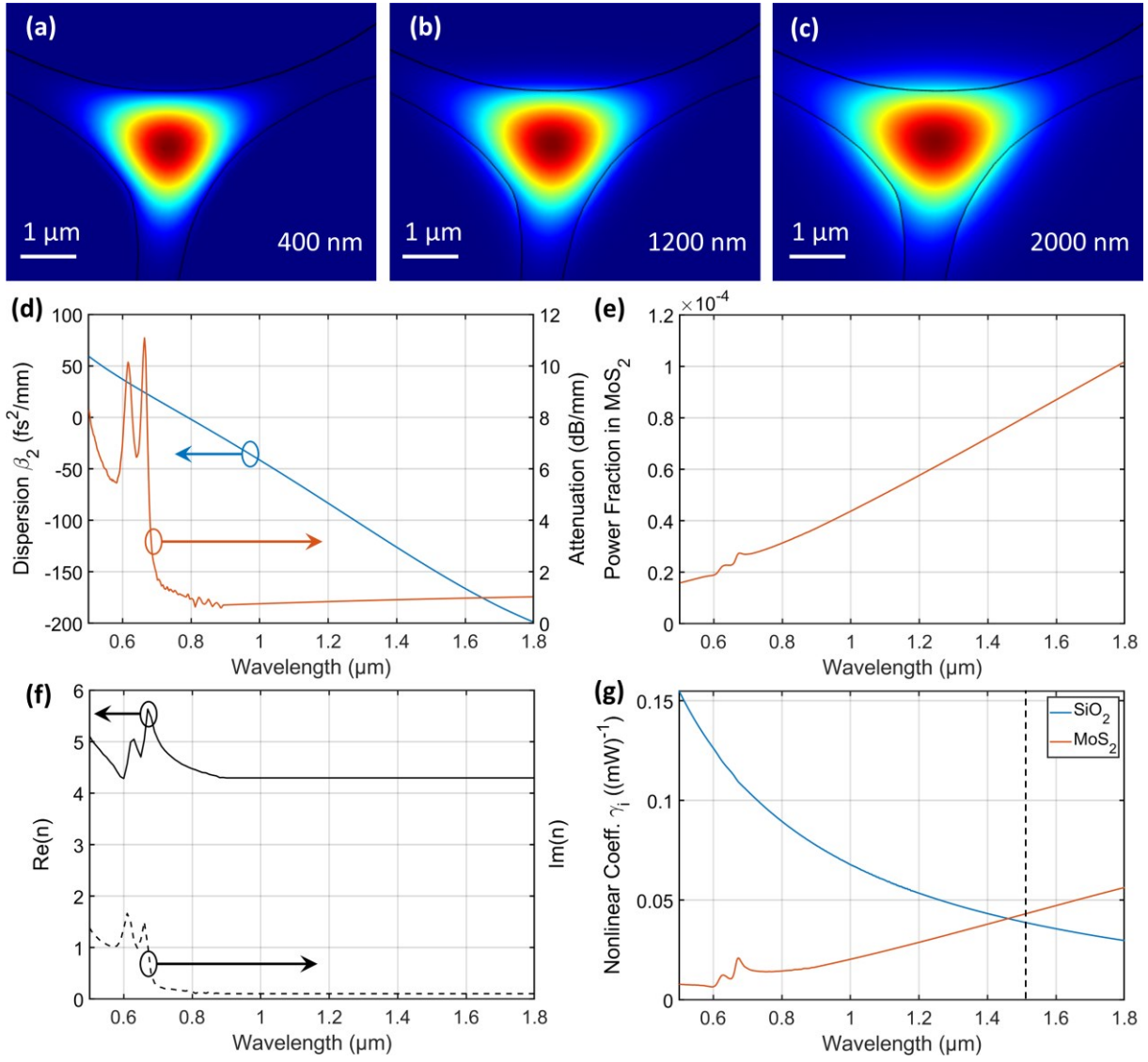
Figure 6.2: Properties of fundamental modes in MoS$_2$-coated ECF. **(a-c)** Normalized electric field at **(a)** 400 nm, **(b)** 1200 nm and **(c)** 2000 nm. **(d)** The group velocity dispersion (blue) and the attenuation (orange) of the ECF. **(e)** Fraction of energy flux (z-component of Poynting vector) in the monolayer MoS$_2$. **(f)** Real and imaginary component of refractive index of monolayer MoS$_2$ was used in this analysis. **(g)** Nonlinear coefficient calculated for both monolayer MoS$_2$ and SiO$_2$ core. Dashed line indicates the wavelength where we have the value of $n_2^{MoS_2}$. Figure is adapted from [146].

Figure 6.2e reveals the tiny fraction power in MoS$_2$ (roughly 0.01 % for $\lambda = 1800$ nm) owing to the strong confinement of the FMs inside the fiber core and the sub-nanometer thickness of monolayer MoS$_2$. The computed magnitude of the Poynting vector z-component for distinct regions within the boundary is shown in Table 6.1. The data are given for two non-degenerate FMs at $\lambda = 1570$ nm with the dominance of power flow belonging to the *x*-polarized FM. Figure 6.2f displays the complex refractive index of MoS$_2$ taken from the literature [206]. We can see the analogy between the attenuation of the MoS$_2$-coated fiber and the imaginary part of the refractive index of the

monolayer MoS2. It is because of the singular contribution of the monolayer MoS2 to the loss of the hybrid system.

A key parameter to evaluate the nonlinearity of the material system is the value of the nonlinear coefficient. The nonlinear effects depend on many inputs, such as the material nonlinearity, the mode overlap, or the evanescent field strength in monolayer TMD and phase matching. The nonlinear strength of waveguides is often benchmarked by the Kerr nonlinearity, which has a direct influence on SPM [139, 141, 263] or by the nonlinear susceptibility [138, 189]. In this work, the coefficient for SPM and THG has been calculated from an overlap integral using the vectorial nature of the guided mode. The SPM coefficient was computed from the method developed in the literature [263] with the vector fields and the integrated area taken from numerical data. Because both TMD and silica fiber have third-order nonlinearity, the overall SPM coefficient γ is the sum of two constituent materials (SiO2 and MoS2) of the system. The sum coefficient is calculated, for example, $\gamma = \gamma_{\text{SiO}_2} + \gamma_{\text{MoS}_2}$, and the contribution of two components is computed according to

$$\gamma_{\text{SiO}_2}(\lambda) = \frac{2\pi}{3\lambda}\frac{\varepsilon_0}{\mu_0} \Re\mathfrak{e}\left(n^{\text{SiO2}}(\lambda)\right) n^{\text{SiO2}}(\lambda)\, n_2^{\text{SiO2}} \frac{\iint_{A_{\text{SiO2}}}(2|\boldsymbol{E}|^4 + |\boldsymbol{E}^2|^2)dA}{\left|\iint_{A\infty}(\boldsymbol{E} \times \boldsymbol{H}^*) \cdot \hat{z}\, dA\right|^2}, \qquad (6.10)$$

$$\gamma_{\text{MoS}_2}(\lambda) = \frac{2\pi}{3\lambda}\frac{\varepsilon_0}{\mu_0} \Re\mathfrak{e}\left(n^{\text{MoS2}}(\lambda)\right) n^{\text{MoS2}}(\lambda)\, n_2^{\text{MoS2}} \frac{\iint_{A_{\text{MoS2}}}(2|\boldsymbol{E}|^4 + |\boldsymbol{E}^2|^2)dA}{\left|\iint_{A\infty}(\boldsymbol{E} \times \boldsymbol{H}^*) \cdot \hat{z}\, dA\right|^2}, \qquad (6.11)$$

where A is the cross-sectional area occupied by the material. $n(\lambda)$ and n_2 are the linear and nonlinear refractive indices of the constituent material, respectively. $\boldsymbol{E}(x, y; \lambda)$ and $\boldsymbol{H}(x, y; \lambda)$ are the electric and magnetic fields of a particular mode propagating inside the fiber at a given wavelength λ. ε_0 and μ_0 are the vacuum permittivity and permeability, respectively. $\hat{z}$ is the unit vector along the propagation direction.

The nonlinear coefficient γ was calculated for the x-polarized FM for both the monolayer MoS2 and the fiber core, as shown in Figure 6.2g. For the wavelengths above 1450 nm, the MoS2 overcomes the silica core in the contribution to the SPM coefficient. It was attributed to the consecutive increase of the energy propagating through the TMD layer, as displayed in Figure 6.2e. For THG experiments, the central wavelength of the pulsed laser is 1570 nm, therefore, an enhancement of the THG signal for the TMD-coated ECF is expected because at this wavelength $\gamma_{\text{MoS}_2} > \gamma_{\text{SiO}_2}$. Remarkably, all linear properties, except losses, are found to be unaffected by the TMD-coating, which is understandable because only 0.8×10^{-4} of the energy flow of the FM is traveling through the TMD (see Figure 6.2e). Although this energy portion is trivial, we found that the TMD-coating has a substantial impact on the ECF's nonlinear properties due to their strong nonlinearity. At $\lambda_0 = 1570$ nm, the SPM coefficient $\gamma_{\text{MoS}_2}(\lambda_0) = 0.046\,(\text{Wm})^{-1}$ is slightly

higher than that of silica, $\gamma_{\mathrm{SiO_2}}(\lambda_0) = 0.037\ (\mathrm{Wm})^{-1}$. This distribution is ascribed to the weak nonlinearity of silica: $n_2^{\mathrm{SiO_2}} = 3 \times 10^{-20}\ \mathrm{m^2/W}$ [191], which is almost four orders of magnitude smaller than that of MoS2; $n_2^{\mathrm{MoS_2}} = 2.7 \times 10^{-16}\ \mathrm{m^2/W}$ measured at 1550 nm [141]. We chose this value as a source of our calculation due to the similarity in the growth method, the same range of excitation wavelength, and the deposition of the monolayer MoS2 on a waveguide system. Figure 6.2g was plotted with fixed values of $n_2^{\mathrm{MoS_2}}$ and $n_2^{\mathrm{SiO_2}}$ to simplify the calculation, but due to the large difference in the value of the nonlinear refractive index between them, our calculation still provides a good evaluation of the contribution of monolayer TMD to the hybrid waveguide.

THG efficiency in a waveguide is greatly dependent on the simultaneous interplay of mode matching and phase matching, thus, efficient THG may only be observed within the phase-matching region, where the effective refractive index of the FW mode n^{FW} and refractive index of the TH mode n_k^{TH} satisfy the condition $\Delta n = |n^{\mathrm{FW}} - n_k^{\mathrm{TH}}| < \lambda_0/(\pi L_c)$. Here k is the index of the high-order mode (HOM), and L_c is the typical length of an MoS2 monolayer, which is 29.5 μm. Consequently, the maximum refractive index mismatch $\Delta n = 0.017$. For ECFs in this work, only HOMs at third-harmonic frequency are phase-matched, and no FMs can be excited in the THG process due to the chromatic dispersion of ECFs. This can be confirmed by the TH modes coming from the output of the fiber captured by an sCMOS camera.

As discussed above, both silica fiber and TMD coating can generate THG, the overlap coefficient of the THG is a sum of the material contributions $\gamma_k^{(\mathrm{THG})} = \gamma_{\mathrm{SiO_2},k}^{(\mathrm{THG})} + \gamma_{\mathrm{MoS_2},k}^{(\mathrm{THG})}$, which has a distinct value depending on the involvement of the specific HOMs at the TH wavelength, and k denotes the arbitrary mode index.

Here, the overlap coefficient is defined as follows

$$\gamma_{m,k}^{(\mathrm{THG})}(\lambda) = \sum_{ijnl} \frac{n_{2,ijnl}^m \iint_{A_m} \boldsymbol{E}_{i,k}\left(\frac{\lambda}{3}\right) \boldsymbol{E}_j^*(\lambda)\boldsymbol{E}_n^*(\lambda)\boldsymbol{E}_l^*(\lambda)dA}{\sqrt{\iint_{A\infty} \boldsymbol{E}_{i,k}\boldsymbol{E}_{i,k}^* dA \iint_{A\infty} \boldsymbol{E}_j\boldsymbol{E}_j^* dA \iint_{A\infty} \boldsymbol{E}_n\boldsymbol{E}_n^* dA \iint_{A\infty} \boldsymbol{E}_l\boldsymbol{E}_l^* dA}}, \qquad (6.12)$$

where m denotes the constituent materials such as SiO2 and MoS2, the subscripts $ijnl$ denote the polarization direction of the electric field. $\boldsymbol{E}_{i,k}$ is the electric field of the third harmonic high-order mode with mode index k. $\boldsymbol{E}_j$, $\boldsymbol{E}_n$, and $\boldsymbol{E}_l$ denote the fundamental mode at the fundamental wavelength (FW). Because the fields are mostly polarized in x and y-direction, and there is no significant value for the out-of-plane nonlinear tensor of the TMD (see Equations 6.2-6.3), the equation simplifies to

$$\gamma_{\mathrm{SiO2},k}^{(\mathrm{THG})}(\lambda) = \frac{n_{2,xxxx}^{\mathrm{SiO2}} \iint_{A_{\mathrm{SiO2}}} E_{x,k}\left(\frac{\lambda}{3}\right) E_x^*(\lambda) E_x^*(\lambda) E_x^*(\lambda) dA}{\sqrt{\iint_{A\infty} E_{x,k}\left(\frac{\lambda}{3}\right) E_{x,k}^*\left(\frac{\lambda}{3}\right) dA \left(\iint_{A\infty} E_x(\lambda) E_x^*(\lambda) dA\right)^3}} \tag{6.13}$$

$$\gamma_{\mathrm{MoS2},k}^{(\mathrm{THG})}(\lambda) = \frac{n_{2,xxxx}^{\mathrm{MoS2}} \iint_{A_{\mathrm{MoS2}}} E_{x,k}\left(\frac{\lambda}{3}\right) E_x^*(\lambda) E_x^*(\lambda) E_x^*(\lambda) dA}{\sqrt{\iint_{A\infty} E_{x,k}\left(\frac{\lambda}{3}\right) E_{x,k}^*\left(\frac{\lambda}{3}\right) dA \left(\iint_{A\infty} E_x(\lambda) E_x^*(\lambda) dA\right)^3}} \tag{6.14}$$
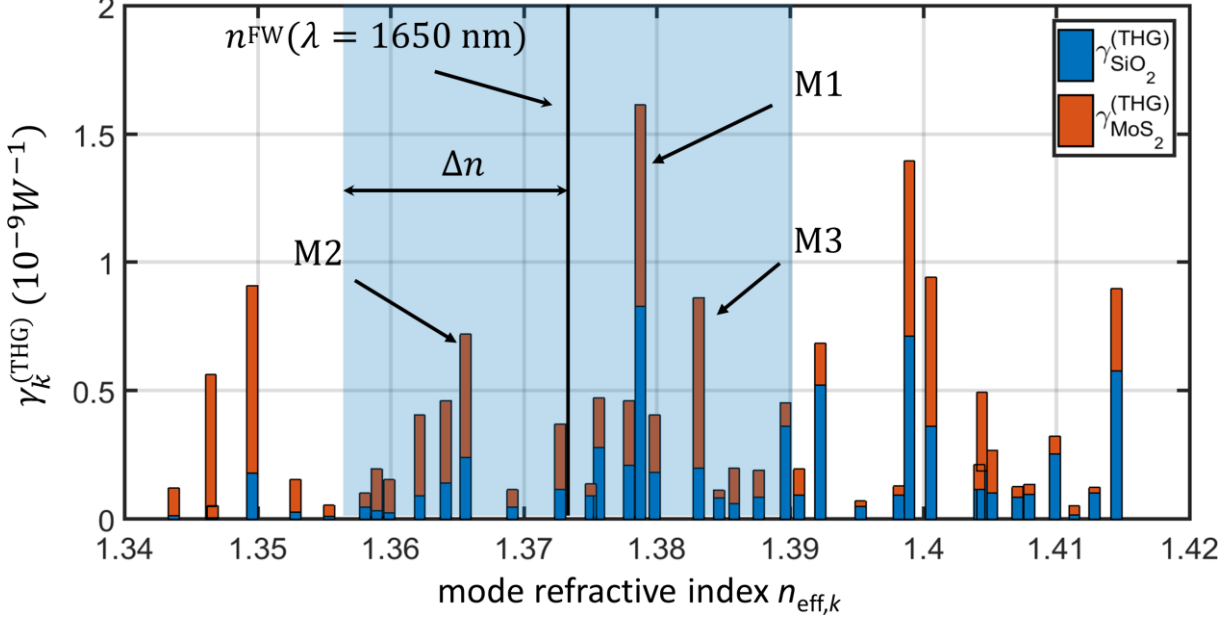

Figure 6.3: Modal THG overlap coefficients $\gamma_k^{(\mathrm{THG})}$ at the third-harmonic wavelength of 550 nm, calculated for all HOMs k, which are close to the phase matching point at $n_{\mathrm{eff}}^{\mathrm{FW}} = 1.373$. The phase-matching region with $\Delta n < 0.017$ is marked in blue shading. The stacked colored bars indicate the contributions of the SiO2 core (blue) and the monolayer MoS2 (orange) to $\gamma_k^{(\mathrm{THG})}$, respectively. Figure is adapted from [146].

Figure 6.3 displays their respective values $\gamma_k^{(\mathrm{THG})}$ for 30 distinct TH-HOMs, which are close to the phase matching (PM) point. The reason to calculate the $\gamma_k^{(\mathrm{THG})}$ at 550 nm is to match the experimental results that will be discussed in the next section. The contribution of SiO2 (blue) and MoS2 (orange) to the overlap coefficients is displayed in the bar shape. Since THG depends crucially on the phase-matching condition, therefore we are considering only the HOMs in the PM region indicated by the blue shading. There are 18 HOMs in this region, and we shall only discuss the three modes with the largest $\gamma_k^{(\mathrm{THG})}$. The most dominant contribution for both the bare and the MoS2-coated ECF is from the M1 mode at $n_{\mathrm{eff,M1}} = 1.379$. Its overlap value $\gamma_{\mathrm{M1}}^{(\mathrm{THG})}$ is approximately doubled due to the MoS2-coating. The simulated mode profile of the M1 mode is depicted in Figure 6.4b. The second strongest contribution for the bare ECF is the M2 mode at $n_{\mathrm{eff,M2}} = 1.366$, here $\gamma_{\mathrm{M2}}^{(\mathrm{THG})}$ increases approximately 2.5 times by the TMD-coating, and its profile is shown in Figure 6.4a. Although the M2 mode has an important contribution after the coating; however, it is succeeded by the M3 mode at $n_{\mathrm{eff,\ M3}} = 1.383$, which triples its $\gamma_{\mathrm{M3}}^{(\mathrm{THG})}$ upon the

influence of the monolayer. Simulated modes profiles of M3 can be seen in Figure 6.4c. Each mode has at least one field maximum close to the top surface of the ECF, where the 2D TMDs are deposited. It is thus obvious that the overlap coefficients grow greatly upon the contribution of the TMD coating for all three modes.
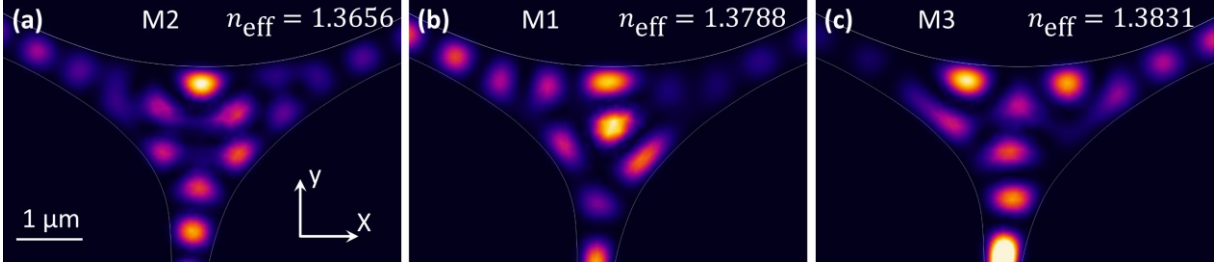

Figure 6.4: $|E_x|^2$ of the three fundamental modes M1, M2, and M3 which have been selected due to their strongest contribution for the THG-process of the ECFs. **(a)** M1 at $n_{\text{eff}} = 1.3788$, which is the dominant mode for the bare and MoS$_2$-coated ECF. **(b)** M2 at $n_{\text{eff}} = 1.3656$, which has the second largest overlap coefficient for the bare ECF. **(c)** M3 at $n_{\text{eff}} = 1.3831$, which has the second largest overlap coefficient for the MoS$_2$-coated ECF. Figure is adapted from [146].

The nonlinear polarization field at TH wavelength should provide some useful information at the interface of SiO$_2$ and MoS$_2$ because of the large difference in the nonlinearity. Here, the nonlinear polarization field $\boldsymbol{P}^{(3)}\left(\frac{\lambda_0}{3}\right)$ is numerically computed for the silica core and monolayer MoS$_2$ and displayed in Figure 6.5 on a logarithmic scale using the following formula

$$\boldsymbol{P}^{(3)}\left(\frac{\lambda_0}{3}\right) = E_x^3(x, y; \lambda_0) \cdot \chi_{xxxx}^{(3)}(x, y)\boldsymbol{e}_x, \tag{6.15}$$

where $E_x(x, y)$ is the x-component of the electric field of the FW mode, and $\chi_{xxxx}^{(3)}$ is the component of the nonlinear tensor which contributes the most to the THG process [146].
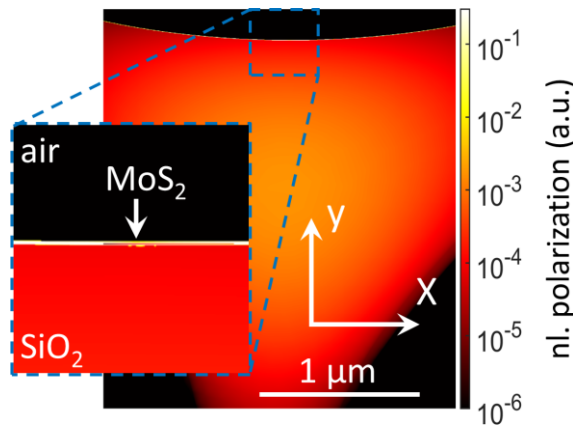
Figure 6.5: Logarithmic plot of the nonlinear polarization field in the core region. The field is generated by the cubed electric field and the nonlinear response of SiO$_2$ and MoS$_2$. The inset is a zoom of the exposed surface, displaying the strong and highly localized nonlinear polarization from the monolayer MoS$_2$. Figure is adapted from [146].

The contribution from the SiO$_2$ core is a spatially smooth polarization over a large area, whereas the monolayer TMD has a greater nonlinear polarization field but is also position-dependent, which can be seen from the inset. The TH-radiation is then distributed to the TH modes and proportional

to the overlap coefficient $\gamma_k^{(THG)}$ for every mode with index k. It is straightforward that the impact of the MoS$_2$ coating on these coefficients depends intensely on the shape and polarization of each TH-HOM. For example, HOMs localized close to the functionalized surface and with predominant x-polarization benefit more from the coating. It is the result of the substantial in-plane nonlinear tensor of the monolayer MoS$_2$.

6.3 THG experiment in TMD-coated ECFs

THG experiments were carried out with a pulsed laser (Toptica FemtoFiber pro IRS-II) operating at a central wavelength $\lambda_0 = 1570$ nm, a repetition rate of 80 MHz, and an FWHM pulse duration of 34 fs (see Figure 6.6) for pulse reconstruction). The experimental setup is similar to the PL spectroscopy in Figure 3.6, except we used an aspheric lens (Thorlabs C230TMD-C) for input coupling and an optical spectrum analyzer (ANDO 6315A) to collect the TH signal. For the bare ECFs, we attain a coupling efficiency of 29 % without noticeable propagation loss (less than 1 dB/m) [144]. The coupling efficiency was assumed the same for the MoS$_2$-coated ECF with an equal length. Nevertheless, the transmitted power is roughly 60 % lower at identical settings with the presence of MoS$_2$ monolayers, leading to an overall net loss of 0.1 dB/mm. The MoS$_2$-coated ECF has a filling factor of 5.4 %, as determined by Figure 4.5b. This result means that the MoS$_2$ monolayers on the ECF are responsible for a loss of approximately 1.8 dB/mm. This value is consistent with simulations (see Figure 6.2d), which predict a value of 1.2 dB/mm, and an independent cut-back measurement with an MoS$_2$-coated ECF gave a loss of 1.3 dB/mm, validating the range of this parameter.
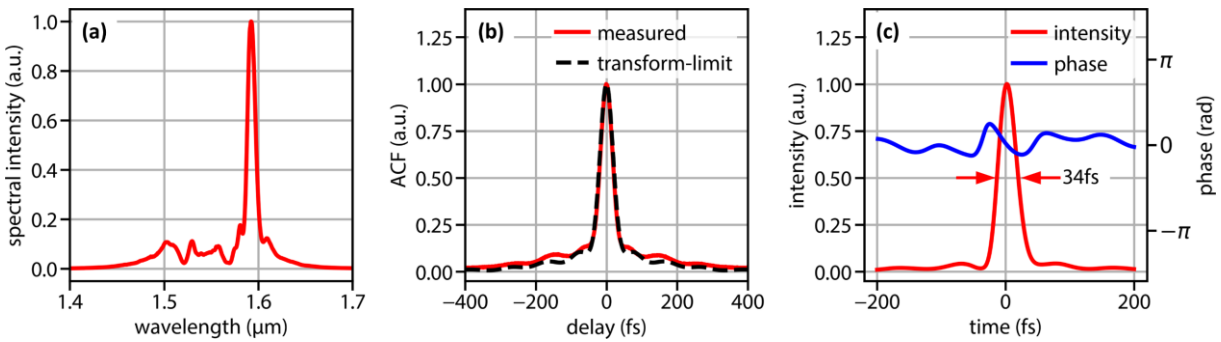
Figure 6.6: Laser pulse characteristics. **(a)** Normalized laser spectrum at the input of the fiber. **(b)** Measured intensity autocorrelation (red) compared with the autocorrelation of the transform-limited pulse (dashed line). **(c)** Transform-limited pulse as calculated from the spectrum propagated numerically through the fiber-coupling optics. Figure is adapted from [146].

The IR pulsed laser was characterized, and the pulse duration was determined by measuring the spectrum and the non-collinear intensity autocorrelation of the pulse incoming to the fiber, as shown in Figure 6.6a-b. The measured autocorrelation in Figure 6.6b was compared to the value of the transform-limited pulse and calculated from the measured spectrum. Both the measured pulse

and the transform-limited counterpart are found equivalently in shape, including the central peak region and the wings. The FWHM pulse duration is close to the transform limit of 30 fs. The final value for the pulse duration is 34 fs (Figure 6.6c) at the fiber facet, and it was obtained by further numerical propagation through the aspheric lens.

We now discuss THG in MoS_2-coated ECFs, where only HOMs at third-harmonic wave are phase matched with FMs at fundamental wave because of the chromatic dispersion [146, 264, 265]. Figure 6.7a shows the spectra of the third harmonic wave for three different input powers measured with a pair of bare and MoS_2-coated ECFs with an equal length. The transmitted powers are identical for both ECFs. An increase of THG in MoS_2-coated ECF was observed for all input energies. This behavior is expected because the atomic monolayer has substantial nonlinearity. Here, the spectral shape of the third harmonic wave is identical for both the bare and coated ECF, indicating that the PM between FW and TH is unaffected by the coating. It is consistent with the previous discussion that only the attenuation of the fiber is affected by subnanometer-thin crystals.
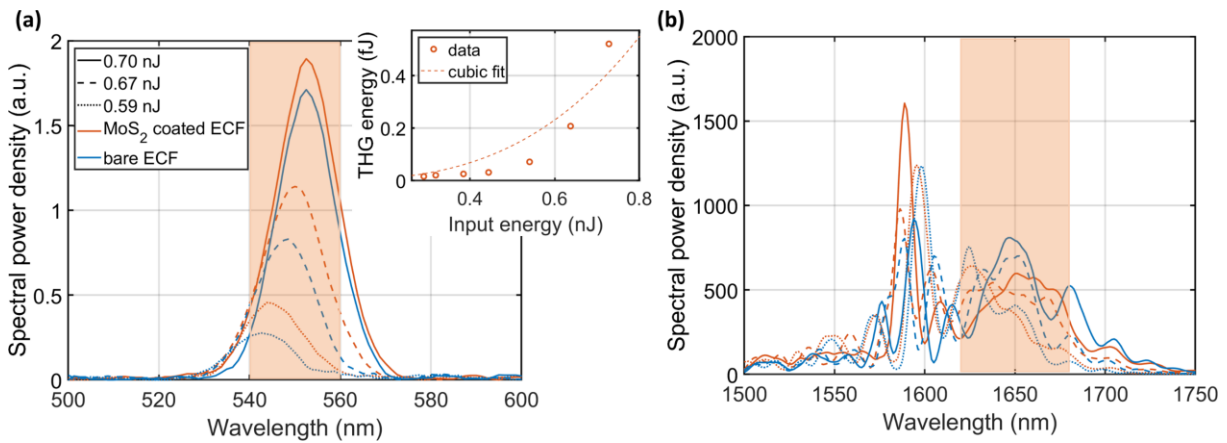
Figure 6.7: Third harmonic and infrared spectra for MoS_2 coated and bare ECFs at different input energies. **(a)** Third harmonic spectra of both fibers. The THG band from 540 to 560 nm is marked in orange shading. Inset: THG energy vs input energy from the MoS_2-coated ECF with a cubic fit. **(b)** Fundamental wave spectra were recorded simultaneously with third harmonic spectra. The orange shading specifies the fundamental wave band, which is responsible for the THG shading in **(a)**. Same legend as in **(a)**. Figure is adapted from [146].

Due to the higher loss by coating, about 40 % of the input energy left the output of the MoS_2-coated ECF, whereas, for the bare ECF, the complete pulse energy contributes to THG over the entire fiber length. The TH is generated in a spectral band ranging mostly from 540 nm to 560 nm, marked as an orange band in Figure 6.7a. The FW spectrum must be a band between 1620 nm and 1680 nm, which is not well-matched with the central wavelength of the pulsed laser at 1570 nm. It means that the FW must experience a spectral broadening before significant TH can be generated, which may explain the fairly stronger-than-cubic scaling in the inset of Figure 6.7a. From our calculation plotted in Figure 6.2g, the SPM coefficient is significant and under the propagation of ultrashort pulses, the spectral broadening in ECFs is expected. Simultaneously recorded spectra of FW are

displayed in Figure 6.7b. The corresponding FW band from 1620 nm to 1680 nm is marked in orange. A corrected efficiency will be calculated based on this band for three input energies.

From Figure 6.7, there is no noticeable modification of PM upon the deposition of the monolayer MoS2. All linear mode properties are unchanged, except for the higher loss due to the high extinction coefficient from MoS2. As there is no modification of the PM conditions by the coating, THG enhancement is attributed to the TMD-induced change of the nonlinear polarization field, as plotted in Figure 6.5.

Because of a higher loss, the MoS2 coated ECF has less pulse energy to drive the THG process than the bare fiber. Clearly, we have observed an increase of THG for different input energies, for instance, a 47 % growth in THG for an input energy of 0.59 nJ, 41 % for 0.67 nJ and 18 % for 0.70 nJ. The enhancement is calculated by the ratio $\epsilon_{THG} = E_{MoS_2}^{THG}/E_{Bare}^{THG}$ and presented in the first row of Figure 6.8.

Here, the amount of energy from FW to generate TH was compared between MoS2 coated and bare ECFs. The corresponding ratio ϵ_{FW} is calculated as $\epsilon_{FW} = \int_{1620 \text{ nm}}^{1680 \text{ nm}} E_{Bare}(\lambda)d\lambda / \int_{1620 \text{ nm}}^{1680 \text{ nm}} E_{MoS_2}(\lambda)d\lambda$. This ratio is presented in the center row of Figure 6.8, and we attain $\epsilon_{FW} = 0.96$ for $E = 0.59$ nJ, $\epsilon_{FW} = 1.03$ for $E = 0.67$ nJ and $\epsilon_{FW} = 1.12$ for $E = 0.70$ nJ. This means that there is more energy of FW involved in the THG process for bare ECF than the coated one.
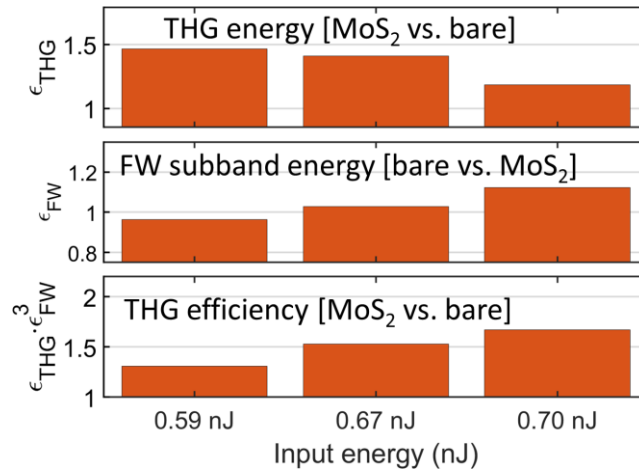
Figure 6.8: Third harmonic generation from constituent materials. A bar chart to show the ratio of THG energy (upper), the ratio of FW energy in the range from 1620 nm to 1680 nm (center), and the relative THG efficiency (lower) of the MoS2 coated ECF and the bare ECF as a function of the input energy. Figure is adapted from [146].

To obtain the relative efficiency of THG process, we use the fact that the THG efficiency has the cubic relationship with the FW energy and a linear connection with the TH energy. Here, we can calculate the relative efficiency of the THG process of the MoS2-coated ECF and the bare ECF as $\epsilon_{THG} \cdot \epsilon_{FW}^3$. The results are shown in the bottom row of Figure 6.8 with a corrected enhancement

factor of 30 % for $E = 0.59$ nJ, 53 % for $E = 0.67$ nJ, and 67 % for $E = 0.70$ nJ, respectively. This corrected enhancement factor is significantly greater than the uncorrected value and highlights that the THG process is indeed enhanced by the monolayer MoS_2.
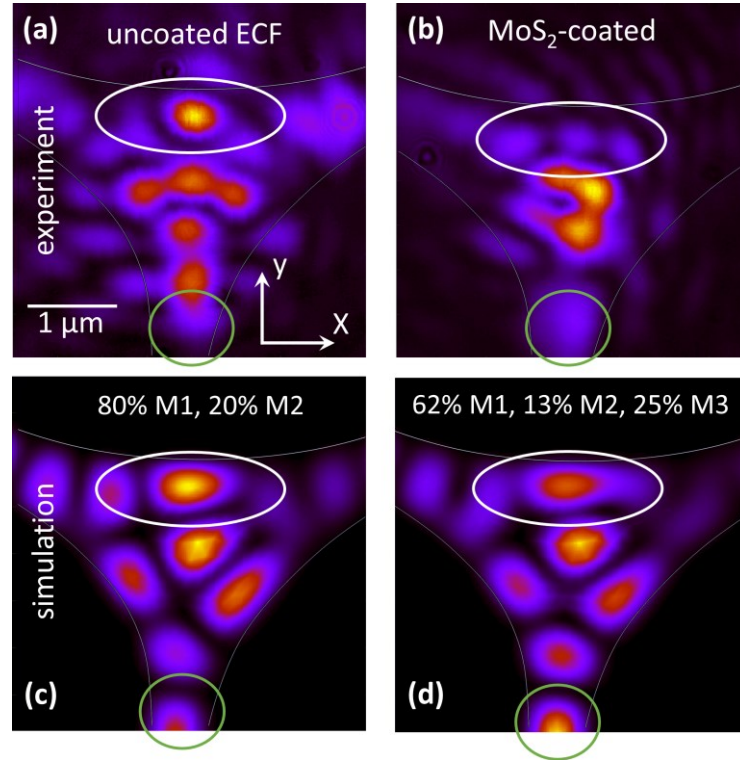
Figure 6.9: HOMs at THG band. **(a)** Experimentally measured image of the mode pattern from the THG at the end of a bare ECF. **(b)** Experimentally measured image of the mode pattern from the THG at the end of an MoS_2-coated ECF. **(c)** Simulated mode pattern as a superposition of the modes M1 and M2 with an 80/20 power distribution, according to the overlap coefficients for the bare ECF. **(d)** Simulated mode pattern as a superposition of the modes M1, M2, and M3 with a ratio 62/13/25 in power distribution according to the overlap coefficients for the MoS_2-coated ECF. Figure is adapted from [146].

From Figure 6.3 and Figure 6.4, the overlap coefficient is higher for some specific HOMs, which means that the THG process depends on the spatial shape and the polarization of the TH mode. In the phase matching band, there are three modes M1, M2, and M3 which have a substantial overlap coefficient and can contribute the most to the experimentally recorded HOMs at TH frequency. Figure 6.9a-b exhibits the spatial distribution of the TH modes recorded by a camera for a bare and an MoS_2-coated ECF, respectively. There are some striking features marked by the white and blue ovals. For instance, the single peak at the top of the bare ECF is replaced by weaker triple peaks near the center of the MoS_2-coated ECF. By using the superposition of M1, M2, and M3 modes with an adjusted contribution from computation, the modal spatial distribution is quite well-reproduced for both bare and MoS_2-coated ECFs. The simulated TH modes are shown in Figure 6.9c-d. This finding reveals that there is more room for the improvement of the THG process by controlling the overlap coefficient for specific HOMs at a certain wavelength, for example, by changing the fiber geometry or by thin film coatings.

6.4 Summary of the results

In this chapter, we have shown that 2D materials can be used to modify and tailor the nonlinear wave dynamics in fibers significantly while leaving the linear waveguiding properties mostly unaffected. Specifically, we have demonstrated enhanced third-harmonic generation phase-matched to high-order modes in MoS_2-coated exposed core optical fibers, an intermodal phase matching. This phase matching with HOMs was confirmed by the recorded HOMs at the third harmonic from the fiber output. From the simulation, we found that the 2D materials induce a local nonlinear polarization field, which alters the nonlinear overlap coefficient between fiber modes. It demonstrates the high nonlinearity of such thin semiconductors compared to bulk silica fiber. This approach may be applied in future fiber-based devices to tailor nonlinear interaction processes between modes and promote design freedom for highly nonlinear fibers. Another approach to increase THG further is bringing the resonance between the TH band and exciton energy, which has been investigated intensively for SHG.

Altogether, the direct growth of 2D materials on waveguides is opening a novel path toward the scalable and reproducible functionalization of waveguides, fibers, and other integrated optical systems with 2D materials. It may elevate transition metal-dichalcogenides from a highly-fascinating subject for materials science and photonics to a novel and powerful tool for future applications in integrated photonics and sensing. In the case of THG, an inkjet printing [266] of 2D materials on ECFs can be considered because there is no requirement for crystal symmetry in this nonlinear process, and ECFs support a gateway to printing solution on the fiber core.

7. Second-harmonic generation in hybrid waveguides

7.1 Fundamentals of SHG in 2D materials

SHG is an important nonlinear process that plays a key role in frequency conversion systems and active photonic nanodevices. Additionally, the SHG response is strongly dependent on the inversion symmetry of the nonlinear medium. In general, SHG will vanish in inversion symmetric or amorphous materials, such as glasses and optical fibers, except for an insignificant surface SHG coming from the broken symmetry at the interface of the medium. After demonstrating the strong nonlinearity of TMD crystals with the THG process, in this chapter, SH nonlinear response will be investigated on similar waveguides. Monolayer TMDs or odd-numbered layers in the 2H phase are noncentrosymmetric, therefore SHG is not forbidden. In contrast, it is forbidden in even-numbered layers. Interestingly, the inversion symmetry from even-layer 2D materials can be broken by an external excitation [267-269], chemical doping [270, 271], structural inhomogeneity [252, 272-274], and strain [275]. Exceptionally, 3R-phase TMD crystals are not centrosymmetric with even-numbered layers [276, 277] and are promising for $\chi^{(2)}$-based waveguides. However, the scalability of the 3R phase is still a challenge and uncontrollable by the CVD technique. Besides, a strong $\chi^{(2)}$ process, for instance, SHG from monolayer TMDs on a planar substrate has been reported [97, 101].

Following the general nonlinear optical response of a material in Equation 2.4, the SHG process can be expressed by

$$P_i^{(2)}(2\omega) = \varepsilon_0 \sum_{jk} \chi_{ijk}^{(2)}(\omega)\, E_j(\omega) E_k(\omega), \tag{7.1}$$

here i, j, k refer to the Cartesian components of the incident fields.

From a first-principle analysis, monolayer TMDs are predicted to have a significant $\chi^{(2)}$ magnitude that is comparable to those of highly nonlinear bulk crystals [102]. In contrast to the monolayer TMD, the $\chi^{(2)}$ value of bulk MoS_2 is trivial, less than 0.1 pm/V [278]. Consequently, the SHG intensity from the monolayer MoS_2 is three orders of magnitude stronger than from the surface of bulk MoS_2, which is centrosymmetric [105]. Furthermore, SHG efficiency will be enhanced when there is a resonance between SH frequency and A, B [118, 271, 279], or C-excitons [97] of 2D TMDs. This resonance is also investigated by a theoretical model and attributed to the impact of bound electron-hole pairs [280]. In other words, the $\chi^{(2)}$ magnitude is a function of the wavelength and has a higher value near the excitonic frequencies.
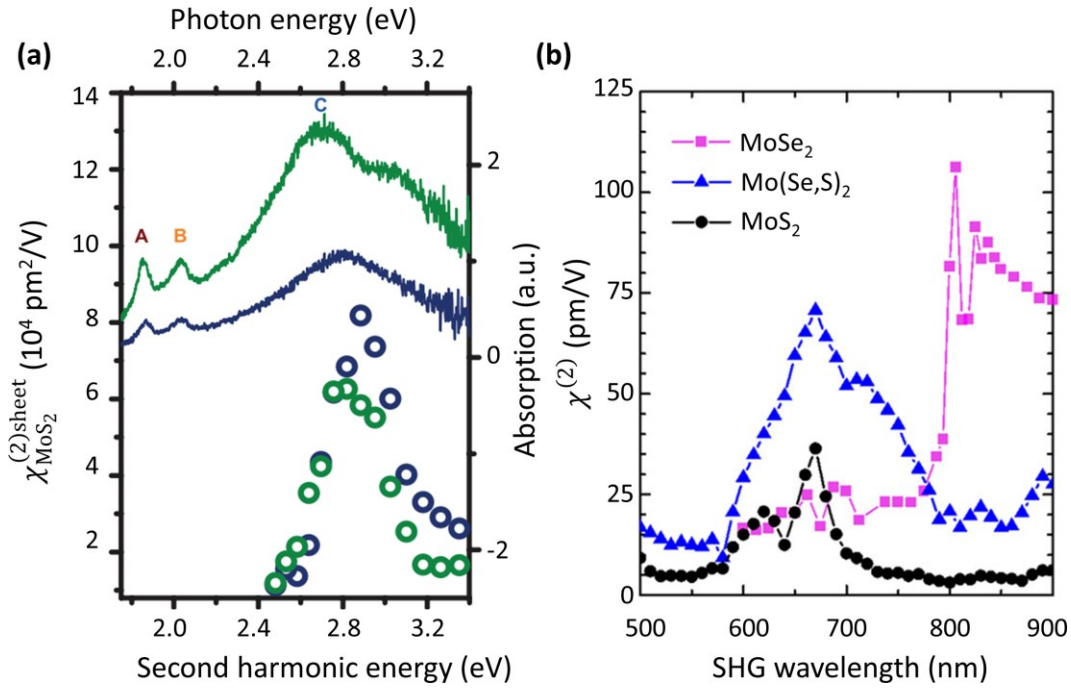
Figure 7.1: (a) Second-order susceptibility of monolayer MoS₂ (blue circles) vs trilayer MoS₂ (green circles) measured over a range of second harmonic energy and overlap with C-exciton energy. Solid lines are the linear absorption spectra (right scale) of the monolayer (blue line) and the trilayer (green line). The subfigure is adapted from [97]. **(b)** SHG spectra of monolayer alloy with the doping of Se atoms measured over A and B excitons. The subfigure is adapted from [271].

In Figure 7.1a, Malard *et al.* characterized a monolayer MoS₂ with the absorption and SHG spectra [97]. This work showed the absorption of monolayer MoS₂ over A, B, and C-excitons, observed by three distinct peaks in the range from 1.9 - 2.8 eV. The $\chi^{(2)}$ value was measured in the range from 2.4 - 3.2 eV and exhibited a peak at 2.8 eV corresponding to the C-exciton. In a similar work, Le *et al.* have reported the higher $\chi^{(2)}$ value of monolayer MoS₂ in resonance to A and B excitons as depicted in Figure 7.1b (black dotted line) [271]. Both these works were performed on MoS₂ monolayers deposited on a planar substrate. The enhancement of SHG over excitonic band energies might be a reliable tool to examine the quality of 2D materials and provides a basis for the active design of narrowband resonators.

Noticeably, the dependence of SHG of 2D TMDs on the layer thickness [97, 99, 105, 115] and the crystal orientation [281, 282] has been studied intensively. Exploiting the high sensitivity to the crystal structures, such as the layer number, the crystal orientation, and the phase transition, SHG could be an effective and non-destructive characterization tool [283]. For instance, Li *et al.* showed that they can distinguish the odd- or even-numbered layers of hBN by monitoring SHG signals [105]. Besides, Zeng *et al.* revealed the quadratic increase of SHG intensity to the thickness of 3R-phase WS₂ [284]. Thus, the layer numbers (thickness) of 2D materials could be probed through the SHG intensity. Furthermore, the two polarization components of SHG in a monolayer TMD depend on the crystal orientation, and hence, SHG can be used to probe the crystallographic orientations

as well. Moreover, SHG is demonstrated as a versatile tool to monitor the strain from TMD crystals [281, 282, 285], which makes TMD-coated ECF a new non-destructive platform for stress or strain sensing.

Some works have been carried out to prove the significant nonlinearity of hybrid systems between 2D materials and optical fibers using thermal poling of the step-index fiber [142] or using hollow-core fibers and photonic crystal fibers [143]. In the former approach, the two enclosed air holes near the fiber core were deposited with multilayer MoS_2 from a solution-based deposition method. In this work, multilayer MoS_2 interacted with the guided modes to enhance the nonlinear coefficient up to 10 %. The closest distance from the edges of two air holes to the fiber center is in the range from 7.2 µm to 13.6 µm. The fiber has a core diameter of 4 µm. This large distance between the location of the multilayer MoS_2 and the fiber core has limited the strength of the evanescent field overlapping with the MoS_2 multilayers. Moreover, the enclosed air holes would make the scalable integration of the MoS_2 to the optical fiber more difficult, then hamper its application for integrated photonics. The latter method is a two-step growth of TMD crystals from an aqueous precursor and a CVD process. The loading of Mo sources into the fiber's air holes by capillarity is an obstacle to scalability, and it is time-consuming. Also, the lack of access to the localized TMD crystals inside the air holes will further restrict the optoelectronic applications of the hybrid system, such as remote sensing or single photon sources. Some other works reported the integration of monolayer TMDs with waveguides relied on the mechanical transfer of TMDs on waveguides [137, 138, 286]. These approaches are not suitable for mass production. In previous chapters, ECFs have proved their potential in PL and THG processes, then they are expected to establish a novel second-order nonlinear platform with the growth of monolayer TMDs.

Monolayer TMDs belongs to the point group D_{3h}, therefore it has only one independent, nonvanishing susceptibility tensor element [97, 99, 280]

$$\chi_{1L}^{(2)} = \chi_{1L,xxx}^{(2)} = -\chi_{1L,xyy}^{(2)} = -\chi_{1L,yxy}^{(2)} = -\chi_{1L,yyx}^{(2)}, \tag{7.2}$$

where x is the armchair direction of the monolayer and y is the orthogonal zigzag direction. Equation 7.2 shows that only in-plane nonlinear tensors exist for this material group. Figure 7.2a illustrates the three atomic planes of the monolayer MoS_2 with the Cartesian coordinate. The XY plane is the in-plane of the monolayer, whereas the out-of-plane contains the Z component. Thus, the excitation field should have polarization in the monolayer plane to achieve maximal efficiency.
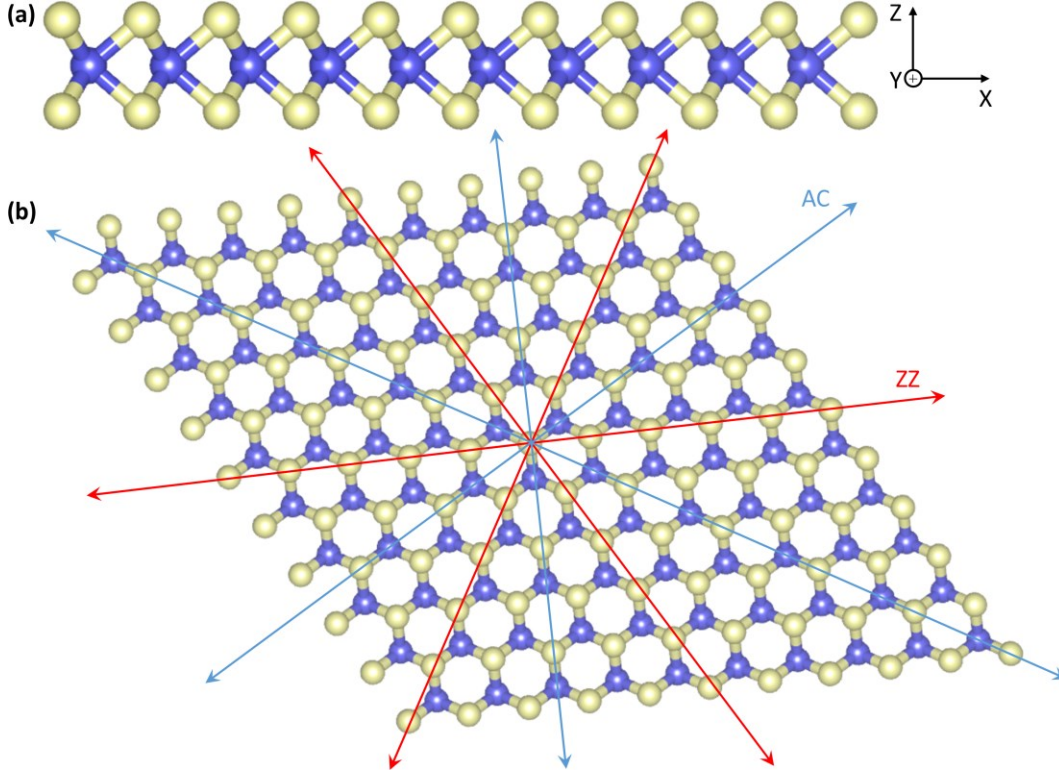
Figure 7.2: (a) Side view of monolayer MoS$_2$ where Mo is displayed in blue and S is displayed in yellow. **(b)** Basal plane view of monolayer MoS$_2$ with zigzag (ZZ) and armchair (AC) directions. The three-fold rotation symmetry is clearly presented for zigzag and armchair directions.

From Equation 7.1, the SHG process can be confirmed by the quadratic dependence of the SHG intensity ($I_{2\omega}$) on the pump intensity (I_ω), expressed by $I_{2\omega} = A \times I_\omega^2$, with A is a coefficient or prefactor. A logarithmic fitting with a slope of 2.0 at the SH wavelength is the fingerprint to confirm the observation of SHG from our hybrid waveguides. Furthermore, SHG exhibits polarization dependence on the relative angle between the armchair direction and input polarization of FWs. The armchair and zigzag direction of monolayer TMD is the specific crystallographic direction formed by the arrangement of atoms within the lattice structure and is recognized from the basal plane view in Figure 7.2b. The three-fold rotation symmetry happens for both zigzag and armchair directions.

The polarization resolved SHG intensity can be expressed by [97, 287]

$$I_{SHG}^{\parallel} = I_0 \cos^2(3\theta + \varphi),$$
$$I_{SHG}^{\perp} = I_0 \sin^2(3\theta + \varphi), \tag{7.3}$$

where I_0 is the maximum SHG intensity, θ is the angle between the incident laser polarization and x-direction of the experimental coordinate system, and φ is the angle between the armchair direction of the crystal and x-direction. This coordinate is shown in Figure 7.3a. $I_{SHG}^{\parallel}$ is the SH intensity collected when the input and output polarizations are parallel, whereas $I_{SHG}^{\perp}$ is the SH intensity collected when the input and output polarizations are perpendicular to each other.
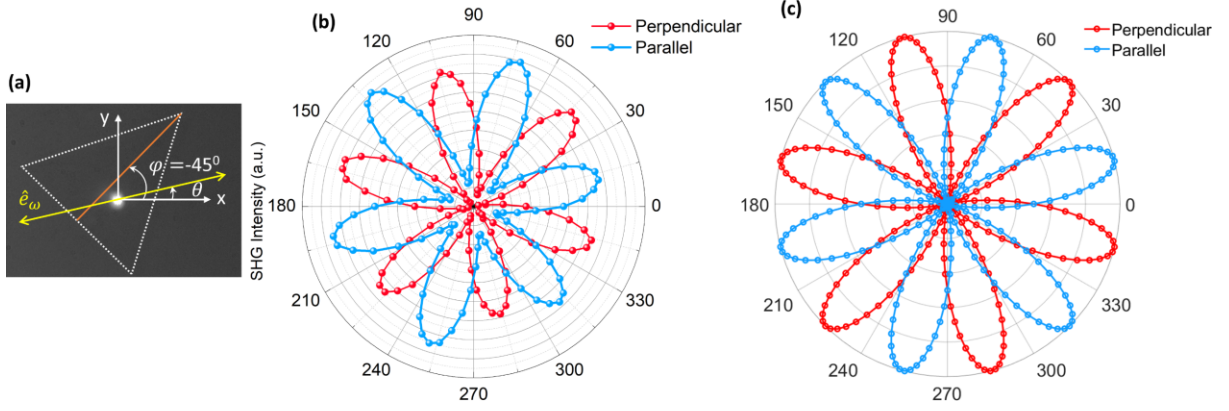
Figure 7.3: Polar plot of SHG from monolayer MoS$_2$ in relation to the laser polarization. **(a)** The monolayer is marked by the triangular shape, $\hat{e}_\omega$ is the laser polarization, the orange line shows the armchair direction of the monolayer. **(b)** The SH intensity was measured in both cases in relation to the angle θ. **(c)** The normalized SH intensity was plotted using equation 7.3 with a known angle $\varphi = -45^0$ between x axis and the armchair direction.

From Equation 7.3, one can see the sum SHG $I_{SHG} = I_{SHG}^{\parallel} + I_{SHG}^{\perp}$ at an arbitrary angle is constant. In the measurement of SHG from bare ECFs and from TMD-coated ECFs, there was no selection of the emitted SH polarization. Additionally, the polar plot of SHG intensity relating to the linear polarization axis can reveal the crystallographic orientation. The SHG gets maximum when the input polarization points along the armchair (zigzag) direction of the crystal for the parallel (perpendicular) configuration. For example, a triangle monolayer TMD will show a six-fold pattern by rotating the sample while fixing excitation polarization and analyzer [252, 288-290]. This six-fold pattern is connected to the triangular shape of the crystal and exhibits three-fold rotational symmetry. In our experiment, the input polarization of the pump laser has been rotated with respect to the x-direction.

Figure 7.3a shows a triangle monolayer MoS$_2$ grown on a SiO$_2$ wafer by our modified CVD process, and the SH emission can be seen by the bright spot at the position of the laser on the monolayer after filtering the FW by band-pass filters. There was no observable SH emission when the laser was at the position of the bare substrate. Figure 7.3b displays the measured SH intensity from the crystal in two cases: $I_{SHG}^{\parallel}$ and $I_{SHG}^{\perp}$. There is a phase shift of 30^0 between them coming from the sine and cosine functions in Equation 7.3. The SHG shows the dependence on the angle between the laser polarization $\hat{e}_\omega$ and the x-direction. Using Equation 7.3, one can vary the φ value until the calculated pattern in Figure 7.3c matches the experimentally measured pattern in Figure 7.3b to determine the crystallographic orientation of the monolayer. In our case, with an estimated angle of $\varphi = -45^0$, the six-fold patterns of $I_{SHG}^{\parallel}$ and $I_{SHG}^{\perp}$ in Figure 7.3c are completely matched with the measured results. It confirms that SHG can be used to measure the crystallographic orientation of monolayer TMDs. In another scenario, a 4-fold pattern can be resolved when rotating the excitation polarization with a fixed sample and analyzer [291].

7.2 SHG in TMD-coated ECFs
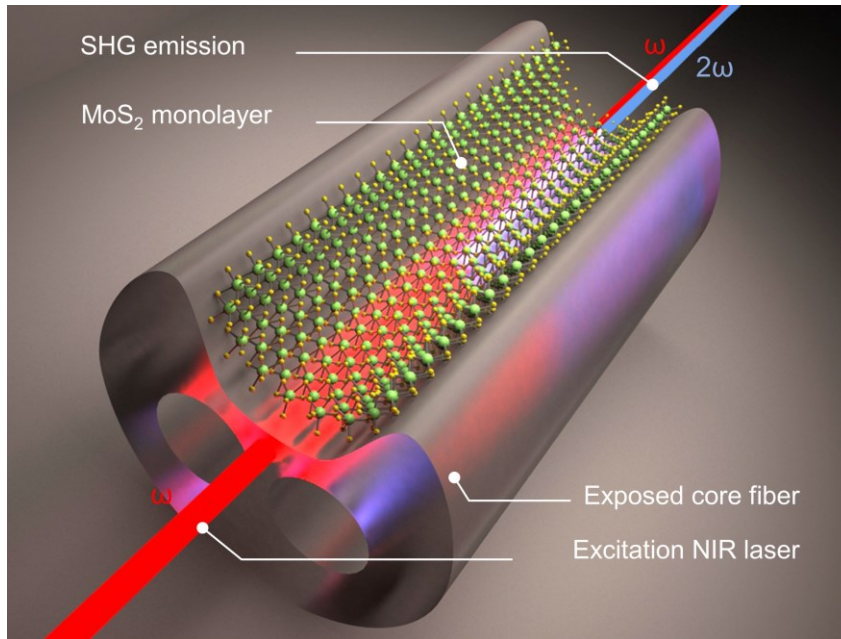
Figure 7.4: Illustration of the concept to demonstrate SHG with as-grown monolayer MoS$_2$ on an ECF. Figure is adapted from [205].

The concept of SHG on the TMD-functionalized optical fibers is illustrated in Figure 7.4. Due to the nature of an amorphous and centrosymmetric material, the bare silica fiber should not exhibit any SHG when interacting with an intense electromagnetic field except for the trivial surface SHG arising from the broken symmetry at the interface. The coating of highly nonlinear monolayer TMDs on the fiber core can establish an efficient nonlinear platform to generate second harmonic waves. Similar to PL and THG, the interaction between the guided modes and monolayer TMDs is supported by the evanescent field. The emission of SHG from monolayer TMDs can be detected via guided modes.

In this chapter, two main lasers have been used for different investigations. SHG from ensembles of TMD atomic crystals on optical fibers have been excited with a Coherent Micra Ti:Sapphire short pulse oscillator system, which has the central wavelength at 800 nm and a Mira OPO-X from APE pumped by a Ti:Sapphire mode-locked laser (Chameleon Ultra II from Coherent) which can be tuned from 1000-1600 nm. Both systems are operating with a repetition rate of $f = 80$ MHz.

The Micra operated at a central wavelength of $\lambda_0 = 800$ nm. The pulse autocorrelation function is displayed in Figure 7.5a. The FWHM of the pulse itself is estimated as $T = T_{\text{ACF}}/\sqrt{2}$ from the FWHM duration of the autocorrelation T_{ACF}. The pulse spectrum was also measured and showed a spectral FWHM of approximately 70 nm. These numbers demonstrated that the pulse is heavily chirped, as the FWHM of the spectrum would allow for a pulse duration of fewer than 35 fs.
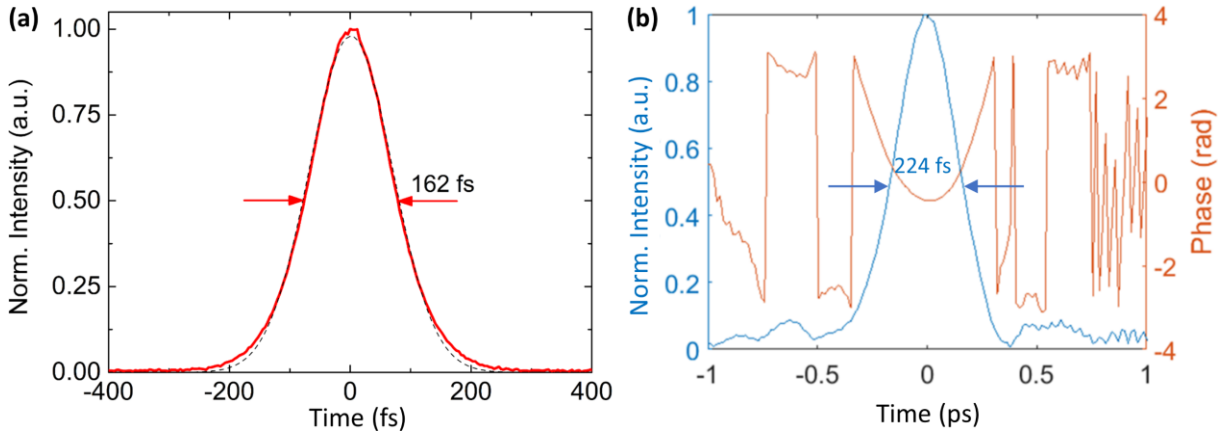
Figure 7.5: Pulse parameters. **(a)** The measured intensity autocorrelation (red) and the Gaussian fit (dotted black) of the pulse at 800nm for NIR laser. **(b)** Pulse intensity and phase of the OPO at 1400 nm. Figure is adapted from [205].

For the measurement of SHG as a function of excitation wavelengths, the Ti:Sapphire/OPO combination was used with tunable pulses from 1.0 μm to 1.6 μm. The pulse duration was estimated by measuring the autocorrelation of the pulse. The temporal pulse shape and temporal phase of the pulse were extracted from the autocorrelation by careful analysis of the autocorrelation's fringe pattern [292]. The pulse is propagated through the used aspheric lens and displayed in Figure 7.5b. We estimate a near transform-limited pulse duration of 224 fs. The pulse parameter has been found to not vary significantly by tuning the wavelength.
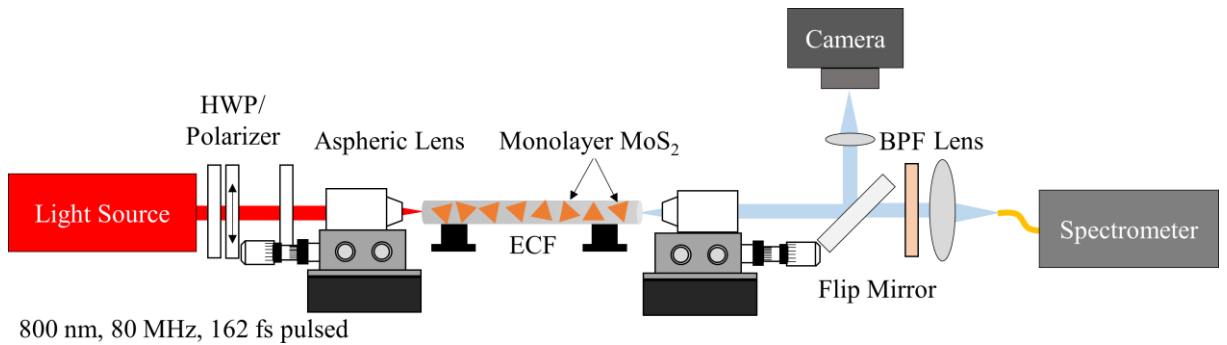
Figure 7.6: Schematic diagram of the experimental setup for SHG measurements. HWP: half-wave plate, BPF: band-pass filter. ECF: exposed-core fiber. Figure is adapted from [205].

Figure 7.6 shows the schematic of the experimental setup that has been used to investigate in-fiber SHG. In this section, high-density coated ECFs were measured with a Ti:Sapphire pulsed laser from Coherent, which has a central wavelength of around 800 nm. Some main parameters of the laser are the repetition rate of 80 MHz and the pulse width of 162 fs, as plotted in Figure 7.5a. The incident pulses were coupled into the fiber core using an aspheric lens (C330TMD-B) with a focal length of 3.1 mm and NA = 0.7. We use an aspheric lens instead of a microscope objective to reduce the dispersion of the pulse. Light leaving the fiber was collimated with a 40x objective and coupled into a spectrometer (Horiba Jobin Yvon Triax) with a cooled Si-CCD-detector to measure the FW and SH spectra after passing through a series of band-pass filters at 400 nm. The input

optical power was controlled by combining a half-wave plate and a linear polarizer, as shown in the schematic experimental setup. The input polarization was adjusted by a second half-wave plate in front of the aspheric lens.
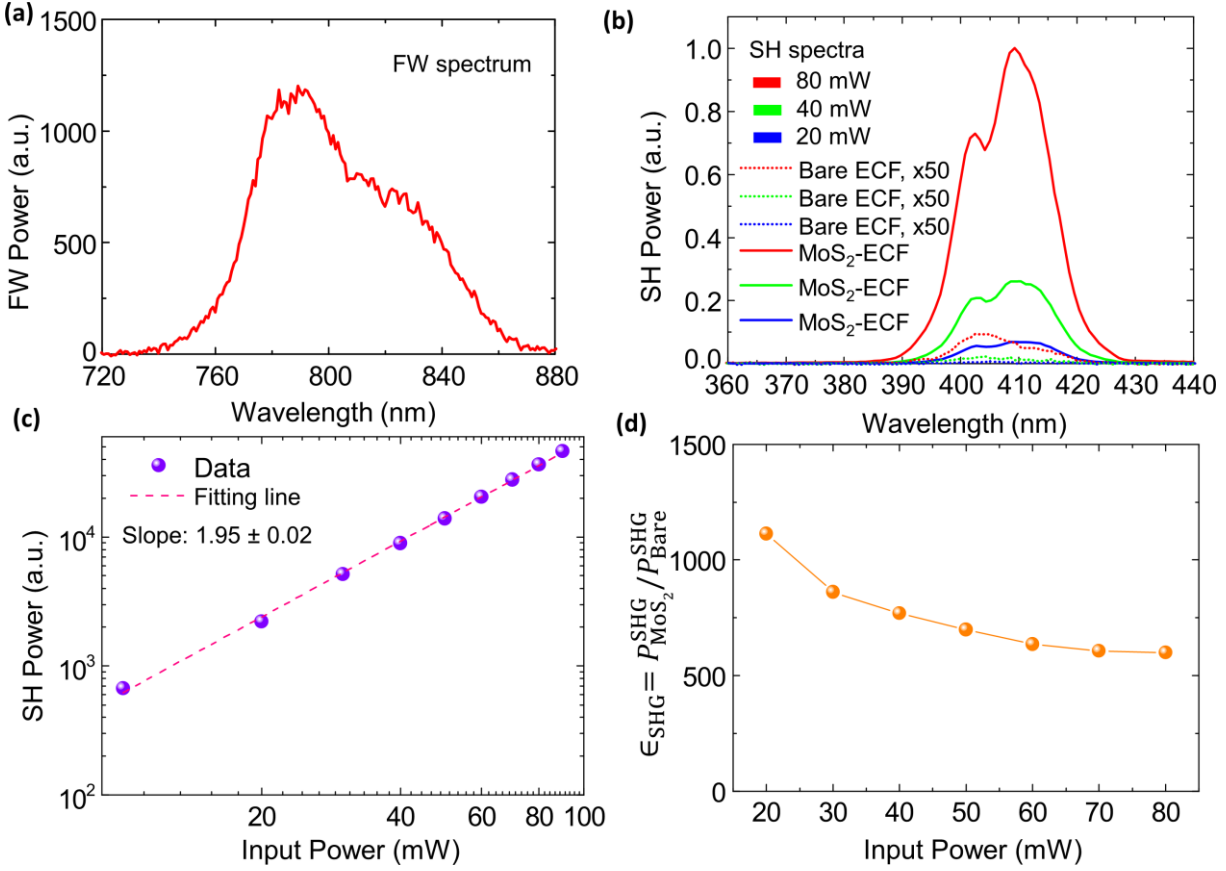
Figure 7.7: In-fiber SHG from bare and MoS$_2$-coated ECFs. The input light has the horizontal polarization with respect to the functionalized surface. **(a)** Fundamental-wave spectrum of MoS$_2$-coated fiber at an incident optical power of 80 mW. **(b)** Normalized SHG spectra of both bare and MoS$_2$-coated fibers measured at different input powers. The spectra from bare ECF was multiplied by a factor of 50 for ease of presentation. **(c)** Log-log plot between SHG power vs input power for the MoS$_2$-coated fiber. **(d)** Calculated SHG enhancement $\epsilon_{\text{SHG}} = P_{\text{MoS}_2}^{\text{SHG}}/P_{\text{Bare}}^{\text{SHG}}$ for a range of input powers. Figure is adapted from [205].

While bulk silica itself has almost zero second-order susceptibility because it is a centrosymmetric medium, except for a minor contribution originating from the interface of the fiber core [191]. The boundary of the silica core has a broken symmetry with a normal vector pointing perpendicular to the optical axis leading to a trivial surface SHG. In this work, the SHG from an MoS2-coated ECF is compared to surface SHG from a bare fiber with the same length to qualify the hybrid waveguides. During the experimental measurements, both the spectra of the SH and the driving FW were recorded simultaneously. Here, the MoS2-coated ECF has a length of 3.5 mm to minimize loss-related effects and the breakup of the propagating pulses.

Figure 7.7a presents the recorded spectrum of the FW from the output of the fiber for an averaged input power of 80 mW. Figure 7.7b displays the recorded SH spectra for a pair of ECFs with the same length and demonstrates that the SHG of the MoS$_2$-coated ECF is much greater than the

surface SHG of the bare ECF for different input powers. From the spectra in Figure 7.7b, the SH power was calculated as the spectral integration of the SH intensity in the range from 390 nm to 430 nm. For ease of display, the SH intensity from the bare ECF has been multiplied by a factor of 50. The discrepancy between the shape of the SH spectrum between the MoS$_2$-coated fiber and the bare fiber is attributed to the frequency dependence of the nonlinear response of the monolayer MoS$_2$. The nature of SHG in the MoS$_2$-coated ECF is confirmed by a quadratic dependence of SH intensity on the input power in Figure 7.7c, where the log-log plot reveals a slope of 1.95.

The enhancement factor ϵ_{SHG} of SHG between the 3.5 mm-long MoS$_2$-coated ECF and the identical plain fiber is plotted in Figure 7.7d. For 20 mW input power, the enhancement factor is roughly 1110-fold, and it declines gradually for higher powers. Interestingly, the surface SHG from a bare fiber shows a fitted exponent higher than a quadratic with a slope of 2.34, displayed in Figure 7.8. It helps to explain the decrease of ϵ_{SHG} with increasing powers in Figure 7.7d. The decrease of the enhancement factor in the higher power is likely due to the faster increase of surface SHG from the fiber itself (a slope of 2.34) compared to the SHG from MoS$_2$ monolayers (a slope of 1.95). However, the absolute amount of SH power still increases proportionally to the input power. Such substantial enhancement of SHG is attributed to the contribution of MoS$_2$ monolayers on the ECF, and the deposition of monolayer MoS$_2$ turns ECFs into a $\chi^{(2)}$-based nonlinear system.
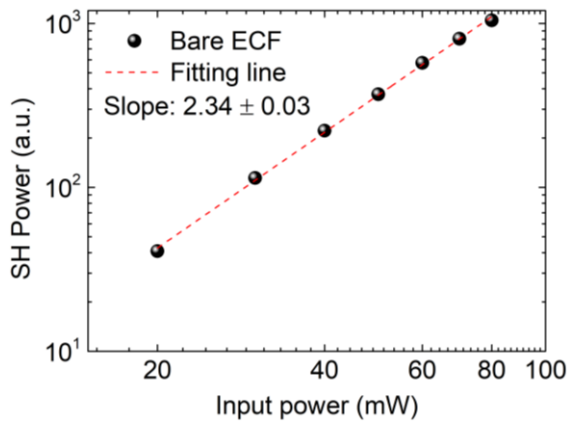
Figure 7.8: SHG for horizontally polarized input light with respect to the functionalized surface in the center of a bare ECF. Log-log plot between SHG power vs input power for the bare fiber with a slope of 2.34.

Investigating the SHG from an MoS$_2$-coated ECF while varying the fiber length may provide some useful information to get the maximum nonlinear conversion efficiency. At first, the polarization of the incident light was fixed horizontally to the functionalized surface of the ECF. The incident power varied from 10 to 80 mW, and the collected spectra were analyzed to extract the SH power. The setting was unchanged throughout this measurement. The fiber has an original length of 12 mm with a highly dense coating of the monolayer MoS$_2$.

The SHG power was plotted in Figure 7.9a. The violet balls present the data of the 12 mm-long fiber with the dotted line fitting very well with a quadratic equation. Then, the fiber was cut short

to only 3.5 mm and coupled to the excitation light source. The shorter fiber, displayed by the orange triangles, exhibits greater SH power than the original one. SH power also follows a quadratic dependence on the input power, confirming that the signal was the second-harmonic wave. The SHG power increased 2.5 times for the short fiber at 80 mW. It is mostly due to the higher coupling efficiency in the case of 3.5 mm-long fiber, leading to 1.4x increase in the transmitted power compared to the 12 mm-long fiber. Because the SH power is proportional to FW power square, it will increase double in SH power for the short fiber. The increase of coupling efficiency seems to be related to additional propagation losses experienced by the FW wave in the longer fiber. Also, the deposition of MoS_2 monolayers is inhomogeneous throughout the fiber length, and it can be the case that most of the monolayers are located in the 3.5 mm-long section of the fiber. Hence, the shorter fiber retained the contribution of MoS_2 monolayers to the collected SH power while reducing the propagation loss significantly. The additional explanation could be the stronger influence of phase mismatch and the increased impact from the pulse breakup in the longer fiber, decreasing the SH power.
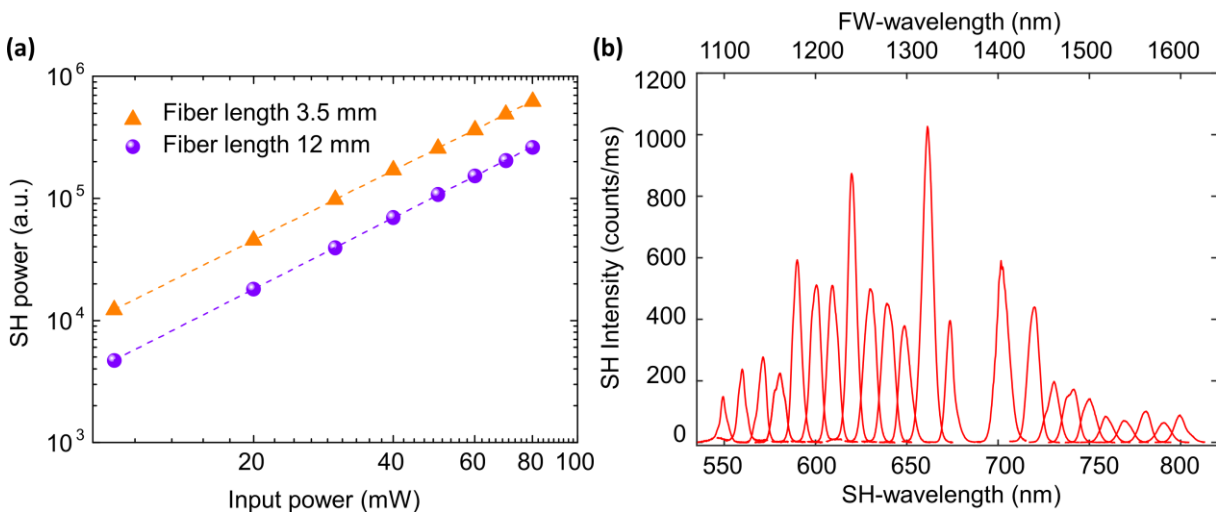
Figure 7.9: Nonlinear dynamics of SHG in MoS_2-coated fibers. **(a)** SHG power of the 3.5 mm-long MoS_2-ECF vs the 12 mm-long MoS_2-ECF measured with a cut-back technique. **(b)** The feature of SHG over a wide range of FW excitation. Figure is adapted from [205].

Figure 7.9b reveals the SH spectra recorded from a Si-cooled spectrometer when the fiber was coupled and excited by a tunable OPO laser with a repetition rate of 80 MHz and a pulse width of 180 fs. The transmitted power was kept at 10mW for all FWs, and the output signal was collected. From Figure 7.9b, the FWs have been tuned from 1100 nm to 1600 nm with a gap from 1380-1390 nm due to the instability of the laser at these wavelengths. The correspondent SH is expected in the range from 550 nm to 800 nm, which is over the A and B excitons energy of MoS_2 monolayers. The A exciton of the monolayer MoS_2 is around 680 nm (1.82 eV), while the B-exciton is around 620 nm (2.0 eV). The recorded spectra reveal the enhancement of the SHG process when the SH wave is near exciton band energies. The highest enhancement is determined to be at 660 nm, which

is near the A exciton, whereas the second highest enhancement is at 620 nm, which is near the B exciton band. The stronger enhancement of the A exciton can be explained by the dominant PL of this exciton compared to the B exciton. Remarkably, the SHG near A and B-excitons is from 2 to 10 times higher than that of off-resonance wavelengths. The behavior of the SHG process of the MoS_2-coated ECF is equivalent to other works carried out on planar substrates [97, 118, 271, 279]. Hence, this measurement demonstrates that ECFs can be a versatile platform to qualify the optical properties of 2D materials.

7.3 Isolated monolayers on ECF

Since phase-matching intensely influences the SHG efficiency, the random distribution of many monolayers on the fiber core will lead to an incoherent and partially destructive SH signal. That is elusive to evaluate the effective nonlinear susceptibility of the system in that case. Therefore, we have utilized a pulsed laser to thermally ablate unwanted crystals on the fiber, just keeping one crystal in the phase matching length. A low-density MoS_2-coated ECF has been chosen as a sample to measure the $\chi^{(2)}$ value. The MoS_2-coated ECF was characterized by PL mapping along the fiber length of 12 millimeters to locate the position of each monolayer on the fiber core. The result turned out that each monolayer has a distance from tens to hundreds of micrometers to the nearby crystals. A monolayer with a good PL and the armchair direction pointing along the fiber axis was selected to retain while the other crystals will be removed. The horizontally polarized input light will have the maximum coupling with the nonlinear tensor in this chosen monolayer because they are both in the monolayer plane.
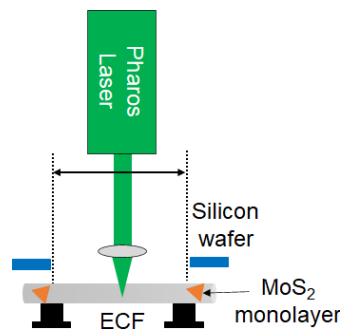
Figure 7.10: The thermal ablation process to establish isolated crystals on ECF. Figure is adapted from [205].

Figure 7.10 illustrates the thermal ablation process to remove all unwanted crystals on the fiber core. A Pharos pulsed laser with a pulse width of 200 fs, a central wavelength of 1030 nm with a frequency doubled to 515 nm, and a repetition rate of 100 kHz has been used to generate the heat and focus on the core region. The laser was mounted on a translational stage and traveled with a scanning speed of 100 μm/s. The excitation light was focused by a 200 mm focal lens to create a

focus with a width of approximately 60 μm. By the pulse energy of 4 μJ, the thermal heat can remove all crystals on the fiber core and side walls in the ablated region.

To protect the chosen monolayers, a silicon wafer with a size of 1 x 1 cm was put on top of the fiber during the ablation process. Eventually, we obtained the chosen monolayer with a well-defined crystal orientation near the left edge and another monolayer with a big size near the right edge. To confirm the successful ablation, the fiber was analyzed again using the identical PL microscopy and checked for every position on the fiber core to verify the complete removal of unwanted monolayers and the preservation of the chosen one.
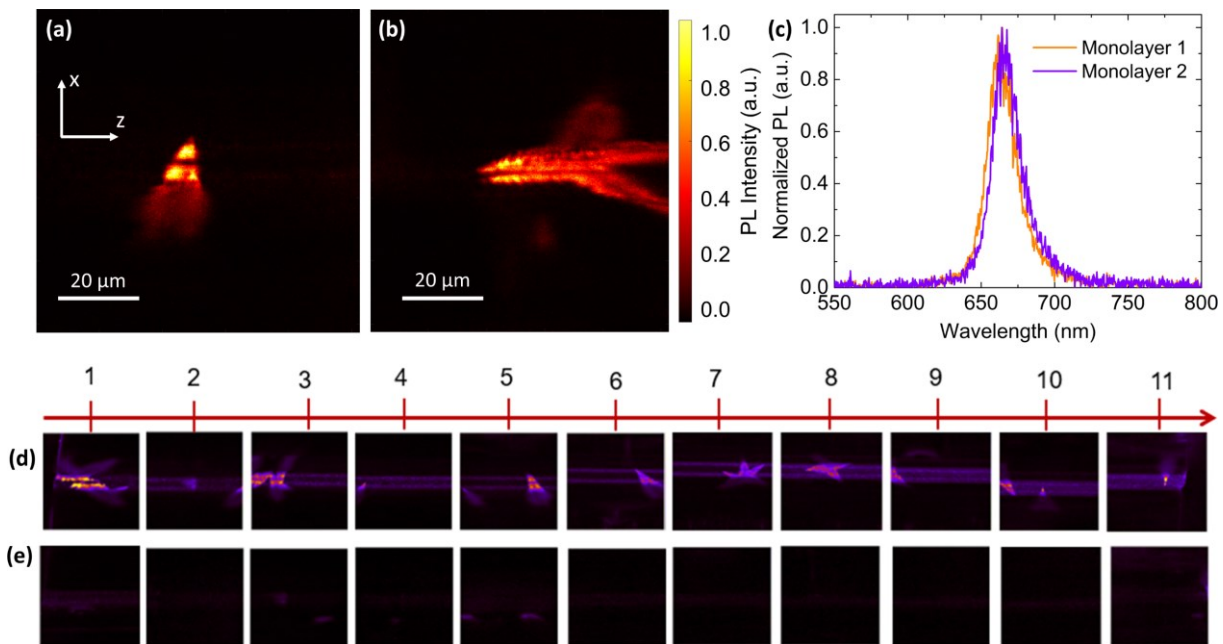
Figure 7.11: Isolated MoS$_2$ monolayers on the fiber's core. **(a)** PL emission of the first monolayer on the left side. **(b)** PL emission of the second monolayer on the right side of the fiber. **(c)** The normalized PL spectra of both monolayers after the ablation process. **(d-e)** MoS$_2$ monolayers at different positions on the fiber's core before and after the ablation process. The color bar is identical for subfigures **(d-e)**. Figure is adapted from [205].

Figure 7.11a-b exhibit the PL map of isolated monolayers, where the first monolayer has the armchair direction parallel to the fiber axis, and the second monolayer has a large size with undefined crystallographic orientation. The PL recorded from both monolayers is displayed in Figure 7.11c to confirm the high quality of such monolayers after the ablation process. Figure 7.11d-e reveal various monolayers located in different positions on the fiber core before and after the ablation, respectively. The black image in Figure 7.11e proved the success of removing unwanted monolayers by a pulsed laser. Both Figure 7.11d and Figure 7.11e have the same color bar, and the fiber core is in the center of all images.

A sketch of the experimental setup to record the SHG from the MoS$_2$-coated ECF before and after the ablation process and to evaluate the surface SHG from a bare ECF is depicted in Figure 7.12. A tunable Mira OPO-X from APE pumped by a Ti:Sapphire modelocked laser (Chameleon Ultra

II, Coherent) was focused into the fiber's core using an aspheric lens. We must clarify that the tunable OPO laser and the experimental setup in this section are different from the tunable laser and the setup used to create Figure 7.9b. The light coupling onto the fiber is optimized by an infrared Xenics camera. The SH light from the fiber's core was imaged onto the visible Thorlabs camera (CC215MU) after passing through a pair of 850 nm short-pass filters. For each data point in the calculation, the images were corrected by subtracting the noise from the lab environment. The settings were kept unchanged for all fibers in this section.
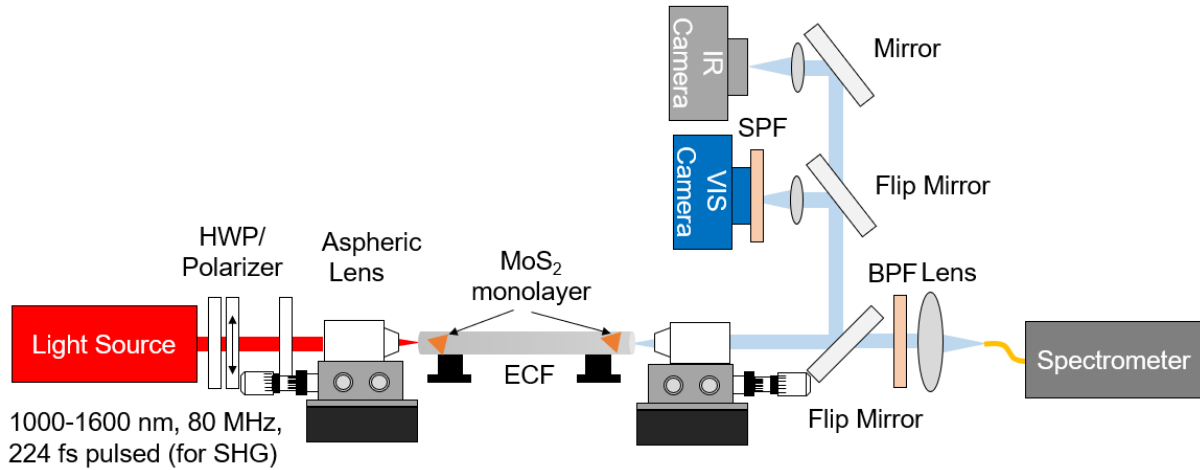
Figure 7.12: Experimental setup to measure SHG from MoS$_2$-coated ECF before and after ablation process. ECF: exposed core fiber, HWP: half-wave plate, BPF: band-pass filter. SPF: short-pass filter. Figure is adapted from [205].

Due to the weak signal from isolated monolayers, a visible camera was utilized to collect the SH signal imaging from the output of the fiber after filtering the pump laser. The fundamental wavelengths were selected from 1280 to 1400 nm because of some factors. The loss is less pronounced, and the reference data of the $\chi^{(2)}$ value is reliable in this range. Besides, the pulsed laser has good stability in the selected range. The corresponding SH will be from 640 nm to 700 nm, which is over the A-exciton band, then can give more information about the nonlinear properties of MoS$_2$ monolayers. From wavelength-dependent SHG in Figure 7.9b, A-exciton has shown a better enhancement than B-exciton, therefore SH wave near this exciton band is expected to have a higher nonlinear susceptibility. The setup was calibrated to obtain the absolute SH power from the greyscale images by converting ADU (analog to digital unit) to the electron and then from the electron to the photon. This thermoelectrically cooled sCMOS camera has a medium read noise of 1.4746 e$^-$ (r.m.s.) and a gain of 0.4853 e$^-$ per ADU. The signal loss in this setup was determined as high as 36.6% and will be compensated for the collected number of photons. The transmitted power was kept at 7 mW through the fiber.

The original coated fiber has about thirty crystals that contributed to the SH power, and after the removal, we retained two isolated crystals on each side of the fiber. Figure 7.13a displays the SH

power for both fibers in the range from 640 nm to 700 nm. For both fibers, the SH power was highest at 680 nm, which is at the A-exciton band of MoS_2 monolayers. This finding indicates that the origin of the enhancement comes from monolayers. The SH power was dropped by a factor of 15 to 25 for the case of isolated crystals, depending on the wavelengths. The reduction of the SH power with declining nonlinear crystal length is expected. The variation of the SH power ratio between the two cases is likely caused by the random crystallographic orientation, length, and spacing, leading to the incoherence of SHG from each monolayer. The higher SH power ratio between two fibers near B-exciton energy is probably due to the different dynamics of this exciton. Additionally, only A-exciton was observed in Figure 7.11c, therefore, the role of B-exciton in the case of isolated crystals is less noticeable.
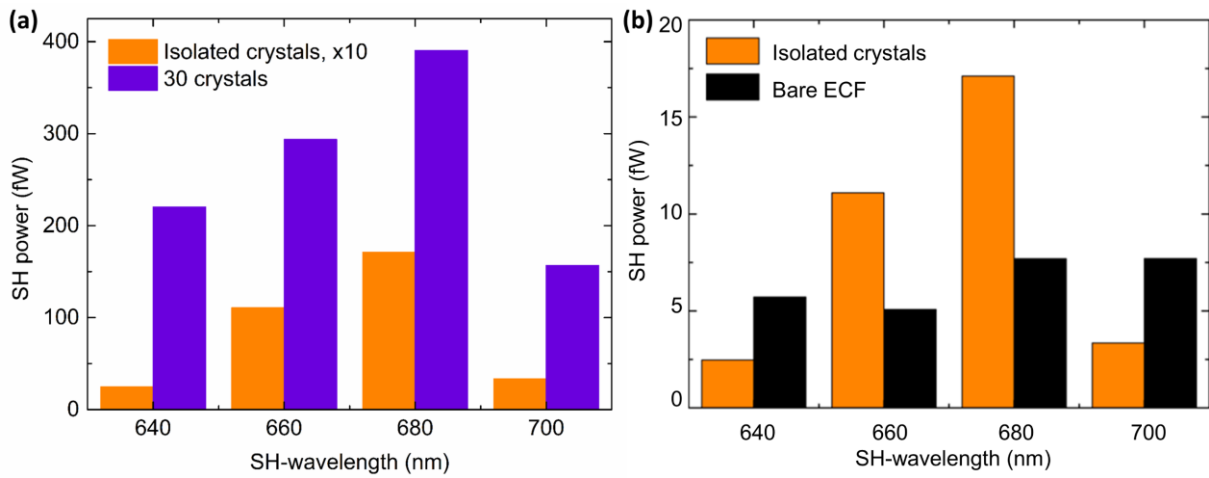
Figure 7.13: (a) Measured SH power emitting from thirty MoS_2 monolayers on 12 mm-long ECF (before the laser ablation) vs isolated MoS_2 monolayers on 12 mm-long ECF (after the laser ablation). **(b)** Measured SH power emitting from only 02 monolayers vs from 12 mm-long ECF. Subfigure **(a)** is adapted from [205].

With the known surface SH power measured from the bare ECF, we can calculate the sole contribution from isolated crystals. Figure 7.13b displays the SH power calculated for isolated monolayers after the ablation and the surface SHG from a bare ECF. While the enhancement of SHG over A exciton can be observed for MoS_2 monolayers, the surface SHG is almost independent of the wavelengths. This confirms that the enhancement of SHG is solely coming from the monolayers. Remarkably, the SH power emitted by isolated crystals with a total length of 30 μm is twice as much as the surface SH power from the entire fiber with a total length of 12 mm.

7.4 Nonlinear simulation and analysis

Because the monolayer TMD has only the in-plane second-order susceptibility tensor, thus any excitation field which has polarization in the crystal plane can generate SH efficiently. The large curvature radius of the exposed surface where the TMD flakes are located results in higher

efficiency for horizontal polarization of the FW. Here, the polarization of FW in the experimental setup is represented as the x and y axes (Figure 7.14a), while the coordinate system of the monolayer TMD is shown by the xm and ym axes. In the experimental condition, we considered the two FMs at FW contributing to the generated SH, therefore the projection of the E_x^{FW} and E_y^{FW} into the monolayer plane along the exposed core at an arbitrary point can be expressed as

$$E_{xm}^{FW} = E_x^{FW}\cos\alpha - E_y^{FW}\sin\alpha \tag{7.4}$$

$$E_{ym}^{FW} = E_x^{FW}\sin\alpha + E_y^{FW}\cos\alpha, \tag{7.5}$$

here α is the angle between the monolayer plane and the x axis at the calculated point, as illustrated in Figure 7.14a.
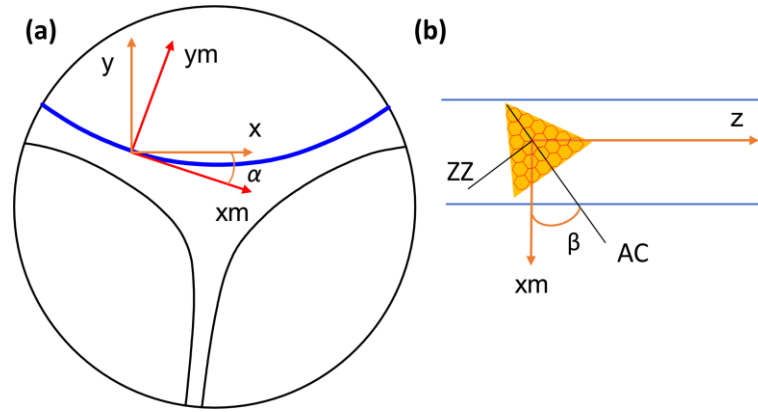
Figure 7.14: (a) The decomposition of electric field strength at a random point on the curvature of the fiber core. x,y denotes the coordinate from the experimental setup. xm, ym show the coordinate of the monolayer. **(b)** The random orientation of a monolayer MoS$_2$ with an angle β in relation to the xm axis. AC is the armchair direction and ZZ is the zigzag direction of the monolayer.

The value of the angle α along the curvature of the exposed core varies depending on the position. Therefore, the contributions from E_x^{FW} and E_y^{FW} also depend on the location. Near the center of the fiber core, the angle α reaches the minimum, then E_x^{FW} has a greater impact on E_{xm}^{FW} than E_y^{FW}. Nevertheless, the vertically polarized input field remains nontrivial in the SHG process.

For the entire curvature of the exposed core, the projected electric fields in the monolayer plane can be written as

$$E_{xm}^{FW} = \sum_{i=1}^{n}(E_x^{FW}\cos\alpha - E_y^{FW}\sin\alpha) \tag{7.6}$$

$$E_{ym}^{FW} = \sum_{i=1}^{n}(E_x^{FW}\sin\alpha + E_y^{FW}\cos\alpha) \tag{7.7}$$

$$E_{zm}^{FW} = \sum_{i=1}^{n}E_z^{FW}, \tag{7.8}$$

where n is the number of calculated points on the blue curve in Figure 7.14a.

Similarly, the generated electric field of SH in the monolayer plane can be written as

$$E_{xm}^{SH} = \sum_{i=1}^{n} (E_x^{SH}\cos\alpha - E_y^{SH}\sin\alpha) \tag{7.9}$$

$$E_{ym}^{SH} = \sum_{i=1}^{n} (E_x^{SH}\sin\alpha + E_y^{SH}\cos\alpha) \tag{7.10}$$

$$E_{zm}^{SH} = \sum_{i=1}^{n} E_z^{SH} \tag{7.11}$$

To calculate the projection of the electric field at FW on the monolayer plane with some random orientations, we assumed a monolayer that has the armchair direction oriented an angle β to the xm direction in Figure 7.14b. The monolayer plane is indicated by the xm-z plane, whereas ym-z is the out-of-plane. Due to the six-fold pattern of the SH intensity in relation to the angle β, within each 60^0, the projection of the electric field on the armchair (AC) and zigzag (ZZ) direction of the monolayer is given by

$$E_{AC}^{FW} = \sum_{\beta=0}^{\frac{\pi}{3}} (E_{xm}^{FW}\cos\beta + E_z^{FW}\sin\beta) \tag{7.12}$$

$$E_{ZZ}^{FW} = \sum_{\beta=0}^{\frac{\pi}{3}} (-E_{xm}^{FW}\sin\beta + E_z^{FW}\cos\beta) \tag{7.13}$$

$$E_{AC}^{SH} = \sum_{\beta=0}^{\frac{\pi}{3}} (E_{xm}^{SH}\cos\beta + E_z^{SH}\sin\beta) \tag{7.14}$$

$$E_{ZZ}^{SH} = \sum_{\beta=0}^{\frac{\pi}{3}} (-E_{xm}^{SH}\sin\beta + E_z^{SH}\cos\beta) \tag{7.15}$$

TMDs belong to the D_{3h} point symmetry, so the polarization dependence of SHG for a monolayer can be written in the form

$$\begin{pmatrix} P_x^{(2)}(2\omega) \\ P_y^{(2)}(2\omega) \\ P_z^{(2)}(2\omega) \end{pmatrix} = \varepsilon_0 \begin{pmatrix} \chi_{xxx}^{(2)} & \chi_{xyy}^{(2)} & 0 & 0 & 0 & 0 \\ 0 & 0 & 0 & 0 & 0 & \chi_{yyx}^{(2)} \\ 0 & 0 & 0 & 0 & 0 & 0 \end{pmatrix} \begin{pmatrix} E_x^2(\omega) \\ E_y^2(\omega) \\ E_z^2(\omega) \\ 2E_y(\omega)E_z(\omega) \\ 2E_x(\omega)E_z(\omega) \\ 2E_x(\omega)E_y(\omega) \end{pmatrix}, \tag{7.16}$$

where x denotes the armchair direction and y denotes the zigzag direction of the crystal. In the case of monolayer MoS$_2$, we neglect the out-of-plane direction (z-component), then the Equation 7.16 becomes

$$\begin{pmatrix} P_{AC}^{(2)}(2\omega) \\ P_{ZZ}^{(2)}(2\omega) \end{pmatrix} = \varepsilon_0 \begin{pmatrix} \chi_{xxx}^{(2)} E_{AC}^2(\omega) + \chi_{xyy}^{(2)} E_{ZZ}^2(\omega) \\ 2\chi_{yyx}^{(2)} E_{AC}(\omega) E_{ZZ}(\omega) \end{pmatrix} \tag{7.17}$$

From Equation 7.2, we know that $\chi_{1L,xxx}^{(2)} = -\chi_{1L,xyy}^{(2)} = -\chi_{1L,yyx}^{(2)}$, so Equation 7.17 reads as

$$\begin{pmatrix} P_{AC}^{(2)}(2\omega) \\ P_{ZZ}^{(2)}(2\omega) \end{pmatrix} = \varepsilon_0 \chi_{xxx}^{(2)} \begin{pmatrix} E_{AC}^2(\omega) - E_{ZZ}^2(\omega) \\ -2E_{AC}(\omega) E_{ZZ}(\omega) \end{pmatrix} \tag{7.18}$$

Equation 7.18 shows that the interaction of two electric field vectors with the same polarization, for instance, both along AC or ZZ direction will yield a nonlinear polarization pointing along the AC direction. Whereas, the coupling of two electric fields with orthogonal polarization will result in a nonlinear polarization pointing along the ZZ direction.

The SH overlap coefficient $\chi_{\mathrm{eff}}^{(2)}$ governed by the overlap between the excited FW and the generated SH for every MoS$_2$ flake with different orientation is given as

$$\chi_{\mathrm{eff}}^{(2)} \sim \int_0^l \left\{ E_{\mathrm{SH,AC}}^* \left(E_{\mathrm{FW,AC}}^2 - E_{\mathrm{FW,ZZ}}^2 \right) - 2E_{\mathrm{SH,ZZ}}^* E_{\mathrm{FW,AC}} E_{\mathrm{FW,ZZ}} \right\} dl, \tag{7.19}$$

where l is the length of the boundary containing the data points such as the blue curve in Figure 7.14a. Due to the random distribution of the monolayers on the boundary, the $\chi_{\mathrm{eff}}^{(2)}$ coefficient was calculated as the average value for all possible orientations.

The SHG process profoundly depends on the phase matching and mode matching between the FMs of the FW and the HOMs of the SH. As discussed in the THG process, our ECFs support the intermodal phase matching between the FWs and their SHs. For ease of presentation, we considered only the two FMs with mostly horizontal and vertical polarization that have been excited in the experiment. Figure 7.15a shows the electric field distribution inside the core region of the horizontally polarized FM at 800 nm. Since the excitation laser has a central wavelength at 800 nm, the simulation was calculated for the range from 700-900 nm, which fully covers the spectral frequencies of the pulsed laser. Figure 7.15b shows the calculated refractive mode indices for two degenerate FMs from 700-900 nm and 50 HOMs at SH from 350-450 nm. The region of interest is marked in the gray area corresponding to the recorded SH spectra from the measurement. The effective mode indices of FMs are displayed in the solid lines, whereas the HOMs of SH wavelengths are shown as colored dots. The phase matching occurs within a length scale of crystal, which is determined by the following condition: $\Delta n = \left| n^{\mathrm{FW}} - n^{\mathrm{SH}} \right| < \lambda_0 / (\pi L_c)$, with λ_0 is the

fundamental wavelength, and $L_c \approx 7$ μm is the typical length of an MoS_2 monolayer on the fiber core, leading to $\Delta n \approx 0.03$. Only the modes that fulfill such conditions can be considered, and they are within the yellow phase-matched band in Figure 7.15b. Figure 7.15c reveals the normalized overlap factor, which is calculated using Equation 7.19. From our calculation, the SH modes will be the most efficient with an *x*-polarized excitation beam (the blue bars) compared to the *y*-polarization in red bars.
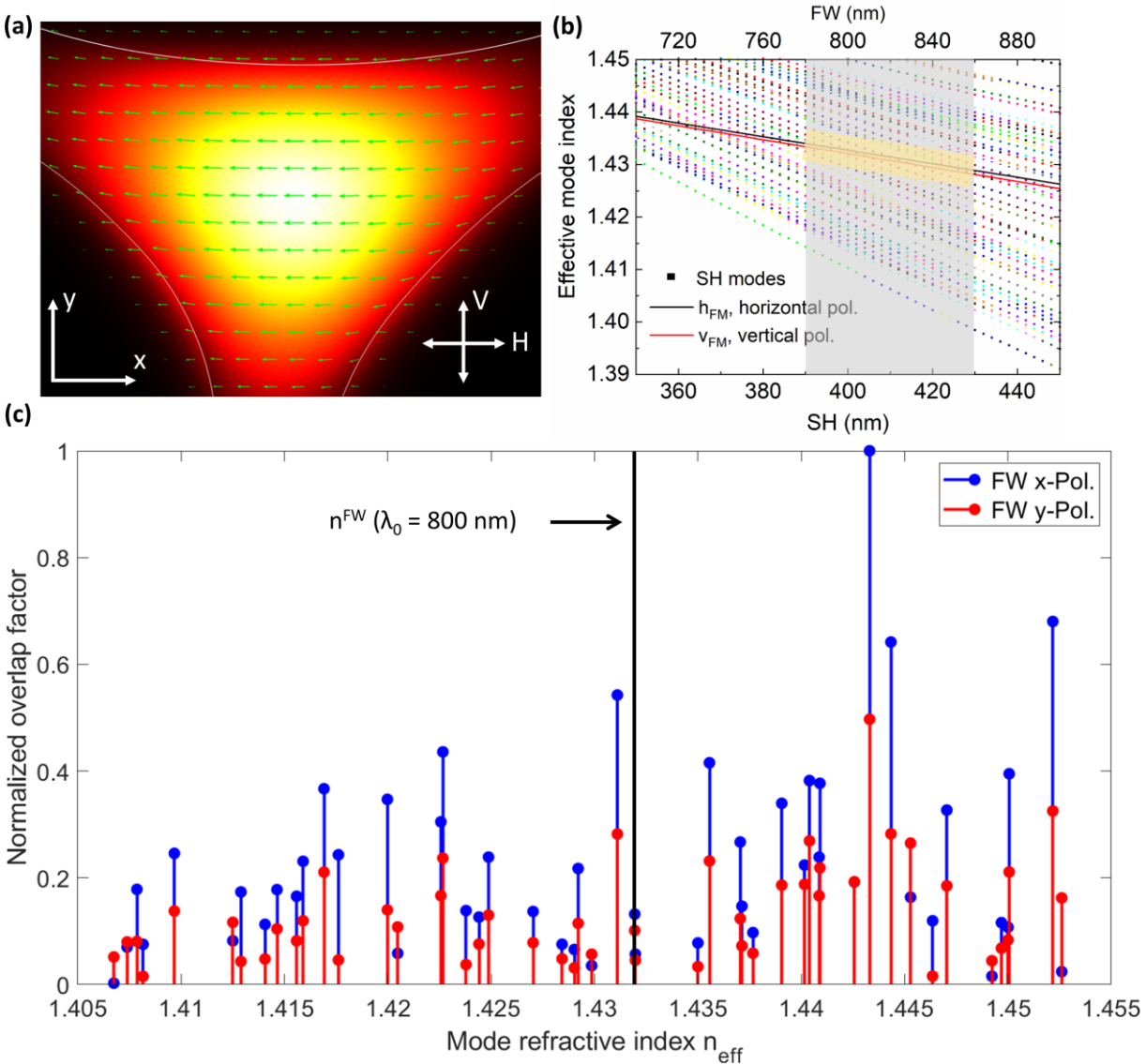
Figure 7.15: Numerical simulation of SHG process in MoS_2-coated ECF. **(a)** Simulated norm of the electric field distribution of the horizontally polarized FM at 800 nm (The white double-headed arrows denote vertical and horizontal polarization). **(b)** Effective mode indices of FMs (full lines) and SH modes (dotted lines) in the frequency between 700 - 900 nm and 350 - 450 nm, respectively (grey area: pulse spectrum, yellow area: phase-matching region with $\Delta n \leq$ 0.03). **(c)** Calculated normalized overlap factors for SH modes for both horizontal- and vertical-polarization of FW within the phase matching region. The black line is the phase matching point $n^{FW} = 1.432$.

The SHG efficiency is not equal for all modes in the phase match band due to the mode profiles and the overlap between the exciting FMs and the coupling HOMs. The polarization of the coupled pulsed beam will be maintained inside the ECF. Because the monolayer TMDs have only the in-

plane nonlinear susceptibility tensor, any polarization of the FWs which lies in the monolayer plane will have the maximum coupling efficiency. The generated SH field of the monolayers will also polarize along the fiber surface, but only its transversal component can excite or couple back to a relevant SH mode. The final SH field is the interplay of the interaction of FW with monolayer TMDs and the transfer of SH output from TMDs to a particular SH mode of the fiber. As the TMD crystals are oriented randomly on the fiber core, their contribution to the SHG can be slightly different due to the size and the orientation, but there is no influence on the polarization behavior of the SH mode.

Because of the unequal contribution of x- and y-polarized FW together with an asymmetry of the fiber, the SHG varies for different input polarization. We investigated the dependence of SHG intensity on the input polarization by fixing the input power and rotating the input polarization by a half-wave plate. Figure 7.16a presents the experimental data plotted as the black line. The SH power is maximum for the horizontal polarization, which is parallel to the bottom of the exposed surface. By rotating the polarization further, the SH power decreases gradually to the minimum at 40° before increasing back and getting another peak at 90°. The lowest SHG efficiency in the range from 40° to 50° can be explained by the weak overlap between FW and the SH modes. Furthermore, the FMs at FWs tend to support better horizontal and vertical polarization, which might affect the SHG efficiency as well. The higher efficiency of the horizontally polarized FW in comparison with the efficiency of the vertically polarized FW is mainly supported by the in-plane nonlinear tensor of the monolayer TMD and the higher overlap factor.

To reproduce the tunability of SHG as a function of input polarization, we have calculated the conversion efficiency for all HOMs in the phase-matching region. We also assumed the random distribution and random orientation of crystals along the functionalized surface. The calculated results are the average of the contribution for all possibilities, which may lead to the discrepancy with the real coated ECF. Since we activated the SHG process with the two virtually degenerate FMs, which have the x and y polarization, we will use both two FMs for the numerical calculation. The second harmonic power has a relationship with the SH overlap coefficient, expressed by

$$P_{\text{SHG}} \sim \left| \chi_{\text{eff}}^{(2)} \right|^2 \tag{7.20}$$

From Equations 7.6-7.19, $\boldsymbol{E}$ field components of $\chi_{\text{eff}}^{(2)}$ are modulated by squared sine and cosine functions. The product of squared sine and cosine depends strongly on the fiber geometry. Hence, the SH power is calculated using the following equation

$$P_{\text{SHG}} \approx P_0[\cos^4(\theta) + Q \sin^4(\theta)], \tag{7.21}$$

where θ is the polarization angle with respect to the x-axis, and P_0 is the nonlinear response coming from all possible SH modes at $\theta = 0°$. Q is the relative impact of a horizontally polarized FW over a vertically polarized FW in the SHG of hybrid waveguides. A value of $Q = 1.23$ is found from the experimental data, whereas from the numerical simulation, $Q = 4.0$ is found based on our assumption and the simplicity of our model. This discrepancy is unavoidable due to the complexity of the material system, the random distribution and orientation of as-grown monolayers, and the involvement of multiple modes in reality. However, we could obtain an agreement between experimental and numerical data that the horizontally polarized FW has a better SHG efficiency than the vertically polarized FW.
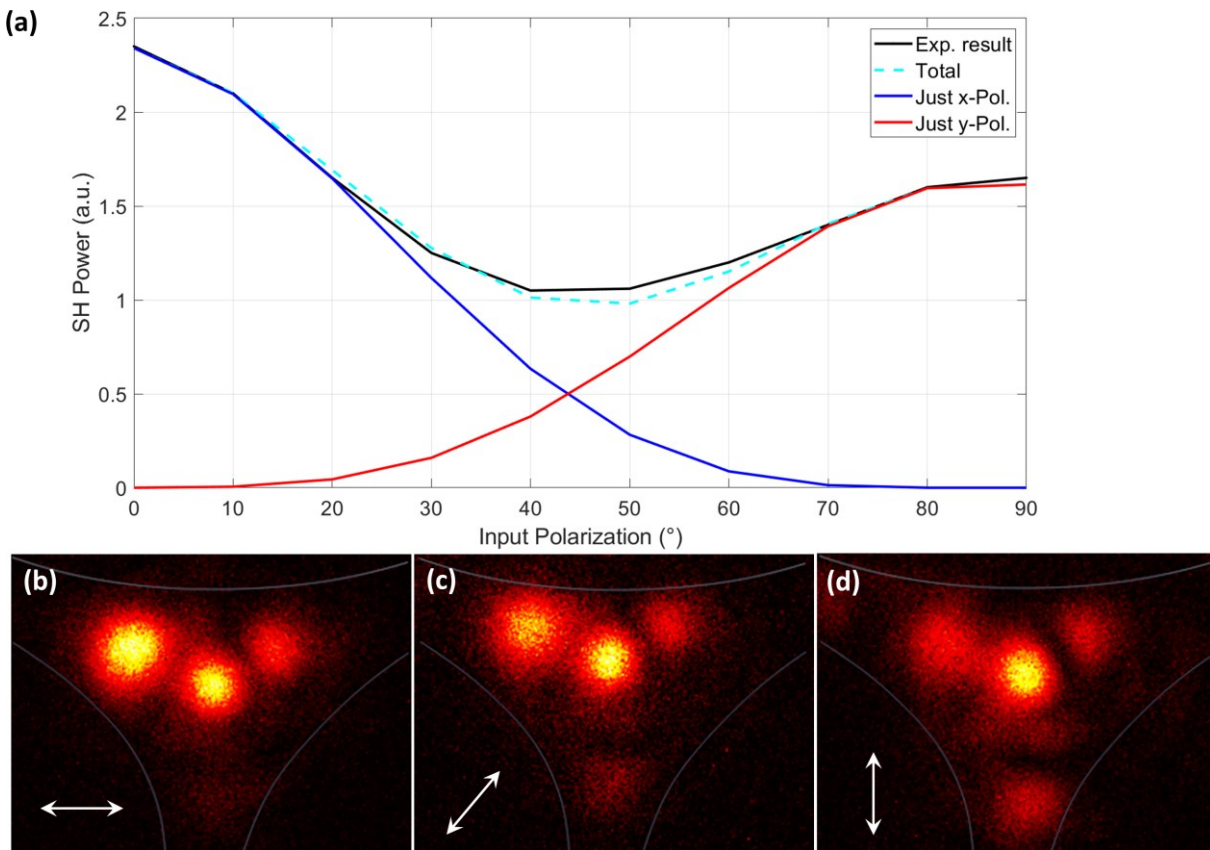
Figure 7.16: SHG tunability by rotating the input polarization. **(a)** SH intensity vs. input polarization in comparison with the functionalized surface, 0° indicates horizontal polarization and 90° indicates vertical polarization for both experimental result and numerical calculation. x- and y-polarizations mean the near-degenerate fundamental modes with mostly horizontally or vertically polarization directions, respectively. **(b-d)** Experimentally recorded images of the mode pattern during the SHG process at the facet of an MoS$_2$-coated ECF. **(b)** Input polarization at 0°. **(c)** Input polarization at 40°. **(d)** Input polarization at 90°. Figure is adapted from [205].

The qualitative conversion efficiency of SHG as a function of input polarization is displayed in Figure 7.16a as a dashed cyan line. It is the sum contribution from both x and y polarized components. The intrinsic contributions of the x- and y-polarization components are shown in the blue and red solid lines, respectively. With an adjustment factor $Q = 1.23$, the characteristics of the SHG from the MoS$_2$-coated ECF are numerically reproduced. This behavior is presented by cosine and sine functions in Equation 7.19, which is derived from the projection of the FH field onto the

horizontal and vertical parts of the ECF surface. The square of the FW field in the SHG power formula leads to the modulation of the fourth power of the cosine and sine of the polarization angle, as expressed in Equation 7.21.

The structure of the SH modes recorded at the output of the fiber is depicted in Figure 7.16b-d. All recorded images at SH wavelength showing a multi-lobed feature of the guided modes have proved the intermodal phase matching between FMs at FW and HOMs at SH. This finding is consistent with the phase-matching condition pointed out in Figure 7.15b. The intensity of the field profiles is asymmetric for both zero and 90 degrees, which can be attributed to the non-symmetry of the fiber. The HOMs at the second-harmonic wavelength do not differ much with the change of input polarization, except for the variance of the localized field inside the fiber core. The spatial shape and polarization of the HOMs will have an important effect on the highly localized nonlinear polarization of the crystals, similar to the THG process, leading to the tunability of SH power.

7.5 Effective nonlinear susceptibility of TMD-coated ECFs

As an attempt to evaluate the $\chi^{(2)}$ value of our TMD-coated ECFs quantitatively, we have used the measured SH power and numerical data for the calculation. In the experiment, a pulsed laser was utilized to excite the fiber, and the relation from peak intensity to time-averaged power is constructed assuming Gaussian-shaped pulses and Gaussian beam optics. The average SH power $P_{\mathrm{SH},jk}$, which is generated in the jth mode of the fiber and excited with an unchirped Gaussian pulsed laser is given by [116, 205, 293]

$$P_{\mathrm{SH},jk} = \frac{1}{1.06\sqrt{2}Tf}\eta_{jk}L^2 P_{\mathrm{FW},k}^2 \left[\frac{\sin(\delta_{jk})}{\delta_{jk}}\right]^2,$$ (7.22)

where η_{jk} is the conversion efficiency of the kth fundamental wave into the jth second harmonic mode, L is the nonlinear interaction length, $P_{\mathrm{FW},k}$ is the average power of propagating fundamental wave in the kth mode, T is the full-width at half-maximum of the pulse duration, f is the repetition rate, and $\delta_{jk} = \left(k_k^{\mathrm{FW}} - k_j^{\mathrm{SH}}/2\right)L$ is the phase mismatch of the kth fundamental mode and the jth second harmonic mode. The components of conversion efficiency can be extracted from numerical eigenmode solutions, which were calculated from the spatial distribution of the guided modes using a FEM-based solver (COMSOL).

From sections 7.2 and 7.3, the enhancement of SHG is maximum at the wavelength $\lambda_{\mathrm{SHG}} = 680$ nm, which is in resonance with the A-exciton, then the corresponding fundamental wavelength is $\lambda_{\mathrm{FW}} = 1360$ nm. Near the narrow band of the exciton, a slight change in fundamental wavelengths can bring a remarkable variation in the nonlinear response of the monolayer MoS_2.

Here, the nonlinear susceptibility will be calculated for this A-exciton band energy. The phase mismatch plays an important role and strongly affects the generated SH power. Hence, only the modes in the phase matching can be observed and contributed to the SHG process. The phase matching is only satisfied within a certain length of the crystal, and the modes need to fulfill the condition: $\Delta n_{jk} = \left|n_k^{\mathrm{FW}} - n_j^{\mathrm{SH}}\right| < \lambda_0/(\pi L_c)$, where $L_c \approx 7$ µm is the mean length of the monolayer MoS2, and λ_0 is the excitation wavelength. It results in $\Delta n < 0.03$. In the experiment, the input polarization was mostly kept horizontally, thus, the k-index might be negligible. From Figure 7.15b and Figure 7.16b-d, the FMs at the FWs phase match only with high-order SH modes, so the HOMs at SH wavelengths will be included in the calculation.

The nonlinear conversion efficiency for a TMD crystal oriented with its symmetry direction across the fiber, from FW mode k^{th} to SH mode j^{th} is defined as [205]

$$\eta_{jk} = \frac{8\pi^2}{\epsilon_0 c \lambda_0^2 n^{\mathrm{FW}^2} \, n_j^{\mathrm{SH}}} \frac{\xi_{jk}^2}{A_{jk}} d_{\mathrm{eff}}^2, \tag{7.23}$$

where ϵ_0 is the vacuum permittivity, c is the speed of light, n^{FW} and n_j^{SH} are the effective refractive indices of the fundamental mode at λ_0 and the high-order mode at the second harmonic, respectively. d_{eff} is the effective nonlinear susceptibility tensor component of the nonlinear material, which in the case of a monolayer TMD is $d_{\mathrm{eff}} = \frac{1}{2}\chi_{xxx}^{(2)}$. ξ_{jk} is the field overlap, and A_{jk} is the effective mode area. The nonlinear response is completely excited by the in-plane component of the electric field to the monolayer surface. In TMD-coated fiber, the tensorial x-direction is not only in-plane with the chosen monolayer's surface but also perpendicular to the propagation z-direction displayed in Figure 7.11a.

To determine the d_{eff} value in Equation 7.23, some parameters, such as the phase matching coefficient $(\sin\delta/\delta)^2$, and the mode overlap coefficient ξ^2/A_{eff}, have been numerically calculated for HOMs at $\lambda_{\mathrm{SHG}} = 680$ nm corresponding to $\lambda_{\mathrm{FW}} = 1360$ nm. The mode conversion efficiency η/d_{eff}^2 is used as an indicator to determine which mode has the most contribution to the observed SHG. The SHG process is supported by the intermodal phase matching between the FMs at FW and the HOMs at SH, so all the HOMs which are in the matching region will be calculated for phase matching coefficient $(\sin\delta/\delta)^2$. Figure 7.17a displays the calculated phase matching coefficient for different HOMs at 680 nm. The black dotted line indicates the effective mode index of the FW in correlation with effective mode indices of HOMs. Figure 7.17b exhibits the mode overlap coefficient ξ^2/A_{eff}, and Figure 7.17c presents the mode conversion efficiency η/d_{eff}^2. To

calculate the effective nonlinear susceptibility, we used the mode M1 because this mode has the highest potential contribution to generated SH.

Remarkably, Equation 7.23 shows that the conversion efficiency η is controlled by two main components, the first is the field overlap ξ_{jk}, which measures the spatial mode overlap factor between the driven FW and SH modes in the interaction area and is expressed by [205]

$$\xi_{jk} = \frac{\iint_{\text{TMD}}\left(\boldsymbol{E}^*_{\text{FW},k} \cdot \boldsymbol{e}_{||}(x)\right)^2 \left(\boldsymbol{E}_{\text{SH},j} \cdot \boldsymbol{e}_{||}(x)\right) dxdy}{\left|\iint_{\text{TMD}}\left|\boldsymbol{E}_{\text{FW},k}\right|^2 \boldsymbol{E}_{\text{FW},k} dxdy\right|^{\frac{2}{3}} \left|\iint_{\text{TMD}}\left|\boldsymbol{E}_{\text{SH},j}\right|^2 \boldsymbol{E}_{\text{SH},j} dxdy\right|^{\frac{1}{3}}}, \tag{7.24}$$

where $\boldsymbol{E}_{\text{FW},k}$ and $\boldsymbol{E}_{\text{SH},j}$ are the vectorial electric fields of the kth FW mode and j^{th} SH mode, respectively; $\boldsymbol{e}_{||}(x)$ is the in-plane unit vector. The integral is performed over the region, where the 2D material is located. Depending on the spatial pattern of the specific mode, the spatial mode overlap has a typical value between $10^{-2} < \xi_{jk} < 1$ and thus does not strongly affect the overall SHG efficiency. This small spatial mode overlap is due to the trivial fraction of energy located in TMD and the infinitesimal thickness.

The second component is the effective mode area, given by [205]: $A_{jk} = \left(A^2_{\text{FW},k} A_{\text{SH},j}\right)^{\frac{1}{3}}$

$$A_{\text{FW},k} = \frac{\left(\iint_{A\infty}\left|\boldsymbol{E}_{\text{FW},k}\right|^2 dxdy\right)^3}{\left|\iint_{\text{TMD}}\left|\boldsymbol{E}_{\text{FW},k}\right|^2 \boldsymbol{E}_{\text{FW},k} dxdy\right|^2} \tag{7.25}$$

$$A_{\text{SH},j} = \frac{\left(\iint_{A\infty}\left|\boldsymbol{E}_{\text{SH},j}\right|^2 dxdy\right)^3}{\left|\iint_{\text{TMD}}\left|\boldsymbol{E}_{\text{SH},j}\right|^2 \boldsymbol{E}_{\text{SH},j} dxdy\right|^2}, \tag{7.26}$$

where $A\infty$ indicates the entire cross-section area of the boundary, whereas the denominator is only integrated over the cross-section defined by the TMD. The effective mode area is, therefore, a large number, much greater than the conventional cross-section area of the mode or the waveguide, due to the significant difference in the integral area. We have to stress that the effective area here is not an actual geometrical area but rather indicates how well the modes are confined within the nonlinear part of the waveguide. The large effective mode area, in this case, shows that the mode is not well confined within the TMD area. That is true because the TMD area is so small compared to the area of the guided mode. Typical values for TMD-coated fiber are in the order of $0.003 \text{ m}^2 < A_{jk} < 0.1 \text{ m}^2$. These values are very large and thus limit the SH efficiency dramatically, as can be seen from Equation 7.23.

Figure 7.17: Parameters of HOMs SHG at $\lambda_{FW} = 1360$ nm, excited by FW with x-polarization. All HOMs were calculated using Comsol v.5.5 with ECF geometry taken from an SEM image. **(a)** The phase matching coefficient for HOMs vs. their respective effective mode index n_{eff}. The effective mode index of FW is marked with a black dotted line. **(b)** Mode overlap coefficient ξ^2/A_{eff}, which is an important factor in the nonlinear conversion efficiency. **(c)** Mode conversion efficiency η/d_{eff}^2 is the ratio of conversion efficiency η of SHG process normalized to effective nonlinear susceptibility of the material d_{eff}. Modes with large values will contribute most to the SH observed in an experiment. **(d-f)** z-component of the Poynting vector of the three modes with the largest mode conversion efficiency. Figure is adapted from [205].

In the case of isolated MoS_2 monolayers on the fiber, the chosen crystal is within the range of the coherent length, so the phase-matching is satisfied ($\Delta kL \approx 0$). Using Equation 7.22 with a known crystal length L and parameters from the lasers, we can determine the overall conversion efficiency of the process η_{jk}. Numerical data such as ξ_{jk} and A_{jk} can be extracted from the FEM-based solver. Finally, using Equation 7.23, the effective nonlinear susceptibility d_{eff} is calculated and $\chi^{(2)} = 2d_{eff}$ is the susceptibility coefficient of the TMD-coating. Because the nonlinear second-order susceptibility is the intrinsic property of the material, it should be the same for all modes. However, the mode overlap coefficient is not identical for all modes. We found three modes marked as M1-M3 in Figure 7.17, which have the strongest overlap coefficients and should have the highest the contribution to SHG. We, therefore, use the overlap coefficient for the (M1) mode at $\lambda_{SH} = 680$ nm and the known parameters from the experiment for the SH and FW powers to find an estimation for d_{eff}, which being $d_{eff} \approx 22$ pm/V and is well within the range of literature values [97, 99, 100, 103, 104, 271, 294]. Using calculated d_{eff} we can get values for $\chi^{(2)} = 2d_{eff} = 44$ pm/V and also for the sheet nonlinearity, assuming a thickness of 0.65 nm, then $\chi^{(2)}_{sheet} \approx 2.9 \times 10^{-20} m^2/V$, which is in good agreement with literature values [97, 103, 116, 294].
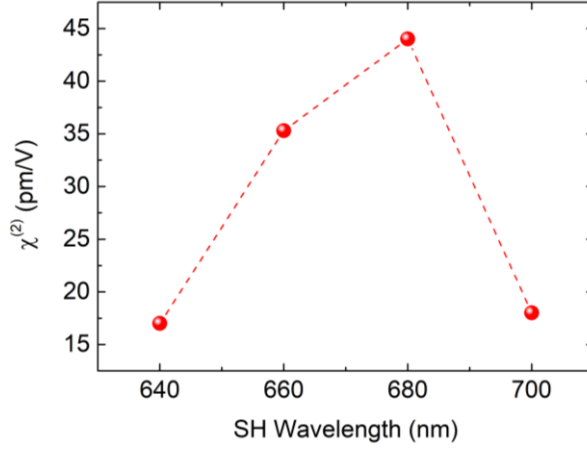
Figure 7.18: Second-order nonlinear susceptibility of the monolayer MoS_2 grown on the ECF for different excitation wavelengths.

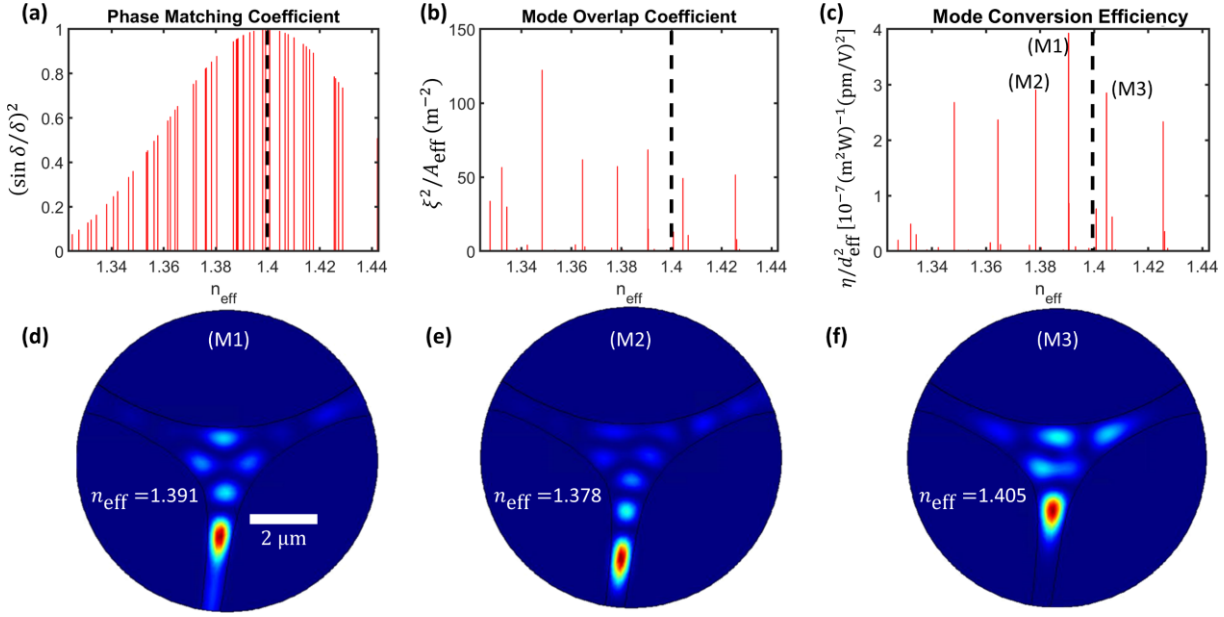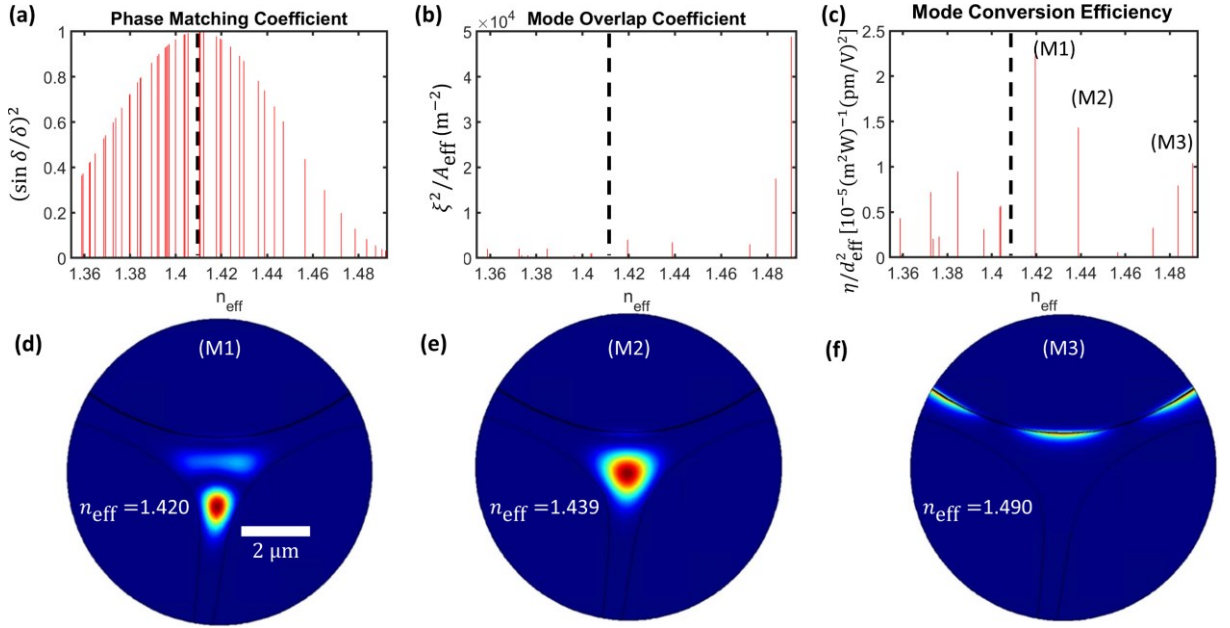**Figure 7.19:** Parameters of HOMs SHG at $\lambda_{FW} = 1360$ nm, excited by FW with x-polarization. All HOMs were calculated using Comsol v.5.5 with ECF geometry taken from an SEM image but with a 25 nm layer of HfO_2 superimposed on the top surface of the ECF. **(a)** The phase matching coefficient for HOMs vs. their respective effective mode index n_{eff}. The effective mode index of FW is marked with a black dotted line. **(b)** Mode overlap coefficient ξ^2/A_{eff}, which is an important factor in the nonlinear conversion efficiency. **(c)** Mode conversion efficiency η/d_{eff}^2 is the ratio of conversion efficiency η of SHG process normalized to effective nonlinear susceptibility of the material d_{eff}. Modes with large values will contribute most to the SH observed in an experiment. **(d-f)** z-component of the Poynting vector of the three modes with the largest mode conversion efficiency. Figure is adapted from [205].

Figure 7.18 displays the calculated $\chi^{(2)}$ value for different second harmonic wavelengths. Analogous to Figure 7.13a, the $\chi^{(2)}$ value gets a maximum at $\lambda_{SH} = 680$ nm, which is expected due to its highest SH power in resonance with A-exciton. This exhibits the efficiency of the TMD material and the ECF geometry for nonlinear application, explores its scalability, and compares it to existing nonlinear waveguides which have been reported. Taking the calculation for $\lambda_{SH} = 680$ nm, we can determine an experimental conversion efficiency of $\eta_{Exp} = 0.2 \times 10^{-3}(m^{-2}W^{-1})$.

By the same process but with the coating of a 25nm layer of HfO$_2$ on top of the monolayer MoS$_2$, we can see the influence of this dielectric coating on the mode overlap coefficient and mode conversion efficiency. The numerical results are depicted in Figure 7.19. The mode conversion efficiency increases nearly 100 times after the coating of HfO$_2$. It can be explained by the shift of the mode towards the monolayer TMD, then increasing the mode overlap coefficient.

The above nonlinear parameters can be used to compare the TMD-coated ECF with two major platforms for nonlinear guided wave, namely LiNbO$_3$ waveguides [293] and poled Germanium-doped glass [295]. More importantly, we found a way to increase the nonlinear conversion efficiency η by increasing the mode overlap factor and decreasing the effective mode area, as presented in Figure 7.19. By coating with a high dielectric thin film, for instance, 25 nm HfO$_2$, we can boost the ratio ξ^2/A_{eff} from 120 (m^{-2}) to 50×10^3 (m^{-2}), then we could achieve a η value in the range of $\eta_{\text{Exp}} \approx 0.1$ (m^{-2}W^{-1}). All nonlinear benchmarked parameters are given in Table 7.1.

Table 7.1: Nonlinear parameters in this work in comparison with other nonlinear platforms.

Parameters	TMD-coated ECF	Hypothetical ECF (25 nm HfO$_2$)	LiNbO$_3$ waveguide [293]	Poled Ge-Glass (bulk only) [295]
$\chi^{(2)}$ (pm/V)	44	44	Type II: 54 Type I: 8.6	1
$\dfrac{\xi^2}{A_{\text{eff}}}$ (m^{-2})	120	50×10^3	N/A	N/A
η (m^{-2}W^{-1})	0.2×10^{-3}	83×10^{-3}	734×10^{-3}	N/A
L (μm)	7	500	8000	N/A
ηL^2 (W^{-1})	9.8×10^{-15}	2.1×10^{-8}	47×10^{-3}	N/A

7.6 Summary of the results

In summary, we have demonstrated second-harmonic generation from exposed optical fibers functionalized with MoS$_2$ monolayers. The scalable CVD-based deposition process can be applied to other fiber architectures and 2D materials. It establishes a highly versatile photonic platform to further investigate the optoelectronic properties of 2D TMDs. While the demonstration was carried out in a non-optimized system, we believe that an oriented growth of highly nonlinear crystals together with the further control of phase matching, mode overlap, and field strengths inside the 2D materials, opens great perspectives for enhanced integrated SHG sources, optical signal processing, or SPDC based photon-pair sources. Additionally, the longer interaction length and

unusual polarization geometry may also help explore excitonic properties, e.g. related to dark excitons in MSe_2-type materials. Moreover, monitoring the tuning of SHG on ECF by stress or strain may also leverage the applicability of fiber-based sensors and active fiber networks.

From the nonlinear conversion efficiency, we find that the TMD-coated ECFs, which we are using here, are not yet ready for use as nonlinear devices. However, the nonlinear susceptibility of our hybrid fiber (44 pm/V) is much larger than that of poled Germanium-doped glass (1 pm/V). From our understanding, it is the highest-reported value for fiber-based second-order nonlinear optics until the published date of our paper. Also, the high nonlinear susceptibility of TMDs can compensate for their trivial mode overlap when compared to other bulk materials such as doped glass.

For application, $LiNbO_3$ waveguides can be a gold standard for light conversion because their conversion efficiency ηL^2 can reach 4.7 % per Watt input for a few millimeters in length. Since TMD is more suitable for the nanophotonic device because it has a minuscule thickness and short length, we should consider the conversion efficiency per unit length η to compare. Assuming the further coating of 25 nm HfO_2, we calculated that the conversion efficiency η of TMD-coated ECFs can be boosted by more than 400-folds and can reach $83 \times 10^{-3} \text{m}^{-2} \text{W}^{-1}$, which is approaching the value of $LiNbO_3$ $\left(734 \times 10^{-3} \text{m}^{-2} \text{W}^{-1}\right)$ as given in Table 7.1. Furthermore, HfO_2 can be a protective layer for as-grown monolayer TMDs, similar to Ga_2O_3 glass, which has been used as an encapsulation for monolayer WS_2 while it retains the monolayer quality [296].

We thus believe that TMD-coated ECFs are a practicable platform for nonlinear fiber optics if the length of the nonlinear crystals can be increased and/or if the mode overlap can be engineered. Furthermore, there is a 3R phase of TMDs in which SHG is proportional to the thickness, and they have intrinsic broken symmetry for each layer [277]. Hence such crystals can increase the mode overlap and nonlinear conversion efficiency if a multilayer of 3R phase can be grown on ECF. For example, from our calculation, a 10 nm-thick 3R MoS_2 deposited on ECF will boost the mode overlap coefficient ξ^2/A_{eff} to 17×10^4 (m^{-2}), which is nearly 4 times larger than the case of 25nm HfO_2 coating and more than 10^3 times higher than the case of monolayer TMD. Besides, the fiber can be designed to get better mode matching and phase matching, then contribute to the enhancement of nonlinear conversion efficiency. Given that fiber design and TMD growth are active areas of research, and there are no fundamental limits for the development here, we expect that TMD-coated ECFs may become a backbone for nonlinear fiber optics in the future.

8. Conclusion & Outlook

In this thesis, different proofs-of-concept from TMD-coated ECFs have been demonstrated, and many optical properties of monolayer TMDs are discussed. These findings contribute to the development of nonlinear optics, fiber-based sensing, fiber-based optoelectronics, and quantum light sources. In this chapter, we shall summarize the results that have been obtained in this thesis and discuss the ongoing directions of this topic, which can be developed from the given ideas or results hereinbefore.

First of all, the successful growth of high-quality monolayer TMDs on ECFs has been demonstrated via reliable techniques, including optical microscope, PL, AFM, and Raman. It confirms that TMDs can grow conformally on the curved surface of optical fiber and adhere to silica only by a weak van der Waals force. The high temperature during the fabrication of all-silica ECFs make them suitable for a CVD process, which requires materials with good heat resistance up to 800 $^\circ$C. By adjusting the flow rate of precursors as well as the position of ECFs in the reaction zone, the crystal size and density can be partially controlled. Although the handling of optical fiber in the reaction zone is not simple, we have found a way to overcome that by fixing the optical fiber on a glass substrate, also made of fused silica. The controllable manner of optical fiber and growth process gives us more freedom to make the whole process scalable and can be applied for mass production.

In the family of microstructured optical fibers, ECFs have been chosen to grow atomically thin semiconductors such as TMDs because of their open access to the fiber core. This exposed region supports the direct growth of monolayer TMDs on the fiber core, and it also provides a way to tailor the properties of this hybrid system, for instance, by a dielectric coating. The initial idea of using ECF was for fluorescence-based sensing in the real-time domain because any photon emitters, i.e., drop-casting quantum dots on the exposed core, and the target gas can interact instantly with the photon emitters via open access. The specific design of ECF has triggered the idea of functionalizing the fiber core with 2D materials. Even though the ECFs used in this thesis are not designed intentionally for embedding with 2D materials, the obtained results demonstrated that they are an excellent platform to grow and characterize the fascinating properties of such crystals. In principle, we can actively design the geometry of optical fibers to support the growth of larger crystal sizes and to control the mode matching and phase matching effectively with low-order modes.

In terms of PL and exciton excitation, monolayer TMDs have high quantum yield thanks to the direct bandgap compared to its bulk counterpart. With TMD-coated ECFs, we can examine the excitonic nature of monolayers by transmission spectroscopy through the fiber modes. The

observation of exciton species via the transmission and PL through the functionalized ECFs shows the potential of this platform to characterize excitons from 2D materials. There is no benefit from TMD multilayer in this case due to the nature of the indirect bandgap, hence lowering the quantum yield of PL. Any approach to increasing the PL efficiency is highly desired, for instance, by patterned growth of TMD [193] to increase the filling factor on optical fibers or by increasing the mode overlap with as-grown monolayers. In the latter case, we have shown an increase in the power fraction in the monolayer MoS_2 (see Figure 5.6b) with the coating of a 25nm-HfO_2 film. This encapsulation results in the significant enhancement of light-matter interaction from several times to tens of times depending on the excitation frequencies. There is no restriction to HfO_2 in this approach, and any high refractive index film (TiO_2, Ga_2O_3 or Ta_2O_5, etc) is also applicable.

Exciton-based sensing has demonstrated its potential to detect toxic gas such as NH_3 in Chapter 5. From DFT calculation, many other gases such as NO_2, NO, SO_2, and CO can also be detectable by monitoring the dynamics of exciton in 2D materials. Our functionalized ECF can support the examination of excitons via transmission spectroscopy, then in principle, can be an alternative to detect the gases beside PL. The enhancement of light-matter interaction in the previous discussion will boost the relative sensitivity of our ECF and leverage the applicability of this platform in remote sensing. In my opinion, ECFs are an ideal platform to grow 2D materials by different methods, such as liquid precursors or MOCVD, which can boost further the filling factor of one-atom-thick photoemitters. The scalability of ECF might be helpful for distributed gas sensing over long distances and in harsh areas where an electronic sensor is unsuitable.

ECFs also support the growth of any phase of TMD, and 3R-MoS_2 multilayers have shown their high potential in nonlinear optics due to their natural non-centrosymmetry. Xu *et al.* have demonstrated that the nonlinear optical enhancement of such multilayers is four orders of magnitude stronger than monolayer MoS_2 and the nonlinear conversion efficiency of SHG is comparable to $LiNbO_3$ but with a much shorter interaction length [297]. If this multilayer can be grown on the optical fiber or waveguide by a scalable method, the future of $\chi^{(2)}$-based nanophotonic devices is within reach. Note that the conversion efficiency is proportional to the square of the interaction length, then a 100 nm thick multilayer can increase the conversion efficiency theoretically by four orders of magnitude if the phase matching is maintained.

Thanks to the intermodal phase matching, our ECF with the nature of multimode supports the phase match between FMs at FWs and HOMs at TH frequencies. The fiber itself also has a significant $\chi^{(3)}$ value which can emit TH, and this can be observed by the naked eye. The growth of highly nonlinear monolayer TMDs indeed enhances the THG process and has been demonstrated in

Chapter 6. Since THG is independent of the symmetry of the crystals, odd-numbered layers can generate TH, therefore, a thick multilayer might give stronger THG than an ultrathin monolayer due to more light-matter interaction [99]. Furthermore, the coatings of a dielectric thin film, for example, 25 nm HfO_2, may further increase the nonlinear γ coefficient of the monolayer MoS_2 ten times at 1550 nm. This enhancement is ascribed to the increase in mode overlap and light-matter interaction.

To sum up, this thesis contributed to the field of photonics and material science by introducing a hybrid platform having a large potential for applications. The combination of nano semiconductors and microstructured optical fiber has brought the best of each constituent together. The findings in this thesis can apply to numerous types of waveguides and 2D materials; thus, the potential of this hybrid platform is not limited to what has been shown here. The special architecture of ECF allows us to drop cast any SPEs, such as hBN, to make a new single-photon source. Besides, the defects in as-grown TMD crystals might be interesting to enable a single quantum source based on ECF. This fiber also can be used to investigate the dark excitons in TMDs by the excitation of the out-of-plane electric field. With the success of turning ECF into an efficient nonlinear medium; other nonlinear phenomena, for instance, SPDC or SCG [298, 299], might be studied shortly.

9. Zusammenfassung

In dieser Arbeit wurden verschiedene Proofs-of-Concept von TMD-beschichteten ECF demonstriert, und viele optische Eigenschaften von Monolayer-TMDs wurden diskutiert. Diese Erkenntnisse tragen zur Entwicklung von nichtlinearer Optik, faserbasierter Sensorik, faserbasierter Optoelektronik und Quantenlichtquellen bei. In diesem Kapitel fassen wir die in dieser Arbeit erzielten Ergebnisse zusammen und erörtern die weiteren Richtungen dieses Themas, die sich aus den hier dargelegten Ideen und Ergebnissen entwickeln lassen.

Zunächst wurde das erfolgreiche Wachstum von qualitativ hochwertigen einlagigen TMDs auf ECFs mit zuverlässigen Techniken, einschließlich Lichtmikroskop, PL, AFM und Raman, nachgewiesen. Es bestätigt, dass TMDs konform auf der gekrümmten Oberfläche der optischen Faser wachsen können und nur durch eine schwache Van-der-Waals-Kraft an Siliziumdioxid haften. Aufgrund der hohen Temperatur bei der Herstellung von ECFs aus reinem Siliziumdioxid eignen sie sich für ein CVD-Verfahren, das Materialien mit einer guten Hitzebeständigkeit bis 800 °C erfordert. Durch Anpassung der Durchflussrate der Rohmaterialien sowie der Position der ECFs in der Reaktionszone können die Kristallgröße und -dichte teilweise gesteuert werden. Obwohl die Handhabung der optischen Faser in der Reaktionszone anspruchsvoll ist, haben wir einen Weg gefunden, dies zu überwinden, indem wir die optische Faser auf einem Glassubstrat, ebenfalls aus Quarzglas, befestigen. Die kontrollierbare Art der optischen Faser und des Wachstumsprozesses gibt uns mehr Freiheit, den gesamten Prozess skalierbar zu machen und für die Massenproduktion zu nutzen.

In der Familie der mikrostrukturierten optischen Fasern wurden ECFs ausgewählt, um atomar dünne Halbleiter wie TMDs wachsen zu lassen, weil sie einen offenen Zugang zum Faserkern haben. Dieser freiliegende Bereich unterstützt das direkt Wachstum von Monolayer-TMDs auf dem Faserkern und bietet außerdem die Möglichkeit, die Eigenschaften dieses Hybridsystems anzupassen, z. B. durch eine dielektrische Beschichtung. Die ursprüngliche Idee, die ECF zu verwenden war die fluoreszenzbasierte Sensorik im Echtzeitbereich, da beliebige Photonenemitter, d. h. Drop-Casting-Quantenpunkte auf dem exponierten Kern, und das Zielgas über einen offenen Zugang sofort mit den Photonenemittern interagieren können. Das spezifische Design der ECF war Grunlage für die Idee der Funktionalisierung des Faserkerns mit 2D-Materialien. Obwohl die in dieser Arbeit verwendeten ECFs nicht absichtlich für die Einbettung von 2D-Materialien entworfen wurden, haben die erzielten Ergebnisse gezeigt, dass sie eine geeignet Plattform für die Züchtung und Charakterisierung der faszinierenden Eigenschaften solcher Kristalle sind. Im Prinzip können wir die Geometrie der optischen Fasern aktiv gestalten, um das Wachstum größerer Kristallgrößen

zu unterstützen und die Modenanpassung und Phasenanpassung mit Moden niedriger Ordnung effektiv zu steuern.

In Bezug auf PL und Exzitonenanregung haben Monolage-TMDs dank der direkten Bandlücke eine hohe Quantenausbeute im Vergleich zu ihrem Volumenkristall-Gegenstück. Mit TMD-beschichteten ECF können wir die exzitonische Natur von Monoschichten durch Transmissionsspektroskopie durch die Fasermoden untersuchen. Die Beobachtung von verschiedener Arten von Exzitonen mittels Transmission und PL durch die funktionalisierten ECFs zeigt das Potenzial dieser Plattform zur Charakterisierung von Exzitonen aus 2D-Materialien. TMD-Multischichten sind in diesem Fall aufgrund der indirekten Bandlücke nicht von Vorteil, wodach die Quantenausbeute der PL sinkt. Es ist möglich die Effizienz der PL z. B. durch strukturiertes Wachstum von TMD [193] zur Erhöhung des Füllfaktors auf optischen Fasern oder durch Erhöhung der Modenüberlappung mit gewachsenen Monoschichten zu steigern. Im letzteren Fall haben wir einen Anstieg des Leistungsanteils in der Monolage MoS_2 (siehe Abbildung 5.6b) mit der Beschichtung eines 25nm-HfO_2-Films gezeigt. Dies führt zu einer signifikanten Verbesserung der Licht-Materie-Wechselwirkung, die sich je nach Anregungsfrequenz um das Mehrfache bis Zehnfache erhöht. Bei diesem Ansatz gibt es keine Beschränkung auf HfO_2, und jede Schicht mit hohem Brechungsindex (TiO_2, Ga_2O_3 oder Ta_2O_5 usw.) ist ebenfalls anwendbar.

Die auf Exzitonen basierende Sensorik hat in Kapitel 5 ihr Potenzial zum Nachweis toxischer Gasen wie NH_3 unter Beweis gestellt. Aus DFT-Berechnungen geht hervor, dass auch viele andere Gase wie NO_2, NO, SO_2 und CO durch Überwachung der Exzitonendynamik in 2D-Materialien nachgewiesen werden können. Unser funktionalisiertes ECF kann die Untersuchung von Exzitonen durch Transmissionsspektroskopie unterstützen und kann somit eine Alternative zum Nachweis von Gasen neben PL sein. Die Verbesserung der Licht-Materie-Wechselwirkung in der vorangegangenen Diskussion wird die relative Empfindlichkeit unserer ECF erhöhen und die Anwendbarkeit dieser Plattform in der Fernerkundung vorantreiben. ECFs sind demzufolge eine ideale Plattform, um 2D-Materialien mit verschiedenen Methoden zu züchten, z. B. mit flüssigen Precursor oder MOCVD, was den Füllfaktor von ein Atom dicken Photoemittern weiter erhöhen kann. Die Skalierbarkeit von ECF könnte für die verteilte Gassensorik über große Entfernungen und in harsche Umgebung, in denen ein elektronischer Sensor ungeeignet ist ermöglichen.

ECFs unterstützen auch das Wachstum jeder TMD-Phase, und 3R-MoS_2-Multischichten haben aufgrund ihrer natürlichen Nicht-Zentrosymmetrie ihr großes Potenzial für die nichtlineare Optik gezeigt. Xu *et al.* haben gezeigt, dass die nichtlineare optische Verstärkung solcher Multischichten um vier Größenordnungen stärker ist als die von MoS_2-Monoschichten und dass die nichtlineare Umwandlungseffizienz von SHG mit der von $LiNbO_3$ vergleichbar ist, allerdings mit einer viel

kürzeren Wechselwirkungslänge [297]. Wenn diese Multischicht mit einer skalierbaren Methode auf einer optischen Faser oder einem Wellenleiter gezüchtet werden kann, ist die Zukunft von nanophotonischen Geräten auf $\chi^{(2)}$-Basis in Reichweite. Da die Umwandlungseffizienz proportional zum Quadrat der Wechselwirkungslänge ist, kann eine 100 nm dicke Multischicht die Umwandlungseffizienz theoretisch um vier Größenordnungen erhöhen, wenn die Phasenanpassung beibehalten wird.

Dank der intermodalen Phasenanpassung unterstützt unsere ECF mit ihrer Multimode-Eigenschaft die Phasenanpassung zwischen FMs bei FWs und HOMs bei TH-Frequenzen. Die Faser selbst hat auch einen signifikanten $\chi^{(3)}$ Wert, der TH emittieren kann, was mit bloßem Auge beobachtet werden kann. Das Wachstum hochgradig nichtlinearer TMD-Monoschichten verstärkt tatsächlich den THG-Prozess und wurde in Kapitel 6 nachgewiesen. Da THG unabhängig von der Symmetrie der Kristalle ist, können auch ungerade Schichten TH erzeugen, so dass eine dicke Multischicht aufgrund der stärkeren Licht-Materie-Wechselwirkung zu stärkerem THG führen kann als eine ultradünne Monoschicht [99]. Darüber hinaus kann die Beschichtung mit einer dielektrischen Dünnschicht, z. B. 25 nm HfO_2, den nichtlinearen γ-Koeffizienten der Monolage MoS_2 bei 1550 nm um das Zehnfache erhöhen. Diese Verbesserung wird auf die Zunahme der Modenüberlappung und der Licht-Materie-Wechselwirkung zurückgeführt.

Zusammenfassend lässt sich sagen, dass diese Arbeit einen Beitrag zum Gebiet der Photonik und der Materialwissenschaften geleistet hat, indem sie eine hybride Plattform vorstellte, die ein großes Anwendungspotenzial hat. Die Kombination von Nanohalbleitern und mikrostrukturierten optischen Fasern hat das Beste von jedem Bestandteil zusammengebracht. Die in dieser Arbeit gewonnenen Erkenntnisse lassen sich auf zahlreiche Arten von Wellenleitern und 2D-Materialien anwenden; das Potenzial dieser hybriden Plattform ist also nicht auf das hier Gezeigte beschränkt. Die besondere Architektur der ECF ermöglicht es uns, beliebige SPEs, wie z. B. hBN, zu drop casten, um eine neue Einzelphotonenquelle herzustellen. Außerdem könnten die Defekte in gewachsenen TMD-Kristallen interessant sein, um eine Einzelquantenquelle auf der Basis der ECF zu ermöglichen. Diese Faser kann auch verwendet werden, um die dunklen Exzitonen in TMDs durch die Anregung des elektrischen Feldes außerhalb der Ebene zu untersuchen. Wenn es gelingt, ECF in ein effizientes nichtlineares Medium zu verwandeln, könnten in Kürze auch andere nichtlineare Phänomene untersucht werden, z. B. SPDC oder SCG [298, 299].

Appendix A: References

1. Novoselov, K. S.; Geim, A. K.; Morozov, S. V.; Jiang, D.; Zhang, Y.; Dubonos, S. V.; Grigorieva, I. V.; Firsov, A. A. Electric field in atomically thin carbon films. *Science* **306**, 666-669 (2004).

2. Lee, C.; Wei, X.; Kysar, J. W.; Hone, J. Measurement of the elastic properties and intrinsic strength of monolayer graphene. *Science* **321**, 385-388 (2008).

3. Bolotin, K. I.; Sikes, K. J.; Jiang, Z.; Klima, M.; Fudenberg, G.; Hone, J.; Kim, P.; Stormer, H. L. Ultrahigh electron mobility in suspended graphene. *Solid State Commun.* **146**, 351-355 (2008).

4. Geim, A. K. Graphene: Status and Prospects. *Science* **324**, 1530-1534 (2009).

5. Neto, A. H. C.; Guinea, F.; Peres, N. M. R.; Novoselov, K. S.; Geim, A. K. The electronic properties of graphene. *Rev. Mod. Phys.* **81**, 109 (2009).

6. Soldano, C.; Mahmood, A.; Dujardin, E. Production, properties and potential of graphene. *Carbon* **48**, 2127-2150 (2010).

7. Mak, K. F.; Lee, C.; Hone, J.; Shan, J.; Heinz, T. F. Atomically thin MoS_2: A new direct-gap semiconductor. *Phys. Rev. Lett.* **105**, 136805 (2010).

8. Splendiani, A.; Sun, L.; Zhang, Y.; Li, T.; Kim, J.; Chim, C. Y.; Galli, G.; Wang, F. Emerging photoluminescence in monolayer MoS_2. *Nano Lett.* **10**, 1271-1275 (2010).

9. Radisavljevic, B.; Radenovic, A.; Brivio, J.; Giacometti, V.; Kis, A. Single-layer MoS_2 transistors. *Nat. Nanotechnol.* **6**, 147-150 (2011).

10. Li, H.; Yin, Z.; He, Q.; Li, H.; Huang, X.; Lu, G.; Fam, D. W. H.; Tok, A. I. Y.; Zhang, Q.; Zhang, H. Layered Nanomaterials: Fabrication of Single- and Multilayer MoS_2 Film-Based Field-Effect Transistors for Sensing NO at Room Temperature. *Small* **8**, 63-67 (2012).

11. Bernardi, M.; Palummo, M.; Grossman, J. C. Extraordinary sunlight absorption and one nanometer thick photovoltaics using two-dimensional monolayer materials. *Nano Lett.* **13**, 3664-3670 (2013).

12. Yang, L.; Deslippe, J.; Park, C. H.; Cohen, M. L.; Louie, S. G. Excitonic effects on the optical response of graphene and bilayer graphene. *Phys. Rev. Lett.* **103**, 186802 (2009).

13. Mak, K. F.; Shan, J. Photonics and optoelectronics of 2D semiconductor transition metal dichalcogenides. *Nat. Photon.* **10**, 216-226 (2016).

14. Liu, G. Bin; Xiao, D.; Yao, Y.; Xu, X.; Yao, W. Electronic structures and theoretical modelling of two-dimensional group-VIB transition metal dichalcogenides. *Chemical Society Reviews* **44**, 2643-2663 (2015).

15. Xia, F.; Wang, H.; Xiao, D.; Dubey, M.; Ramasubramaniam, A. Two-dimensional material nanophotonics. *Nat. Photon.* **8**, 899-907 (2014).

16. Nemes-Incze, P.; Osvath, Z.; Kamaras, K.; Biro, L. P. Anomalies in thickness measurements of graphene and few layer graphite crystals by tapping mode atomic force microscopy. *Carbon* **46**, 1435-1442 (2008).

17. Zhou, X.; Deng, Q.; Yu, W.; Liu, K.; Liu, Z. The Rise of Graphene Photonic Crystal Fibers. *Adv. Funct. Mater.* **32**, 2202282 (2022).

18. Mayorov, A. S.; Gorbachev, R. V.; Morozov, S. V.; Britnell, L.; Jalil, R.; Ponomarenko, L. A.; Blake, P.; Novoselov, K. S.; Watanabe, K.; Taniguchi, T.; Geim, A. K. Micrometer-scale ballistic transport in encapsulated graphene at room temperature. *Nano Lett.* **11**, 2396–2399 (2011).

19. Morozov, S. V.; Novoselov, K. S.; Katsnelson, M. I.; Schedin, F.; Elias, D. C.; Jaszczak, J. A.; Geim, A. K. Giant intrinsic carrier mobilities in graphene and its bilayer. *Phys. Rev. Lett.* **100**, 016602 (2008).

20. Novoselov, K. S.; Fal'Ko, V. I.; Colombo, L.; Gellert, P. R.; Schwab, M. G.; Kim, K. A roadmap for graphene. *Nature* **490**, 192-200 (2012).

21. Novoselov, K. S.; Geim, A. K.; Morozov, S. V.; Jiang, D.; Katsnelson, M. I.; Grigorieva, I. V.; Dubonos, S. V.; Firsov, A. A. Two-dimensional gas of massless Dirac fermions in graphene. *Nature* **438**, 197-200 (2005).

22. Cao, K.; Feng, S.; Han, Y.; Gao, L.; Hue Ly, T.; Xu, Z.; Lu, Y. Elastic straining of free-standing monolayer graphene. *Nat. Commun.* **11**, 284 (2020).

23. Koppens, F. H. L.; Mueller, T.; Avouris, P.; Ferrari, A. C.; Vitiello, M. S.; Polini, M. Photodetectors based on graphene, other two-dimensional materials and hybrid systems. *Nat. Nanotechnol.* **9**, 780-793 (2014).

24. Nair, R. R.; Blake, P.; Grigorenko, A. N.; Novoselov, K. S.; Booth, T. J.; Stauber, T.; Peres, N. M. R.; Geim, A. K. Fine structure constant defines visual transparency of graphene. *Science* **320**, (2008).

25. Liu, M.; Yin, X.; Ulin-Avila, E.; Geng, B.; Zentgraf, T.; Ju, L.; Wang, F.; Zhang, X. A. A graphene-based broadband optical modulator. *Nature* **474**, 64-67 (2011).

26. Phare, C. T.; Lee, Y.-H. D.; Cardenas, J.; Lipson, M. Graphene electro-optic modulator with 30 GHz bandwidth. *Nat. Photon.* **9**, 511-514 (20215).

27. Mueller, T.; Xia, F.; Avouris, P. Graphene photodetectors for high-speed optical communications. *Nat. Photon.* **4**, 297-301 (2010).

28. Gan, X.; Shiue, R. J.; Gao, Y.; Meric, I.; Heinz, T. F.; Shepard, K.; Hone, J.; Assefa, S.; Englund, D. Chip-integrated ultrafast graphene photodetector with high responsivity. *Nat. Photon.* **7**, 883-887 (2013).

29. Nag, A.; Mitra, A.; Mukhopadhyay, A. C. Graphene and its sensor-based applications: A review. *Sens. Actuators A* **270**, 177-194 (2018).

30. Bonaccorso, F.; Sun, Z.; Hasan, T.; Ferrari, A. C. Graphene photonics and optoelectronics. *Nat. Photon.* **4**, 611-622 (2010).

31. Sun, Z.; Martinez, A.; Wang, F. Optical modulators with 2D layered materials. *Nat. Photon.* **10**, 227–238 (2016).

32. Martinez, A.; Sun, Z. Nanotube and graphene saturable absorbers for fibre lasers. *Nat. Photon.* **7**, 842–845 (2013).

33. Kumar, N.; Kumar, J.; Gerstenkorn, C.; Wang, R.; Chiu, H. Y.; Smirl, A. L.; Zhao, H. Third harmonic generation in graphene and few-layer graphite films. *Phys. Rev. B* **87**, 121406 (2013).

34. Gu, T.; Petrone, N.; McMillan, J. F.; Van Der Zande, A.; Yu, M.; Lo, G. Q.; Kwong, D. L.; Hone, J.; Wong, C. W. Regenerative oscillation and four-wave mixing in graphene optoelectronics. *Nat. Photon.* **6**, 554–559 (2012).

35. El-Kady, M. F.; Shao, Y.; Kaner, R. B. Graphene for batteries, supercapacitors and beyond. *Nat. Rev. Mater.* **1**, 16033 (2016).

36. Jiang, T.; Huang, D.; Cheng, J.; Fan, X.; Zhang, Z.; Shan, Y.; Yi, Y.; Dai, Y.; Shi, L.; Liu, K.; Zeng, C.; Zi, J.; Sipe, J. E.; Shen, Y. R.; Liu, W. T.; Wu, S. Gate-tunable third-order nonlinear optical response of massless Dirac fermions in graphene. *Nat. Photon.* **12**, 430-436 (2018).

37. Smith, A. D.; Niklaus, F.; Paussa, A.; Vaziri, S.; Fischer, A. C.; Sterner, M.; Forsberg, F.; Delin, A.; Esseni, D.; Palestri, P.; Östling, M.; Lemme, M. C. Electromechanical piezoresistive sensing in suspended graphene membranes. *Nano Lett.* **13**, 3237-3242 (2013).

38. Romagnoli, M.; Sorianello, V.; Midrio, M.; Koppens, F. H. L.; Huyghebaert, C.; Neumaier, D.; Galli, P.; Templ, W.; D'Errico, A.; Ferrari, A. C. Graphene-based integrated photonics for next-generation datacom and telecom. *Nat. Rev. Mater.* **3**, 392-414 (2018).

39. Gerstner, E. Nobel Prize 2010: Andre Geim & Konstantin Novoselov. *Nat. Phys.* **6**, 836 (2010).

40. Stoller, M. D.; Park, S. J.; Zhu, Y. W.; An, J. H.; Ruoff, R. S. Graphene-based ultracapacitors. *Nano Lett.* **8**, 3498–3502 (2008).

41. Novoselov, K. S.; Jiang, D.; Schedin, F.; Booth, T. J.; Khotkevich, V. V.; Morozov, S. V.; Geim, A. K. Two-dimensional atomic crystals. *Proc. Natl. Acad. Sci. U. S. A.* **102**, 10451-10453 (2005).

42. Gui, G.; Li, J.; Zhong, J. Band structure engineering of graphene by strain: First-principles calculations. *Phys. Rev. B* **78**, 075435 (2008).

43. Wang, Q. H.; Kalantar-Zadeh, K.; Kis, A.; Coleman, J. N.; Strano, M. S. Electronics and optoelectronics of two-dimensional transition metal dichalcogenides. *Nat. Nanotechnol.* **7**, 699-712 (2012).

44. Shrivastava, M.; Ramgopal Rao, V. A Roadmap for Disruptive Applications and Heterogeneous Integration Using Two-Dimensional Materials: State-of-the-Art and Technological Challenges. *Nano Lett.* **21**, 6359-6381 (2021).

45. Choi, W.; Choudhary, N.; Han, G. H.; Park, J.; Akinwande, D.; Lee, Y. H. Recent development of two-dimensional transition metal dichalcogenides and their applications. *Materials Today* **20**, 116-130 (2017).

46. Mounet, N.; Gibertini, M.; Schwaller, P.; Campi, D.; Merkys, A.; Marrazzo, A.; Sohier, T.; Castelli, I. E.; Cepellotti, A.; Pizzi, G.; Marzari, N. Two-dimensional materials from high-throughput computational exfoliation of experimentally known compounds. *Nat. Nanotechnol.* **13**, 246-252 (2018).

47. Withers, F.; Del Pozo-Zamudio, O.; Mishchenko, A.; Rooney, A. P.; Gholinia, A.; Watanabe, K.; Taniguchi, T.; Haigh, S. J.; Geim, A. K.; Tartakovskii, A. I.; Novoselov, K. S. Light-emitting diodes by band-structure engineering in van der Waals heterostructures. *Nat. Mater.* **14**, 301–306 (2015).

48. Furchi, M. M.; Pospischil, A.; Libisch, F.; Burgdörfer, J.; Mueller, T. Photovoltaic effect in an electrically tunable van der Waals heterojunction. *Nano Lett.* **14**, 4785–4791 (2014).

49. Roy, T.; Tosun, M.; Cao, X.; Fang, H.; Lien, D. H.; Zhao, P.; Chen, Y. Z.; Chueh, Y. L.; Guo, J.; Javey, A. Dual-gated MoS_2/WSe_2 van der Waals tunnel diodes and transistors. *ACS Nano* **9**, 2071–2079 (2015).

50. Rivera, P.; Schaibley, J. R.; Jones, A. M.; Ross, J. S.; Wu, S.; Aivazian, G.; Klement, P.; Seyler, K.; Clark, G.; Ghimire, N. J.; Yan, J.; Mandrus, D. G.; Yao, W.; Xu, X. Observation of long-lived interlayer excitons in monolayer $MoSe_2$–WSe_2 heterostructures. *Nat. Commun.* **6**, 6242 (2015).

51. Ares, P.; Novoselov, K. S. Recent advances in graphene and other 2D materials. *Nano Materials Science* **4**, 3-9 (2022).

52. Castellanos-Gomez, A. Why all the fuss about 2D semiconductors?. *Nat. Photon.* **10**, 202–204 (2016).

53. Gao, E.; Lin, S. Z.; Qin, Z.; Buehler, M. J.; Feng, X. Q.; Xu, Z. Mechanical exfoliation of two-dimensional materials. *Journal of the Mechanics and Physics of Solids* **115**, 248-262 (2018).

54. Silly, M. G.; Jaffrennou, P.; Barjon, J.; Lauret, J. S.; Ducastelle, F.; Loiseau, A.; Obraztsova, E.; Attal-Tretout, B.; Rosencher, E. Luminescence properties of hexagonal boron nitride: cathodoluminescence and photoluminescence spectroscopy measurements. *Phys. Rev. B* **75**, 085205 (2007).

55. Dai, S.; Fei, Z.; Ma, Q.; Rodin, A. S.; Wagner, M.; McLeod, A. S.; Liu, M. K.; Gannett, W.; Regan, W.; Watanabe, K.; Taniguchi, T.; Thiemens, M.; Dominguez, G.; Castro Neto, A. H.; Zettl, A.; Keilmann, F.; Jarillo-Herrero, P.; Fogler, M. M.; Basov, D. N. Tunable phonon polaritons in atomically thin van der Waals crystals of boron nitride. *Science* **343**, 1125–1129 (2014).

56. Museur, L.; Feldbach, E.; Kanaev, A. Defect-related photoluminescence of hexagonal boron nitride. *Phys. Rev. B* **78**, 155204 (2008).

57. Li, L.; Yu, Y.; Ye, G. J.; Ge, Q.; Ou, X.; Wu, H.; Feng, D.; Chen, X. H.; Zhang, Y. Black phosphorus field-effect transistors. *Nat. Nanotechnol.* **9**, 372–377 (2014).

58. Liu, H.; Neal, A. T.; Zhu, Z.; Luo, Z.; Xu, X.; Tománek, D.; Ye, P. D. Phosphorene: an unexplored 2D semiconductor with a high hole mobility. *ACS Nano* **8**, 4033-4041 (2014).

59. Castellanos-Gomez, A.; Vicarelli, L.; Prada, E.; Island, J. O.; Narasimha-Acharya, K. L.; Blanter, S. I.; Groenendijk, D. J.; Buscema, M.; Steele, G. A.; Alvarez, J. V.; Zandbergen, H. W.; Palacios, J. J.; Van Der Zant, H. S. J. Isolation and characterization of few-layer black phosphorus. *2D Mater.* **1**, 025001 (2014).

60. Abate, Y.; Akinwande, D.; Gamage, S.; Wang, H.; Snure, M.; Poudel, N.; Cronin, S. B. Recent progress on stability and passivation of black phosphorus. *Adv. Mater.* **30**, 1704749 (2018).

61. Cassabois, G.; Valvin, P.; Gil, B. Hexagonal boron nitride is an indirect bandgap semiconductor. *Nat. Photon.* **10**, 262–266 (2016).

62. Laturia, A.; Van de Put, M.L.; Vandenberghe, W.G. Dielectric properties of hexagonal boron nitride and transition metal dichalcogenides: from monolayer to bulk. *npj 2D Mater. Appl.* **2**, 6 (2018).

63. Dean, C. R.; Young, A. F.; Meric, I.; Lee, C.; Wang, L.; Sorgenfrei, S.; Watanabe, K.; Taniguchi, T.; Kim, P.; Shepard, K. L.; Hone, J. Boron nitride substrates for high-quality graphene electronics. *Nat. Nanotechnol.* **5**, 722–726 (2010).

64. Aharonovich, I.; Englund, D.; Toth, M. Solid-state single-photon emitters. *Nat. Photon.* **10**, 631-641 (2016).

65. Tran, T. T.; Bray, K.; Ford, M. J.; Toth, M.; Aharonovich, I. Quantum emission from hexagonal boron nitride monolayers. *Nat. Nanotechnol.* **11**, 37–41 (2016).

66. Klimmer, S.; Ghaebi, O.; Gan, Z.; George, A.; Turchanin, A.; Cerullo, G.; Soavi, G. All-optical polarization and amplitude modulation of second-harmonic generation in atomically thin semiconductors. *Nat. Photon.* **15**, 837–842 (2021).

67. Ramasubramaniam, A. Large excitonic effects in monolayers of molybdenum and tungsten dichalcogenides. *Phys. Rev. B* **86**, 115409 (2012).

68. Chernikov, A.; Berkelbach, T. C.; Hill, H. M.; Rigosi, A.; Li, Y.; Aslan, O. B.; Reichman, D. R.; Hybertsen, M. S.; Heinz, T. F. Exciton binding energy and nonhydrogenic Rydberg series in monolayer WS_2. *Phys. Rev. Lett.* **113**, (2014).

69. He, K.; Kumar, N.; Zhao, L.; Wang, Z.; Mak, K. F.; Zhao, H.; Shan, J. Tightly bound excitons in monolayer WSe_2. *Phys. Rev. Lett.* **113**, 026803 (2014).

70. Li, Y.; Chernikov, A.; Zhang, X.; Rigosi, A.; Hill, H. M.; Van Der Zande, A. M.; Chenet, D. A.; Shih, E. M.; Hone, J.; Heinz, T. F. Measurement of the optical dielectric function of monolayer transition-metal dichalcogenides: MoS_2, $MoSe_2$, WS_2, and WSe_2. *Phys. Rev. B* **90**, 205422 (2014).

71. Cho, B.; Kim, A. R.; Park, Y.; Yoon, J.; Lee, Y. J.; Lee, S.; Yoo, T. J.; Kang, C. G.; Lee, B. H.; Ko, H. C.; Kim, D. H.; Hahm, M. G. Bifunctional sensing characteristics of chemical vapor deposition synthesized atomic-layered MoS_2. *ACS Appl. Mater. Interfaces* **7**, 2952-2959 (2015).

72. Lee, K.; Gatensby, R.; McEvoy, N.; Hallam, T.; Duesberg, G. S. High-performance sensors based on molybdenum disulfide thin films. *Adv. Mater.* **25**, 6699-6702 (2013).

73. Järvinen, T.; Lorite, G. S.; Per ntie, J.; Toth, G.; Saarakkala, S.; Virtanen, V. K.; Kordas, K. WS_2 and MoS_2 thin film gas sensors with high response to NH_3 in air at low temperature. *Nanotechnology* **30**, 405501 (2019).

74. Lopez-Sanchez, O.; Lembke, D.; Kayci, M.; Radenovic, A.; Kis, A. Ultrasensitive photodetectors based on monolayer MoS_2. *Nat. Nanotechnol.* **8**, 497–501 (2013).

75. Seo, J.; Lee, J. H.; Pak, J.; Cho, K.; Kim, J. K.; Kim, J.; Jang, J.; Ahn, H.; Lim, S. C.; Chung, S.; Kang, K.; Lee, T. Ultrasensitive Photodetection in MoS_2 Avalanche Phototransistors. *Adv. Sci.* **8**, 2102437 (2021).

76. Wu, S.; Buckley, S.; Schaibley, J. R.; Feng, L.; Yan, J.; Mandrus, D. G.; Hatami, F.; Yao, W.; Vučković, J.; Majumdar, A.; Xu, X. Monolayer semiconductor nanocavity lasers with ultralow thresholds. *Nature* **520**, 69-72 (2015).

77. Yu, J. X.; Xing, S.; Dai, G. Y.; Ling-Hu, S. Y.; Gu, F. X. Direct-Bandgap Bilayer WSe2/Microsphere Monolithic Cavity for Low-Threshold Lasing. *Adv. Mater.* **34**, 2106502 (2022).

78. Mak, K. F.; He, K.; Shan, J.; Heinz, T. F. Control of valley polarization in monolayer MoS2 by optical helicity. *Nat. Nanotechnol.* **7**, 494-498 (2012).

79. Mak, K. F.; McGill, K. L.; Park, J.; McEuen, P. L. The valley hall effect in MoS2 transistors. *Science* **344**, 1489-1492 (2014).

80. Yang, L.; Sinitsyn, N. A.; Chen, W.; Yuan, J.; Zhang, J.; Lou, J.; Crooker, S. A. Long-lived nanosecond spin relaxation and spin coherence of electrons in monolayer MoS2 and WS2. *Nat. Phys.* **11**, 830-834 (2015).

81. Hsu, W. T.; Chen, Y. L.; Chen, C. H.; Liu, P. S.; Hou, T. H.; Li, L. J.; Chang, W. H. Optically initialized robust valley-polarized holes in monolayer WSe2. *Nat. Commun.* **6**, 8963 (2015).

82. Mak, K. F.; Xiao, D.; Shan, J. Light–valley interactions in 2D semiconductors. *Nat. Photon.* **12**, 451-460 (2018).

83. Cao, T.; Wang, G.; Han, W.; Ye, H.; Zhu, C.; Shi, J.; Niu, Q.; Tan, P.; Wang, E.; Liu, B.; Feng, J. Valley-selective circular dichroism of monolayer molybdenum disulphide. *Nat. Commun.* **3**, 887 (2012).

84. Sallen, G.; Bouet, L.; Marie, X.; Wang, G.; Zhu, C. R.; Han, W. P.; Lu, Y.; Tan, P. H.; Amand, T.; Liu, B. L.; Urbaszek, B. Robust optical emission polarization in MoS2 monolayers through selective valley excitation. *Phys. Rev. B* **86**, 081301 (2012).

85. Xiao, D.; Liu, G.-B.; Feng, W.; Xu, X.; Yao, W. Coupled spin and valley physics in monolayers of MoS2 and other group-VI dichalcogenides. *Phys. Rev. Lett.* **108**, 196802 (2012).

86. Chakraborty, C.; Kinnischtzke, L.; Goodfellow, K. M.; Beams, R.; Vamivakas, A. N. Voltage-controlled quantum light from an atomically thin semiconductor. *Nat. Nanotechnol.* **10**, 507-511 (2015).

87. He, Y. M.; Clark, G.; Schaibley, J. R.; He, Y.; Chen, M. C.; Wei, Y. J.; Ding, X.; Zhang, Q.; Yao, W.; Xu, X.; Lu, C. Y.; Pan, J. W. Single quantum emitters in monolayer semiconductors. *Nat. Nanotechnol.* **10**, 497-502 (2015).

88. Koperski, M.; Nogajewski, K.; Arora, A.; Cherkez, V.; Mallet, P.; Veuillen, J. Y.; Marcus, J.; Kossacki, P.; Potemski, M. Single photon emitters in exfoliated WSe2 structures. *Nat. Nanotechnol.* **10**, 503-506 (2015).

89. Srivastava, A.; Sidler, M.; Allain, A. V.; Lembke, D. S.; Kis, A.; Imamoglu, A. Optically active quantum dots in monolayer WSe2. *Nat. Nanotechnol.* **10**, 491-496 (2015).

90. Tonndorf, P.; Schmidt, R.; Schneider, R.; Kern, J.; Buscema, M.; Steele, G. A.; Castellanos-Gomez, A.; van der Zant, H. S. J.; Michaelis de Vasconcellos, S.; Bratschitsch, R. Single-photon emission from localized excitons in an atomically thin semiconductor. *Optica* **2**, 347-352 (2015).

91. Yang, S.; Jiang, C.; Wei, S. H. Gas sensing in 2D materials. *Applied Physics Reviews* **4**, 021304 (2017).

92. Liu, X.; Ma, T.; Pinna, N.; Zhang, J. Two-Dimensional Nanostructured Materials for Gas Sensing. *Adv. Funct. Mater.* **27**, 1702168 (2017).

93. Donarelli, M.; Ottaviano, L. 2D materials for gas sensing applications: A review on graphene oxide, MoS_2, WS_2 and phosphorene. *Sensors* **18**, 3638 (2018).

94. Jiang, F.; Zhao, W. S.; Zhang, J. Mini-review: Recent progress in the development of $MoSe_2$ based chemical sensors and biosensors. *Microelectronic Engineering* **225**, 111279 (2020).

95. Zhao, S.; Xue, J.; Kang, W. Gas adsorption on MoS_2 monolayer from first-principles calculations. *Chem. Phys. Lett.* **595**, 35-42 (2014).

96. Nayeri, M.; Moradinasab, M.; Fathipour, M. The transport and optical sensing properties of MoS_2, $MoSe_2$, WS_2 and WSe_2 semiconducting transition metal dichalcogenides. *Semicond. Sci. Technol.* **33**, 025002 (2018).

97. Malard, L. M.; Alencar, T. V.; Barboza, A. P. M.; Mak, K. F.; De Paula, A. M. Observation of intense second harmonic generation from MoS_2 atomic crystals. *Phys. Rev. B* **87**, 201401 (2013).

98. Autere, A.; Jussila, H.; Dai, Y.; Wang, Y.; Lipsanen, H.; Sun, Z. Nonlinear Optics with 2D Layered Materials. *Adv. Mater.* **30**, 1705963 (2018).

99. Säynätjoki, A.; Karvonen, L.; Rostami, H.; Autere, A.; Mehravar, S.; Lombardo, A.; Norwood, R. A.; Hasan, T.; Peyghambarian, N.; Lipsanen, H.; Kieu, K.; Ferrari, A. C.; Polini, M.; Sun, Z. Ultra-strong nonlinear optical processes and trigonal warping in MoS_2 layers. *Nat. Commun.* **8**, 893 (2017).

100. Woodward, R. I.; Murray, R. T.; Phelan, C. F.; De Oliveira, R. E. P.; Runcorn, T. H.; Kelleher, E. J. R.; Li, S.; De Oliveira, E. C.; Fechine, G. J. M.; Eda, G.; De Matos, C. J. S. Characterization of the second- and third-order nonlinear optical susceptibilities of monolayer MoS_2 using multiphoton microscopy. *2D Mater.* **4**, 011006 (2017).

101. Kumar, N.; Najmaei, S.; Cui, Q.; Ceballos, F.; Ajayan, P. M.; Lou, J.; Zhao, H. Second harmonic microscopy of monolayer MoS_2. *Phys. Rev. B* **87**, 161403 (2013).

102. Pike, N. A.; Pachter, R. Second-Order Nonlinear Optical Properties of Monolayer Transition-Metal Dichalcogenides by Computational Analysis. *J. Phys. Chem. C* **125**, 11075-11084 (2021).

103. Autere, A.; Jussila, H.; Marini, A.; Saavedra, J. R. M.; Dai, Y.; Säynätjoki, A.; Karvonen, L.; Yang, H.; Amirsolaimani, B.; Norwood, R. A.; Peyghambarian, N.; Lipsanen, H.; Kieu, K.; De Abajo, F. J. G.; Sun, Z. Optical harmonic generation in monolayer group-VI transition metal dichalcogenides. *Phys. Rev. B* **98**, 115426 (2018).

104. Lafeta, L.; Corradi, A.; Zhang, T.; Kahn, E.; Bilgin, I.; Carvalho, B. R.; Kar, S.; Terrones, M.; Malard, L. M. Second-and third-order optical susceptibilities across excitons states in 2D monolayer transition metal dichalcogenides. *2D Mater.* **8**, 035010 (2021).

105. Li, Y.; Rao, Y.; Mak, K. F.; You, Y.; Wang, S.; Dean, C. R.; Heinz, T. F. Probing symmetry properties of few-layer MoS_2 and h-BN by optical second-harmonic generation. *Nano Lett.* **13**, 3329-3333 (2013).

106. Franken, P. A.; Hill, A. E.; Peters, C. W.; Weinreich, G. Generation of optical harmonics. *Phys. Rev. Lett.* **7**, 118 (1961).

107. Maiman, T. H. Stimulated optical radiation in Ruby. *Nature* **187**, 493-494 (1960).

108. Rosenberg, W. R.; Myers, L. E.; Byer, R. L.; Drobshoff, A.; Alexander, J. I. 93% pump depletion, 3.5-W continuous-wave, singly resonant optical parametric oscillator. *Opt. Lett.* **21**, 1336-1338 (1996).

109. Cerullo, G.; De Silvestri, S. Ultrafast optical parametric amplifiers. *Review of Scientific Instruments* **74**, 1-18 (2003).

110. Couteau, C. Spontaneous parametric down-conversion. *Contemp. Phys.* **59**, 291-304 (2018).

111. Wu, W.; Wang, L.; Li, Y.; Zhang, F.; Lin, L.; Niu, S.; Chenet, D.; Zhang, X.; Hao, Y.; Heinz, T. F.; Hone, J.; Wang, Z. L. Piezoelectricity of single-atomic-layer MoS_2 for energy conversion and piezotronics. *Nature* **514**, 470-474 (2014).

112. Wu, W.; Wang, L.; Yu, R.; Liu, Y.; Wei, S. H.; Hone, J.; Wang, Z. L. Piezophototronic Effect in Single-Atomic-Layer MoS_2 for Strain-Gated Flexible Optoelectronics. *Adv. Mater.* **28**, 8463-8468 (2016).

113. Yang, Z.; Hao, J. Recent Progress in 2D Layered III–VI Semiconductors and their Heterostructures for Optoelectronic Device Applications. *Advanced Materials Technologies* **4**, 1900108 (2019).

114. You, J. W.; Bongu, S. R.; Bao, Q.; Panoiu, N. C. Nonlinear optical properties and applications of 2D materials: Theoretical and experimental aspects. *Nanophotonics* **8**, 63-97 (2018).

115. Ribeiro-Soares, J.; Janisch, C.; Liu, Z.; Elías, A. L.; Dresselhaus, M. S.; Terrones, M.; Cançado, L. G.; Jorio, A. Second harmonic generation in WSe_2. *2D Mater.* **2**, 045015 (2015).

116. Boyd, R. W. *Nonlinear Optics. Academic Press* (2008).

117. Nikogosyan, D. N. *Nonlinear Optical Crystals: A Complete Survey. Springer Science & Business Media* (2006).

118. Wang, G.; Marie, X.; Gerber, I.; Amand, T.; Lagarde, D.; Bouet, L.; Vidal, M.; Balocchi, A.; Urbaszek, B. Giant Enhancement of the Optical Second-Harmonic Emission of WSe$_2$ Monolayers by Laser Excitation at Exciton Resonances. *Phys. Rev. Lett.* **114**, 097403 (2015).

119. Wei, C.; Luo, H.; Zhang, H.; Li, C.; Xie, J.; Li, J.; Liu, Y. Passively Q-switched mid-infrared fluoride fiber laser around 3 μm using a tungsten disulfide (WS$_2$) saturable absorber. *Laser Phys. Lett.* **13**, 105108 (2016).

120. Liu, X.; Guo, Q.; Qiu, J. Emerging Low-Dimensional Materials for Nonlinear Optics and Ultrafast Photonics. *Adv. Mater.* **29**, 1605886 (2017).

121. Khan, A. R.; Zhang, L.; Ishfaq, K.; Ikram, A.; Yildrim, T.; Liu, B.; Rahman, S.; Lu, Y. Optical Harmonic Generation in 2D Materials. *Adv. Funct. Mater.* **32**, 2105259 (2022).

122. Lee, Y. H.; Zhang, X. Q.; Zhang, W.; Chang, M. T.; Lin, C. Te; Chang, K. Di; Yu, Y. C.; Wang, J. T. W.; Chang, C. S.; Li, L. J.; Lin, T. W. Synthesis of Large-Area MoS$_2$ Atomic Layers with Chemical Vapor Deposition. *Adv. Mater.* **24**, 2320– 2325 (2012).

123. Fu, D.; Zhao, X.; Zhang, Y. Y.; Li, L.; Xu, H.; Jang, A. R.; Yoon, S. I.; Song, P.; Poh, S. M.; Ren, T.; Ding, Z.; Fu, W.; Shin, T. J.; Shin, H. S.; Pantelides, S. T.; Zhou, W.; Loh, K. P. Molecular beam epitaxy of highly crystalline monolayer molybdenum disulfide on hexagonal boron nitride. *J. Am. Chem. Soc.* **139***, 9392-9400 (2017).

124. Muratore, C.; Voevodin, A. A.; Glavin, N. R. Physical vapor deposition of 2D Van der Waals materials: a review. *Thin Solid Films* **688**, 137500 (2019).

125. Shi, Y.; Li, H.; Li, L. J. Recent advances in controlled synthesis of two-dimensional transition metal dichalcogenides via vapour deposition techniques. *Chemical Society Reviews* **44**, 2744-2756 (2015).

126. Song, J. G.; Park, J.; Lee, W.; Choi, T.; Jung, H.; Lee, C. W.; Hwang, S. H.; Myoung, J. M.; Jung, J. H.; Kim, S. H.; Lansalot-Matras, C.; Kim, H. Layer-controlled, wafer-scale, and conformal synthesis of tungsten disulfide nanosheets using atomic layer deposition. *ACS Nano* **7**, 11333-11340 (2013).

127. Kang, K.; Xie, S.; Huang, L.; Han, Y.; Huang, P. Y.; Mak, K. F.; Kim, C. J.; Muller, D.; Park, J. High-mobility three-atom-thick semiconducting films with wafer-scale homogeneity. *Nature* **520**, 656-660 (2015).

128. Hackley, J.; Ali, D.; DiPasquale, J.; Demaree, J. D.; Richardson, C. J. K. Graphitic carbon growth on Si (111) using solid source molecular beam epitaxy. *Appl. Phys. Lett.* **95**, 133114 (2009).

129. Dufferwiel, S.; Schwarz, S.; Withers, F.; Trichet, A. A. P.; Li, F.; Sich, M.; Del Pozo-Zamudio, O.; Clark, C.; Nalitov, A.; Solnyshkov, D. D.; Malpuech, G.; Novoselov, K. S.; Smith, J. M.; Skolnick, M. S.; Krizhanovskii, D. N.; Tartakovskii, A. I. Exciton-polaritons in

van der Waals heterostructures embedded in tunable microcavities. *Nat. Commun.* **6**, 8579 (2015).

130. Lundt, N.; Klaas, M.; Sedov, E.; Waldherr, M.; Knopf, H.; Blei, M.; Tongay, S.; Klembt, S.; Taniguchi, T.; Watanabe, K.; Schulz, U.; Kavokin, A.; Höfling, S.; Eilenberger, F.; Schneider, C. Magnetic-field-induced splitting and polarization of monolayer-based valley exciton polaritons. *Phys. Rev. B* **100**, 121303 (2019).

131. Knopf, H.; Lundt, N.; Bucher, T.; Höfling, S.; Tongay, S.; Taniguchi, T.; Watanabe, K.; Staude, I.; Schulz, U.; Schneider, C.; Eilenberger, F. Integration of atomically thin layers of transition metal dichalcogenides into high-Q, monolithic Bragg-cavities: an experimental platform for the enhancement of the optical interaction in 2D-materials. *Opt. Mater. Express* **9**, 598-610 (2019).

132. Liu, X.; Galfsky, T.; Sun, Z.; Xia, F.; Lin, E. C.; Lee, Y. H.; Kéna-Cohen, S.; Menon, V. M. Strong light-matter coupling in two-dimensional atomic crystals. *Nat. Photon.* **9**, 30-34 (2014).

133. Zhang, L.; Gogna, R.; Burg, W.; Tutuc, E.; Deng, H. Photonic-crystal exciton-polaritons in monolayer semiconductors. *Nat. Commun.* **9**, 713 (2018).

134. Ye, Y.; Wong, Z. J.; Lu, X.; Ni, X.; Zhu, H.; Chen, X.; Wang, Y.; Zhang, X. Monolayer excitonic laser. *Nat. Photon.* **9**, 733-737 (2015).

135. Bucher, T.; Vaskin, A.; Mupparapu, R.; Löchner, F. J. F.; George, A.; Chong, K. E.; Fasold, S.; Neumann, C.; Choi, D. Y.; Eilenberger, F.; Setzpfandt, F.; Kivshar, Y. S.; Pertsch, T.; Turchanin, A.; Staude, I. Tailoring Photoluminescence from MoS_2 Monolayers by Mie-Resonant Metasurfaces. *ACS Photonics* **6**, 1002-1009 (2019).

136. Liu, M.; Zheng, X.-W.; Qi, Y.-L.; Liu, H.; Luo, A.-P.; Luo, Z.-C.; Xu, W.-C.; Zhao, C.-J.; Zhang, H. Microfiber-based few-layer MoS_2 saturable absorber for 2.5 GHz passively harmonic mode-locked fiber laser. *Opt. Express* **22**, 22841-22846 (2014).

137. Zhang, H.; Healy, N.; Runge, A. F. J.; Huang, C. C.; Hewak, D. W.; Peacock, A. C. Optical-resonance-enhanced nonlinearities in a MoS_2-coated single-mode fiber. *Opt. Lett.* **43**, 3100-3103 (2018).

138. Chen, H.; Corboliou, V.; Solntsev, A. S.; Choi, D. Y.; Vincenti, M. A.; de Ceglia, D.; de Angelis, C.; Lu, Y.; Neshev, D. N. Enhanced second-harmonic generation from two-dimensional $MoSe_2$ on a silicon waveguide. *Light Sci. Appl.* **6**, e17060 (2017).

139. Liu, L.; Xu, K.; Wan, X.; Xu, J.; Wong, C. Y.; Tsang, H. K. Enhanced optical Kerr nonlinearity of MoS_2 on silicon waveguides. *Photonics Res.* **3**, 206-209 (2015).

140. Datta, I.; Chae, S. H.; Bhatt, G. R.; Tadayon, M. A.; Li, B.; Yu, Y.; Park, C.; Park, J.; Cao, L.; Basov, D. N.; Hone, J.; Lipson, M. Low-loss composite photonic platform based on 2D semiconductor monolayers. *Nat. Photon.* **14**, 256-262 (2020).

141. Zhang, Y.; Tao, L.; Yi, D.; Xu, J. Bin; Tsang, H. K. Enhanced four-wave mixing with MoS_2 on a silicon waveguide. *J. Opt.* **22**, 025503 (2020).

142. De Lucia, F.; Lewis, A. H.; Englebert, N.; Bannerman, R.; Nunez Velazquez, M. M. A.; Huang, C.-C.; Gates, J. C.; Gorza, S.-P.; Sahu, J.; Hewak, D.; Sazio, P. Enhancement of nonlinear functionality of step-index silica fibers combining thermal poling and 2D materials deposition. *Opt. Express* **28**, 34461-34471 (2020).

143. Zuo, Y.; Yu, W.; Liu, C.; Cheng, X.; Qiao, R.; Liang, J.; Zhou, X.; Wang, J.; Wu, M.; Zhao, Y.; Gao, P.; Wu, S.; Sun, Z.; Liu, K.; Bai, X.; Liu, Z. Optical fibres with embedded two-dimensional materials for ultrahigh nonlinearity. *Nat. Nanotechnol.* **15**, 987-991 (2020).

144. Schartner, E. P.; Dowler, A.; Ebendorff-Heidepriem, H. Fabrication of low-loss, small-core exposed core microstructured optical fibers. *Opt. Mater. Express* **7**, 1496-1502 (2017).

145. Kostecki, R; Ebendorff-Heidepriem, H.; Davis, C.; McAdam, G.; Warren-Smith, S. C.; Monro, T. M. Silica exposed-core microstructured optical fibers. *Opt. Mater. Express* **2**, 1538-1547 (2012).

146. Ngo, G. Q.; George, A.; Schock, R. T. K.; Tuniz, A.; Najafidehaghani, E.; Gan, Z.; Geib, N. C.; Bucher, T.; Knopf, H.; Saravi, S.; Neumann, C.; Lühder, T.; Schartner, E. P.; Warren-Smith, S. C.; Ebendorff-Heidepriem, H.; Pertsch, T.; Schmidt, M. A.; Turchanin, A.; Eilenberger, F. Scalable Functionalization of Optical Fibers Using Atomically Thin Semiconductors. *Adv. Mater.* **32**, 2003826 (2020).

147. Aras, M.; Kiliç, Ç.; Ciraci, S. (2018). Lateral and Vertical Heterostructures of Transition Metal Dichalcogenides. *J. Phys. Chem. C* **122**, 1547-1555 (2018).

148. Koma, A. Van der Waals epitaxy for highly lattice-mismatched systems. *J. Cryst. Growth* **201**, 236-241 (1999).

149. Zhang, Z.; Yang, X.; Liu, K.; Wang, R. Epitaxy of 2D Materials toward Single Crystals. *Advanced Science* **9**, 2105201 (2022).

150. Francis, L. F. *Materials Processing: A Unified Approach to Processing of Metals, Ceramics and Polymers* (2016). doi:10.1016/B978-0-12-385132-1.00008-2.

151. Chhowalla, M.; Shin, H. S.; Eda, G.; Li, L. J.; Loh, K. P.; Zhang, H. The chemistry of two-dimensional layered transition metal dichalcogenide nanosheets. *Nat. Chemistry* **5**, 263-275 (2013).

152. Kang, J.; Liu, W.; Sarkar, D.; Jena, D.; Banerjee, K. Computational study of metal contacts to monolayer transition-metal dichalcogenide semiconductors. *Physical Review X* **4**, 031005 (2014).

153. Lin, Z.; Carvalho, B. R.; Kahn, E.; Lv, R.; Rao, R.; Terrones, H.; Pimenta, M. A.; Terrones, M. Defect eingineering of two-dimensional transition metal dichalcogenides. *2D Mater.* **3**, 022002 (2016).

154. Lv, Q.; Chen, F.; Xia, Y.; Su, W. Recent progress in fabrication and physical properties of 2D TMDC-based multilayerd vertical heterostructures. *Electronics* **11**, 2401 (2022).

155. Kappera, R.; Voiry, D.; Yalcin, S. E.; Branch, B.; Gupta, G.; Mohite, A. D.; Chhowalla, M. Phase-engineered low-resistance contacts for ultrathin MoS_2 transistors. *Nat. Mater.* **13**, 1128-1134 (2014).

156. Ovchinnikov, D.; Allain, A.; Huang, Y. S.; Dumcenco, D.; Kis, A. Electrical transport properties of single-layer WS_2. *ACS Nano* **8**, 8174-8181 (2014).

157. Geim, A. K.; Grigorieva, I. V. Van der Waals heterostructures. *Nature* **499**, 419-425 (2013).

158. Qin, C.; Gao, Y.; Qiao, Z.; Xiao, L.; Jia, S. Atomic-Layered MoS_2 as a Tunable Optical Platform. *Advanced Optical Materials* **4**, 1429-1456 (2016).

159. Van Baren, J.; Ye, G.; Yan, J. A.; Ye, Z.; Rezaie, P.; Yu, P.; Liu, Z.; He, R.; Lui, C. H. Stacking-dependent interlayer phonons in 3R and 2H MoS_2. *2D Mater.* **6**, 025022 (2019).

160. Saito, R.; Tatsumi, Y.; Huang, S.; Ling, X.; Dresselhaus, M. S. Raman spectroscopy of transition metal dichalcogenides. *Journal of Physics Condensed Matter* **28**, 353002 (2016).

161. Voiry, D.; Mohite, A.; Chhowalla, M. Phase engineering of transition metal dichalcogenides. *Chemical Society Reviews* **44**, 2702 (2015).

162. Qian, Z.; Jiao, L.; Xie, L. Phase Engineering of Two-Dimensional Transition Metal Dichalcogenides. *Chinese Journal of Chemistry* **38**, 753-760 (2020).

163. Acerce, M.; Voiry, D.; Chhowalla, M. Metallic 1T phase MoS_2 nanosheets as supercapacitor electrode materials. *Nat. Nanotechnol.* **10**, 313-318 (2015).

164. Choudhary, N.; Islam, M. A.; Kim, J. H.; Ko, T. J.; Schropp, A.; Hurtado, L.; Weitzman, D.; Zhai, L.; Jung, Y. Two-dimensional transition metal dichalcogenide hybrid materials for energy applications. *Nano Today* **19**, 16-40 (2018).

165. Zhou, H.; Wang, C.; Shaw, J. C.; Cheng, R.; Chen, Y.; Huang, X.; Liu, Y.; Weiss, N. O.; Lin, Z.; Huang, Y.; Duan, X. Large area growth and electrical properties of p-type WSe_2 atomic layers. *Nano Lett.* **15**, 709-713 (2015).

166. Najafidehaghani, E.; Gan, Z.; George, A.; Lehnert, T.; Ngo, G. Q.; Neumann, C.; Bucher, T.; Staude, I.; Kaiser, D.; Vogl, T.; Hübner, U.; Kaiser, U.; Eilenberger, F.; Turchanin, A. 1D p–n Junction Electronic and Optoelectronic Devices from Transition Metal Dichalcogenide

Lateral Heterostructures Grown by One-Pot Chemical Vapor Deposition Synthesis. *Adv. Funct. Mater.* **31**, 2101086 (2021).

167. Lee, C.; Yan, H.; Brus, L. E.; Heinz, T. F.; Hone, J.; Ryu, S. Anomalous lattice vibrations of single- and few-layer MoS_2. *ACS Nano* **4**, 2695-2700 (2010).

168. Cheiwchanchamnangij, T.; Lambrecht, W. R. L. Quasiparticle band structure calculation of monolayer, bilayer, and bulk MoS_2. *Phys. Rev. B* **85**, 205302 (2012).

169. Pandey, S. K.; Das, R.; Mahadevan, P. Layer-Dependent Electronic Structure Changes in Transition Metal Dichalcogenides: The Microscopic Origin. *ACS Omega* **5**, (2020).

170. Coehoorn, R.; Haas, C.; Dijkstra, J.; Flipse, C. J. F.; De Groot, R. A.; Wold, A. Electronic structure of $MoSe_2$, MoS_2, and WSe_2. I. Band-structure calculations and photoelectron spectroscopy. *Phys. Rev. B* **35**, 6195 (1987).

171. Back, P.; Zeytinoglu, S.; Ijaz, A.; Kroner, M.; Imamoğlu, A. Realization of an Electrically Tunable Narrow-Bandwidth Atomically Thin Mirror Using Monolayer $MoSe_2$. *Phys. Rev. Lett.* **120**, 037401 (2018).

172. Horng, J.; Martin, E. W.; Chou, Y. H.; Courtade, E.; Chang, T. C.; Hsu, C. Y.; Wentzel, M. H.; Ruth, H. G.; Lu, T. C.; Cundiff, S. T.; Wang, F.; Deng, H. Perfect absorption by an atomically thin crystal. *Phys. Rev. Appl.* **14**, 024009 (2020).

173. Bertolazzi, S.; Brivio, J.; Kis, A. Stretching and breaking of ultrathin MoS_2. *ACS Nano* **5**, 9703-9709 (2011).

174. Yu, H.; Cui, X.; Xu, X.; Yao, W. Valley excitons in two-dimensional semiconductors. *National Science Review* **2**, 57-70 (2015).

175. Yu, P. Y.; Cardona, M. *Fundamentals of Semiconductors. Springer* (2005), pp. 276.

176. Kormányos, A.; Burkard, G.; Gmitra, M.; Fabian, J.; Zólyomi, V.; Drummond, N. D.; Fal'ko, V. **k·p** theory for two-dimensional transition metal dichalcogenide semiconductors. *2D Mater.* **2**, 022001 (2015).

177. Moliton, A. *Solid-State Physics for Electronics. John Wiley & Sons* (2010), pp. 364-368. doi:10.1002/9780470611487.

178. He, X-F. Excitons in anisotropic solids: the model of fractional-dimensional space. *Phys. Rev. B* **43**, 2063 (1991).

179. Kolobov, A. V; Tominaga, J. *Springer Series in Materials Science 239 Two-Dimensional Transition-Metal Dichalcogenides. Springer* vol. 239 (2016).

180. Schuller, J. A.; Karaveli, S.; Schiros, T.; He, K.; Yang, S.; Kymissis, I.; Shan, J.; Zia, R. Orientation of luminescent excitons in layered nanomaterials. *Nat. Nanotechnol.* **8**, 271-276 (2013).

181. Mak, K. F.; He, K.; Lee, C.; Lee, G. H.; Hone, J.; Heinz, T. F.; Shan, J. Tightly bound trions in monolayer MoS_2. *Nat. Mater.* **12**, 207-211 (2013).

182. Reyes-Retana, J. A.; Cervantes-Sodi, F. Spin-orbital effects in metal-dichalcogenide semiconducting monolayers. *Sci. Rep.* **6**, 24093 (2016).

183. Wilson, J. A.; Yoffe, A. D. The transition metal dichalcogenides discussion and interpretation of the observed optical, electrical and structural properties. *Adv. Phys.* **18**, 193-335 (1969).

184. Coehoorn, R.; Haas, C.; De Groot, R. A. Electronic structure of $MoSe_2$, MoS_2, and WSe_2. II. The nature of the optical band gaps. *Phys. Rev. B* **35**, 6203 (1987).

185. Xiao, J.; Zhao, M.; Wang, Y.; Zhang, X. Excitons in atomically thin 2D semiconductors and their applications. *Nanophotonics* **6**, 1309-1328 (2017).

186. Singha, S. S.; Nandi, D.; Singha, A. Tuning the photoluminescence and ultrasensitive trace detection properties of few-layer MoS_2 by decoration with gold nanoparticles. *RSC Adv.* **5**, 24188-24193 (2015).

187. Shen, Y. R. *Principles of Nonlinear Optics. Wiley Press* (2002).

188. Wen, X.; Gong, Z.; Li, D. Nonlinear optics of two-dimensional transition metal dichalcogenides. *InfoMat* **1**, 317-337 (2019).

189. Corcoran, B.; Monat, C.; Grillet, C.; Moss, D. J.; Eggleton, B. J.; White, T. P.; O'Faolain, L.; Krauss, T. F. Green light emission in silicon through slow-light enhanced third-harmonic generation in photonic-crystal waveguides. *Nat. Photon.* **3**, 206-210 (2009).

190. Ciattoni, A.; Marini, A.; Rizza, C.; Conti, C. Phase-matching-free parametric oscillators based on two-dimensional semiconductors article. *Light Sci. Appl.* **7**, 5 (2018).

191. Agrawal, G. P. *Nonlinear Fiber Optics* (2019). doi:10.1016/C2018-0-01168-8.

192. George, A.; Neumann, C.; Kaiser, D.; Mupparapu, R.; Lehnert, T.; Hübner, U.; Tang, Z.; Winter, A.; Kaiser, U.; Staude, I.; Turchanin, A. Controlled growth of transition metal dichalcogenide monolayers using Knudsen-type effusion cells for the precursors. *JPhys Mater.* **2**, 016001 (2019).

193. Gan, Z.; Najafidehaghani, E.; Han, S. H.; Shradha, S.; Abtahi, F.; Neumann, C.; Picker, J.; Vogl, T.; Hübner, U.; Eilenberger, F.; George, A.; Turchanin, A. Patterned Growth of Transition Metal Dichalcogenide Monolayers and Multilayers for Electronic and Optoelectronic Device Applications. *Small Methods* **6**, 2200300 (2022).

194. Ferrari, A. C.; Basko, D. M. Raman spectroscopy as a versatile tool for studying the properties of graphene. *Nat. Nanotechnol.* **8**, 235-246 (2013).

195. Li, H.; Zhang, Q.; Yap, C. C. R.; Tay, B. K.; Edwin, T. H. T.; Olivier, A.; Baillargeat, D. From bulk to monolayer MoS_2: Evolution of Raman scattering. *Adv. Funct. Mater.* **22**, 1385–1390 (2012).

196. Berkdemir, A.; Gutiérrez, H. R.; Botello-Méndez, A. R.; Perea-López, N.; Elías, A. L.; Chia, C. I.; Wang, B.; Crespi, V. H.; López-Urías, F.; Charlier, J. C.; Terrones, H.; Terrones, M. Identification of individual and few layers of WS_2 using Raman Spectroscopy. *Sci. Rep.* **3**, 1755 (2013).

197. O'Brien, M.; McEvoy, N.; Hallam, T.; Kim, H. Y.; Berner, N. C.; Hanlon, D.; Lee, K.; Coleman, J. N.; Duesberg, G. S. Transition metal dichalcogenide growth via close proximity precursor supply. *Sci. Rep.* **4**, 1-7 (2014).

198. Zhang, X.; Han, W. P.; Wu, J. B.; Milana, S.; Lu, Y.; Li, Q. Q.; Ferrari, A. C.; Tan, P. H. Raman spectroscopy of shear and layer breathing modes in multilayer MoS_2. *Phys. Rev. B* **87**, 115413 (2013).

199. Tuschel, D. Photoluminescence spectroscopy using a Raman spectrometer. *Spectrosc.* **31**, 14-21 (2016).

200. Smith, E.; Dent, G. *Modern Raman Spectroscopy: A Practical Approach* (2019). doi:10.1002/0470011831.

201. Lakowicz, J. R. *Principles of Fluorescence Spectroscopy* (2006). doi:10.1007/978-0-387-46312-4.

202. Gauglitz, G.; Vo-Dinh, T. *Handbook of Spectroscopy*, Wiley-VCH GmBH & Co. KgaA (2003).

203. Shree, S.; George, A.; Lehnert, T.; Neumann, C.; Benelajla, M.; Robert, C.; Marie, X.; Watanabe, K.; Taniguchi, T.; Kaiser, U.; Urbaszek, B.; Turchanin, A. High optical quality of MoS_2 monolayers grown by chemical vapor deposition. *2D Mater.* **7**, 015011 (2020).

204. Malitson, I. H. Interspecimen Comparison of the Refractive Index of Fused Silica. *J. Opt. Soc. Am.* **55**, 1205-1209 (1965).

205. Ngo, G. Q.; Najafidehaghani, E.; Gan, Z.; Khazaee, S.; Siems, M. P.; George, A.; Schartner, E. P.; Nolte, S.; Ebendorff-Heidepriem, H.; Pertsch, T.; Tuniz, A.; Schmidt, M. A.; Peschel, U.; Turchanin, A.; Eilenberger, F. In-fibre second-harmonic generation with embedded two-dimensional materials. *Nat. Photon.* **16**, 769–776 (2022).

206. Jung, G. H.; Yoo, S. J.; Park, Q. H. Measuring the optical permittivity of twodimensional materials without a priori knowledge of electronic transitions. *Nanophotonics* **8**, 263-270 (2018).

207. Malic, E.; Selig, M.; Feierabend, M.; Brem, S.; Christiansen, D.; Wendler, F.; Knorr, A.; Berghäuser, G. Dark excitons in transition metal dichalcogenides. *Phys. Rev. Mater.* **2**, 014002 (2018).

208. Li, Z.; Wang, T.; Jin, C.; Lu, Z.; Lian, Z.; Meng, Y.; Blei, M.; Gao, S.; Taniguchi, T.; Watanabe, K.; Ren, T.; Tongay, S.; Yang, L.; Smirnov, D.; Cao, T.; Shi, S. F. Emerging

photoluminescence from the dark-exciton phonon replica in monolayer WSe_2. *Nat. Commun.* **10**, 2469 (2019).

209. Luo, Y.; Liu, N.; Kim, B.; Hone, J.; Strauf, S. Exciton Dipole Orientation of Strain-Induced Quantum Emitters in WSe_2. *Nano Lett.* **20**, 5119-5126 (2020).

210. Robert, C.; Han, B.; Kapuscinski, P.; Delhomme, A.; Faugeras, C.; Amand, T.; Molas, M. R.; Bartos, M.; Watanabe, K.; Taniguchi, T.; Urbaszek, B.; Potemski, M.; Marie, X. Measurement of the spin-forbidden dark excitons in MoS_2 and $MoSe_2$ monolayers. *Nat. Commun.* **11**, 4037 (2020).

211. Heindel, T.; Thoma, A.; Schwartz, I.; Schmidgall, E. R.; Gantz, L.; Cogan, D.; Strauß, M.; Schnauber, P.; Gschrey, M.; Schulze, J. H.; Strittmatter, A.; Rodt, S.; Gershoni, D.; Reitzenstein, S. Accessing the dark exciton spin in deterministic quantum-dot microlenses. *APL Photonics* **2**, 121303 (2017).

212. Wang, G.; Robert, C.; Glazov, M. M.; Cadiz, F.; Courtade, E.; Amand, T.; Lagarde, D.; Taniguchi, T.; Watanabe, K.; Urbaszek, B.; Marie, X. In-Plane Propagation of Light in Transition Metal Dichalcogenide Monolayers: Optical Selection Rules. *Phys. Rev. Lett.* **119**, 047401 (2017).

213. Lægsgaard, J.; Bjarklev, A. Microstructured optical fibers - Fundamentals and applications. *Journal of the American Ceramic Society* **89**, 2-12 (2006).

214. Stewart, G.; Jin, W.; Culshaw, B. Prospects for fibre-optic evanescent-field gas sensors using absorption in the near-infrared. *Sensors Actuators: B. Chemical* **38**, 42-47 (1997).

215. Jensen, J. B.; Pedersen, L. H.; Hoiby, P. E.; Nielsen, L. B.; Hansen, T. P.; Folkenberg, J. R.; Riishede, J.; Noordegraaf, D.; Nielsen, K.; Carlsen, A.; Bjarklev, A. Photonic crystal fiber based evanescent-wave sensor for detection of biomolecules in aqueous solutions. *Optics letters* **29**, 1974-1976 (2004).

216. Rindorf, L; Høiby, P. E.; Jensen, J. B.; Pedersen, L. H.; Bang, O.; Geschke, O. Towards biochips using microstructured optical fiber sensors. *Anal. Bioanal. Chem.* **385**, 1370-1375 (2006).

217. Afshar V., S.; Warren-Smith, S. C.; Monro, T. M. Enhancement of fluorescence-based sensing using microstructured optical fibres. *Opt. Express* **15**, 17891-17901 (2007).

218. Monro, T. M.; Warren-Smith, S.; Schartner, E. P.; Franois, A.; Heng, S.; Ebendorff-Heidepriem, H.; Afshar, S. Sensing with suspended-core optical fibers. *Opt. Fiber Technol.* **16**, 343-356 (2010).

219. García, I.; Zubia, J.; Durana, G.; Aldabaldetreku, G.; Illarramendi, M. A.; Villatoro, J. Optical fiber sensors for aircraft structural health monitoring. *Sensors* **15**, 15494-15519 (2015).

220. Hoo, Y. L.; Jin, W.; Ho, H. L.; Ju, J.; Wang, D. N. Gas diffusion measurement using hollow-core photonic bandgap fiber. *Sensors Actuators: B. Chemical* **105**, 183-186 (2005).

221. Lizé, Y. K.; Mägi, E. C.; Ta'eed, V. G.; Bolger, J. A.; Steinvurzel, P.; J. Eggleton, B. Microstructured optical fiber photonic wires with subwavelength core diameter. *Opt. Express* **12**, 3209-3217 (2004).

222. Webb, A. S. Suspended-core holey fiber for evanescent-field sensing. *Opt. Eng.* **46**, 010503 (2007).

223. Debs, J. E.; Ebendorff-Heidepriem, H.; Quinton, J. S.; Monro, T. M. A fundamental study into the surface functionalization of soft glass microstructured optical fibers via silane coupling agents. *J. Light. Technol.* **27**, 576-582 (2009).

224. Warren-Smith, S. C.; Ebendorff-Heidepriem, H.; Foo, T. C.; Moore, R.; Davis, C.; Monro, T. M. Exposed-core microstructured optical fibers for real-time fluorescence sensing. *Opt. Express* **17**, 18533-18542 (2009).

225. Ding, L.; Ruan, Y.; Li, T.; Huang, J.; Warren-Smith, S. C.; Ebendorff-Heidepriem, H.; Monro, T. M. Nitric oxide optical fiber sensor based on exposed core fibers and CdTe/CdS quantum dots. *Sensors Actuators: B. Chemical* **273**, 9-17 (2018).

226. Wang, L.; Xu, Y.; Geng, Y.; Wang, J.; Du, Y.; Yi, D.; Hong, X.; Li, X. High-sensitivity fiber salinity sensor based on an exposed-core microstructured fiber interferometer. *J. Phys. D. Appl. Phys.* **52**, 495402 (2019).

227. Warren-Smith, S. C.; Afshar V., S.; Monro, T. M. Theoretical study of liquid-immersed exposed-core microstructured optical fibers for sensing. *Opt. Express* **16**, 9034-9045 (2008).

228. Palmisano, T.; Prudenzano, F.; Warren-Smith, S. C.; Monro, T. M. Design of exposed-core fiber for methadone monitoring in biological fluids. *Journal of Non-Crystalline Solids* **357**, 2000-2004 (2011).

229. Motala, M.; Beagle, L. K.; Lynch, J.; Moore, D. C.; Stevenson, P. R.; Benton, A.; Tran, L. D.; Baldwin, L. A.; Austin, D.; Muratore, C.; Jariwala, D.; Glavin, N. R. Selective vapor sensors with thin-film MoS$_2$-coated optical fibers. *J. Vac. Sci. Technol. A* **40**, 032202 (2022).

230. Tyagi, D.; Wang, H.; Huang, W.; Hu, L.; Tang, Y.; Guo, Z.; Ouyang, Z.; Zhang, H. Recent advances in two-dimensional-material-based sensing technology toward health and environmental monitoring applications. *Nanoscale* **12**, 3535-3559 (2020).

231. Kuppadakkath, A.; Najafidehaghani, E.; Gan, Z.; Tuniz, A.; Ngo, G. Q.; Knopf, H.; Löchner, F. J. F.; Abtahi, F.; Bucher, T.; Shradha, S.; Käsebier, T.; Palomba, S.; Felde, N.; Paul, P.; Ullsperger, T.; Schröder, S.; Szeghalmi, A.; Pertsch, T.; Staude, I.; Zeitner, U.; George, A.; Turchanin, A.; Eilenberger, F. Direct growth of monolayer MoS$_2$ on nanostructured silicon waveguides. *Nanophotonics* **11**, 4397-4408 (2022).

232. Huang, B.; Li, Z.; Liu, Z.; Zhou, G.; Hao, S.; Wu, J.; Gu, B. L.; Duan, W. Adsorption of gas molecules on graphene nanoribbons and its implication for nanoscale molecule sensor. *J. Phys. Chem. C* **112**, (2008).

233. Tongay, S.; Zhou, J.; Ataca, C.; Liu, J.; Kang, J. S.; Matthews, T. S.; You, L.; Li, J.; Grossman, J. C.; Wu, J. Broad-range modulation of light emission in two-dimensional semiconductors by molecular physisorption gating. *Nano Lett.* **13**, 13442-13446 (2013).

234. Schneider, L. M.; Lippert, S.; Kuhnert, J.; Ajayi, O.; Renaud, D.; Firoozabadi, S.; Ngo, Q.; Guo, R.; Kim, Y. D.; Heimbrodt, W.; Hone, J. C.; Rahimi-Iman, A. The influence of the environment on monolayer tungsten diselenide photoluminescence. *Nano-Structures and Nano-Objects* **15**, 84-97 (2018).

235. Martín, C.; Kostarelos, K.; Prato, M.; Bianco, A. Biocompatibility and biodegradability of 2D materials: Graphene and beyond. *Chem. Commun.* **55**, 5540-5546 (2019).

236. Wang, S.; Yang, X.; Zhou, L.; Li, J.; Chen, H. 2D nanostructures beyond graphene: Preparation, biocompatibility and biodegradation behaviors. *Journal of Materials Chemistry B* **8**, 2974-2989 (2020).

237. Yue, Q.; Shao, Z.; Chang, S.; Li, J. Adsorption of gas molecules on monolayer MoS_2 and effect of applied electric field. *Nanoscale Res. Lett.* **8**, 1-7 (2013).

238. Cho, B.; Hahm, M. G.; Choi, M.; Yoon, J.; Kim, A. R.; Lee, Y. J.; Park, S. G.; Kwon, J. D.; Kim, C. S.; Song, M.; Jeong, Y.; Nam, K. S.; Lee, S.; Yoo, T. J.; Kang, C. G.; Lee, B. H.; Ko, H. C.; Ajayan, P. M.; Kim, D. H. Charge-transfer-based gas sensing using atomic-layer MoS_2. *Sci. Rep.* **5**, 8052 (2015).

239. Bui, V. Q.; Pham, T. T.; Le, D. A.; Thi, C. M.; Le, H. M. A first-principles investigation of various gas (CO, H_2O, NO, and O_2) absorptions on a WS_2 monolayer: Stability and electronic properties. *J. Phys. Condens. Matter* **27**, 305005 (2015).

240. Wang, Z.; Jingjing, Q.; Wang, X.; Zhang, Z.; Chen, Y.; Huang, X.; Huang, W. Two-dimensional light-emitting materials: Preparation, properties and applications. *Chemical Society Reviews* **47**, 6128-6174 (2018).

241. Mouri, S.; Miyauchi, Y.; Matsuda, K. Tunable photoluminescence of monolayer MoS_2 via chemical doping. *Nano Lett.* **13**, 5944-5948 (2013).

242. Li, H.; Huang, M.; Cao, G. Markedly different adsorption behaviors of gas molecules on defective monolayer MoS_2: A first-principles study. *Phys. Chem. Chem. Phys.* **18**, 15110-15117 (2016).

243. Hoo, Y. L.; Jin, W.; Shi, C.; Ho, H. L.; Wang, D. N.; Ruan, S. C. Design and modeling of a photonic crystal fiber gas sensor. *Appl. Opt.* **42**, 3509-3515 (2003).

244. Cheynet, M. C.; Pokrant, S.; Tichelaar, F. D.; Rouvìre, J. L. Crystal structure and band gap determination of HfO_2 thin films. *J. Appl. Phys.* **101**, 054101 (2007).

245. Warren-Smith, S. C.; Afshar, S.; Monro, T. M. Fluorescence-based sensing with optical nanowires: a generalized model and experimental validation. *Opt. Express* **18**, 9474-9485 (2010).

246. Snyder, A. W.; Love, J. D. *Optical Waveguide Theory. Chapman & Hall* (1984). doi:10.1007/978-1-4613-2813-1.

247. Kedenburg, S.; Vieweg, M.; Gissibl, T.; Giessen, H. Linear refractive index and absorption measurements of nonlinear optical liquids in the visible and near-infrared spectral region. *Opt. Mater. Express* **2**, 1588-1611 (2012).

248. Sani, E.; Dell'Oro, A. Spectral optical constants of ethanol and isopropanol from ultraviolet to far infrared. *Opt. Mater.* **60**, 137-141 (2016).

249. Butcher, P. N.; Cotter, D. *The Elements of Nonlinear Optics* (1990). doi:10.1017/cbo9781139167994.

250. Wang, R.; Chien, H. C.; Kumar, J.; Kumar, N.; Chiu, H. Y.; Zhao, H. Third-harmonic generation in ultrathin films of MoS_2. *ACS Appl. Mater. Interfaces* **6**, 314-318 (2014).

251. Balla, N. K.; O'Brien, M.; McEvoy, N.; Duesberg, G. S.; Rigneault, H.; Brasselet, S.; McCloskey, D. Effects of Excitonic Resonance on Second and Third Order Nonlinear Scattering from Few-Layer MoS_2. *ACS Photonics* **5**, 1235-1240 (2018).

252. Fan, X.; Jiang, Y.; Zhuang, X.; Liu, H.; Xu, T.; Zheng, W.; Fan, P.; Li, H.; Wu, X.; Zhu, X.; Zhang, Q.; Zhou, H.; Hu, W.; Wang, X.; Sun, L.; Duan, X.; Pan, A. Broken Symmetry Induced Strong Nonlinear Optical Effects in Spiral WS_2 Nanosheets. *ACS Nano* **11**, 4892-4898 (2017).

253. Kabaciński, P.; Kardaś, T. M.; Stepanenko, Y.; Radzewicz, C. Nonlinear refractive index measurement by SPM-induced phase regression. *Opt. Express* **27**, 11018-11028 (2019).

254. Vincenti, M. A.; De Ceglia, D.; Grande, M.; D'Orazio, A.; Scalora, M. Third-harmonic generation in one-dimensional photonic crystal with graphene-based defect. *Phys. Rev. B* **89**, 165139 (2014).

255. Margulis, V. A.; Muryumin, E. E.; Gaiduk, E. A. Frequency dependence of optical third-harmonic generation from doped graphene. *Phys. Lett. A* **380**, 304-310 (2016).

256. Liang, J.; Wang, J.; Zhang, Z.; Su, Y.; Guo, Y.; Qiao, R.; Song, P.; Gao, P.; Zhao, Y.; Jiao, Q.; Wu, S.; Sun, Z.; Yu, D.; Liu, K. Universal Imaging of Full Strain Tensor in 2D Crystals with Third-Harmonic Generation. *Adv. Mater.* **31**, 1808160 (2019).

257. Karvonen, L.; Säynätjoki, A.; Huttunen, M. J.; Autere, A.; Amirsolaimani, B.; Li, S.; Norwood, R. A.; Peyghambarian, N.; Lipsanen, H.; Eda, G.; Kieu, K.; Sun, Z. Rapid

visualization of grain boundaries in monolayer MoS_2 by multiphoton microscopy. *Nat. Commun.* **8**, 15714 (2017).

258. Soavi, G.; Wang, G.; Rostami, H.; Purdie, D. G.; De Fazio, D.; Ma, T.; Luo, B.; Wang, J.; Ott, A. K.; Yoon, D.; Bourelle, S. A.; Muench, J. E.; Goykhman, I.; Dal Conte, S.; Celebrano, M.; Tomadin, A.; Polini, M.; Cerullo, G.; Ferrari, A. C. Broadband, electrically tunable third-harmonic generation in graphene. *Nat. Nanotechnol.* **13**, 583-588 (2018).

259. Feng, Q.; Cong, H.; Zhang, B.; Wei, W.; Liang, Y.; Fang, S.; Wang, T.; Zhang, J. Enhanced Optical Kerr Nonlinearity of Graphene/Si Hybrid Waveguide. *Appl. Phys. Lett.* **114**, 071104 (2019).

260. Dudley, J. M.; Provino, L.; Grossard, N.; Maillotte, H.; Windeler, R. S.; Eggleton, B. J.; Coen, S. Supercontinuum generation in air–silica microstructured fibers with nanosecond and femtosecond pulse pumping. *J. Opt. Soc. Am. B* **19**, 765-771 (2002).

261. Lühder, T. A. K.; Schaarschmidt, K.; Goerke, S.; Schartner, E. P.; Ebendorff-Heidepriem, H.; Schmidt, M. A. Resonance-Induced Dispersion Tuning for Tailoring Nonsolitonic Radiation via Nanofilms in Exposed Core Fibers. *Laser Photonics Rev.* **14**, 1900418 (2020).

262. Inoue, K. Four-Wave Mixing in an Optical Fiber in the Zero-Dispersion Wavelength Region. *J. Light. Technol.* **10**, 1553-1561 (1992).

263. Shahraam Afshar, V.; Monro, T. M.; de Sterke, C. M. Understanding the contribution of mode area and slow light to the effective Kerr nonlinearity of waveguides. *Opt. Express* **21**, 18558-18571 (2013).

264. Warren-Smith, S. C.; Wie, J.; Chemnitz, M.; Kostecki, R.; Ebendorff-Heidepriem, H.; Monro, T. M.; Schmidt, M. A. Third harmonic generation in exposed-core microstructured optical fibers. *Opt. Express* **24**, 17860-17867 (2016).

265. Warren-Smith, S. C.; Chemnitz, M.; Schneidewind, H.; Kostecki, R.; Ebendorff-Heidepriem, H.; Monro, T. M.; Schmidt, M. A. Nanofilm-induced spectral tuning of third harmonic generation. *Opt. Lett.* **42**, 1812-1815 (2017).

266. Li, J.; Naiini, M. M.; Vaziri, S.; Lemme, M. C.; Östling, M. Inkjet printing of MoS_2. *Adv. Funct. Mater.* **24**, 6524-6531 (2014).

267. Yu, H.; Talukdar, D.; Xu, W.; Khurgin, J. B.; Xiong, Q. Charge-Induced Second-Harmonic Generation in Bilayer WSe_2. *Nano Lett.* **15**, 5653-5657 (2015).

268. Brun, S. J.; Pedersen, T. G. Intense and tunable second-harmonic generation in biased bilayer graphene. *Phys. Rev. B* **91**, 205405 (2015).

269. Klein, J.; Wierzbowski, J.; Steinhoff, A.; Florian, M.; Rösner, M.; Heimbach, F.; Müller, K.; Jahnke, F.; Wehling, T. O.; Finley, J. J.; Kaniber, M. Electric-field switchable second-

harmonic generation in bilayer MoS₂ by inversion symmetry breaking. *Nano Lett.* **17**, 392-398 (2017).

270. Kim, D. H.; Lim, D. Optical second-harmonic generation in few-layer MoSe₂. *J. Korean Phys. Soc.* **66**, 816-820 (2015).

271. Le, C. T.; Clark, D. J.; Ullah, F.; Jang, J. I.; Senthilkumar, V.; Sim, Y.; Seong, M. J.; Chung, K. H.; Kim, J. W.; Park, S.; Rhim, S. H.; Kim, G.; Kim, Y. S. Impact of selenium doping on resonant second-harmonic generation in monolayer MoS₂. *ACS Photonics* **4**, 38-44 (2017).

272. Yin, X.; Ye, Z.; Chenet, D. A.; Ye, Y.; O'Brien, K.; Hone, J. C.; Zhang, X. Edge nonlinear optics on a MoS₂ atomic monolayer. *Science* **344**, 488-490 (2014).

273. Lin, X.; Liu, Y.; Wang, K.; Wei, C.; Zhang, W.; Yan, Y.; Li, Y. J.; Yao, J.; Zhao, Y. S. Two-Dimensional Pyramid-like WS₂ Layered Structures for Highly Efficient Edge Second-Harmonic Generation. *ACS Nano* **12**, 689-696 (2018).

274. Hsu, W. T.; Zhao, Z. A.; Li, L. J.; Chen, C. H.; Chiu, M. H.; Chang, P. S.; Chou, Y. C.; Chang, W. H. Second harmonic generation from artificially stacked transition metal dichalcogenide twisted bilayers. *ACS Nano* **8**, 2951-2958 (2014).

275. Rhim, S. H.; Kim, Y. S.; Freeman, A. J. Strain-induced giant second-harmonic generation in monolayered 2H -MoX₂ (X = S, Se, Te). *Appl. Phys. Lett.* **107**, 241908 (2015).

276. Zhao, M.; Ye, Z.; Suzuki, R.; Ye, Y.; Zhu, H. Y.; Xiao, J.; Wang, Y.; Iwasa, Y.; Zhang, X. Atomically phase-matched second-harmonic generation in a 2D crystal. *Light Sci. Appl.* **5**, e16131 (2016).

277. Shi, J.; Yu, P.; Liu, F.; He, P.; Wang, R.; Qin, L.; Zhou, J.; Li, X.; Zhou, J.; Sui, X.; Zhang, S.; Zhang, Y.; Zhang, Q.; Sum, T. C.; Qiu, X.; Liu, Z.; Liu, X. 3R MoS₂ with Broken Inversion Symmetry: A Promising Ultrathin Nonlinear Optical Device. *Adv. Mater.* **29**, 1701486 (2017).

278. Wagoner, G. A.; Persans, P. D.; Van Wagenen, E. A.; Korenowski, G. M. Second-harmonic generation in molybdenum disulfide. *J. Opt. Soc. Am. B* **15**, 1017-1021 (1998).

279. Clark, D. J.; Senthilkumar, V.; Le, C. T.; Weerawarne, D. L.; Shim, B.; Jang, J. I.; Shim, J. H.; Cho, J.; Sim, Y.; Seong, M. J.; Rhim, S. H.; Freeman, A. J.; Chung, K. H.; Kim, Y. S. Strong optical nonlinearity of CVD-grown MoS₂ monolayer as probed by wavelength-dependent second-harmonic generation. *Phys. Rev. B* **90**, 121409 (2014).

280. Trolle, M. L.; Seifert, G.; Pedersen, T. G. Theory of excitonic second-harmonic generation in monolayer MoS₂. *Phys. Rev. B* **89**, 235410 (2014).

281. Liang, J.; Zhang, J.; Li, Z.; Hong, H.; Wang, J.; Zhang, Z.; Zhou, X.; Qiao, R.; Xu, J.; Gao, P.; Liu, Z. Z.; Liu, Z. Z.; Sun, Z.; Meng, S.; Liu, K.; Yu, D. Monitoring Local Strain Vector

in Atomic-Layered MoSe$_2$ by Second-Harmonic Generation. *Nano Lett.* **17**, 7539-7543 (2017).

282. Mennel, L.; Paur, M.; Mueller, T. Second harmonic generation in strained transition metal dichalcogenide monolayers: MoS$_2$, MoSe$_2$, WS$_2$, and WSe$_2$. *APL Photonics* **4**, 034404 (2019).

283. Zhang, J.; Zhao, W.; Yu, P.; Yang, G.; Liu, Z. Second harmonic generation in 2D layered materials. *2D Mater.* **7**, 042002 (2020).

284. Zeng, Z.; Sun, X.; Zhang, D.; Zheng, W.; Fan, X.; He, M.; Xu, T.; Sun, L.; Wang, X.; Pan, A. Controlled Vapor Growth and Nonlinear Optical Applications of Large-Area 3R Phase WS$_2$ and WSe$_2$ Atomic Layers. *Adv. Funct. Mater.* **29**, 1806874 (2019).

285. Mennel, L.; Furchi, M. M.; Wachter, S.; Paur, M.; Polyushkin, D. K.; Mueller, T. Optical imaging of strain in two-dimensional crystals. *Nat. Commun.* **9**, 516 (2018).

286. Kilinc, M.; Cheney, A.; Neureuter, C.; Tarasek, S.; Xu, G.; Thomay, T. Intracavity second harmonic generation from a WSe$_2$ monolayer in a passively mode-locked picosecond fiber laser. *Opt. Mater. Express* **11**, 1603-1613 (2021).

287. Liang, J.; Ma, H.; Wang, J.; Zhou, X.; Yu, W.; Ma, C.; Wu, M.; Gao, P.; Liu, K.; Yu, D. Giant pattern evolution in third-harmonic generation of strained monolayer WS$_2$ at two-photon excitonic resonance. *Nano Res.* **13**, 3235-3240 (2020).

288. Rosa, H. G.; Ho, Y. W.; Verzhbitskiy, I.; Rodrigues, M. J. F. L.; Taniguchi, T.; Watanabe, K.; Eda, G.; Pereira, V. M.; Gomes, J. C. V. Characterization of the second- and third-harmonic optical susceptibilities of atomically thin tungsten diselenide. *Sci. Rep.* **8**, 1-7 (2018).

289. Janisch, C.; Wang, Y.; Ma, D.; Mehta, N.; Elías, A. L.; Perea-López, N.; Terrones, M.; Crespi, V.; Liu, Z. Extraordinary second harmonic generation in Tungsten disulfide monolayers. *Sci. Rep.* **4**, 5530 (2014).

290. Cheng, J.; Jiang, T.; Ji, Q.; Zhang, Y.; Li, Z.; Shan, Y.; Zhang, Y.; Gong, X.; Liu, W.; Wu, S. Kinetic Nature of Grain Boundary Formation in As-Grown MoS$_2$ Monolayers. *Adv. Mater.* **27**, 4069-4074 (2015).

291. Li, D.; Xiong, W.; Jiang, L.; Xiao, Z.; Rabiee Golgir, H.; Wang, M.; Huang, X.; Zhou, Y.; Lin, Z.; Song, J.; Ducharme, S.; Jiang, L.; Silvain, J. F.; Lu, Y. Multimodal Nonlinear Optical Imaging of MoS$_2$ and MoS$_2$-Based van der Waals Heterostructures. *ACS Nano* **10**, 3766-3775 (2016).

292. Geib, N. C.; Zilk, M.; Pertsch, T.; Eilenberger, F. Common pulse retrieval algorithm: a fast and universal method to retrieve ultrashort pulses. *Optica* **6**, 495-505 (2019).

293. Luo, R.; He, Y.; Liang, H.; Li, M.; Lin, Q. Highly tunable efficient second-harmonic generation in a lithium niobate nanophotonic waveguide. *Optica* **5**, 1006-1011 (2018).

294. Clark, D. J.; Le, C. T.; Senthilkumar, V.; Ullah, F.; Cho, H. Y.; Sim, Y.; Seong, M. J.; Chung, K. H.; Kim, Y. S.; Jang, J. I. Near bandgap second-order nonlinear optical characteristics of MoS_2 monolayer transferred on transparent substrates. *Appl. Phys. Lett.* **107**, 131113 (2015).

295. Myers, R. A.; Mukherjee, N.; Brueck, S. R. J. Large second-order nonlinearity in poled fused silica. *Opt. Lett.* **16**, 1732-1734 (1991).

296. Wurdack, M.; Yun, T.; Estrecho, E.; Syed, N.; Bhattacharyya, S.; Pieczarka, M.; Zavabeti, A.; Chen, S. Y.; Haas, B.; Müller, J.; Lockrey, M. N.; Bao, Q.; Schneider, C.; Lu, Y.; Fuhrer, M. S.; Truscott, A. G.; Daeneke, T.; Ostrovskaya, E. A. Ultrathin Ga_2O_3 Glass: A Large-Scale Passivation and Protection Material for Monolayer WS_2. *Adv. Mater.* **33**, 2005732 (2021).

297. Xu, X.; Trovatello, C.; Mooshammer, F.; Shao, Y.; Zhang, S.; Yao, K.; Basov, D. N.; Cerullo, G.; Schuck, P. J. Towards compact phase-matched and waveguided nonlinear optics in atomically layered semiconductors. *Nat. Photon.* **16**, 698–706 (2022).

298. Dudley, J. M.; Genty, G.; Coen, S. Supercontinuum generation in photonic crystal fiber. *Rev. Mod. Phys.* **78**, 1135 (2006).

299. Gorbach, A. V. Graphene plasmonic waveguides for mid-infrared supercontinuum generation on a chip. *Photonics* **2**, 825-837 (2015).

300. RF Module User's Guide, version 4.3a, COMSOL, Inc, www.comsol.com.

Appendix B: Bibliography

Peer Reviewed Journal Papers

[1] G. Q. Ngo, E. Najafidehaghani, Z. Gan, S. Khazaee, M. P. Siems, A. George, E. P. Schartner, S. Nolte, H. Ebendorff-Heidepriem, T. Pertsch, A. Tuniz, M. A. Schmidt, U. Peschel, A. Turchanin, and F. Eilenberger. In-fibre second-harmonic generation with embedded two-dimensional materials. *Nat. Photon.* **16**, 769-776 (2022).

[2] A. Kuppadakkath, E. Najafidehaghani, Z. Gan, A. Tuniz, G. Q. Ngo, H. Knopf, F. Löchner, F. Abtahi, T. Bucher, S. Shradha, T. Käsebier, S. Palomba, N. Felde, P. Paul, T. Ullsperger, S. Schröder, A. Szeghalmi, T. Pertsch, I. Staude, U. Zeitner, A. George, A. Turchanin, and F. Eilenberger. Direct Growth of Monolayer MoS$_2$ on Nanostructured Silicon Waveguides. *Nanophotonics* **11**, 4397-4408 (2022).

[3] E. Najafidehaghani, Z. Gan, A. George, T. Lehnert, G. Q. Ngo, C. Neumann, T. Bucher, I. Staude, D. Kaiser, T. Vogl, U. Hübner, U. Kaiser, F. Eilenberger, and A. Turchanin. 1D p–n Junction Electronic and Optoelectronic Devices from Transition Metal Dichalcogenide Lateral Heterostructures Grown by One-Pot Chemical Vapor Deposition Synthesis. *Adv. Funct. Mater.* **31**, 2101086 (2021).

[4] G. Q. Ngo, A. George, R. T. K. Schock, A. Tuniz, E. Najafidehaghani, Z. Gan, N. C. Geib, T. Bucher, H. Knopf, S. Saravi, C. Neumann, T. Lühder, E. P. Schartner, S. C. Warren-Smith, H. Ebendorff-Heidepriem, T. Pertsch, M. A. Schmidt, A. Turchanin, and F. Eilenberger. Scalable functionalization of optical fibers using atomically thin semiconductors. *Adv. Mater.* **32**, 2003826 (2020).

In Preparation

G. Q. Ngo, C. Cholsuk, M. Hilbert, Z. Gan, S. Thiele, A. George, H. Ebendorff-Heidepriem, E. P. Schartner, M. Schmidt, J. Pezoldt, A. Turchanin, T. Vogl, F. Eilenberger. Real-time gas sensing with two-dimensional materials. In preparation.

Featured Images in Peer Reviewed Journal Papers

[1] G. Q. Ngo, E. Najafidehaghani, Z. Gan, S. Khazaee, M. P. Siems, A. George, E. P. Schartner, S. Nolte, H. Ebendorff-Heidepriem, T. Pertsch, A. Tuniz, M. A. Schmidt, U. Peschel, A. Turchanin, and F. Eilenberger. In-fibre second-harmonic generation with embedded two-dimensional materials. *Nature Photonics, November issue* (2022). https://www.nature.com/nphoton/, accessed on 01 November 2022.

[2] E. Najafidehaghani, Z. Gan, A. George, T. Lehnert, G. Q. Ngo, C. Neumann, T. Bucher, I. Staude, D. Kaiser, T. Vogl, U. Hübner, U. Kaiser, F. Eilenberger, and A. Turchanin. Lateral Heterostructures: 1D p–n Junction Electronic and Optoelectronic Devices from Transition Metal Dichalcogenide Lateral Heterostructures Grown by One-Pot Chemical Vapor

Deposition Synthesis. *Adv. Funct. Mater.* **31** (27) (2021). https://doi.org/10.1002/adfm.202170198

[3] G. Q. Ngo, A. George, R. T. K. Schock, A. Tuniz, E. Najafidehaghani, Z. Gan, N. C. Geib, T. Bucher, H. Knopf, S. Saravi, C. Neumann, T. Lühder, E. P. Schartner, S. C. Warren-Smith, H. Ebendorff-Heidepriem, T. Pertsch, M. A. Schmidt, A. Turchanin, and F. Eilenberger. Integrated Photonics: Scalable functionalization of optical fibers using atomically thin semiconductors. *Adv. Mater.* **32** (47) (2020). https://doi.org/10.1002/adma.202070354

Conference Talks

[1] G. Q. Ngo, E. Najafidehaghani, S. Khazaee, M. P. Siems, A. George, A. Tuniz, H. Ebendorff-Heidepriem, A. Turchanin, M. A. Schmidt, F. Eilenberger. *Towards a versatile photonic platform with 2D materials grown on exposed-core fibers*. In CLEO/Europe-EQEC. Munich, Germany (2023).

[2] G. Q. Ngo, E. Najafidehaghani, Z. Gan, S. Khazaee, M. P. Siems, A. George, U. Peschel, A. Tuniz, M. A. Schmidt, A. Turchanin, F. Eilenberger. *Functionalizing optical waveguide systems with 2D materials*. Invited Talk *In OPTICSMEET 2023*. Brussels, Belgium (2023).

[3] G. Q. Ngo, E. Najafidehaghani, Z. Gan, S. Khazaee, M. P. Siems, A. George, U. Peschel, A. Tuniz, M. A. Schmidt, A. Turchanin, F. Eilenberger. *Second Harmonic Generation in 2D-Embedded Optical Fibers. In PHOTOPTICS 2023*. Lisbon, Portugal (2023).

[4] G. Q. Ngo, E. Najafidehaghani, Z. Gan, S. Khazaee, M. P. Siems, A. George, U. Peschel, A. Tuniz, H. Ebendorff-Heidepriem, M. A. Schmidt, A. Turchanin, F. Eilenberger. *Nonlinear Dynamics in Optical Waveguides with CVD-Grown 2D-Material Coating. In CLEO-PR 2022/ISOM'22/ODF'22*. Sapporo, Japan (2022).

[5] G. Q. Ngo, E. Najafidehaghani, Z. Gan, S. Khazaee, M. P. Siems, A. George, U. Peschel, M. A. Schmidt, A. Turchanin, and F. Eilenberger. *Nonlinear Dynamics in Optical Waveguides with 2D-Material.* In *ICQNN*. Jena, Germany (2022).

[6] H. Knopf, G. Q. Ngo, F. A. Abtahi, S. Bernet, A. George, E. Najafidehaghani, Z. Gan, L. Lukas, C. Rupprecht, H. Shan, M. Weissflog, T. Vogl, A. Turchanin, U. Schulz, S. Schröder, C. Schneider, S. Höfling, F. Eilenberger. *Enhanced Light-Matter Interaction in TMDC-Materials by Integration in Resonant Layer Architectures. In Frontiers in Optics / Laser Science*, OSA Technical Digest (Optical Society of America, 2021).

[7] H. Knopf, M. Zilk, S. Bernet, G. Q. Ngo, F. A. Abtahi, A. George, E. Najafidehaghani, Z. Gan, M. Weissflog, T. Vogl, A. Turchanin, U. Schulz, S. Schröder, F. Eilenberger. *Second Harmonic Generation in monolayer WS₂ with double resonant Bragg-Cavities. In CLEO/Europe-EQEC*. Munich, Germany (2021).

[8] G. Q. Ngo, E. Najafidehaghani, A. George, A. Turchanin, F. Eilenberger. *Monolayer TMDs Functionalized Exposed Core Fibers*. In *DokDok.* Jena, Germany (2021).

[9] G. Q. Ngo, A. George, A. Tuniz, E. Najafidehaghani, Z. Gan, T. Bucher, H. Knopf, S. Saravi, T. Lühder, S. Warren-Smith, H. Ebendorff-Heidepriem, A. Turchanin, M. Schmidt,

and F. Eilenberger. *Functionalization of Exposed-Core Fibers with CVD-Grown Monolayer Transition Metal Dichalcogenides: Photolumiescence and Nonlinearity*. In *AAAFM-UCLA International Conference*. LA, USA (2021).

[10] G. Q. Ngo, A. George, A. Tuniz, E. Najafidehaghani, Z. Gan, T. Bucher, H. Knopf, S. Saravi, T. Lühder, S. Warren-Smith, H. Ebendorff-Heidepriem, A. Turchanin, M. Schmidt, and F. Eilenberger. *Scalable Functionalization of Exposed-Core Fibers with CVD-Grown Monolayer Transition Metal Dichalcogenides*. In *Material Science & Nanotechnology Conference*. Lisbon, Portugal (2021).

[11] G. Q. Ngo, A. George, R. K. T. Schock, A. Tuniz, E. Najafidehaghani, N. C. Geib, T. Bucher, H. Knopf, C. Neumann, T. Lühder, S. Warren-Smith, H. Ebendorff-Heidepriem, A. Turchanin, M. Schmidt, and F. Eilenberger. *Photoluminescence and Third Harmonic Generation in Directly-Grown MoS_2 and WS_2 Exposed-Core Fibers*. In *Frontiers in Optics / Laser Science*, OSA Technical Digest (Optical Society of America, 2020), paper FTu2D.5.

[12] N. C. Geib, H. Knopf, G. Q. Ngo, T. Pertsch, and F. Eilenberger. *Common pulse retrieval algorithm: a fast and universal method to retrieve ultrashort pulses*. In *Conference on Lasers and Electro-Optics*, OSA Technical Digest (Optical Society of America, 2020), paper SM3H.3.

[13] G. Q. Ngo, R. T. K. Schock, A. George, H. Ebendorff-Heidepriem, A. Turchanin, M. Schmidt, T. Bucher, and F. Eilenberger. *MoS_2 monolayers grown on exposed core fibers*. In *DokDok*. Eisenach, Germany (2019).

Conference Poster

[1] G. Q. Ngo, E. Najafidehaghani, Z. Gan, S. Khazaee, M. Siems, A. Tuniz, U. Peschel, H. Ebendorff-Heidepriem, M. A. Schmidt, A. Turchanin, and F. Eilenberger. *Nonlinear dynamics in optical fiber with embedded 2D-material*. In *Sino-German Symposium FNMS*. Gießen, Germany (2023).

[2] G. Q. Ngo, E. Najafidehaghani, Z. Gan, S. Khazaee, A. George, U. Peschel, A. Tuniz, H. Ebendorff-Heidepriem, M. A. Schmidt, A. Turchanin, and F. Eilenberger. *Second-Harmonic Generation in Directly-Grown MoS_2 Monolayers on Exposed-Core Fibers*. In *Frontiers in Optics / Laser Science*, OSA Technical Digest (Optical Society of America, 2021).

[3] G. Q. Ngo, A. George, A. Tuniz, E. Najafidehaghani, Z. Gan, T. Bucher, H. Knopf, S. Saravi, T. Lühder, S. Warren-Smith, H. Ebendorff-Heidepriem, A. Turchanin, M. A. Schmidt, F. Eilenberger. *Scalable Integrated Waveguide with CVD-Grown MoS_2 and WS_2 Monolayers on Exposed-Core Fibers*. In *CLEO/Europe-EQEC*. Munich, Germany (2021).

[4] R. T. K. Schock, G. Q. Ngo, A. George, C. Neumann, H. Ebendorff-Heidepriem, B. Doherty, A. Turchanin, M. Schmidt, T. Bucher, M. Steinert, and F. Eilenberger. *Single layers MoS_2 directly grown on exposed core optical fibers: A new approach to guided wave transition metal dichalcogenide photonics*. In *CLEO/Europe-EQEC*. Munich, Germany (2019).

Appendix C: Additional numerical calculation of ECF

In this appendix, I describe the usage of mode analysis in COMSOL to find the mode profiles and mode overlap of the optical fibers with different structure configurations. The use of COMSOL for finding modes of an ECF is similar to a waveguide, and its description can be found in its user guide [300]. First, we want to investigate the impact of the fiber core diameter on the mode overlap with monolayer TMD deposited on top of the core. Using a simple model, we calculated the evanescent field in the exposed region for different wavelengths and numerous core diameters. A scattering boundary with a diameter of 9 µm was applied, meanwhile, a monolayer MoS_2 (0.65 nm) was included in the model. The fundamental modes are well confined inside the boundary, and hence, we do not need to extend further the calculated area. Figure C1 displays the fundamental mode with the x-polarization for different core diameters at 532 nm. These models have been used to calculate the relative sensitivity plotted in Figure 5.6 in Chapter 5. The calculated Poynting vector z-component at the excitation wavelength of 532 nm is given in Table C1. It is noticeable that the smaller cores have less mode confinement than the larger ones, hence the power fraction in the three air holes and the exposed area increases when the core diameter decreases. Remarkably, the power fraction in the monolayer grows significantly when the core is getting smaller, thus, the enhancement of light-matter interaction is also improved just by changing the fiber core.
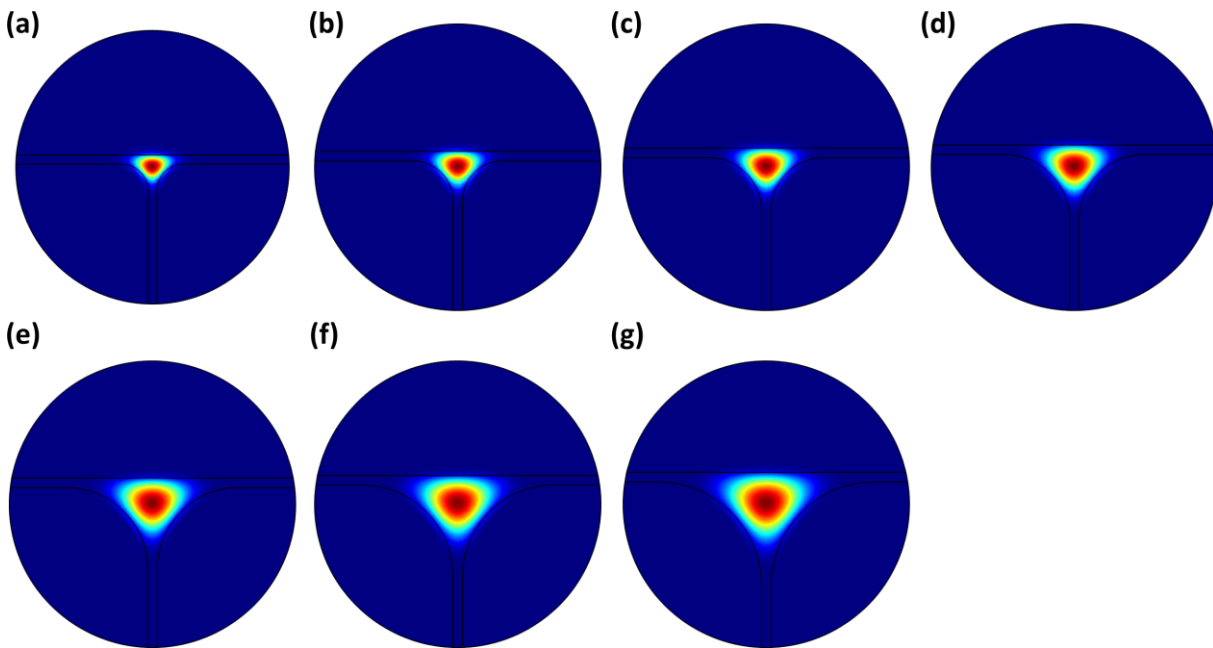
Figure C1: Electric field distribution of fundamental mode inside the fiber with various core diameter at $\lambda_0 = 532$ nm. **(a)** 0.8µm. **(b)** 1.0µm. **(c)** 1.2µm. **(d)** 1.4µm. **(e)** 1.6µm. **(f)** 1.8µm. **(g)** 2.0µm.

Table C1: Calculated Poynting vector z-component for *x*-polarized fundamental mode of the ECFs at $\lambda_0 = 532$ nm in the relation to core diameter.

Region of the ECF	d = 0.8 μm	d = 1.0 μm	d = 1.2 μm	d = 1.4 μm	d = 1.6 μm	d = 1.8 μm	d = 2.0 μm
Three air regions (%)	2.08	1.14	0.70	0.46	0.29	0.23	0.17
Exposed region only (%)	1.109	0.626	0.383	0.247	0.157	0.123	0.091
Monolayer (%)	0.0175	0.0099	0.0061	0.0040	0.0026	0.0020	0.0015

Using the same settings but with a real SEM fiber geometry, we can calculate precisely the mode properties from the bare ECF, MoS$_2$-coated ECF, and MoS$_2$-coated ECF with HfO$_2$ coating. The FMs at $\lambda_0 = 1360$ nm for three different structures are depicted in Figure C2. The simulation data reveal that there is no change in the profile of the fundamental modes, as displayed in Figure C2b-c.
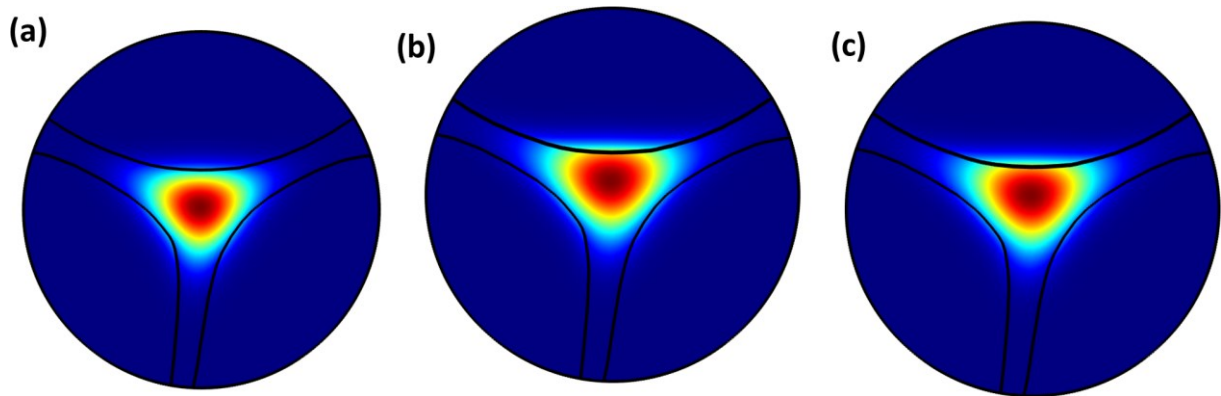
Figure C2: Electric field distribution of fundamental mode inside the fiber with different coatings at $\lambda_0 = 1360$ nm. **(a)** without HfO$_2$. **(b)** 25 nm HfO$_2$ on MoS$_2$. **(c)** 25 nm HfO$_2$ under MoS$_2$.

The coating of HfO$_2$ can boost up the light-matter interaction with TMDs, no matter if HfO$_2$ is sandwiched between silica core and monolayer TMD, or TMD is sandwiched between silica core and HfO$_2$. Table C2 reveals the calculated Poynting vector z-component for the x-polarized FM at 1360 nm. The deposition of a high refractive index layer on the exposed side will drag the mode shifted upward and increase the overlap with the monolayer. Monolayer TMD has a negligible influence on the mode profiles because of its atomically thin thickness (0.65 nm) compared to the 25nm thickness of HfO$_2$. This finding will make the TMD functionalized ECF more suitable for both linear and nonlinear optics and gas sensing. In the case of gas sensing, HfO$_2$ or any other thin film can be coated along the fiber core to modify the guided modes, and TMD or 2D materials can be deposited on top of them to contact directly with the gases. Then, the principle of gas sensing is

unchanged, except with the higher PL efficiency from TMD monolayers because of more light energy overlapping with the monolayers. For the case of nonlinear optics, the coating of HfO_2 or another thin film on top of TMD or 2D materials can protect them from the influence of the environment and enhance the light-matter interaction.

Table C2: Calculated Poynting vector z-component for *x*-polarized fundamental mode of the ECFs at $\lambda_0 = 1360$ nm.

Cross-Sectional part of the ECF	Bare ECF	MoS_2 coated ECF	25nm HfO_2 on top of MoS_2	25nm HfO_2 under MoS_2
Three air regions (%)	2.355	2.431	5.731	5.700
Exposed region only (%)	1.084	1.175	4.970	3.945
Monolayer (%)	N/A	0.007	0.028	0.024

Appendix D: Fabrication process of ECFs

The all-silica ECF was manufactured using a silica rod of 12 mm in diameter and a 6 m-tall drawing tower. Figure D1 displays the fabrication process of ECFs. First, a 120 mm-long preform made of F300 fused silica from Heraeus Quarzglass was drilled by an ultrasonic mill to make three holes, then an opening along the whole length of the preform was created to make the exposed side. The contaminants were removed by nitric acid and acetone overnight, and the preform was dried with nitrogen. The preform was caned and inserted into a jacket tube before the drawing process. During the drawing process, the glass and air holes were heated to the glass transition temperature in a furnace at a typical temperature range of 1900 °C – 2000 °C, then drawn into an ECF.
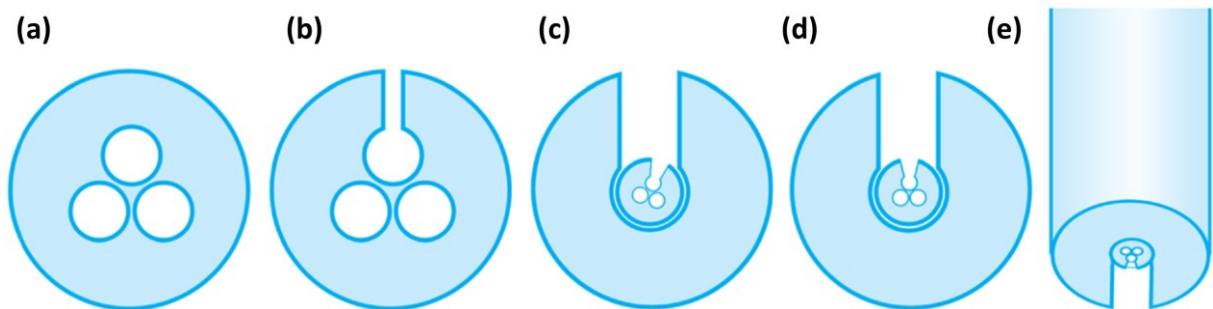
Figure D1: Fabrication process of ECFs. **(a)** Three holes are drilled by an ultrasonic mill on the preform. **(b)** An opening is cut along the length of preform. **(c-d)** The preform is caned and inserted into a jacket tube. **(e)** The initial preform is drawn to ECF. Figure is adapted from [144].
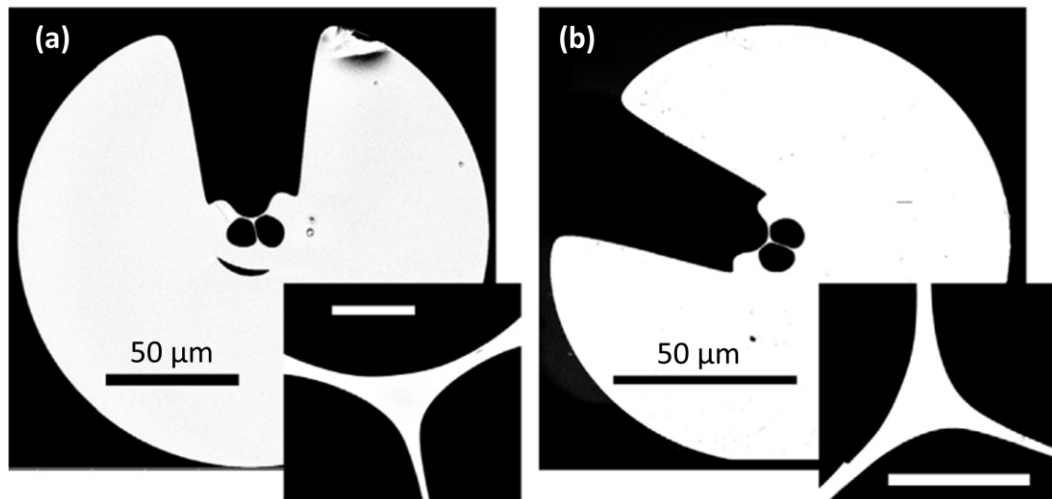
Figure D2: ECF after the drawing process. **(a)** An ECF with a core diameter of 2.35 μm. **(b)** Core diameter of 1.65 μm. The scale bar shows 3 μm in the insets. Figure is adapted from [144].

The ECF has an analogous geometry to the preform, except for the smaller size and the much longer length. The fabricated ECF has an outer diameter of 175 μm and an effective core diameter of 2 μm. Thanks to the chemically inert and temperature-stable process, silica ECF has minimal internal stress during heating and cooling. It can work well with both the temperature and the atmospheric condition of the CVD process. The cross-section and geometry of our ECFs are shown in Figure D2. By varying the outer diameter of the fiber and the gap between the holes set to be 0.4 mm, the

ECFs with different core diameters were fabricated, as depicted in Figure D2. The core diameters are 2.35 μm and 1.65 μm, respectively. The low loss from an ECF with a core of 2 μm was confirmed in Figure D3, which is less than 1dB/m for the wide range from Visible to NIR.
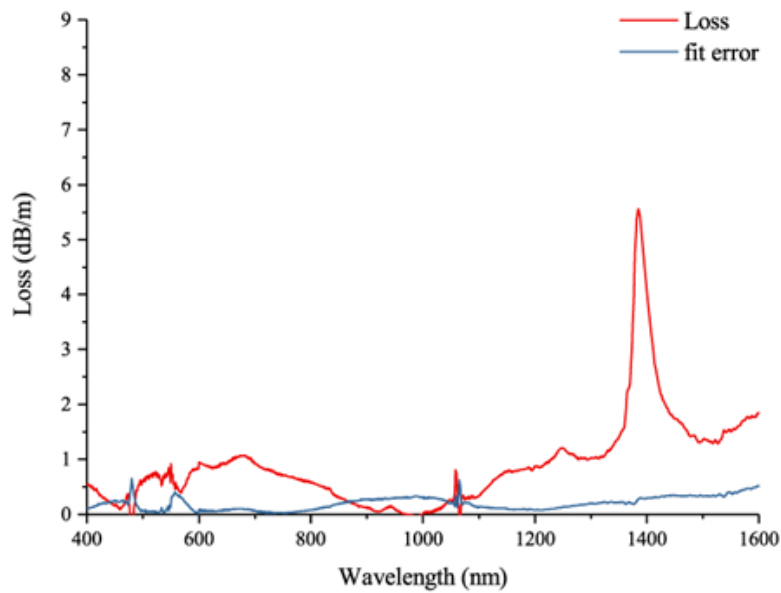

Figure D3: Loss measurement of an ECF with a core diameter of 2 μm. The red line shows loss result and the blue line shows the error for each wavelength. Figure is adapted from [144].

Appendix E: CVD-based growth of TMDs on ECFs

Different TMD crystals have been grown on the ECFs during this research, for instance, MoS_2, WS_2, WSe_2, and $MoSe_2$. The procedure to grow monolayer TMDs on the ECFs is analogous to the method that has been used for planar substrates. Thanks to the all-silica ECF, there is no obstacle to the high temperature from the CVD reactor. Here, we utilized a modified CVD process where the sulfur precursor is delivered by a Knudsen-type effusion cell. The transition metal precursor of TMD comes from the metal oxide powder MoO_3 or WO_3. The chalcogen precursors are created from sulfur or selenium powders. For each type of TMD, two precursors were put in two different zones, which were heated independently. The illustration of a modified CVD process is shown in Figure 2.11. The sulfur powder was put in a reusable quartz container (Knudsen cell) and was heated to 200 $^\circ$C. The sulfur precursors were delivered to the reaction zone at a controllable evaporation rate. MoO_3 powder was sprinkled on a small SiO_2/Si wafer and placed in the second zone, where the temperature was 770 $^\circ$C, and kept at that temperature for 20 minutes.
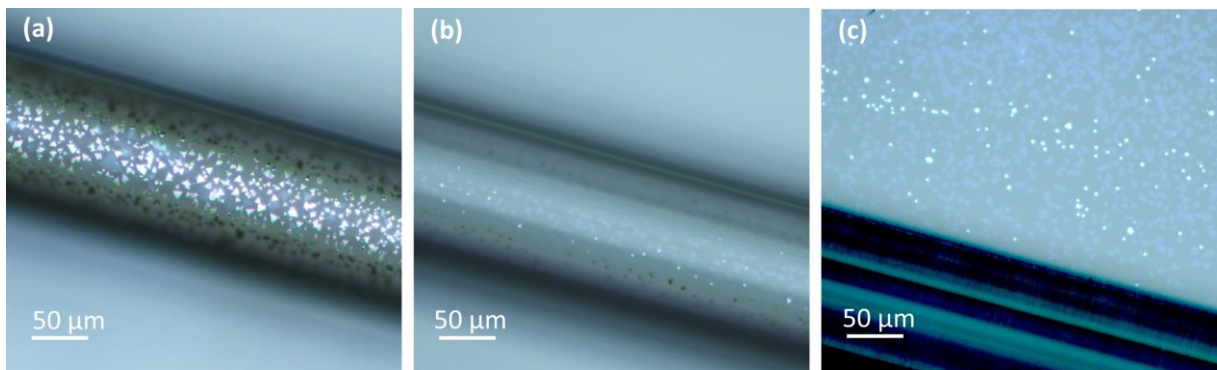
Figure E1: Microscopic images of MoS$_2$ crystals. (a) A section of ECF with low density of single crystal. **(b)** A section of the same ECF with a high density of single crystal. **(c)** High-density growth of MoS_2 monolayers on the SiO_2 substrate.

The ECFs have been fixed on a glass substrate with an upward orientation of the exposed surface. In this way, the chance to grow TMDs on the exposed core is better because the gas can flow along the trench of the ECF. As a consequence, TMD crystals grew freely along the trench as well as on all surfaces of the ECFs. For those crystals located on the exposed side of the core, they can interact with the guided modes and generate the PL and nonlinear response. Depending on the specific growth conditions, we achieved both monolayer and multilayer TMDs on the ECFs. Figure E1 displays the microscopic images of MoS_2 crystals grown on ECFs. The low density of the monolayer can be seen in Figure E1a, whereas Figure E1b is the region where the monolayers are grown the most. Figure E1c displays the densely coated monolayer MoS_2 on the SiO_2 substrate.

In addition to the crystal density, by changing the growth parameters, we can obtain a bigger crystal size but with a separate distance between each monolayer MoS_2. This batch of fiber has been used

in a thermal ablation process to create isolated crystals on the fiber core and is displayed in Figure E2. As discussed hereinbefore, ECFs can be applied to all 2D materials. Figure E3 displays $MoSe_2$ monolayers grown on the fiber. The fiber was coupled with a CW-laser which has a central wavelength of 532 nm. Several peaks around 600 nm are distributed to the Raman emission from the bare ECF. The PL from $MoSe_2$ monolayers through the fiber has a central peak at 786 nm with an FWHM of 33 nm. Figure E4 shows WSe_2 monolayers grown on the fiber. The grown crystals have different sizes and shapes. The fiber was scanned with a pulsed laser which has a central wavelength of 530 nm. The PL from WSe_2 monolayers on the core region has a central peak at 743 nm with an FWHM of 55 nm.
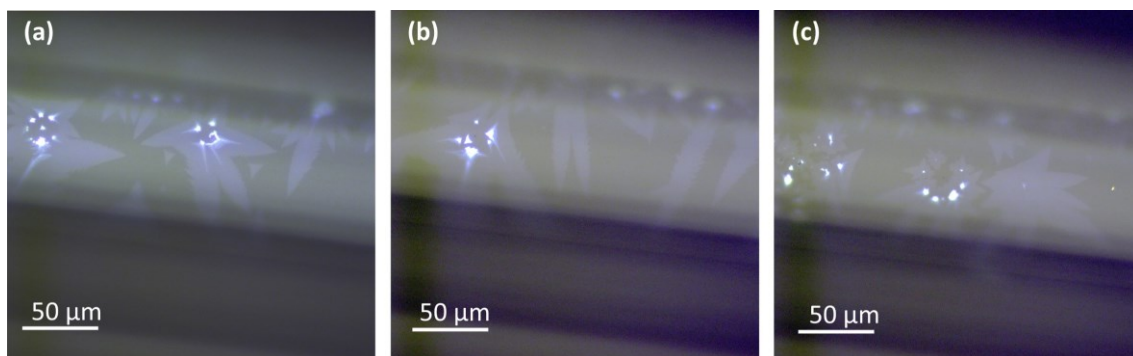
Figure E2: Microscopic images of MoS₂ crystals. (a-c) Three different sections of an ECF grown with MoS₂ monolayers with a large crystal size.
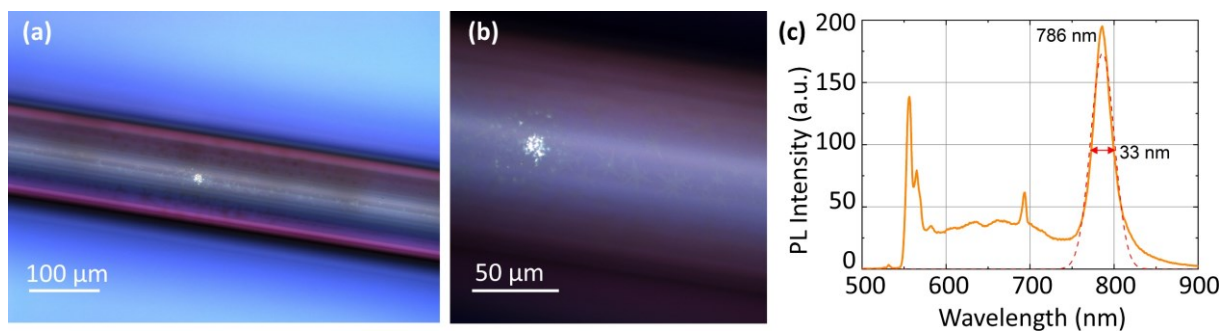
Figure E3: Microscopic images of MoSe₂ crystals. (a) An entire section of a MoSe₂-coated ECF under the microscope. **(b)** The zoom-in region to show clearly the monolayers on ECF. **(c)** In-fiber PL spectrum recorded by the excitation of a 532nm-CW laser.
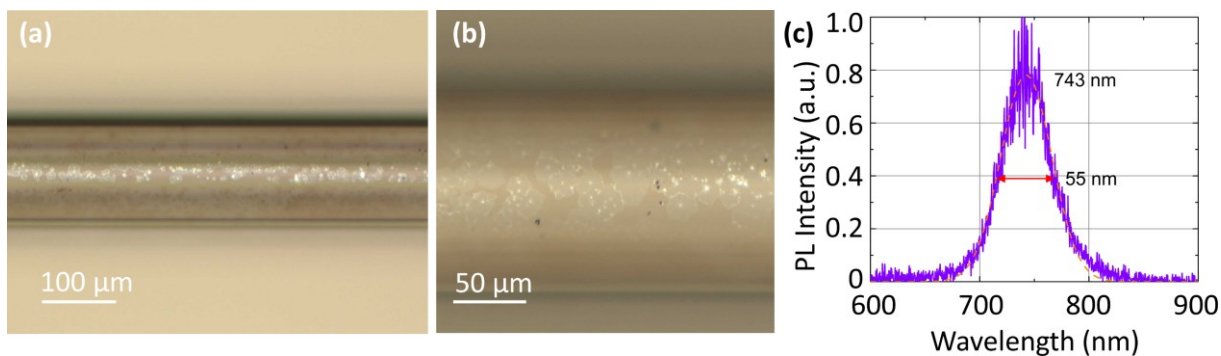

Figure E4: Microscopic images of WSe2 crystals. (a) An entire section of a WSe₂-coated ECF under the microscope. **(b)** The zoom-in region to show clearly the monolayers on ECF. **(c)** PL spectrum recorded by the excitation of a 530nm-pulsed laser from WSe₂ monolayer on the fiber core.

Appendix F: Abbreviations

2D	Two-dimensional	$MoSe_2$	Molybdenum diselenide
3D	Three dimensional	OPO	Optical parametric oscillator
AC	Armchair	PM	Phase matching
AFM	Atomic force microscopy	PL	Photoluminescence
CCD	Charge coupled device	SCG	Supercontinuum generation
CVD	Chemical vapor deposition	SEM	Scanning electron microscope
CW	Continuous wave	SH	Second harmonic
DFT	Density functional theory	SHG	Second-harmonic generation
ECF	Exposed-core fiber	SPDC	Spontaneous parametric down conversion
FCF	Fluorescence capture fraction	SPE	Single photon emitter
FM	Fundamental mode	SPM	Self-phase modulation
FW	Fundamental wave	TH	Third harmonic
hBN	Hexagonal Boron Nitride	THG	Third-harmonic generation
HOM	High-order modes	THz	Terahertz
$LiNbO_3$	Lithium niobate	TMD	Transition-metal dichalcogenide
NIR	Near infrared	UV	Utraviolet
MOCVD	Metal organic chemical vapor deposition	VIS	Visible
		WS_2	Tungsten disulfide
MoO_3	Molybdenum trioxide	WSe_2	Tungsten diselenide
MoS_2	Molybdenum disulfide	ZZ	Zigzag

Appendix G: Symbols

Symbol	Meaning/Description
$E_{b,n}$	Binding energy of the electron-hole pair
E_0	Effective Rydberg constant
E_G	Bandgap energy of the material
μ_{ex}^*	Reduced effective mass of the electron-hole system
m_e^*	Effective mass of the electron
m_h^*	Effective mass of the hole
$\hbar$	Reduced Planck constant
e	Elementary charge
n	Principal quantum number
$\boldsymbol{P}_i^{(2)}$	Nonlinear polarization field in SHG process along i^{th} Cartesian direction of the incident field
$\chi_{ijk}^{(2)}$	Second-order nonlinear susceptibility in i^{th} Cartesian direction with the interplay of the electric fields in j^{th} and k^{th} Cartesian directions
$\boldsymbol{P}_i^{(3)}$	Nonlinear polarization field in THG process along i^{th} Cartesian direction of the incident field
$\chi_{ijkl}^{(3)}$	Third-order nonlinear susceptibility in i^{th} Cartesian direction with the interplay of the electric fields in j^{th}, k^{th} and l^{th} Cartesian directions
$\boldsymbol{E}_{x,y,z}$	x, y, z component of the electric field
ω	The angular frequency
ε_0	Vacuum permittivity
Δk	Momentum mismatch
k_i	Wavenumber at i^{th} frequency
k_0	Wavenumber in free space
ε_r	Relative permittivity
n_i	Refractive index at i^{th} frequency
L	Length of nonlinear medium
$\gamma^{(THG)}$	Spatial overlap between the fundamental mode at fundamental wave and high-order mode at third harmonic wave
n_2	Nonlinear refractive index of the nonlinear medium
d_{eff}	Effective nonlinear susceptibility

c	Light speed in vacuum
λ_0	Vacuum wavelength
a	Radius of fiber core
n_{co}	Refractive index of the fiber core
n_{cl}	Refractive index of the cladding
NA	Numerical aperture
V	Fiber parameter
$I_{\mathrm{s},\lambda}$	Transmitted light intensity at the output of 2D-coated fiber
$I_{0,\lambda}$	Transmitted light intensity at the output of bare fiber
T_λ	Transmission of 2D-coated fiber
E_{ad}	Adsorption energy
ρ	Charge density
$\alpha(\lambda)$	Absorption coefficient of the measured gas
C	Gas concentration
r	Relative sensitivity coefficient
$\boldsymbol{H}^*_{x,y,z}$	Complex conjugate of x, y, z component of the magnetic field
n_{eff}	Effective refractive index of the guided mode
n_{r}	Refractive index of the gas
μ_0	Vacuum permeability
FCF_j	Fraction of fluorescence that is excited by mode j
NOI	Normalized field-matter overlap integral
A_{eff}	Effective mode area
$S_j(\vec{r})$	z-component of the Poynting vector of the jth mode
ξ	The fluorophore efficiency
$n_F^{A_s}$	The refractive index in the exposed region at the fluorescence wavelength
γ	The attenuation coefficient
ω_i	Angular frequency at i^{th} resonance of silica
B_i	Strength of ith resonance

λ_i	Vacuum wavelength at i^{th} resonance
β	Mode propagation of a pulse at angular frequency ω_0
β_2	Group velocity dispersion of fiber at angular frequency ω_0
$\mathbf{S}_z$	z-component of time-averaged Poynting vector
$I_{\text{SHG}}^{\parallel}$	Second harmonic intensity from TMD crystal with the fundamental harmonic and second harmonic polarized parallel to each other
$I_{\text{SHG}}^{\perp}$	Second harmonic intensity from TMD crystal with the fundamental harmonic and second harmonic polarized perpendicular to each other
θ	Angle between the incident laser polarization and *x*-direction of the experimental coordinate system
φ	Angle between the armchair direction of the crystal and *x*-direction
I_0	Maximum SHG intensity
α	Angle between crystal plane and *x*-direction
β	Angle between the armchair direction and the *x*-direction projected to crystal plane
η_{jk}	Conversion efficiency of the kth fundamental wave into the jth second harmonic mode
$P_{\text{FW},k}$	Average power of propagating fundamental wave in the kth mode
$P_{\text{SH},jk}$	Average SH power generated in the jth mode of the fiber and excited by k^{th} mode of fundamental harmonic
δ_{jk}	Phase mismatch of the kth fundamental mode and the jth second harmonic mode
f	Repetition rate of pulsed laser
T	Full-width at half-maximum of the pulse duration
ξ_{jk}	Field overlap between the kth fundamental mode and the jth second harmonic mode
A_{jk}	Effective mode area formed by the kth fundamental mode and the jth second harmonic mode

Appendix H: Acknowledgements

Thank you to all members of 2D in the Photonics group, Integrated Quantum Systems group, and Nanooptics group for open discussion in the group seminar, spending time together after work, and gathering at Vietfresh to make my Ph.D. life more colorful. I would like to express my gratitude to my colleagues, who have spent time reading and sharing their ideas on how to make my thesis better.

Last but not least, I would like to express my profound gratitude to my family, especially my beloved wife and son, who have always been beside me with unfailing support and continuous encouragement. Thank you so much to believe in me!

> *Ph.D. is a long journey, and we may stumble many times. We will be stronger every time we fall. We may face our darkest days, but in the darkness, be the light. Thank you, Duyen Dao and Bao Chau, for always being with me.*

Appendix I: Ehrenwörtliche Erklärung

Ich erkläre hiermit ehrenwörtlich, dass ich die vorliegende Arbeit selbständig, ohne unzulässige Hilfe Dritter und ohne Benutzung anderer als der angegebenen Hilfsmittel und Literatur angefertigt habe.

Die aus anderen Quellen direkt oder indirekt übernommenen Daten und Konzepte sind unter Angabe der Quelle gekennzeichnet.

Bei der Auswahl und Auswertung folgenden Materials haben mir die nachstehend aufgeführten Personen in der jeweils beschriebenen Weise unentgeltlich geholfen:

1. Die CVD-Wachstumsprozedur der MoS_2-Monolagen wurde durch die Arbeitsgruppe um Prof. Andrey Turchanin vom Institut für Physikalische Chemie der Friedrich-Schiller-Universität Jena, insbesondere durch Anleitung von Emad Najafidehaghani, Ziyang Gan und Antony George durchgeführt.
2. Freigelegte Kernfasern wurden von Gruppen von Prof. Heike Ebendorff-Heidepriem und Prof. Markus Schmidt zur Verfügung gestellt.
3. Die SHG-Messung mit hochbeschichteten Fasern als Funktion der Wellenlängen wurde von Dr. Alessandro Tuniz durchgeführt.
4. Die Modellierung der SHG für die Eingangspolarisation wurde von Sara Khazaee in Absprache mit mir durchgeführt.
5. Die Ablation von MoS_2-Kristallen auf ECF wurde zusammen mit Malte Per Siems, Institut für Angewandte Physik der Friedrich-Schiller-Universität Jena, durchgeführt.
6. 6-fache Mustersymmetrie der SHG von MoS_2-Monolagen auf SiO_2-Wafern wurde zusammen mit Fatemeh Alsadat Abtahi, Institut für Angewandte Physik der Friedrich-Schiller-Universität Jena, durchgeführt.
7. Die rasterelektronenmikroskopische Aufnahme der Faser wurde zusammen mit Dr. Heiko Knopf durchgeführt.
8. Die Impulscharakterisierung von Mira OPO-X von APE wurde von Maximilian Weissflog durchgeführt und die Impulscharakterisierung von Toptica FemtoFiber pro IRS-II wurde von Nils Geib durchgeführt.
9. Die Gasmessung mit NH_3 wurde unter meiner Aufsicht und zusammen mit Magdalena Hilbert, Institut für Angewandte Physik der Friedrich-Schiller-Universität Jena, durchgeführt.

Weitere Personen waren an der inhaltlich-materiellen Erstellung der vorliegenden Arbeit nicht beteiligt. Insbesondere habe ich hierfür nicht die entgeltliche Hilfe von Vermittlungs- bzw. Beratungsdiensten (Promotionsberater oder andere Personen) in Anspruch genommen. Niemand hat von mir unmittelbar oder mittelbar geldwerte Leistungen für Arbeiten erhalten, die im Zusammenhang mit dem Inhalt der vorgelegten Dissertation stehen.

Die Arbeit wurde bisher weder im In- noch im Ausland in gleicher oder ähnlicher Form einer anderen Prüfungsbehörde vorgelegt.

Die geltende Promotionsordnung der Physikalisch-Astronomischen Fakultät ist mir bekannt.

Ich versichere ehrenwörtlich, dass ich nach bestem Wissen die reine Wahrheit gesagt und nichts verschwiegen habe.

Jena, 17.08.2023   Unterschrift d. Verfassers

Gia Quyet Ngo